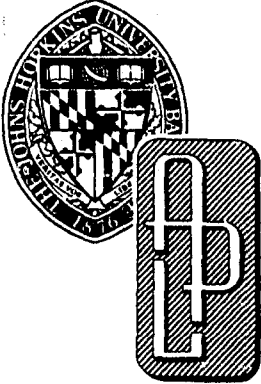


JHU/APL DST-7
FISCAL YEAR 1979

LEVEL

(12)



APPLIED PHYSICS LABORATORY

DEVELOPMENTS IN SCIENCE AND TECHNOLOGY

AD A 098095

DTIC FILE COPY

Approved for public release; distribution unlimited.

DTIC
ELECTE
S APR 23 1981 D

A

THE JOHNS HOPKINS UNIVERSITY • APPLIED PHYSICS LABORATORY
Johns Hopkins Road, Laurel, Maryland 20810
Operating under Contract N00024-78-C-5384 with the Department of the Navy

8 1 4 23 015

REPORT DOCUMENTATION PAGE

<p>1. REPORT NUMBER JHU/APL DST-7</p>	<p>2. GOVT ACCESSION NO. AD-A098095</p>	<p>3. RECIPIENT'S CATALOG NUMBER</p>
<p>4. TITLE (and Subtitle) Developments in Science and Technology</p>		<p>5. TYPE OF REPORT & PERIOD COVERED Annual Report Fiscal Year 1979</p>
<p>7. AUTHOR(s) Various</p>		<p>6. PERFORMING ORG. REPORT NUMBER JHU/APL DST-7</p>
<p>9. PERFORMING ORGANIZATION NAME & ADDRESS The Johns Hopkins University Applied Physics Lab. Johns Hopkins Road Laurel, Maryland 20810</p>		<p>8. CONTRACT OR GRANT NUMBER(s) N00024-78-C-5384</p>
<p>11. CONTROLLING OFFICE NAME & ADDRESS Naval Plant Representative's Office Johns Hopkins Road Laurel, Maryland 20810</p>		<p>10. PROGRAM ELEMENT, PROJECT, TASK AREA & WORK UNIT NUMBERS Various</p>
<p>14. MONITORING AGENCY NAME & ADDRESS Naval Plant Representative's Office Johns Hopkins Road Laurel, Maryland 20810</p>		<p>12. REPORT DATE Fiscal Year 1979</p>
<p>16. DISTRIBUTION STATEMENT (of this Report)</p>		<p>13. NUMBER OF PAGES 165</p>
<p>17. DISTRIBUTION STATEMENT (of the abstract entered in Block 20, if different from Report)</p>		<p>15. SECURITY CLASS. (of this report) Unclassified</p>
<p>18. SUPPLEMENTARY NOTES</p>		<p>15a. DECLASSIFICATION/DOWNGRADING SCHEDULE</p>
<p>19. KEY WORDS (Continue on reverse side if necessary and identify by block number) See attached list</p>		
<p>20. ABSTRACT (Continue on reverse side if necessary and identify by block number) This is a compilation of brief accounts of the Laboratory's significant accomplishments during Fiscal Year 1979 that can be reported on an unclassified level. The following areas are covered: military systems technology, space science and technology, computer technology applications, energy research and development, bio-medical science and engineering, ocean science and technology, fundamental research, and urban technology.</p>		

19.

aids for handicapped
airborne research flights
antenna patterns
chemically induced magnetic polarization
cruise missiles
distributed processing handbook
economic modeling of geothermal energy
environmental assessment of cooling towers
external ECG recorder
fire fatalities
flamable gases from plastic
geothermal energy market study
geothermal reservoir analysis
hydrogen transport
hyperfine interactions
intracellular calcium crystals
intracranial pressure
laser Doppler velocimeter
lidar tracer
Loran Navigation Receiving System
low-energy swell systems
Magnetic Field Satellite
OTEC heat exchanger
phase transitions
pH data collector
radiation-produced displacement
RAM aerodynamics
satellite cryogenic refrigerator
Satellite Missile Tracking System
software engineering system
sun glitter fluctuations
Surface Effect Ship seal dynamics
tactical speech synthesis
theory of vision
Towed Underwater Launch Platform
UHF communications
vehicle-follower control law
Voyager at Jupiter

14

JHU/APL-DST-7
FISCAL YEAR 1979

9 Annual report for FY 1979.



11 1979

12 157

APPLIED PHYSICS LABORATORY

6 **DEVELOPMENTS
IN SCIENCE
AND TECHNOLOGY.**

Approved for public release; distribution unlimited.

THE JOHNS HOPKINS UNIVERSITY • APPLIED PHYSICS LABORATORY
Johns Hopkins Road, Laurel, Maryland 20810
Operating under Contract with the Department of the Navy

15

031 650

mt

FOREWORD

The Applied Physics Laboratory (APL), a division of The Johns Hopkins University, is located in Howard County, Maryland, midway between Baltimore and Washington. Its work is carried out under contractual agreements between the University and the federal, state, and local governments. About 95 percent of its effort is covered by a contract with the Department of the Navy. APL employs a staff of more than 2500 including 1300 professional scientists and engineers, of whom more than half have advanced degrees. Their ideas are implemented and extended through several field activities and a network of associate contractors and collaborators from coast to coast.

The primary mission of APL is to enhance national security and welfare by applying advanced science and technology to the solution of problems important to national objectives. The Laboratory conducts programs in fundamental and applied research, exploratory and advanced development, component engineering, systems engineering and integration, and test and evaluation of operational systems. It has increased its efforts in nondefense areas, including space research, to over 15 percent, with the concurrence of the Department of Defense.

APL was established in 1942 at the urgent request of the Office of Scientific Research and Development to demonstrate that science and technology could advance national security more effectively through an active partnership of military and civilian technologists than through the traditional buyer-supplier relationship. The concept was validated in less than a year when APL developed the first practical variable time (VT) fuze. This initial product proved to be a major contributor to the air defense of the Fleet and to Allied victories in the air war over Britain and the Battle of the Bulge.

After the war, at the request of the Secretary of the Navy, the University agreed to continue the Laboratory as an important national resource. APL quickly became a leader in guided missile technology and, with its associate contractors, produced missiles for the Fleet. It then became necessary to integrate those missiles with launchers, computers, radars, displays, and other elements of a ship. This activity continues as new weapons and new ships come into being and as old ships are modernized. APL is now involved in developing the methods to integrate, communicate, and operate a Battle Group consisting of several ships.

In addition to the Laboratory's varied systems activities on behalf of the surface fleet, it continues to provide technical evaluation of the operational Fleet Ballistic Missile System. Quantitative test and evaluation procedures are applied to every newly commissioned ballistic missile submarine — Polaris, Poseidon, and Trident — when it joins the Fleet. Similarly, APL currently provides precise evaluation of the Army's Pershing missile programs. Significant programs are also under way for Naval strategic communications and tactical targeting.

FOREWORD

The Applied Physics Laboratory (APL), a division of The Johns Hopkins University, is located in Howard County, Maryland, midway between Baltimore and Washington. Its work is carried out under contractual agreements between the University and the federal, state, and local governments. About 95 percent of its effort is covered by a contract with the Department of the Navy. APL employs a staff of more than 2500 including 1300 professional scientists and engineers, of whom more than half have advanced degrees. Their ideas are implemented and extended through several field activities and a network of associate contractors and collaborators from coast to coast.

The primary mission of APL is to enhance national security and welfare by applying advanced science and technology to the solution of problems important to national objectives. The Laboratory conducts programs in fundamental and applied research, exploratory and advanced development, component engineering, systems engineering and integration, and test and evaluation of operational systems. It has increased its efforts in nondefense areas, including space research, to over 15 percent, with the concurrence of the Department of Defense.

APL was established in 1942 at the urgent request of the Office of Scientific Research and Development to demonstrate that science and technology could advance national security more effectively through an active partnership of military and civilian technologists than through the traditional buyer-supplier relationship. The concept was validated in less than a year when APL developed the first practical variable time (VT) fuze. This initial product proved to be a major contributor to the air defense of the Fleet and to Allied victories in the air war over Britain and the Battle of the Bulge.

After the war, at the request of the Secretary of the Navy, the University agreed to continue the Laboratory as an important national resource. APL quickly became a leader in guided missile technology and, with its associate contractors, produced missiles for the Fleet. It then became necessary to integrate those missiles with launchers, computers, radars, displays, and other elements of a ship. This activity continues as new weapons and new ships come into being and as old ships are modernized. APL is now involved in developing the methods to integrate, communicate, and operate a Battle Group consisting of several ships.

In addition to the Laboratory's varied systems activities on behalf of the surface fleet, it continues to provide technical evaluation of the operational Fleet Ballistic Missile System. Quantitative test and evaluation procedures are applied to every newly commissioned ballistic missile submarine — Polaris, Poseidon, and Trident — when it joins the Fleet. Similarly, APL currently provides precise evaluation of the Army's Pershing missile programs. Significant programs are also under way for Naval strategic communications and tactical targeting.

APL has contributed to fundamental knowledge in such areas as high-altitude physics, spectroscopy, flame propagation, the origin and evolution of the universe, supersonic combustion, supersonic and hypersonic aerodynamics, chemical kinetics, and magnetic resonance. A major contribution to national security and space technology was made when APL conceived, demonstrated, and reduced to practice new principles of navigation through the Transit Navigation Satellite System. The system currently provides the Navy and commercial vessels with worldwide positioning information that is far more accurate than was previously possible.

APL is a substantial contributor to national objectives other than defense. Biomedical research and engineering; transportation; fire research; reduction of pollution of the biosphere; ocean thermal, geothermal, and flywheel energy systems; air traffic control; leak detection in natural-gas distribution lines; and advanced education are some examples of the areas to which attention has been devoted in recent years. The Laboratory has also become a leader in developing scientific satellites and exploring physical phenomena in solar planetary and interstellar space, as well as in applying satellite sensors to the precise measurement of terrestrial characteristics.

The role of computer applications within APL has become so interwoven in all of the Laboratory's technical, systems, and administrative functions that progress in this area is difficult to report as separate accomplishments. However, by extensive and intensive use of integrated circuits and microprocessor logic in satellites, in radar and other naval systems, and in biomedical engineering and other civil areas, APL has become a recognized leader in this area of computer technology. Furthermore, it continues to pioneer in innovative applications of computers of all sizes to problems of national importance. This trend is underscored throughout the document by the frequent references to computing as an integral part of most of the accomplishments reported herein.

To support its R&D activities through knowledge and experience in advanced research, the Laboratory performs basic research in biological, chemical, mathematical, and physical sciences related to its various missions. Through unique applications of system engineering, science, and technology to the needs of society, APL has enhanced the University's tradition of excellence while gaining worldwide recognition of its own.

This report contains only selected samples of APL technical accomplishments in Fiscal Year 1979 (1 October 1978 through 30 September 1979). Some major programs were excluded because they are still in process. Others were omitted in order to keep the report unclassified. Still other projects are so broad in scope as to be unsuitable for concise reporting at this time. Thus, the accomplishments reported herein are not an exhaustive presentation of APL activities. However, they encompass many of the types of technical effort carried on during the reporting period.

CONTENTS

MILITARY SYSTEMS TECHNOLOGY

Introduction	12
Aerodynamics of the Rolling Airframe Missile <i>L. E. Tisserand</i>	14
Review of Technology Improvement Areas for Cruise Missiles <i>L. L. Cronvich and H. P. Liepman</i>	16
Development Program for Loran Navigation Receiving System <i>W. J. Peters III, J. E. Boyd, and L. F. Fehlner</i>	18
Conceptual Study of the Towed Underwater Launch Platform <i>J. J. Wozniak</i>	23
A Statistical Approach to Determining Antijam Requirements for UHF Communications <i>R. L. Holland, K. T. Plessner, and A. E. Scheck</i>	25

SPACE SCIENCE AND TECHNOLOGY

Introduction	30
Operation of Satellite Cryogenic Refrigerators in Space <i>C. S. Leffel, Jr.</i>	32
Voyagers 1 and 2 Encounters with Jupiter <i>E. P. Keath and S. M. Krimigis</i>	34
The NASA Magnetic Field Satellite (MAGSAT) <i>L. D. Eckard, Jr.</i>	37
The MAGSAT Magnetometer Boom <i>J. F. Smola</i>	39
Attitude Signal Processor for MAGSAT <i>T. Zaremba, W. A. Swartz, K. J. Heffernan, and G. H. Fournrain</i>	43
Evaluation of SATRACK System Performance <i>R. J. Anderson, L. J. Levy, T. Thompson, and R. B. Hester</i>	46
SATRACK Post Flight Receiver <i>L. L. Warnke</i>	49

COMPUTER TECHNOLOGY APPLICATIONS

Introduction	54
An Automatic System for Measuring Antenna Patterns <i>R. L. Trapp and C. H. Ronnenburg</i>	56
The Computer Assisted Software Engineering System <i>M. H. Gates and W. S. Amey</i>	59
A Distributed Processing Handbook <i>S. A. Kahn</i>	62

Tactical Speech Synthesis 64
D. F. Sterne

ENERGY RESEARCH AND DEVELOPMENT

Introduction	68
Environmental Assessment of Saline Drift from the Chalk Point Natural Draft Cooling Tower <i>E. A. Davis and J. H. Meyer</i>	70
Testing of the APL OTEC Heat Exchanger as an Evaporator <i>P. P. Pandolfini, J. L. Keirse, and J. A. Funk</i>	74
Geothermal Energy Market Study on the Atlantic Coastal Plain <i>W. J. Toth</i>	76
Geothermal Reservoir Analysis <i>K. Yu and F. C. Paddison</i>	80
Economic Modeling of Geothermal Energy in the Eastern United States <i>W. F. Barron (Metro Center) and W. J. Toth, F. C. Paddison, and K. Yu (APL)</i>	83

BIOMEDICAL SCIENCE AND ENGINEERING

Introduction	89
Low-Cost Voice-Actuated Controller for the Handicapped <i>A. E. Davidoff</i>	90
Portable pH Data Collector <i>W. Schneider and D. B. Klein</i>	92
Intracranial Pressure during Wakefulness and Sleep <i>L. J. Viernstein (APL) and G. Gucer (JHMI)</i>	94
Three-Dimensional Laser Doppler Velocimeter <i>O. J. Deters and C. B. Bargeron</i>	96
Occurrence and Identification of Intracellular Calcium Crystals in Pulmonary Specimens <i>V. J. Vigorita, P. K. Gupta, and J. K. Frost (JHMI) and C. B. Bargeron (APL)</i>	99
External ECG Recorder System for Use with the Automatic Implantable Defibrillator <i>R. E. Fischell, C. A. Blackburn, and S. F. Oden</i>	101

OCEAN SCIENCE AND TECHNOLOGY

Introduction	107
Analytical Investigation of a Simplified Model to Study Temporal Fluctuations of Sun Glitter <i>F. W. Riedel</i>	108
Detection of Low-Energy Swell Systems with the SEASAT SAR <i>R. C. Beal</i>	110

Airborne Research Flights in Antarctica and Greenland	113
<i>R. L. Hickerson</i>	
Laser Radar Instrument for Measuring Seal Dynamics in the Surface Effect Ship	116
<i>T. M. Rankin and M. J. Mayr</i>	

FUNDAMENTAL RESEARCH

Introduction	123
<i>Ab Initio</i> Calculation of the Transport Properties of Hydrogen	124
<i>L. Monchick (APL) and J. Schäfer (Max-Planck Institute)</i>	
Excitation of an Elastic Half-Space by a Buried Line Source of Conical Waves	125
<i>A. N. Jette and J. G. Parker</i>	
Valence Bond Study of Hyperfine Interactions and Structure of Kr_2F and the F_3^- Defect in LiF	128
<i>F. J. Adrian and A. N. Jette</i>	
Theory of Chemically Induced Magnetic Polarization: Effect of the S-T ₁ Mixing in Strong Magnetic Fields	131
<i>F. J. Adrian and L. Monchick</i>	
Ising Model of Phase Transitions	134
<i>R. A. Farrell and S. Fuvin (APL) and J. T. Sullivan, S. Vimolvanich, and P. H. E. Meijer (Catholic University)</i>	
Theory of Vision	136
<i>J. F. Bird</i>	

URBAN TECHNOLOGY

Introduction	140
Implementation of a Vehicle-Follower Control Law for Short-Headway AGT Systems	142
<i>A. J. Pue</i>	
Human Fatalities from Unwanted Fires	144
<i>W. G. Berl and B. M. Halpin</i>	
Determination of the Flammable Gases Evolving from a Burning Plastic	146
<i>L. W. Hunter</i>	
A New Lidar/Fluorescent Tracer Technique for Atmospheric Research	147
<i>J. R. Rowland and T. G. Konrad</i>	

PATENTS

152

PUBLICATIONS AND PRESENTATIONS

156

AUTHOR INDEX

164

MILITARY SYSTEMS TECHNOLOGY

INTRODUCTION

Many changes in Navy missiles have occurred since APL pioneered in the 1950's in designing the first missiles to be deployed in defense of the Fleet. However, many major characteristics of the early designs have been retained. The new Standard Missile-2 (SM-2) has far greater capability than its predecessors, the beam-riding Terrier and the basic Tartar. On the other hand, SM-2 operates within the same RF band, uses similar guidance laws, and has the same airframe diameter. The retention of these and other basic characteristics has greatly facilitated improving and upgrading the Terrier/Tartar/Standard Missile family while maintaining Fleet readiness. Rather than being constraints, early engineering decisions have proven in many cases to be the key to subsequent developments.

The Laboratory has been a world leader in developing airbreathing missiles for Naval forces beginning in 1945 with the Cobra, the first accelerating supersonic ramjet. The Talos ramjet missile, developed in the 1950's, became operational in 1958 and was retired from active service in December 1979 after providing long-range air defense to the Fleet for more than two decades.

Over the years, APL's role has changed from design agent to technical support advisor to the Navy. The Laboratory has continued its active participation in many ongoing missile programs by working closely with the Department of Defense and numerous prime contractors for missile systems. The SM-2 program is an example of APL's involvement in virtually all phases of a missile development program that has successfully progressed from concept formulation through design engineering to at-sea testing. Other programs to which the Laboratory is making major contributions include Harpoon and Tomahawk and the self-defense RAM Missile System. Investigations are being carried out in connection with the exploration of wide area guidance concepts and advanced work on new propulsion systems, with emphasis on the integral rocket-ramjet.

Two articles in this section are representative of tasks pursued at APL in 1979 in support of missile programs. APL has provided substantial technical support to NAVSEA as the RAM Missile System has progressed through concept validation flight tests and advanced development, finally entering full-scale engineering development in 1979. One article addresses all aspects of this continuing support. It describes unique wind-tunnel measurements for predicting the aerodynamic forces and moments of the RAM missile. The tests represent the first known attempt to measure in a wind tunnel a spinning body-canard-tail configuration that exercises canard steering in phase with body roll position.

Cruise missile system development is considered in the next article. It provides an overview of recent advances in the areas of aerodynamics, propulsion, and structures/materials related to cruise missiles and recommends research that will lead to an integrated approach to overall performance improvement.

Since the inception of the Polaris missile development program, APL has provided technical evaluation of the operational Fleet Ballistic Missile System. Quantitative test and evaluation procedures have been developed and applied to

every newly commissioned ballistic missile submarine and associated weapon system — Polaris, Poseidon, and Trident. (Similar evaluations are performed for the Army's Pershing Missile System and for the Naval Strategic Communications Systems.) The continuing development of strategic weapon systems results in a demand for more advanced evaluation techniques and capabilities. One benefit often realized from an improved evaluation capability is an improved operational capability.

The Loran Navigation Receiving System, described in this section, is the most accurate Loran-C positioning system developed to date. It can track eight Loran-C signals simultaneously. As weapon system evaluation and oceanographic research become more sophisticated, greater accuracy — such as this system can provide — is required to determine a ship's position. The system was developed for the Navy's Nuclear-Powered Fleet Ballistic Missile Submarine (SSBN) tests, but benefits for other Navy and commercial programs may eventually be realized.

During the development of a new fleet ballistic missile or submarine, underwater launches establish the in-tube and underwater portions of missile flight. The introduction of the new Trident weapon system has resulted in the design of the weapon system test support facility described in the next article. The study demonstrated the feasibility of a towed submersible platform to support an underwater launch test program. This concept can provide enhanced capability to evaluate systems, with greater flexibility than full-scale system tests at significant cost savings.

During the design and development of U.S. Navy missiles, radars, and communications systems, careful consideration must be given to the environment in which they are expected to operate. In any modern conflict, this environment would include hostile enemy electronic countermeasures (ECM) that are intended to degrade or defeat U.S. system capabilities. Large-scale use of ECM was seen during the Southeast Asia conflict and the 1973 war in the Middle East. Thus, an ECM environment should be considered the normal operating environment for modern electronic military systems. APL's work with missile, radar, and communications systems has led to the evaluation of hostile ECM capabilities and electronic counter-countermeasures (ECCM) requirements for Navy systems.

The last article deals with a model developed to analyze system requirements of Navy communications systems in an ECM environment. It describes a mathematical model developed to evaluate the requirement for anti-jam ultrahigh frequency (UHF) communications within a Navy battle group. The model presents a statistical approach to UHF propagation that gives a closer approximation of actual communications performance.

During the last decade, both United States and foreign naval combat forces and weapons systems have become increasingly complex while the potential pace of battles between such forces has accelerated. This trend, which is expected to continue in the decade ahead, has required the development of improved systems and techniques to coordinate and control the complex forces. APL is playing an expanding role in the technical evolution of the systems, from concept to Fleet deployment.

AERODYNAMICS OF THE ROLLING AIRFRAME MISSILE

A unique investigation into the aerodynamics of the Block I Rolling Airframe Missile (RAM) has been carried out. It was the first known attempt to measure in a wind tunnel the aerodynamic forces and moments that act on a spinning body-canard-tail configuration that exercises canard steering in phase with body roll position. The brief exploratory test has demonstrated that a better understanding and a more complete definition of the aerodynamics of rolling, steering vehicles can be developed by way of simulative wind-tunnel testing.

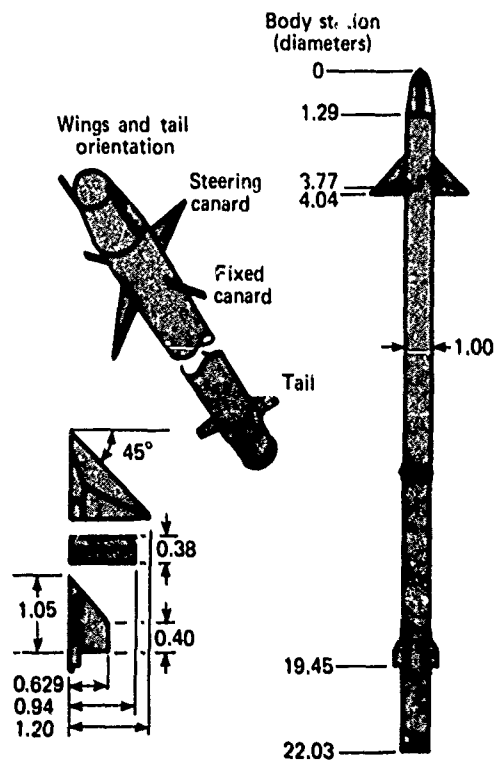
BACKGROUND

For guidance-related reasons, there is considerable interest in rolling airframes having single-plane steering capability. Prior to this effort, aerodynamic characteristics used in designing and evaluating rolling, steering missiles have been derived from wind-tunnel data collected on nonspinning models and from the cumulative experience gained from analyses of flight-test data. Those aerodynamic descriptions of rolling airframes emphasize their longitudinal stability and control characteristics but ignore the possibility of induced side forces and yawing moments.

A short exploratory test was planned (Ref. 1) and carried out using the newly fabricated free-to-spin model (Fig. 1) of the RAM configuration (a) to check out the model, the test procedures, and data acquisition and (b) to probe its aerodynamics under dynamic-flight conditions at representative transonic and supersonic speeds. It was recognized that follow-on testing would be required to define the aerodynamics of the configuration throughout its performance envelope, and also to conduct the configurational breakdown investigations appropriate to identifying and sizing relevant aerodynamic causes and effects.

DISCUSSION

The model body is 42.41 in. long and its outer diameter is 1.925 in. A special sting support was designed and fabricated to be compatible with this very large length-to-diameter ratio. Packaged inside the model are (a) a five-component strain-gauge balance to measure the orthogonal components of the total aerodynamic forces (less drag) and moments that act on the model, (b) a DC motor to provide roll torque supplemental to aerodynamic rolling-driving moment, and (c) an interchangeable steering cam to produce mechanically sinusoidal deflection of the steering surfaces in phase with body roll position. The



Note: Dimensions normalized with body diameter (1.92 in.)

Fig. 1 External geometry of model.

sting support, balance, motor, and cam are locked together as one unit that does not spin; the model is slip-fitted over, and fastened to, a spin-bearing case that is free to rotate. The roll rate of the model can be controlled remotely by regulating the power supply to the torque motor.

Pretests showed that the model's mass asymmetry in roll is quite small and that the effects of motor-generated heat and of magnetic fields on the performance of the balance are negligible. The resonant frequencies of the cantilevered model-balance-sting combination are 12, 22, and 24 Hz.

A dynamic variable to be duplicated in tunnel testing is the missile's spin parameter, $\phi d/2V$ (where d is the diameter and V the total velocity of the vehicle), rather than the missile's roll rate, ϕ . Hence, to simulate the flight conditions associated with missile roll rates of 8 to 15 Hz, it is necessary for the 0.385-scale model to experience steady-state roll rates of 15 to 30 Hz. Resonant frequencies within the simulative

range of model roll rates would have been a serious problem had it not been for the ability to control the roll rate of the model remotely. Figure 2 shows, for Mach 1.2 and 2.5, the model roll rates tested and the equivalent missile roll rates (evaluated at sea level) determined from the equivalence of the missile's spin parameter.

Measurements were obtained over an angle-of-attack range up to about 16° . The effects of data-sampling rate, roll rate, Reynolds number, Mach number, and steering control (directed *in* and *out* of the angle-of-attack plane) on the configuration's "rigid-body" aerodynamics were examined. The pertinent results follow (viewed in an axis system that pitches with the model but does not spin with it). Additional details are given in Ref. 2.

The normal force and pitching moment data provide smooth definitions of the configuration's longitudinal stability and control characteristics. These forces and moments are not sensitive to the tested roll rates or to Reynolds number.

Small side forces and associated yawing moments, induced out of the plane of maneuver, show dependence on Mach number, angle of attack, steering-deflection amplitude (i), and spin parameter. Figure 3 shows the effects of angle of attack and steering-deflection amplitude on side force and yawing moment coefficients at Mach 1.19. In this illustration, the 20° peak-steering deflection occurs *in* the angle-of-attack plane. Before this test, aerodynamic descriptions of rolling, steering airframes omitted aerodynamics induced in the yaw plane because there were no experimental data on which to base predic-

tions. The importance of the induced side forces and yawing moments to the airframe's dynamic-flight behavior can be evaluated in future investigations.

Aerodynamic contributors to rolling characteristics were investigated. During the data-taking periods, the model's roll rate was maintained accurately at a constant value by the remote roll-rate controller with its roll-rate feedback loop engaged. Using the tachometer output, the balance roll-gauge output, and aerodynamic roll-driving moments (evaluated from nonspin test runs), the airframe's roll-damping characteristics were calculated by solving the equation of motion in roll under steady-state conditions. Figure 4 shows the effects of angle of attack and roll rate on calculated roll-damping coefficients at Mach 2.51. Damping characteristics previously were taken to be linearly dependent on roll rate. Other results show that steering control directed in or out of the angle-of-attack plane can affect substantially the aerodynamic contributors to rolling characteristics.

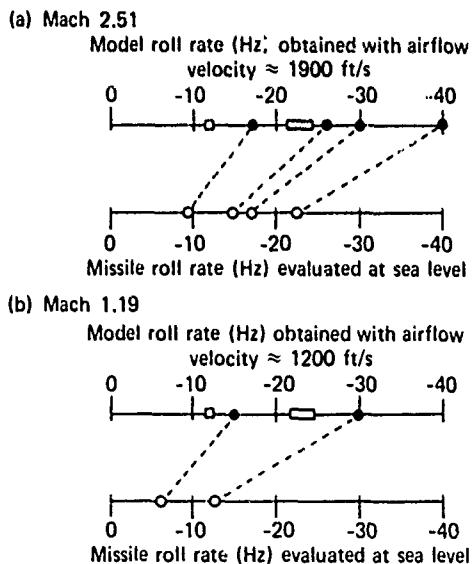


Fig. 2 Model roll rates tested and equivalent missile roll rates.

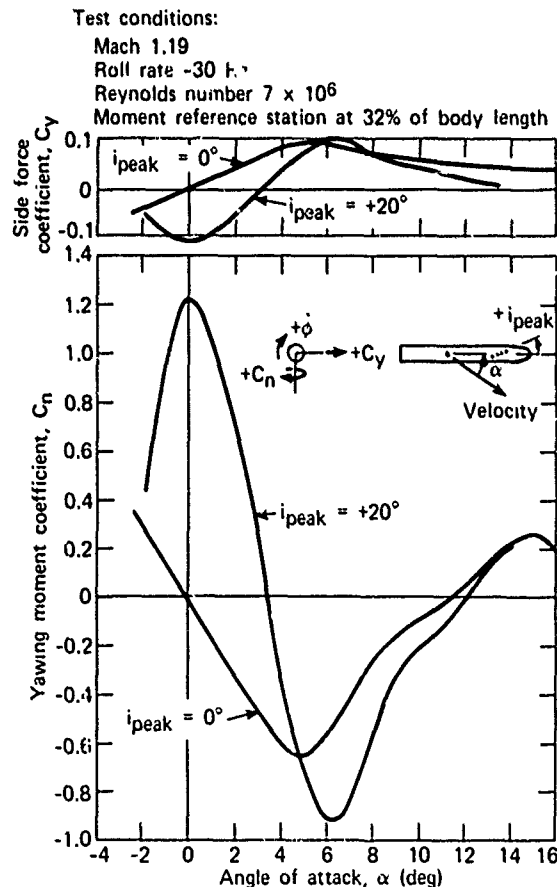


Fig. 3 Variation in induced side force and yawing moment coefficients with angle of attack and steering-deflection amplitude.

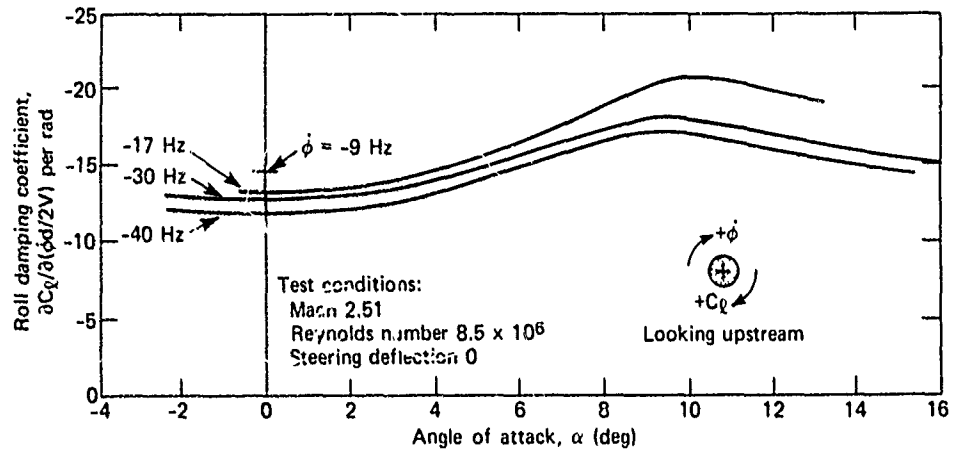


Fig. 4 Variation in roll damping coefficient with angle of attack and roll rate.

REFERENCES

1. L. E. Tisserand, *Test Plan for Wind Tunnel Investigation in the 0.385-Scale ASMD Block I Rolling, Steering Airframe - Phase One*, APL/JHU BF-D-1-77-032, 30 Nov 1977.

2. L. E. Tisserand, *Wind Tunnel Investigation by APL/JHU of the 0.385-Scale Block I Rolling Airframe Missile - Results from Phase One Testing*, APL/JHU BF-D-1-79-012, 31 Jul 1979

Author: L. E. Tisserand

Support: NAVSEASYSKOM, PMS-404-50

REVIEW OF TECHNOLOGY IMPROVEMENT AREAS FOR CRUISE MISSILES

Research advances in the technologies of aerodynamics, propulsion, and structures/materials are related in this review to performance improvements in cruise missile systems for subsonic to hypersonic speeds. The broad definition of cruise missile is used, i.e., a missile that operates for most of its flight time at nearly constant altitude and speed. Recommendations are made for research in several specific areas of those technologies and in a related area — suppression of the sensor signature — so that such research will lead to significant improvement in overall performance.

BACKGROUND

The NASA Langley Research Center is assessing the significance of advanced aerodynamic, propul-

sion, and structural technology for cruise missile systems to provide a rationale for planning a research program in those areas and the outline of a plan for such a program. APL was asked to contribute to the assessment by applying its experience in missile research and development to the specific question of improving cruise missile performance through advanced technologies and their interactions (Ref. 1).

DISCUSSION

Areas for potential improvement in cruise missile performance (penetrativity, range, time to target, terminal accuracy, and prelaunch survivability) and for economic improvement (cost reduction, simplicity, and logistics) have been related to physical

and design factors such as observables, speed, maneuverability, producibility, and operability, each of which involves one or more of the technologies under consideration. Since improvements in range and time to target involve essentially the same technologies, these two parameters can be reduced to one, range. The same is true for improvements in terminal accuracy and in prelaunch survivability, both of which imply greater maneuverability. Hence, the five areas can be reduced to three: penetrativity, range, and maneuverability.

The status of current cruise missiles and of research related thereto was reviewed briefly, and specific topics of research and development that

might contribute to performance improvements were listed. Figure 1 illustrates this process for one performance parameter, penetrativity. In this example, ten research topics that would improve penetrativity are identified. Similar charts were prepared for range and maneuverability.

Twenty-five specific topics of research were identified in this manner, a number much too large for practical planning with available resources. By considering which topics would be the greatest help to system analysts and designers in their trade-off studies for advanced missile concepts, the number was reduced to sixteen. Table 1 shows how six recommended research topics to improve penetrativity can

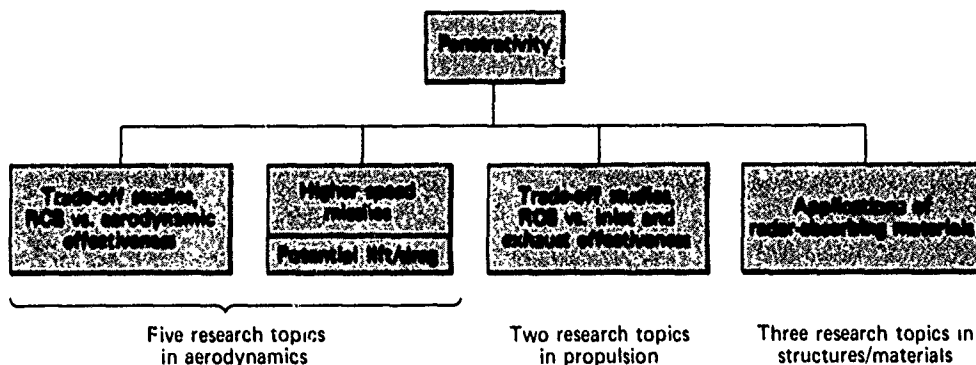


Fig. 1 Technology improvement areas related to penetrativity.

TABLE I
PENETRATIVITY IMPROVEMENT AND TECHNOLOGY AREAS

Technologies	Aerodynamics	Propulsion	Structures/Materials	Signature
Measures of merit	Aerodynamic forces and moments Stability margins Control effectiveness	Inlet drag, pressure recovery, air capture Exit nozzle net thrust	Weight Volume Ease of manufacture	Radar, IR, optical as function of aspect angle, wavelength, polarization, etc.
Missile components	Body Surfaces Full configurations	Inlet(s) Exit nozzle(s) Full configurations	Conventional structural elements and radar absorbing material (RAM) Radar absorbing primary structural elements (RAPS) Fully assembled configurations	
Recommended research topics	Aerodynamics-signature trade-off Airframe-engine integration	Inlet-signature trade-off Nozzle-signature trade-off	Analysis methods for structural trade-offs RAM-coated structure versus RAPS	

be selected from among ten (Fig. 1) because they relate specifically to measures of merit and missile components involved in the iterative design trade-off cycle. Similar charts were made for the other areas.

RECOMMENDATION

Since the sixteen priority research topics may be more than a realistic research budget can support, the final recommendation was reduced to six, two in each of the three technology areas, as listed below.

Aerodynamics

1. **Aerodynamics-Signature Trade-Off** — measurements of the radar cross section (RCS) and relevant aerodynamic characteristics of configurations and their components (bodies, fixed and movable surfaces, protuberances, depressions, gaps, fillets, and radii of leading and trailing edges), and trade-off studies between RCS and aerodynamic effectiveness for modifications in the geometry or location of those components.
2. **High-Angle-of-Attack Aerodynamics** — continued research in aerodynamics at high angle of attack and in methods to reduce or control resultant dynamic coupling.

Propulsion

1. **Inlet-Signature Trade-Off** — measurements of RCS and propulsion parameters (mass capture, pressure recovery, cowl drag, and uniformity of flow into engine) of inlets of various shapes and body lo-

cations, and trade-off studies between RCS and inlet performance.

2. **Fuel Development** — further development of fuels (liquid, liquid plus additives, and solid) to improve energy per unit volume or weight, to increase density, and to improve physical characteristics (strength, safety, and combustion efficiency).

Structure/Materials

1. **RAM-Coated Structure versus RAPS** — development of RAPS, and comparison with non-radar-attenuating primary structure that is coated with RAM to reduce RCS.
2. **Development and Application of Composites** — development of low-cost fabrication methods, process technology, methods of attachment, methods of stress analysis, and criteria for instability and buckling of advanced composite materials applied to missiles.

REFERENCE

1. L. L. Cronvich and H. P. Liepman, *A Review of Technology Improvement Areas for Cruise Missiles*, APL JHU BI D-0-79-001, Apr 1979.

Authors: L. L. Cronvich and H. P. Liepman

Support: NASA Langley Research Center

DEVELOPMENT PROGRAM FOR LORAN NAVIGATION RECEIVING SYSTEM

The objective of the Loran Navigation Receiving System (LONARS) Program was to develop an accurate Loran-C navigation system (200 ft radial (rss) real time and 50 ft radial (rss) post mission) (rss is the root sum square of the uncertainty in the mean and the standard deviation for each axis). It was to be used by the U.S. Navy during SSBN Demonstration and Shakedown Operations (DASO) to evaluate initial-condition launch errors of the Polaris/Poseidon/Trident weapon systems, to evaluate the performance of the navigation system, and to provide real-time position for the acquisition of missiles by the range safety radar during launches. LONARS became operational in February 1979; it has demonstrated a real-time geodetic accuracy of better than 80 ft radial (rss) and a post-mission accuracy of 30 ft radial (rss) in areas where the system was calibrated. LONARS is unique because of its advanced computerized signal processing technology, its ability to track both the A and the B phase codes from up to eight Loran-C transmitters, and the significant improvement in accuracy over other Loran-C radio navigation systems.

BACKGROUND

Weapon system evaluation and range safety require a very accurate position reference system for DASO tests on SSBN's. A survey and comparison of several commercial radio navigation systems was conducted by APL in 1975 to find a system with suitable accuracy and capability. It had to provide the necessary accuracy at least out to 60 nmi from shore and be able to recover from loss of signal at sea. The study and field test failed to locate a system that could meet these requirements (Ref. 1).

Experience with Loran-C convinced many people that it had the potential to provide positioning with greater accuracy than usual (Ref. 2). Under a U.S. Air Force contract, APL had designed a Loran-C super receiver in 1972 (Ref. 3), but no hardware was produced. This experience, together with the announced improvements in Loran-C coverage for the U.S. coastal confluence zone, prompted APL to propose a highly accurate Loran-C system for submarine testing. The proposed system, LONARS, was approved by the Navy's Strategic Systems Project Office, and development was begun in April 1977.

SYSTEM DEVELOPMENT

The first phase of LONARS development was to assemble a prototype system to demonstrate that

the accuracy requirements could be achieved. The 50 ft radial (rss, post mission) goal was met (Ref. 4). During the next phase, three shipboard sets (LONARS-SS) were assembled. The complete LONARS system was installed and calibrated in the fall of 1978. Additional calibration exercises were conducted in February and May 1979 after some initial defects in the complex software were corrected. LONARS became operational in February 1979. It is operated by personnel of the Naval Ordnance Test Unit (NOTU).

DESCRIPTION

The primary functions of LONARS are to provide accurate real-time ship's position and an accurate record of the positions after the ship has returned to port. To support the post-mission use of the data, a pattern monitor station (LONARS-PMS) is installed at a known, fixed location on shore. Position errors indicated by the PMS are attributed to irregularities in the Loran-C signals, and the data from the shipboard LONARS are corrected correspondingly. This process minimizes the effect of irregularities in the emission times of the loran signals.

The LONARS-SS and LONARS-PMS are depicted in Fig. 1. The commercially available Hewlett-Packard and Kennedy components have been installed in special electronics boxes suitable for transporting and installing temporarily aboard a submarine.

The APL loran sensor comprises a tuned R1 receiver that has been modified to permit computer control of receiver gain, an oscilloscope for display, an analog-to-digital converter, and a digital interface set for computer communications. The sensor uses a built-in 5 MHz crystal oscillator but can accept a cesium beam standard or other external clock. Four manually adjustable notch filters are available on the Austron receiver. Built-in circuitry supplies a variable-amplitude 100 kHz test signal for calibration and checkout.

To operate the system, the computer program is loaded from a tape cartridge in the terminal. Greenwich mean time is set, the program is started, and search mode commences. In the present configuration, LONARS searches for two master stations: Carolina Beach, N.C. (GRI code 9930) and Malone, Fla. (GRI code 7980). When the second master is found, the program enters settle/track

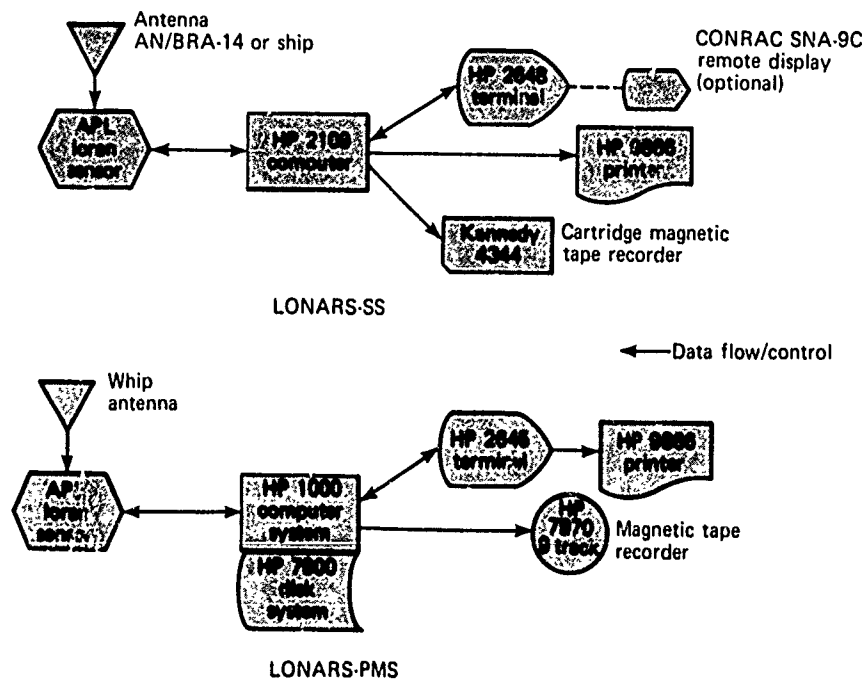


Fig. 1 Block diagrams of LONARS-SS and LONARS-PMS.

mode. In this mode, the program adjusts the receiver gain for each signal, positions each quadrature (zero crossing) strobe on a positive-going zero crossing, and locates the standard track point on each pulse. Each Loran-C station's A and B phase code group is considered to be a separate signal and is tracked separately. A signal pair from a station is regarded as settled when both signals are adjusted in gain, are satisfactorily phase locked to the standard track point, and are giving the same time of arrival. When both Jupiter signals are settled, a time correction is computed and applied to synchronize LONARS time with coordinated universal time (UTC). This step ensures that pattern monitor corrections will be synchronized accurately with the data from the set aboard ship.

When the signals from the four primary stations are settled, a "data-good" indication is provided in the output status word and on the CRT display. The display is a representation of the Florida coastline and operating areas; cross hairs indicate present ship's position. The displayed data give the measured time differences, UTC, latitude, longitude, speed north and east, a status word containing coded program information, and a predicted dead-reckoned position. The screen is updated with new data about once per second, and time of arrival data are collected for recording at the same rate.

As the LONARS program continues in settle/track mode, a background routine called a nuisance search attempts to locate other loran signals being received. These signals are placed in track, and data from the four primary stations are not taken when a cross-rate conflict occurs. If the nuisance signal is quite weak, it is dropped from track to make way for stronger signals that could cause more serious cross-rate interference. LONARS can track up to 16 loran signals or the A and B phase code pairs of eight stations.

CALIBRATION

The purpose of the calibration was to determine empirically the values of the parameters to be used to transform LONARS measured time differences to latitude and longitude. The parameters were the effective time-difference propagation velocities, the effective mission delays, and two coordinate pairs assigned to be equivalent, thereby establishing a direct relationship between the time difference and latitude/longitude coordinate systems. Three calibrations were performed: in November 1978 and in February and May 1979.

During the May 1979 calibration, two LONARS-SS were installed side by side, connected to

a common antenna but isolated by very wide band attenuators. The position reference for this test was the three-range DM-43 Autotape System. The LONARS and Autotape antennas were installed side by side on the highest mast located amidships on the USNS *Range Sentinel*. The LONARS-PMS was run continuously during the two at-sea calibration days.

The current parameters determined from the third calibration are presented in Table 1. It was necessary to adjust the coordinates of the PMS 36 ft north and 38 ft west of the surveyed location in order to remove a small bias of LONARS at sea.

PERFORMANCE

The measured time differences from the at-sea data were converted to latitude and longitude using the transformation parameters of Table 1 for comparison with the Autotape at-sea reference. The processed differences were then plotted and analyzed. Figures 2 and 3 depict the LONARS post-mission error in latitude and longitude. The track of the survey ship is plotted in Fig. 4. A statistical summary of the data in Figs. 2 and 3 is presented in Table 2

CONCLUSIONS

The results of the calibration data analysis show conclusively that LONARS accuracy exceeds the real-time and post-mission requirements. The system accuracy is estimated to be 80 ft (rss) real time and 30

TABLE 1
LONARS CALIBRATION PARAMETERS

	Time Difference A	Time Difference B
Loran GRI code	9930	7980
Stations	Carolina Beach, N.C. Jupiter, Fla.	Malone, Fla. Jupiter, Fla.
Effective propagation speed (m/ μ s)	299.764	299.513
Effective emission delay (μ s)	13 694.144	45 199.707
Assigned PMS coordinates	28°25'2.76"N	80°36'25.18"W

TABLE 2
AT-SEA LONARS CORRECTION STATISTICS*

	Latitude (ft)	Longitude (ft)
Mean	-3	1
rms	10	13
rss of rms	16	

*Based on 4818 comparisons with Autotape data taken at sea, 23 May 1979.

ft (rss) post mission in the Cape Canaveral operating area (Table 3). The uncertainty in the mean shown in Table 3 reflects an allowance for errors in the survey

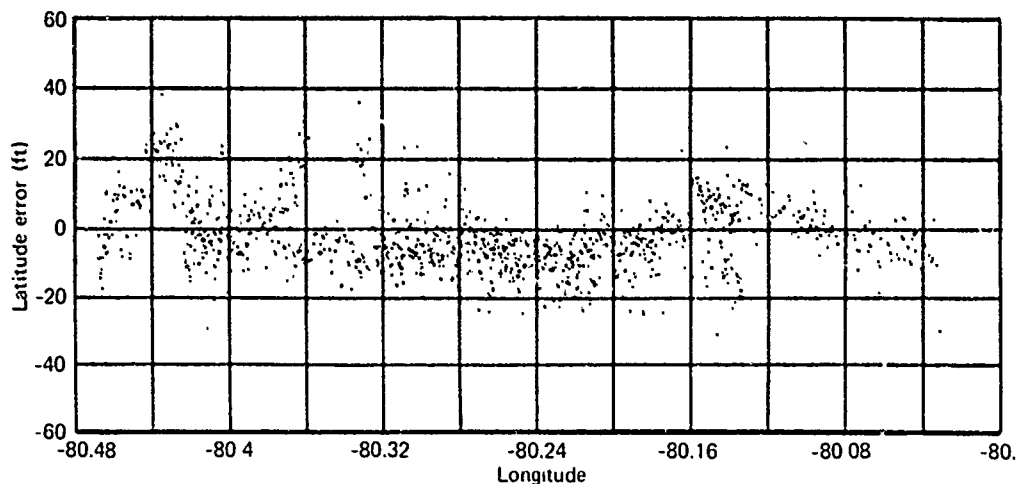


Fig. 2 LONARS post-mission error in latitude.

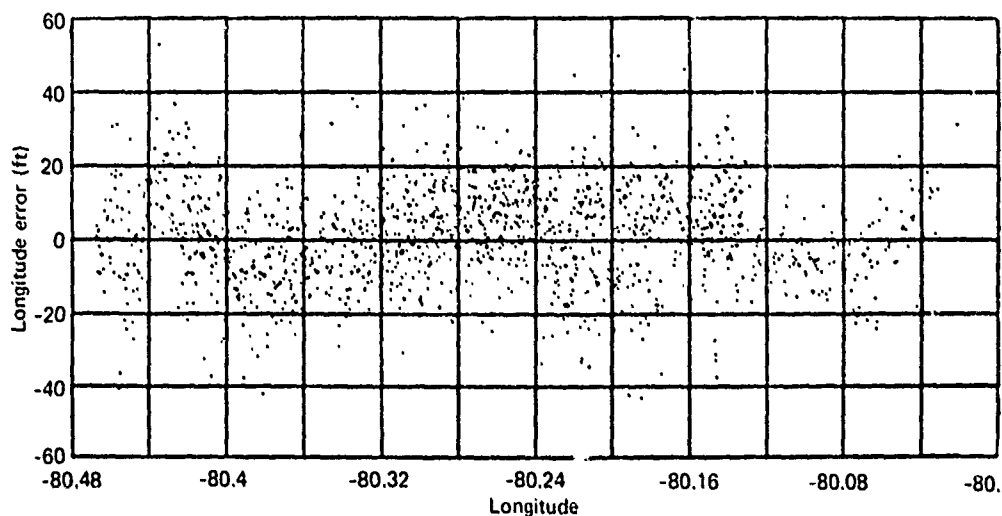


Fig. 3 LONARS post-mission error in longitude.

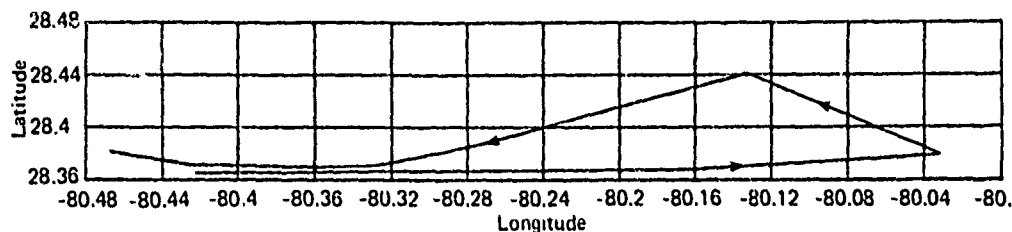


Fig. 4 Track of USNS Range Sentinel, 23 May 1979.

TABLE 3
ESTIMATED LONARS ACCURACY

	Real Time		Post Mission	
	Latitude	Longitude	Latitude	Longitude
Mean Error	0	0	0	0
Uncertainty of mean (ft)	50	50	15	15
Standard deviation (ft)	30	30	10	15
rss	80		30	

of Autotape responder sites, systematic Autotape error, and (for real time only) allowance for variations in the Loran-C signals.

REFERENCES

- 1 A. K. Halso, Jr., I. G. Parsons, D. A. Brown, and W. J. Peters III, *PREDEM Test Results*, APL JHU POR-2040, 17 Dec. 1979
- 2 I. F. Fehlner and T. A. McCarty, "How to Harvest the Full Potential of Loran-C," *Inst. Navig.* 21, No. 3, Fall 1974, pp. 223-233
- 3 I. F. Fehlner et al., *Summary Report on USAF Super Receiver/Navigator Development*, APL JHU IC 1220, Jun 1973
- 4 J. E. Boyd et al., *Loran Navigation Receiver System (LONARS) Phase I Development Report*, APL JHU POR-2670, 30 Apr 1978

Authors: W. J. Peters III, J. E. Boyd, and L. F. Fehlner

Support: Strategic Systems Project Office, SP-205 and SP-25

CONCEPTUAL STUDY OF THE TOWED UNDERWATER LAUNCH PLATFORM

The concept of a towed submersible platform for underwater launch tests in support of the development of advanced Trident missile and launcher systems was explored. This concept offers more flexibility than does a fixed underwater platform and may be more economical.

BACKGROUND

During the development of the Polaris and Poseidon systems, many underwater launches made use of an inert test vehicle to investigate the in-tube and underwater portions of flight. Those full-scale tests were conducted at the Naval Ocean Systems Center (NOSC) "pop-up" facility, off San Clemente Island, California, using platforms fixed to the ocean floor. To achieve more flexibility to meet the expanded test requirements for advanced Trident missile systems, APL embarked on a fresh approach to testing.

The general guidelines for testing require (a) full-scale tests over the range of tactical launch depths, (b) a wide range of fore-aft (crossflow) flow velocities, and (c) simulation of the flow condition about the deck and muzzle-hatch regions of the Trident submarine. In addition, it was desirable to keep the test facility costs low since testing was planned for an 18 month period after which the facility would be closed.

DISCUSSION

Platform Description

Platforms fixed to the sea bed are inherently expensive and are difficult to adjust over the range of launch depths. The concept of a submersible platform evolved to avoid such problems. Other factors to be considered were low resistance to forward movement and a high vertical virtual mass to moderate platform recoil in response to the launch impulse. The principal components of the Towed Underwater Launch Platform (TULP) are shown in Fig. 1. The basic structure consists of a deck frame formed by an I-beam matrix. A skewed flange welded to the curved casting on a Trident II mount tube adapts the tube to the deck frame. Four free-flooding tubular support struts between the deck frame and the mount tube provide

lateral and torsional rigidity. Plates secured to the top of the deck frame on two sides and along the bow aid in streamlining the flow and entrapping seawater to moderate the vertical response of the platform to the launch impulse. A free-flooding fairwater deck is included to approximate the flow field about the Trident submarine deck and muzzle hatch regions.

The mount tube is housed in a faired structure to provide a watertight compartment for test instrumentation and launching equipment, to permit access when on the surface, and to streamline the flow.

Platform buoyancy is provided by the faired housing and hard tanks mounted to the frame. One of the small tanks also provides nitrogen for tube pressurization. Engineering estimates of the principal

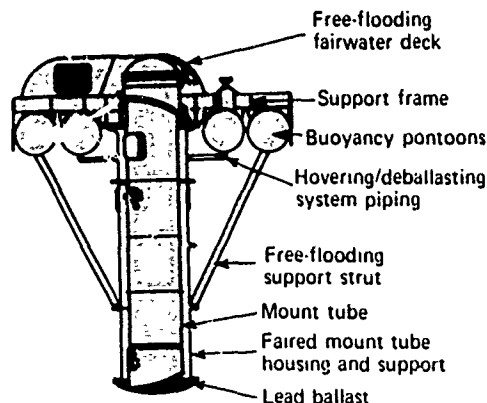
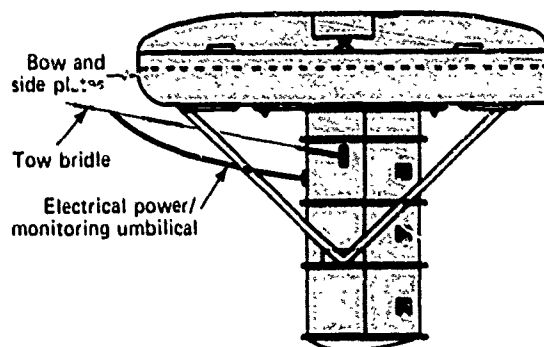


Fig. 1 Side and sectional views of the TULP.

features and some of the hydrodynamic characteristics of the TULP are shown in Table 1, taken from Ref. 1.

The concept includes a hovering deballasting system for platform submersion and recovery and for depth keeping while it is in tow. The two large innermost tanks serve as seawater blow and flood tanks. Each innermost tank is divided into two compartments, and the port-forward and the aft-starboard compartments serve as the blow tank; the other two serve as the flood tank. This arrangement ensures that seawater blowing out or flooding in will not cause the platform to list or pitch. A digital microprocessor located on the tow ship commands the flow control valves within the tanks. An analysis of the requirements and a preliminary design for the hovering/deballasting system are contained in Ref. 2.

The pitch and roll stability, the expected recoil to launch impulse, and the post-launch motion of the platform are analyzed in Ref. 1.

A study of the tow cable requirements (Ref. 3) has shown that a moderate-sized steel or stranded Kevlar cable could be used. Trail distances of 1000 to 1500 ft for the required range of forward-way speeds could be obtained with minor adjustments from neutral buoyancy using the hovering/deballasting system.

Site Selection

There are several possible sites for operating the TULP. One is at the Naval Submarine Base, Bangor, Washington. It has an Explosive Handling Wharf (EHW), which is designed for loading missiles

into Trident submarines. The EHW bay is enclosed, will readily hold the TULP, and is deep enough. A location for actual testing might be the Navy Torpedo Range in Dabob Bay, a protected, deep-water test range about 10 miles from the EHW. The range is heavily instrumented, with a three-dimensional acoustic tracking station and shore based photo-optical equipment. Photographic coverage could be obtained of the early portions of the test vehicle launch if cameras and lighting were installed on the deck of the TULP. The range also has several Navy support craft (YF-451 and YF-520) that would be well suited to support TULP operations. Figure 2 is an artist's concept of a crossflow launch of a Trident II test vehicle from the TULP.

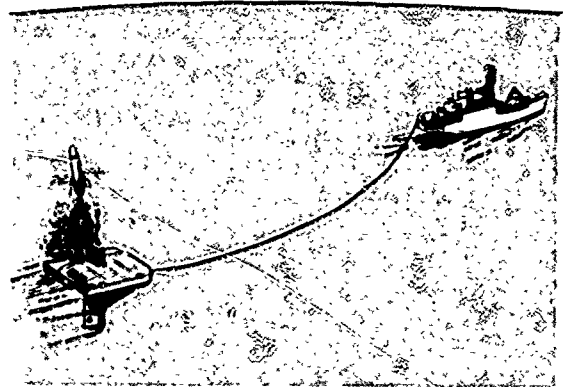


Fig. 2 Artist's concept of a crossflow launch of a Trident II test vehicle from the TULP.

TABLE 1
ESTIMATED PRINCIPAL CHARACTERISTICS
OF TOWED UNDERWATER LAUNCH PLATFORM

Principal dimensions (ft)	
Overall length	60
Overall beam	40
Overall height	47.5
Surfaced draft	39.5
Physical characteristics	
Weight (excluding test vehicle and reserve trim)	380 000 to 450 000 lb
Submerged displacement (excluding free flooding)	260 to 295 short tons
Reserve buoyancy	20 000 lb
Roll and pitch moment of inertia	3.0×10^6 slug-ft ²
Hydrodynamic characteristic:	
Center-of-gravity/center-of-pressure separation	1.7 to 2.2 ft
Forward-way drag at 5.0 kt	30 000 lb
Submerged tow at 5.0 kt	450 hp
Heave added mass (including free flooding)	1.65×10^5 slugs
Roll and pitch added moment of inertia	6.25×10^6 slug-ft ²
Roll and pitch natural period	18 to 19 seconds

The launch test vehicle could be recovered by using the range's remotely controlled recovery vehicle to locate it and secure a hook. A large ship could complete the recovery.

REFERENCES

1. J. J. Wozniak, *Follow-on Study of the Towed Underwater Launch Platform (TULP) Concept for Trident II Testing*, APL/JHU PM-8342, Oct 1978.

2. M. A. Konodi, *Preliminary Analysis of a Depth Control System for Towed Underwater Launch Platform*, APL/JHU PM-8367, Oct 1978.
3. B. F. Fuess, *Catenaries Computed for the Towed Underwater Launch Platform*, APL/JHU, BFD-3-78-009, 30 Nov 1978.

Author: J. J. Wozniak

Support: Strategic Systems Project Office, SP-22

A STATISTICAL APPROACH TO DETERMINING ANTIJAM REQUIREMENTS FOR UHF COMMUNICATIONS

A mathematical model has been developed to represent the stochastic process of ultra-high frequency (UHF) signal propagation over a finitely conducting rough surface. Heretofore, the absence of such a model has made it virtually impossible for a communications analyst to determine the statistics associated with single-signal propagation, much less to attempt a statistical characterization of the ratio of two or more interfering signals.

BACKGROUND

The Chief of Naval Operations requested APL to ascertain the value of antijamming protection to Navy tactical communications within a task force at sea. Implicit in this task was an analysis of the nature of UHF propagation over an ocean surface because the preponderance of Navy intra-task force links operate in that portion of the radio spectrum.

The most important fundamental conclusion to be drawn regarding the strength of a received UHF transmission near the earth's surface is that it is a stochastic quantity that may vary significantly, even when the transmitter (or transmitters) and receiver have fixed locations. The simple inverse-distance-squared computational procedure (and its concomitant deterministic result) is inadequate at best and it may yield misleading results because it implies a geometric boundary around a receiver beyond which

communications are denied and within which communications are unimpeded.

The procedure described here permits the communications analyst to calculate a probability of connectivity, P_c , for any transmitter-receiver-jammer encounter and further permits the calculation of the level of antijamming required to achieve a specified minimum probability of connectivity for that encounter.

DISCUSSION

Figure 1 depicts the basic circumstances associated with the reception of a UHF communications transmission at sea. The resultant electric field at the receiver has direct and reflected components associated with both the transmitter and the jammer.

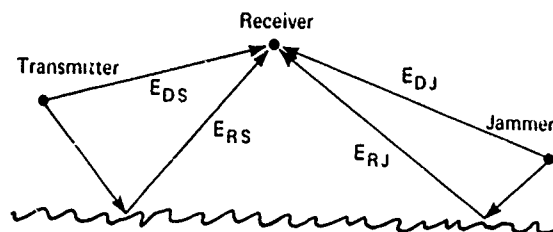


Fig. 1 Mixed propagation paths over a rough surface.

For illustration, we shall consider the transmitter to be a coherent source of radiation and the jammer to be an incoherent (noise) source, although an analogous technique has been developed for coherent jammers as well.

For the coherent transmitted signal, E_{DS} , the direct field phasor is deterministic rather than stochastic; however, the reflected field phasor, E_{RS} , is stochastic (Rayleigh distributed) because of the scattering characteristics of the ocean surface. The statistical variation of the amplitude of the resultant electric field is given by the Rice-Nakagami density function:

$$p(e_s) = \frac{2e_s}{\langle E_{RS}^2 \rangle} \left[\exp \left(-\frac{e_s^2 + E_{DS}^2}{\langle E_{RS}^2 \rangle} \right) \right] \cdot I_0 \left(\frac{2e_s E_{DS}}{\langle E_{RS}^2 \rangle} \right), \quad (1)$$

where I_0 is the modified Bessel function of order zero. Notice that $p(e_s)$ is determined whenever E_{DS} and $\langle E_{RS}^2 \rangle$ are both specified. When the ratio $E_{DS}/\langle E_{RS}^2 \rangle$ is sufficiently large, Eq. 1 can be closely approximated by a Gaussian probability density; therefore

$$p(e_s) = \frac{1}{\sqrt{2\pi}D(E_s)} \exp \left(-\frac{(e_s - \langle E_s \rangle)^2}{2D(E_s)} \right), \quad (2)$$

where $\langle E_s \rangle$ and $D(E_s)$ are the mean and the variance, respectively, of the resultant total electric field determined by Eq. 1.

For the incoherent jammer signal, the direct field phasor is not deterministic but rather is a quantity whose phase is uniformly distributed between 0 and 2π . The reflected field is Rayleigh distributed as before. The amplitude of the resultant electric field due to the jammer is given by the Rayleigh density function, thus

$$p(e_j) = \frac{2e_j}{\langle E_j^2 \rangle} \exp \left(-\frac{e_j^2}{\langle E_j^2 \rangle} \right), \quad (3)$$

where $\langle E_j^2 \rangle = \langle E_{DJ}^2 \rangle + \langle E_{RJ}^2 \rangle$. Note again that $p(e_j)$ is determined whenever $\langle E_{DJ}^2 \rangle$ and $\langle E_{RJ}^2 \rangle$ are specified.

The signal-to-jamming ratio (S/J), which is the quotient of two random variables, is also a random variable whose probability distribution function, $F(s/j)$, may be derived (laboriously) from the distributions $p(e_s)$ and $p(e_j)$. $F(s/j)$ is the probability that S/J assumes a value that is less than or equal to a

specific value of s/j . If this is so, then $P(S/J > s/j) = 1 - F(s/j)$. Figure 2 illustrates the general appearance of this function.

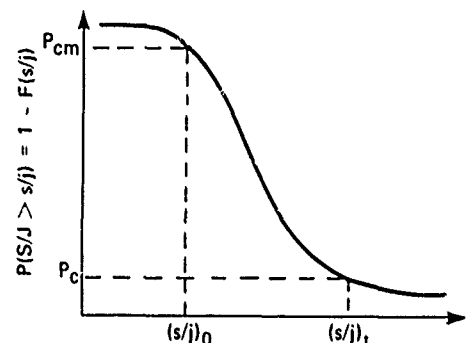


Fig. 2 Relationship of the S/J distribution function, link connectivity, and required antijamming protection link.

For a specific type of communications link, the associated transceivers have an intrinsic signal-to-jamming threshold value, $(s/j)_t$. Communications link connectivity is considered to exist only when $S/J > (s/j)_t$; therefore, the probability of connectivity may be defined as $P_c = 1 - F[(s/j)_t]$. Further, the communications analyst may specify a minimum acceptable probability of connectivity, P_{cm} . Associated with this value will be a minimum signal-to-jamming ratio $(s/j)_0$ such that $P_{cm} = 1 - F[(s/j)_0]$.

We define the minimum required antijamming protection level to be the improvement in S/J required to make equal the minimum acceptable and the actual connectivity probabilities. Such an antijamming level would, in essence, shift the statistics of S/J so as to make $P_{cm} = 1 - F[(s/j)_t]$. Therefore, the minimum required antijamming protection level is defined as

$$R = \frac{(s/j)_t}{(s/j)_0}$$

When $R > 0$ dB, antijamming protection is necessary to maintain a link connectivity probability of P_{cm} . If $R \leq 0$ dB, then $P_c \geq P_{cm}$, so no antijamming protection is required.

To apply this technique to a particular tactical scenario, the initial positions and velocity histories of the transmitter, receiver, and jammer platforms are input to a computer model. The antijamming protection required for the specified P_{cm} , as well as the

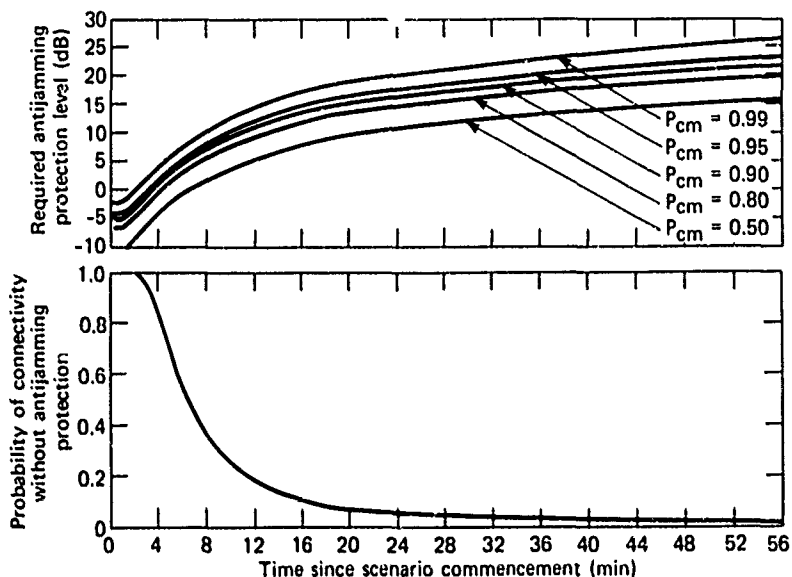


Fig. 3 Results of the statistical antijamming algorithm for a typical scenario.

probability of connectivity without antijamming protection, are computed and plotted as a function of time. Figure 3 is an illustration of the output for a typical scenario.

In this scenario, the separation between the transmitter and the receiver became larger as time progressed, while the jammer-receiver separation remained essentially constant. Consequently, the requisite amount of antijamming protection increased while the connectivity probability without antijamming protection decreased.

By identifying points in time at which critical communications events transpire, one may specify the amount of antijamming protection necessary for mission success. This protection may be applied to a

communications link by a variety of methods, such as increased power level, directive antennas, or spread-spectrum modulation. If, for example, it were critical to pass a message 28 minutes after the start of the scenario, the P_c without antijamming protection is about 5%. The application of 12 dB of protection would raise the probability to 50%, while 21 dB would be required to achieve 99%.

Authors: R. L. Holland, K. T. Plessler,
and A. E. Scheck

Support: Chief of Naval Operations, OP-96

SPACE SCIENCE AND TECHNOLOGY

INTRODUCTION

The Laboratory's involvement in space programs began in the postwar years when Aerobee and captured V-2 rockets carried Geiger tubes, magnetometers, and optical spectrometers high above the earth's surface. The flights provided the first high-altitude measurements of cosmic rays, the geomagnetic field, and atmospheric constituents such as ozone, and were conducted by pioneers James A. Van Allen, John J. Hopfield, and S. Fred Singer (who were then APL staff members). In 1946, a V-2 rocket carried the first camera installed by APL, to look at the earth from an altitude of 100 miles. From these distinguished beginnings, APL's record of accomplishments proceeds, including the conception, design, and development of the Transit Navigation Satellite System for the Navy.

The satellite activities spawned a multitude of "firsts" by APL, including the development of the first gravity-gradient satellite, the first photographs of the entire earth from synchronous satellites, the first solid-state particle detectors flown on a satellite, and the first extremely accurate measurements of the geomagnetic field.

The space activities at APL have been supported by a small but active program of basic research directed toward understanding the chemical and physical processes involved in the earth's atmosphere, ionosphere, and magnetosphere and in interplanetary phenomena. Some significant Laboratory achievements include the first detection of solar cosmic rays with satellite-borne solid-state detectors, the design and construction of one of the longest lived and most productive scientific satellites ever launched (1963-38C), the first measurement of short-period magnetohydrodynamic waves near synchronous altitude, the discovery of heavy ions trapped in the earth's radiation belts, the experimental confirmation of large-scale field-aligned currents in the auroral regions, the demonstration of the effect of stratospheric pressure variations on the ionosphere, and the development of radio astronomy techniques for predicting geomagnetic storms that can disturb terrestrial radio transmissions. The research activities have involved international collaborations with scientists from more than a dozen academic and defense organizations.

Other research programs include scholarly investigations of ancient astronomical records, which led to the suggestion that Ptolemy was a fraud; the discovery of plasma acceleration regions behind the earth that can generate charged particles with energies up to hundreds of thousands of electron volts; investigation of the interaction between the interplanetary magnetic field and the geomagnetic field (a possible link between solar activity and terrestrial weather); and the discovery that Jupiter is a prominent source of energetic particles in the earth's vicinity that previously were thought to originate in the sun.

NASA has selected scientists and engineers from APL to participate in a record number of interplanetary missions including Voyagers 1 and 2; Galileo, which is scheduled to orbit Jupiter; and Solar Polar, which will orbit over the poles of the sun. The Laboratory supports the joint APL/Max-Planck Institute Active Magnetospheric Particle Tracer Explorer (AMPTE) for NASA and the Federal Republic of Germany. Its purpose is to create an artificial ion cloud outside the earth's magnetosphere in order to investigate the mechanisms responsible for forming the Van Allen radiation belts.

The articles in this section discuss the following four topics:

The first satellite to use mechanical refrigerators to cool high resolution gamma ray spectrometers was launched in February 1979. The cryogenic refrigerators were developed by APL.

During March and July 1979, Voyager spacecrafts 1 and 2 passed by the planet Jupiter, carrying low-energy charged-particle measurement instruments developed by APL. The instruments have provided the first detailed look at the high-energy plasma environment within the Jovian magnetosphere.

The MAGSAT satellite, launched successfully in October 1979, was built by APL to support NASA and U.S. Geological Survey requirements for measurements to be used by the Survey for magnetic field charts and maps. Two outstanding features of the MAGSAT satellite are the magnetometer boom and the attitude signal processor. The magnetometer boom is a lightweight extendable structure that can precisely position instruments sensitive to spacecraft magnetic fields at considerable distances from sources of those fields in the spacecraft. The boom positions the sensors of a vector magnetometer and a scalar magnetometer accurately. Post-launch performance indicates that the boom is maintaining position well within allowable limits. The attitude signal processor is the basis of the MAGSAT attitude control system and probably represents the first CMOS technology microprocessor used in a satellite.

The requirement for a very accurate missile tracking capability in support of the Improved Accuracy Program and the introduction of the Trident missile have resulted in the development of the SATRACK system reported in earlier volumes of *APL Developments in Science and Technology*. The next article in this section discusses APL's evaluation of the overall performance of the SATRACK system. The evaluation has demonstrated that the hardware and software developed by the Navy and APL are able to meet their projected measurement and estimation capabilities. The final article reports on the successful development of a key component of the SATRACK system, the SATRACK Post Flight Receiver.

OPERATION OF SATELLITE CRYOGENIC REFRIGERATORS IN SPACE

The P78-1 satellite, the first satellite to contain high-resolution gamma ray spectrometers cooled by mechanical refrigerators, was launched on 24 February 1979. The refrigerators were developed by APL and were operating satisfactorily as of 30 September 1979, the date of this report. This is the first application of mechanical refrigeration to the cooling of gamma ray detectors and the first time that mechanical refrigerators for any application have survived in space for more than a few hundred hours.

BACKGROUND

The advantages of cooling radiation detectors in space have long been appreciated (Ref. 1). In 1973, under the sponsorship of the Defense Advanced Research Projects Agency (DARPA), APL began the development of a mechanical refrigerator to cool germanium gamma ray detectors mounted in a satellite to cryogenic temperatures (≈ 77 K). A previous experiment (Ref. 2) using a solid cryogen had collected a limited amount of gamma ray spectra, but the mechanical refrigerator offered the advantages of lighter weight, longer life in space, and greater experimental flexibility. The Stirling cycle refrigerator with helium as the working fluid was chosen as the most promising candidate. Six refrigerators were constructed, four of which were to be launched in a satellite containing two high-resolution gamma ray spectrometers.

The newly developed intrinsic germanium detector can be warmed to ambient temperature without destroying its sensitivity or resolution. Therefore, by cooling the detector with a mechanical refrigerator that can be turned on and off at will, it is possible not only to limit the spectra-gathering and the refrigerator's operation to periods of interest but also to study the effects of warming the spectrometer to the ambient temperature of the satellite. Since the launch, the experimenter, Lockheed Palo Alto Research Laboratory (LPARL), has been able to take advantage of this flexibility in order to acquire an unprecedented amount of gamma ray spectra in space and also valuable information on radiation damage to intrinsic germanium detectors in the space environment.

DISCUSSION

The design, construction, and laboratory test results for the APL satellite refrigerator are discussed

in Ref. 3. The mechanical part of the refrigerator, constructed by Philips Laboratories, is an adaptation for satellite application of the two-stage Philips Stirling cycle cryogenic refrigerator. The motor drive electronics and refrigerator instrumentation were designed and constructed at APL.

The LPARL experiment contains two spectrometers, gamma 003 and gamma 004, each cooled with two refrigerators (Fig. 1), which LPARL designates serial nos. 1 and 2 on gamma 003 and serial nos. 3 and 4 on gamma 004. The crossbar joining the second stages of the refrigerators is connected to a copper bar, which is the thermal link to the germanium detector. Each refrigerator was designed to cool the detector to 80 K or less; two refrigerators ensure redundancy, quick cool-down if required, and

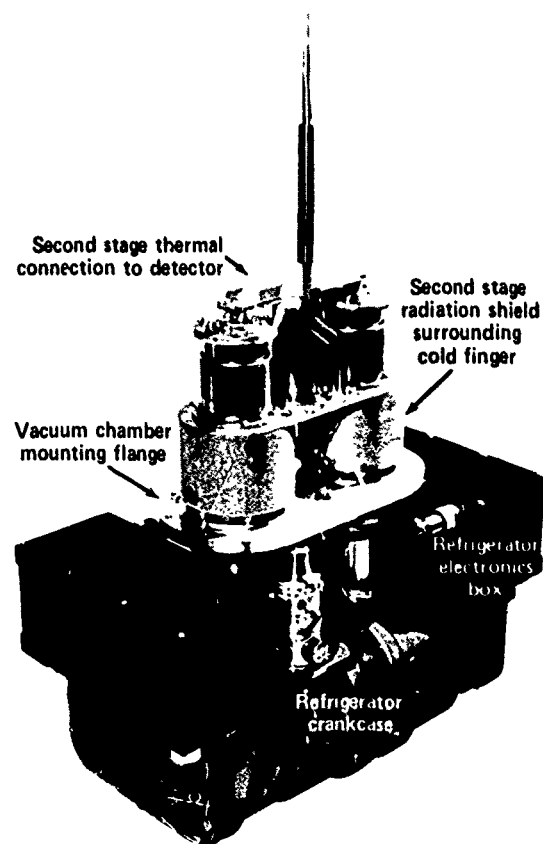


Fig. 1 Mounting of APL refrigerators for LPARL experiment.

sufficiently low temperatures as performance degrades. The P78-1 satellite was designed to provide power to only two refrigerators at a time.

In November 1978, APL recharged the four flight model refrigerators to 71 psia. At that time, it was possible to determine that the helium leak rate varied from 0.43 to 0.67 psi per month. A loss of 1 psi of pressure results in a temperature rise of 2.6 K on the second stage of a refrigerator with a heat load of 0.3 W.

While recharging the refrigerator, we were able to check the instrumentation. Five measurements are made by APL instruments and telemetered to earth: the second-stage temperature, the helium pressure in the crankcase, the helium plenum pressure, the total current drawn by the refrigerator, and the motor speed (rpm). For experimental reasons, LPARL does not directly measure the temperature of the germanium detectors; thus the detector temperature must be inferred from the temperature of the refrigerator's second stage.

The P78-1 satellite was successfully launched into a sun-synchronous polar orbit. Following launch, all four refrigerators were successfully started in turn. The second-stage temperature measurement on no. 3 was inoperative. The pressure transducers on no. 4 indicated that it was losing helium at an excessive rate; the cause of this loss, which developed some time after the refrigerators were recharged, is unknown. In all other respects, operation of the refrigerators and instrumentation appears to be normal.

Following launch, LPARL pursued a somewhat different policy of operation than was originally intended. Gamma 003 was cooled by refrigerator no. 2 and gamma 004 by refrigerator no. 3. Because of power limitations, the refrigerators were operated for seven to ten orbits (100 minutes per orbit), were turned off for one orbit, and were then restarted. This procedure was continued for the first few months and the experiment was not warmed to ambient temperature. The temperature inferred from the second-stage temperature is shown in Fig. 2 for the gamma 004 spectrometer. The temperature has risen from 67 to 118 K in 127 days, about 0.4 K per day. Similar performance was observed for the gamma 003 spectrometer. This rate of temperature rise was less than half that observed by APL in the laboratory life test (Ref. 4).

LPARL estimates that the temperature of the germanium detector cannot exceed that of the refrigerator's second stage by more than 10 K. The resolution of the intrinsic germanium detector degrades rapidly at temperatures in excess of 135 K. Therefore, when the second-stage temperature exceed-

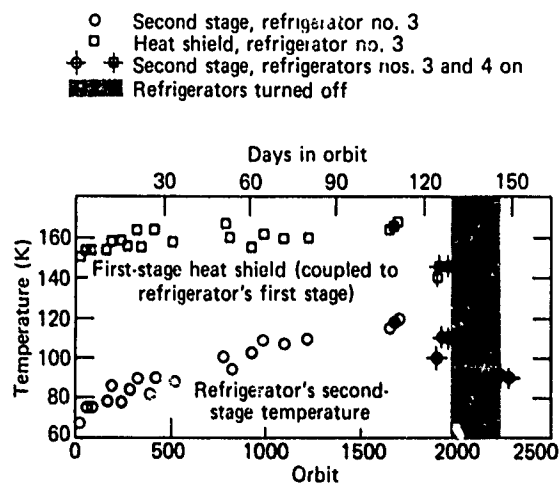


Fig. 2 In-orbit temperature measurements versus time for the gamma 004 spectrometer.

ed 120 K, it was necessary to cut off the refrigerators, allow the detectors to warm to ambient temperature, and then attempt to cool them.

The energy resolution of gamma 003 was about 4.0 keV and that of gamma 004 about 2.7 keV (on the 511 keV annihilation line) at the beginning of the experiment in space. As the experiment continued, degradation in resolution became apparent and the problem became one of distinguishing the effects of radiation damage within the germanium detector from the effects of temperature rise. After 98 days in orbit, gamma 003 was allowed to warm to satellite temperature (≈ 276 K) and was held in this condition for eight days. The detector was then cooled to 80 K, well below the temperature at which resolution is affected, and the resolution at 511 keV was 15 keV. The experience with gamma 004 was similar. After a prolonged warmup and then cooling to 100 K, the resolution after 152 days in orbit was 15 keV.

LPARL now believes that the effects of radiation damage from cosmic rays were discernable after 50 days in orbit. As of 1 August 1979, LPARL believed that by periodically warming the detectors to room temperature, annealing effects would stabilize the resolution. As of 30 September 1979, gamma 003 was operating with a resolution of 15 to 20 keV. After four weeks of continuous operation on both refrigerators 1 and 2, its second-stage temperature was 82 K. Thus, after 220 days in orbit, the refrigerators were cooling the detector to temperatures well below those required for maximum resolution.

RESULTS

Although APL and LPARL have not completed their analysis of thermal performance, the following conclusions can be drawn:

1. The DARPA-APL mechanical refrigerators have been operating in space for 220 days and can meet the specifications for cooling the detectors. This is the first time that a mechanical refrigerator has been operated on a satellite for more than a few weeks.
2. Although LPARL has not yet been able to reduce the bulk of the gamma ray spectral data because of computer programming problems, they have an unprecedented quantity of data with better resolution than can be obtained with a conventional scintillator.
3. Two flexibilities, of cutting off the refrigerator and warming the experiment to ambient temperature and of using two refrigerators to cool the intrinsic germanium detectors to temperatures well below 80 K,

have permitted LPARL to segregate the effects of radiation damage and possibly of impurity freeze-out on the detector. Experiments can now be performed in space that would be impossible with solid or liquid cryogenes as the refrigerant.

REFERENCES

1. T. C. Nast and D. D. Murray, "Orbital Cryogenic Cooling of Sensor Systems," presented at the American Institute of Aeronautics and Astronautics, AIAA Paper No. 76-979, Oct 1976.
2. G. H. Nakano, W. I. Imhof, and R. G. Johnson, "A Satellite Borne High Resolution Ge(Li) Gamma Ray Spectrometer," *ILLI. Trans. Nucl. Sci.* NS-21, 1974, p. 159.
3. C. B. Balas, C. S. Lefel, and C. A. Wingate, "A Stirling Cycle Cooler. Approaching One Year of Maintenance-Free Life," *Adv. Cryog. Eng.* 23, 1978.
4. C. A. Wingate and C. S. Lefel, "An Ultra Reliable Miniature Cryogenic Refrigerator," presented at the Cryogenic Engineering Conference, London, Jun 1978; to be published in *Adv. Cryog. Eng.* 25.

Author: C. S. Lefel, Jr.

Support: Defense Advanced Research Projects Agency

VOYAGERS 1 AND 2 ENCOUNTERS WITH JUPITER

On 5 March and 9 July 1979, respectively, the Voyagers 1 and 2 spacecraft flew by Jupiter carrying APL's Low Energy Charged Particle (LECP) instruments. These detectors, which were designed to provide comprehensive measurements of the composition and distribution of energetic ions and electrons, have provided the first detailed look at the characteristics of the high energy plasma environment within the Jovian magnetosphere.

BACKGROUND

The Voyager LECP instruments were designed to provide detailed measurements of temporal variations in the composition, energy distribution, and flow of energetic particles (Ref. 1). The LECP detector system comprises two subsystems: the low energy

magnetospheric analyzer (LEMPA) and the low energy particle telescope (LEPT). The LEMPA detectors are configured to provide optimum measurements in high particle-flux environments such as planetary magnetospheres, while the LEPT detectors provide a wider range in low flux environments such as the interplanetary regions.

On-board analysis of the output of the 23 solid-state detectors that make up the LEMPA/LEPT system provide rate measurements for particles in 57 categories of energy ranges and particle types. Pulse height analysis of individual particle events allows detailed study of the energy distribution of individual particle species. By appropriate commands, the data system can be configured for optimum measurement of the energetic particle flux over a wide range of environments.

Because the LECP instrument is mounted on an inertially stabilized spacecraft, some means must be provided for measuring the angular distribution of particle velocities, i.e., particle anisotropy. This was accomplished by mounting the detectors on a motor-driven scanning platform that rotates the detectors through 360° in eight steps.

DISCUSSION

The trajectories of the Voyagers 1 and 2 spacecraft are shown in Fig. 1. Voyager 1 (the first to arrive at Jupiter) encountered the Jovian bow shock on 28 February 1979 and the magnetospheric boundary on 1 March. It flew by Jupiter on 4 March at a closest approach distance of slightly less than four Jovian radii ($4 R_J$; $1 R_J = 71\,400$ km) (Ref. 2). Following the encounter, it proceeded outward through the magnetotail, passing through the morning-side magnetosphere boundary on 12 March. Voyager 2 (Ref. 3) followed a slightly different trajectory, which allowed the spacecraft to remain in the magnetospheric tail for a significantly longer time. Its closest approach to Jupiter was approximately $10 R_J$.

The presence of the Jovian magnetosphere was first evident in the Voyager data when bursts of energetic particles were observed streaming away from the planet. The spacecraft at this point was approximately $800 R_J$ from Jupiter. As it approached Jupiter, the frequency and duration of the bursts increased.

The counting rate for several species of particles measured by Voyager 2 at Jupiter is shown in Fig. 2. The entry into the Jovian magnetosphere is marked by the sharp increase in the counting rate on day 186 (5 July). Inside of the plasma boundary, the LECP instrument detected an extremely hot plasma with a temperature on the order of 300 million degrees. Anisotropy measurements of the particle fluxes indicated that this plasma rotates rigidly with the planet. Since the magnetic dipole is offset and tilted from the center of Jupiter, the rotation causes strong 5 and 10 hour variations in the particle intensities. These variations indicate that the hot plasma is confined to a relatively thin disk (plasma disk) centered on the meridional plane of the magnetic dipole.

As the spacecraft penetrated deeper into the Jovian magnetosphere, the LECP instrument measured steadily increasing particle fluxes, modulated by the 10 hour rotation of Jupiter and the presence of the Jovian satellites, which absorb the energetic particles as they sweep through the magnetosphere. In the plasma sheet, the LECP data

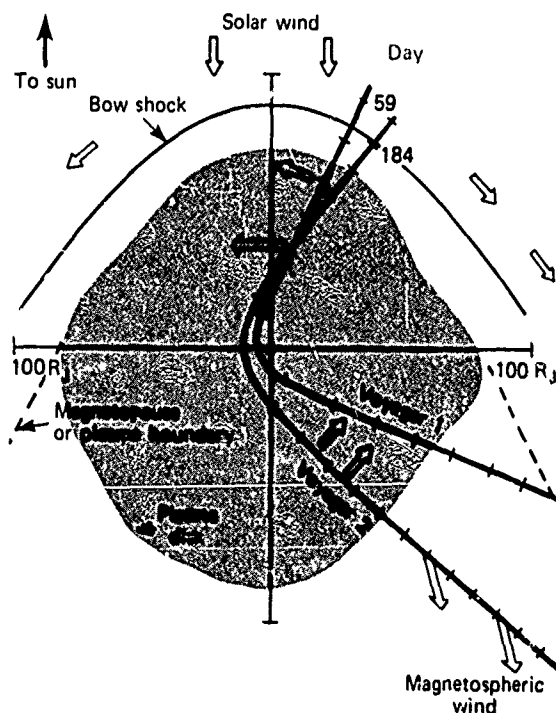


Fig. 1 The Voyagers 1 and 2 trajectories through the Jovian magnetosphere. The arrows along the Voyager 2 trajectory show typical measured flow directions.

indicate that the energy density in the particles is greater than the energy density of the magnetic field and thus is a dominant element in controlling the dynamics of the plasma sheet. This is significantly different from the situation in the earth's magnetosphere where the energy density resides in the magnetic field.

As they moved inward, the LECP instruments also measured an increasing fraction of heavy ions, principally oxygen and sulfur. These ions, which are not present in such abundance in other planetary magnetospheres (or in the sun), have their origin in the volcanic eruptions on the inner Galilean satellite, Io. The presence of this well-defined internal source of easily identified ions provides a unique and powerful means for studying the energization and propagation of the energetic particles.

On the outbound passage through the magnetotail, the LECP detectors observed large periodic variations in the particle fluxes that result from the wobbling of the plasma disk with the rotation of the planet. The flow of the plasma indicates that the plasma in the disk corotates with Jupiter out to the boundary of the magnetosphere instead of only in a relatively small region in the inner magnetosphere

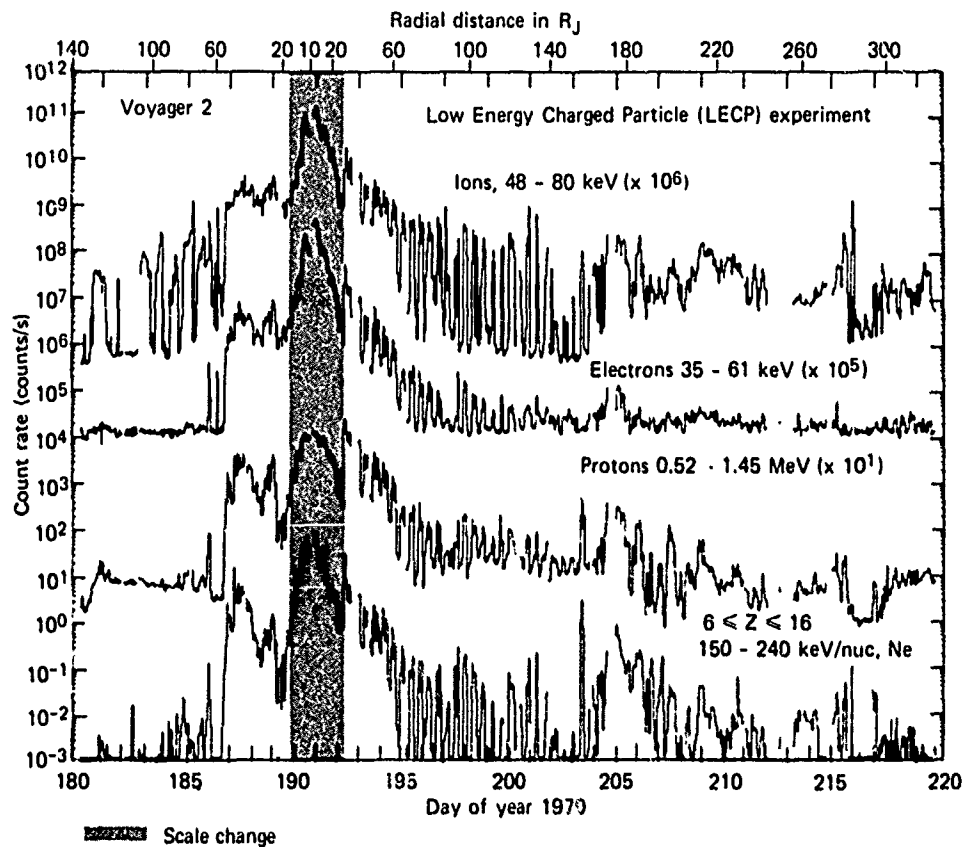


Fig. 2 The counting rate for several of the LCEP channels for the time interval 28 June 1979 (day 179) through 8 August 1979 (day 220).

as is the case for Earth. Voyager 2 measured corotational flows out to a distance of $150 R_J$, at which point the flow changed to a direction that was radially outward from the planet. This radial outflow or "magnetospheric wind" was observed almost continually out to the bow shock on the dawn side of the magnetosphere and was observed with decreasing frequency far out into the solar wind.

The LCEP observations have provided a first look at the character of the high energy plasma environment within the Jovian magnetosphere. The observations have also raised a number of questions about the factors controlling the dynamics of the magnetosphere of Jupiter.

REFERENCES

- 1 S. M. Krimigis et al., "The Low Energy Charged Particle (LECP) Experiment on the Voyager Spacecraft," *Space Sci. Rev.* 21, 1977, p. 329
- 2 S. M. Krimigis et al., "Low Energy Charged Particle Environment at Jupiter: A First Look," *Science* 204, 1979, p. 998
- 3 S. M. Krimigis et al., "Hot Plasma Environment at Jupiter: Voyager 2 Results," *Science* 206, 1979, p. 977

Authors: E. P. Keath and S. M. Krimigis

Support: National Aeronautics and Space Administration

THE NASA MAGNETIC FIELD SATELLITE (MAGSAT)

Although measuring the geomagnetic field from satellites began with the launch of Sputnik 3 in 1958, it has been done only sporadically since. Only the NASA Polar Orbiting Geophysical Observatories (POGO's) have provided a truly accurate global geomagnetic survey. Accordingly, with close United States Geological Survey (USGS) involvement, NASA has undertaken to provide USGS with data for deriving magnetic-field charts and maps that will be accurate for the 1980 epoch. APL was selected to design, build, and test a satellite for measuring the geomagnetic field, using spare components and designs from the Small Astronomy Satellite Programs.

BACKGROUND

One of the goals of the NASA Resource Observation Program is to use space technology to improve our understanding of the dynamic processes that formed the geologic features of the earth and of how these processes relate to natural hazards and to the emplacement of resources.

Before the satellite era, magnetic data from geographic regions were acquired over periods of years by various measurement techniques. For many regions, such as the oceanic and polar, data were either sparse or nonexistent. Three POGO's (OGO-2, -4, and -6), operating between October 1965 and June 1971, used alkali-vapor magnetometers to obtain global measurements of the magnetic field approximately every 0.5 s at an altitude range of 400 to 1500 km. These measurements were intended to map the main geopotential field originating in the earth's core, to determine the long-term temporal or secular variations in that field, and to short-term field perturbations caused by ionospheric currents. Analysis of these data, which disclosed that separable fields exist at lower altitudes because of anomalies in the earth's crust, pointed the way to a new type of investigation. Several geomagnetic field models and crustal anomaly maps based on the POGO data have been published.

DISCUSSION

APL has designed, developed, and tested a spacecraft that will measure the near-earth geomagnetic field in support of the NASA Resource Observation Program. The NASA Magnetic Field Satellite (MAGSAT) will provide precise magnetic-field measurements for geoscientific investigations.

The MAGSAT vector measurements will resolve ambiguities in field modeling and magnetic anomaly mapping. Greater resolution and stronger signal levels from anomalous fields will help overcome deficiencies in the POGO data for mapping anomalies.

MAGSAT carries a scalar magnetometer and a vector magnetometer supplied by NASA as government furnished equipment. The scalar magnetometer will make absolute measurements of the ambient magnetic field to an accuracy of 3 γ . The vector magnetometer will make directional measurements with an overall accuracy of the magnetic vector (including magnitude, direction, sense, and location) of 6 γ rss.

The spacecraft was constructed in two major assemblies, a base module of the SAS-C design incorporating the power system, the telemetry and command systems, and the attitude control system, and an instrument module designed specifically for the mission. An optical bench supports two star cameras. The magnetometers are mounted on a precision platform that is extended 6 m from the spacecraft to reduce the effect of satellite magnetic fields on the sensors. An optical device is installed on the optical bench and the remote instrument platform to measure the relative displacements between the two magnetometers. Known as the attitude transfer system (ATS), it will permit scientists to use star camera data to locate the position in space corresponding to each set of magnetometer measurements.

During Fiscal Year 1979, the spacecraft components were integrated with the base and instrument modules. The instrument module was then subjected to a thermal balance test in vacuum to verify the validity of the thermal design and the thermal analytic model.

During this period, the base module was completed and tested, and the performance of the attitude control system was verified. The magnetometer boom assembly was tested in a unique water-trough float facility simulating a 0-g environment to demonstrate its ability to deploy the instrument platform at the position and angle required for proper operation of the ATS.

The two modules were joined and the spacecraft was taken to NASA's Goddard Space Flight Center to map the star camera fields and to make ATS and magnetic measurements. Environmental acceptance tests, performed at APL, included RFI self-susceptance tests, vibration exposure, and a 15-

day thermal vacuum test. Upon satisfactory completion of this sequence, the spacecraft was returned to Goddard and less extensive star camera and ATS measurements were taken to verify that no shift of alignment had occurred during the environmental tests. This sequence was completed with final magnetic measurements, magnetometer calibrations, and determinations of mass properties. An electrical test sequence was performed at APL (Fig. 1) before shipment to the launch site.

The MAGSAT mission objectives, established jointly by NASA and the USGS, are:

1. To obtain an accurate, up-to-date quantitative description of the earth's main magnetic field (accuracy goals are 6γ rss in each component at the satellite altitude and 20γ rss in each component at the earth's surface in its representation of the field from the earth's core at the epoch of the measurement);
2. To provide data and a worldwide magnetic-field model suitable for USGS update and refinement of world and regional magnetic charts;
3. To compile a global scalar and vector crustal magnetic anomaly map (accuracy goals are 3γ rss in magnitude and 6γ rss in each component; the spatial resolution goal of the anomaly map is 300 km); and
4. To interpret the crustal anomaly map, in conjunction with correlative data, in terms of geoscientific models of the earth's crust to assess natural resources and determine future exploration strategy.

These objectives will be achieved by investigations to be carried out by Goddard, the USGS, and distinguished members of the scientific community. Dr. T. A. Potemra of APL, one of 32 principal investigators, is using the MAGSAT data for magnetosphere/ionosphere studies. Other fields being investigated include geophysics, geology, field modeling, marine studies, and core/mantle studies.

MAGSAT was shipped to Vandenberg AFB, California, on 5 October 1979. Field operations commenced on 9 October and concluded with a successful launch on 30 October. The NASA/DoD Scout launch vehicle placed the spacecraft into a sun-synchronous orbit with a perigee of 352 km and an apogee of 578 km inclined 97° to the earth's equator. The period is 93 minutes. This near-optimum orbit should provide

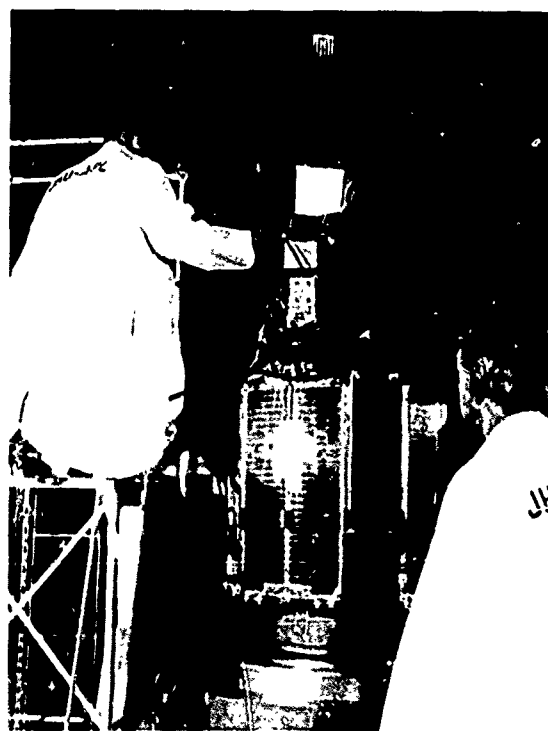


Fig. 1 MAGSAT undergoing tests at APL.

a minimum lifetime of 180 days, depending on solar activity (the planned lifetime was five months).

The stored commands in the Delayed Command System ordered an intricate series of attitude maneuvers during the first orbit to ensure the proper orientation of the solar array for battery charging. Earth lock was achieved on 31 October and the magnetometer boom was extended and locked in place on 1 November. Collection of magnetometer data started the next day. Attitude trimming activities were carried out for the next two weeks, and by 20 November only two Z-coil maneuvers per day were needed to keep the satellite properly oriented.

After 22 days in orbit, all satellite systems were operating properly and NASA was looking forward to a successful mission.

REFERENCES

1. MAGSAT Spacecraft Description, APL JHU SDO 5146 Mar 1979
2. MAGSAT Magnetic Field Satellite Resource Observation Program, NASA GSFC Report, Sep 1979

Author: L. D. Eckard, Jr.

Support: NASA Goddard Space Flight Center

THE MAGSAT MAGNETOMETER BOOM

A continuing requirement exists for lightweight extendable structures to position instruments that are sensitive to magnetic fields at a considerable distance from the sources of those fields in a spacecraft. With more ambitious scientific missions, designs that transcend the state of the art are often needed. The magnetometer boom system is an example of how APL met the rigorous objectives for the Magnetic Field Satellite (MAGSAT).

BACKGROUND

The need for a simple, lightweight, precisely aligned, extendable structure that could overcome the stiffness of sizable multiconductor electrical cabling became apparent during the development of the TRIAD (1972) satellite. An extendable structure based on the scissors concept evolved. A similar device was developed for GEOS-C (1975). By the time the concept was introduced on TIPS II and III (1975 and 1976), many design improvements were implemented. The experience acquired during these programs provided the needed background for developing the magnetometer boom for MAGSAT.

MAGSAT's mission is to provide global vector data on the magnetic field that will (a) update the earth's magnetic field charts for 1980, (b) aid in the search and analysis of large-scale magnetic anomalies in the earth's crust that might lead to the discovery of important mineral deposits, and (c) update mathematical models of the earth's magnetic field. It is the task of an ultrastable, highly accurate vector magnetometer to measure the three vector components of the earth's magnetic field. The task of providing redundancy and an independent confirmation of the total field magnitude was assigned to a companion instrument—a scalar magnetometer.

The sensors of both magnetometers are mounted on a platform with passive and active temperature control. The platform is attached to the tip of the magnetometer boom. On command, the boom uncages and moves the sensor platform 6 m from the spacecraft proper. The boom maintains that platform position so that the center of a plane mirror attached to the back of the vector magnetometer sensor does not wander out of a ± 1.91 cm² target zone centered on an optical axis defined by an infrared light beam emanating from the spacecraft. Within the target zone, the boom keeps the plane mirror orthogonal to the optical axis within 3 arc minutes.

These requirements were imposed by the Attitude Transfer System (ATS), which measures vector magnetometer tilt and relates it to a pair of star cameras mounted to an optical bench in the spacecraft's instrument module.

DISCUSSION

Figure 1 shows the operational configuration of the MAGSAT spacecraft. The magnetometer boom system consists of a 14-link scissors boom, a three-axis gimbal, and the sensor platform. Two independent, pyrotechnically actuated caging systems are used to contain and protect the boom and the sensor platform in their stowed configurations during launch. The three-axis gimbal located at the base of the boom enables the boom to pitch, yaw, and twist for ATS acquisition. The driver for each gimbal function is a synchronous-hysteresis gearmotor coupled to a right angle gearbox. Rotary potentiometers geared to the output shafts of the gearboxes are calibrated to give boom tip position during and after every gimbal operation.

The boom drive consists of a right- and a left-handed ball screw driven by an inverter-powered synchronous-hysteresis gearmotor coupled to a parallel shaft gearbox. A rotary potentiometer geared to the output shaft of the gearbox is calibrated to give boom length during and after deployment. Confirmation of total extension is given by a second potentiometer that is pinned to the boom hinge nearest to the sensor platform.

Weight and thermal distortion dictated the use of graphite epoxy for the boom links. The basic link is 0.94 m long and measures 1.07 by 5.08 cm in cross section (see Fig. 2). Magnesium fittings are fastened to the ends and the center of each link with semirigid epoxy to prevent cracking of the interface because of differential expansion. Each link is a hollow box with a wall 0.076 cm thick. It is covered internally and externally with thin aluminum foil as a moisture barrier (moisture causes dimensional instability in the boom structure). A final wrapping of aluminum tape with an aluminum oxide overcoat maintains the temperature of the link at about 25°C, which corresponds roughly to the temperature of the test facility in which the system alignments and calibrations are made. The links are hinged to each other with pins that are forced through undersized bushings made of

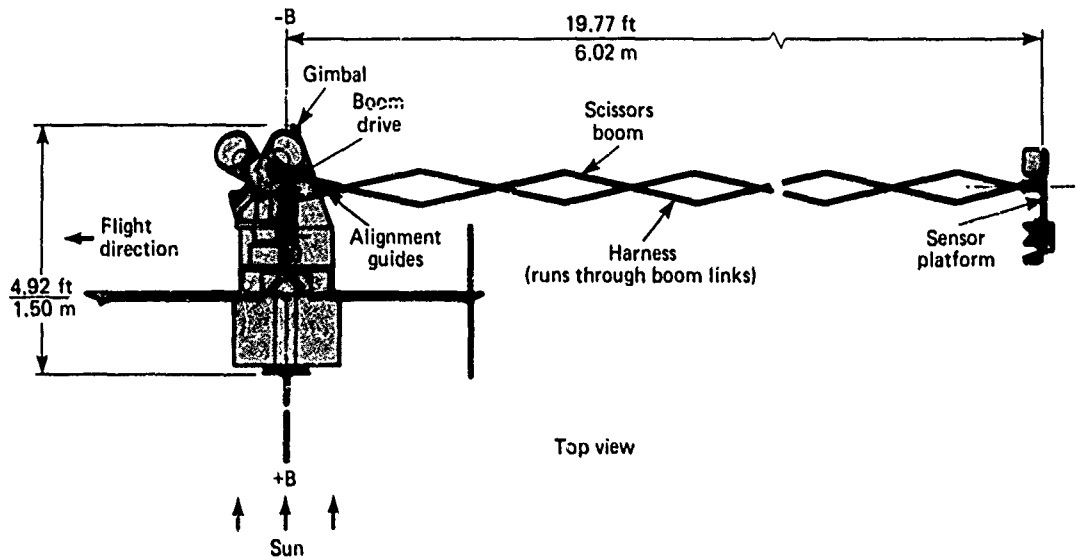


Fig. 1 MAGSAT orbital configuration.

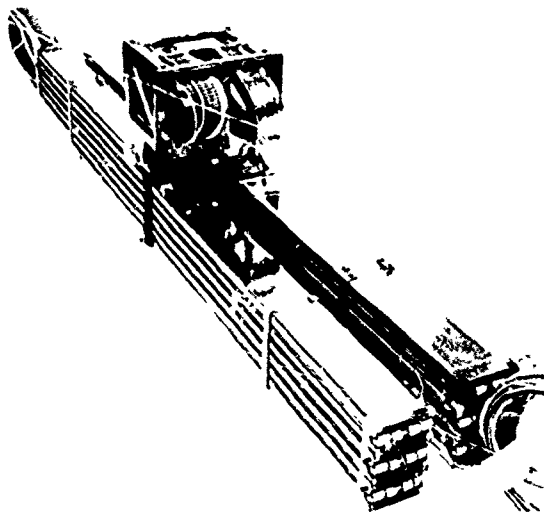


Fig. 2 Magnetometer boom links.

a compliant material. This permits rotation but prevents any mechanical play.

The sensor platform is attached to the tip of the boom by means of a graphite epoxy spacer and a mechanism that enables the sensor platform to translate while its attitude is maintained normal to the boom axis as the boom extends.

Attached to the sensor platform with a kinematic suspension is the thermally controlled vec-

tor magnetometer base. To the base are attached the vector magnetometer, the remote-plane and dihedral ATS mirrors, and a precision sun sensor. The kinematic suspension provides a compliant mount for the base and isolates it from thermally induced structural distortions that would be detrimental to the alignment of the vector magnetometer and the remote mirrors. The scalar magnetometer is attached to a 1.27 cm thick Epoglass thermal isolator that is fastened to the side of the graphite epoxy spacer.

Thermal distortion testing was conducted on a four-link sample of the boom in a solar simulator at NASA Goddard. Temperature data collected during the test were fed into a NASTRAN model of the test specimen. Analytical tip displacements were compared with experimental results. The correlation was excellent and gave great confidence in the NASTRAN model of the 14-link flight boom. On the basis of that model, the predictions in Fig. 3 evolved.

Displacements as small as those in Fig. 3 can be corrected by the gimbal. Values for Δy , Δz , θ_1 , and θ_2 were much too small to be significant. Such small thermal distortions at the end of a structure 6.02 m long are quite remarkable. Displacements an order of magnitude larger (and not correctable by the gimbal) would have resulted if the boom links had been fabricated from more common structural materials.

The secret behind the very small displacements is plastic reinforced with graphite fiber. Its coefficient

of thermal expansion is near zero ($0.3;1 \times 10^{-6}$ cm/cm/ $^{\circ}$ C average value for this boom). It is also important to maintain the smallest possible temperature gradients in the boom links. The largest temperature difference from hot side to cold side experienced by the test boom links was 3° C.

In the case of MAGSAT, gibal adjustments eliminate thermally induced sensor platform misalignments. Subsequent misalignments brought on by seasonal variations in the solar vector are small

enough to keep the ATS from losing lock with the remote mirrors.

Studies of the boom system alignments were conducted in a pair of water troughs 6.1 m long (see Fig. 4). Specially designed floats with gimballed pulleys were attached to the boom link pivots, to simulate a zero-g condition in a plane parallel to the plane of the water. Transverse and/or angular offset of the mirrors could be corrected by gimbaling the boom at its base or introducing shims at the interface

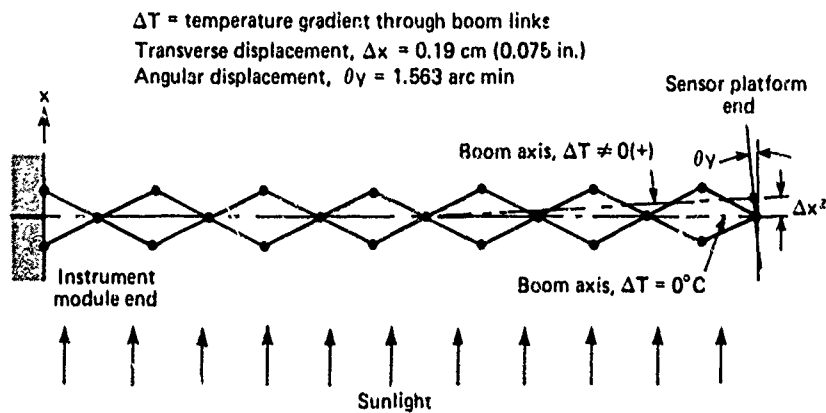


Fig. 3 Predictions based on NASTRAN model.



Fig. 4 Boom alignment test system.

between the base and the sensor platform. The boom system was installed in the spacecraft instrument module, which was attached to a rotary table. Thus the boom could be rotated to its pitch and yaw planes for orthogonal plane zero-g measurements and adjustments. Using the ATS to measure the transverse and angular offset of the plane mirror, the data in Table I were derived.

TABLE I
ALIGNMENT TEST RESULTS FOR MAGSAT
MAGNETOMETER BOOM

Test No.	Mirror Tilt Angle* (arc min)	Mirror Position Offset† (in.)	Transverse Displacement to Correct Mirror Tilt (in.)	Sum of Position Offset and Transverse Displacement‡ (in.)
Rotary Table at 0°				
I	+ 0.75	0	- 0.05	- 0.05
V	+ 1.12	0	+ 0.075	+ 0.075
Rotary Table at 180°				
I	+ 1.87	+ 0.025	+ 0.125	+ 0.150
V	- 4.12	+ 0.050	- 0.275	- 0.225
Rotary Table at 90°				
I	+ 3.75	0	+ 0.25	+ 0.25
V	- 1.12	+ 0.150	- 0.075	+ 0.075
Rotary Table at 270°				
I	- 4.87	+ 0.050	- 0.325	- 0.275
V	- 0.75	+ 0.075	- 0.050	+ 0.025

*Mirror is normal to ATS optical axis when tilt angle is 0.0 arc minutes.

†Mirror is centered on ATS optical axis when position offset is 0.0 in.

‡Operation of the pitch (or yaw) gimbal to produce displacement of this magnitude reduces tilt angle to zero and leaves this position offset. Size of target zone for position offset is ± 0.75 in. in both pitch and yaw.

To check repeatability after vibration testing and to determine what effect removal of the boom system from the alignment test apparatus would have

on mirror alignments, five tests were conducted in the following sequence:

Test	Test Description
I	Baseline. Boom suspended from floats; mirrors aligned.
II	Boom retracted and extended; mirror alignments checked.
III	Boom removed from floats and resuspended; mirror alignments rechecked.
IV	Boom removed from floats, vibrated, and reinstalled in floats; mirror alignments rechecked.
V	Boom retracted and extended; mirror alignments rechecked.

The results of tests I and V, shown in Table I, indicated that the MAGSAT magnetometer boom system would meet its mission requirements.

ORBIT PERFORMANCE

MAGSAT was launched on 30 October 1979. Boom extension occurred on 11 November 1979. Unexpectedly, the ATS indicated that both remote mirrors on the sensor platform were in view and would require very little adjustment to be acquired within the linear range of the ATS. On the following day, the necessary gimbal adjustments were made. Telemetry indicated that the plane mirror was set at angles of 7 arc seconds in pitch and yaw (± 180 arc seconds are allowed). Probably because of interactions of the ATS with the boom and the sensor platform and because of thermal distortions resulting from the slight coning action of the spacecraft relative to the solar vector about the nominal angles, 15 arc second oscillations were also observed. Somewhat greater activity was observed in the ATS roll measurement. Peak-to-peak angles as large as 120 arc seconds were observed; ± 300 arc seconds were allowed.

Author: J. F. Smola

Support: National Aeronautics and Space Administration

ATTITUDE SIGNAL PROCESSOR FOR MAGSAT

The Attitude Signal Processor (ASP) is the heart of the MAGSAT Attitude Control System, which we believe comprises the first CMOS (complementary metal oxide semiconductor) microprocessor to be used in a satellite, the first microcomputer-based attitude control system to be produced at APL, and the first microcomputer programmed in a high level language to be used in a spacecraft.

MAGSAT is maintained in a three-axis stabilized mode by a semiautonomous control system. The control system is basically that of the SAS-C spacecraft but with a greater degree of on-board decision-making capability provided by a microcomputer built into the ASP. This additional complexity is required because the very low MAGSAT orbit causes large aerodynamic torques on the spacecraft.

The Attitude Control System (a) keeps the solar panels and the precision sun sensor pointed toward the sun, (b) keeps the star cameras pointed sufficiently far away from the sun and the earth, and (c) maintains low body rates (jitter) so that the

orientation of the spacecraft can be measured with an accuracy of 11 arc seconds rms.

DISCUSSION

Structure and Functions

The MAGSAT Attitude Control System (Fig. 1) is composed of the ASP, a magnetic torquing coil, vector magnetometers, a reaction wheel, an infrared horizon scanner, a pitch axis gyro, a roll-yaw axis nutation damper, and a yaw axis aero trim boom. The system provides automatic and ground-initiated roll-yaw axis control, five modes of pitch axis control, two modes of reaction wheel momentum dumping, and nutation damping.

Attitude Signal Processor

The ASP is the MAGSAT control system's adaptive controller and real-time signal processor. As

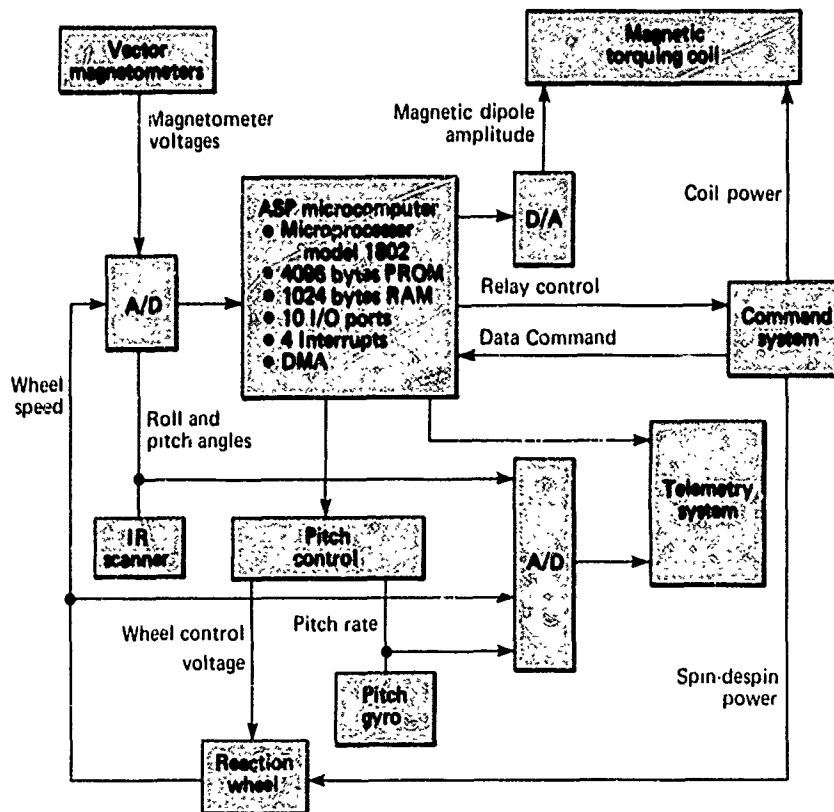


Fig. 1 MAGSAT Attitude Control System.

shown in Fig. 2, it consists of an auxiliary electronics subsystem and a microcomputer subsystem that includes the ASP firmware. It has two primary external interfaces with the MAGSAT Command and Telemetry Systems.

Auxiliary Electronics Subsystem

The ASP auxiliary electronics subsystem consists largely of analog circuitry to support the ASP microcomputer subsystem.

Microcomputer Subsystem and Interfaces

The ASP microcomputer subsystem consists largely of digital circuitry that implements a microprocessor-based embedded computer. The embedded computer is programmed through firmware to provide most of the attitude control functions. It also supports interfaces with the Command and Telemetry Systems.

There are two interfaces, for data command and for relay control, between the ASP microcomputer and the Command System. The data command is generated by the Command System under ground control and is used to control ASP mode selection, to alter coefficients used in calculations, to alter critical program sequencing points, and to adjust the program clock. The relay control is generated by the

ASP microcomputer for the Command System to alter the state of relays that affect magnetic torquing coil power, magnetic dipole sense selection, and reaction wheel spin-despin power.

The Telemetry System interface supports the connection of two telemetry subcommutators and a reaction wheel speed monitor. The frame of one subcommutator is four bits wide; the other is 128 bytes wide. Each subcommutator receives serial transmissions of telemetry data. The Telemetry System controls the transmissions; the ASP microcomputer serializes them.

Microcomputer Subsystem Firmware

The basic firmware structure involves a system initialization process followed by entrance into a background processing loop that can be suspended temporarily to execute interrupt management and time-dependent procedures for foreground control-law processing.

When the microcomputer reset mechanism is activated, it initializes the state of the microprocessor, storage, and input/output (I/O) interfaces, and places the Attitude Control System in a stable mode. When the initialization process is completed, the system enters limited foreground-background processing until a data command is received, verified, and stored. Then the program clock is started, the Attitude Con-

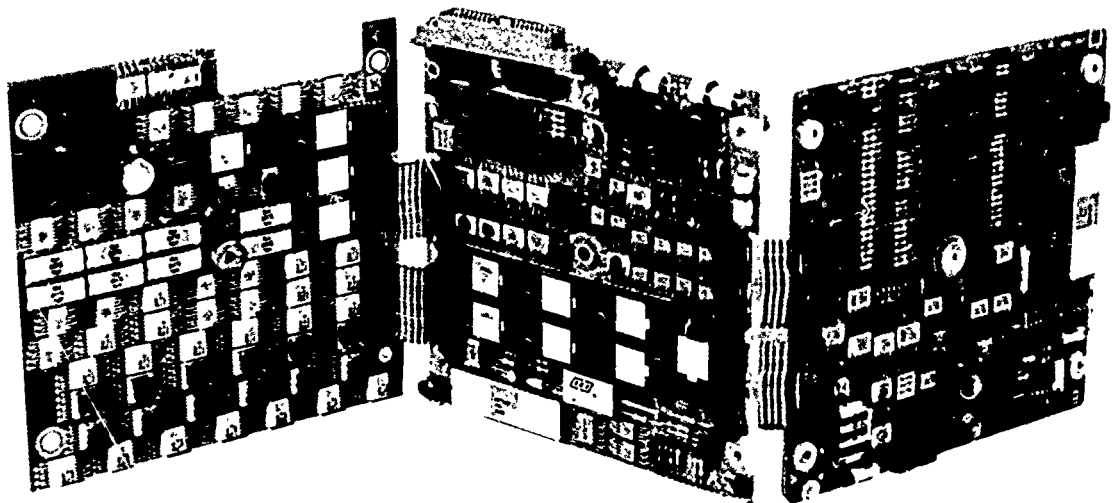


Fig. 2 MAGSAT Attitude Signal Processor. Each board is 5.9 in. square.

rol System is placed in a command-driven control mode, and full foreground-background processing is initiated.

Command verification, command-related diagnostics, and machine-related diagnostics are performed in the background. In the foreground, processing is driven by four interrupts, which are, in order of priority, command, telemetry, analog-to-digital conversion, and time. The first three handle direct-memory access and interrupt-driven I/O features of the microcomputer's I/O interface. The time interrupt updates the program clock and initiates the scheduling of rate-dependent procedures, which include command storage, programmed I/O, attitude control laws, and interrupt-driven I/O initialization.

The ASP firmware consists of executive modules, control law modules, utility modules, constants, permanent (named) variables, and temporary (data stack) variables. The executive modules provide initialization, scheduling, interrupts, I/O, and error management. The control law modules implement the actual attitude control logic and digital signal processing, including pitch and roll angle filtering, pitch and roll-yaw axes control, momentum dumping, and scheduling of command updating. The utility modules enhance the logic of the basic high-level language (MicroFORTH) arithmetic, stack manipulation, and data-type primitives.

ASP Development and Performance

The ASP development involved two equipment and software configurations that supported tests performed on the complete ASP package and on ASP microcomputer firmware and hardware.

Overall tests of the ASP package involved the use of a Command and Telemetry Systems simulator, a MAGSAT Dynamics and Attitude Control System simulator, and various data display devices. The Command and Telemetry Systems simulator was based on a single-board microcomputer (RCA 1802) modified and programmed to simulate the interface functions of these systems with the ASP microcomputer. It allowed data commands to be entered and telemetry data to be displayed. The MAGSAT Dy-

namics and Attitude Control System simulator was based on a Honeywell 316 minicomputer programmed to permit long-running closed-loop tests of the ASP package. It represented satellite dynamics and necessary elements of the Attitude Control System.

The principal equipment and software configuration used to develop and test ASP microcomputer hardware and firmware included an HP 1615A timing and bus-state analyzer, an RCA micromonitor (real-time, in-circuit, hardware and firmware debug monitor), a Data I/O PROM Programmer, a TI Silent 743 Terminal, an RCA COSMAC Development System II (firmware development and test system), and a MicroFORTH language system.

The MicroFORTH language is a modular, structured (single-entry, single-exit module) extensible programming tool based on the concept of threaded-code interpretation. It was modified to support multitasking and was extended to include various development support functions.

The MAGSAT ASP met all initial functional and performance requirements. Requirements in the areas of self-diagnostics, system autonomy, and insensitivity to operational errors were exceeded.

REFERENCES

1. F. Zuremba and D. B. Klein, *MAGSAT Attitude Signal Processor Microcomputer Subsystem Architecture and Firmware Development Document*, API/JHU BCE-T-0768.
2. B. E. Fossman et al., *MAGSAT Attitude Control System Description*, API/JHU S4A-3-028A, 25 Jan 1978.
3. G. H. Fountain, B. E. Fossman, and W. A. Swartz, *MAGSAT Semiautonomous Attitude Control and the Attitude Signal Processor*, API/JHU S4A-3-016, 19 Sep 1977.
4. *User Manual for the CDP1802 COSMAC Microprocessor*, RCA Corp., Somerville, N.J., 1976.
5. J. D. Patterson, *MAGSAT Simulation on the Honeywell H316*, JHU/API BCE-T-0735, 12 Oct 1978.
6. *MicroFORTH Technical Manual—Version 2*, FORTH, Inc., Manhattan Beach, Cal., May 1977.
7. *MicroFORTH Primer for RCA 1802*, FORTH, Inc., Manhattan Beach, Cal., Dec 1976.

Authors: T. Zuremba, W. A. Swartz,
and K. J. Heffernan, and G. H. Fountain

Support: NASA Goddard Space Flight Center

EVALUATION OF SATRACK SYSTEM PERFORMANCE

The overall performance of the Satellite Missile Tracking System (SATRACK) has been evaluated at APL using the data derived from three flight tests of a U.S. Navy development missile (designated C4X). This evaluation has demonstrated that all components of the system developed by the Navy and APL meet the projected measurement and estimation capabilities. They therefore provide a way to assess the validity of the model of the missile guidance system. The expected ephemeris precision of the Global Positioning System (GPS) has not yet been achieved.

BACKGROUND

SATRACK is a unique, highly complex missile tracking system that has been designed, developed, and validated under the technical direction of APL. It was developed in order to provide a very accurate missile tracking capability in support of the Improved Accuracy Program (IAP), whose objective is to determine potential improvements in accuracy of existing and future weapon systems (Ref. 1). The system was conceived at APL in 1973. Active development of the current configuration began in late 1974. The program has been managed by the Instrumentation Branch of the Navy's Strategic Systems Project Office. Equipment for missile instrumentation was developed by the Lockheed Missiles and Space Co. and special ship and ground station equipment by the Interstate Electronics Corp.

In addition to providing technical direction, APL has developed the unique and extensive processing facility required for SATRACK, including challenging design tasks in hardware, software, and process control areas. The Post Flight Receiver, a significant special-purpose hardware design, is reported elsewhere in this section. The extensive software system is on-line, and a configuration control procedure has been developed to manage the processing facility.

DISCUSSION

SATRACK (Fig. 1) uses a network of NAVSTAR GPS satellites, a missile-borne signal translator, surface station equipment, and the post-flight data processing facility at APL. The missile is tracked by measuring the RF between the satellites and the ground stations by means of a missile signal translator. In certain cases, the ground stations, acting as pseudosatellites, transmit signals like those of

the GPS and also a second signal in order to measure the ionospheric refraction error in the RF path between the surface station and the missile. The satellite-to-missile path uses the GPS L-band frequency, L_1 (1575.42 MHz), and the station-to-missile path uses both an L_1 and L_2 (393.855 MHz) transmission.

In addition to collecting missile tracking data, the surface stations recover missile telemetry data in order to get trajectory estimates from the guidance system.

All the collected data are sent to APL for post-flight processing. Estimates of initial conditions and parameter errors for the missile trajectory and guidance system are determined by a Kalman filter smoother located in the post-flight processor, which compares the guidance-derived quantities with the corresponding SATRACK-measured quantities. Systematic differences are attributed to various error sources in the system.

Specific accuracy objectives were formulated for SATRACK in concert with the IAP objectives. As a basis for system development, goals were set for the accuracy of reconstructed missile trajectories. The error recovery capability of the powered flight trajectories for C4X test missiles (including initial position and velocity) was projected to be within 40 ft in position and 0.05 ft/s in velocity along each of three orthogonal axes.

The major sources of error in the trajectory estimate are:

1. GPS ephemeris and clock errors,
2. Signal propagation errors, and
3. Corruption of the signal in the system hardware.

Prior to, and concurrent with, the C4X flight tests, major parts of SATRACK had been evaluated by means of detailed simulations and with a specially designed test satellite, TRANSAT. The results reported here are concerned with the assessment of SATRACK obtained from analysis of the C4X-18, -19, and -21 flights. These tests were the concluding phase of the SATRACK validation program.

GPS Ephemeris and Clock Errors. When the initial error budget was established for SATRACK, it was believed that the GPS errors experienced at the missile (i.e., a user-equivalent error concept) would be 12 ft and 0.005 ft/s (one sigma) on each satellite-to-missile link. To assess GPS precision independently, a

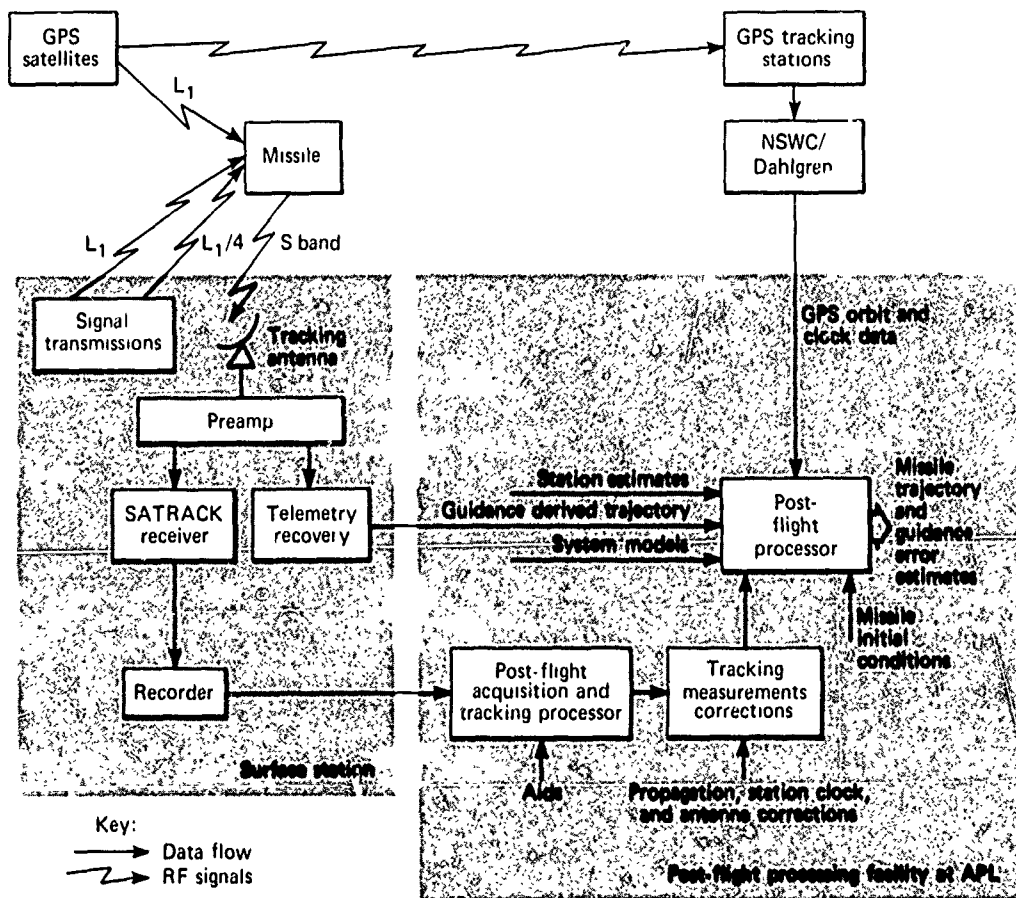


Fig. 1 Basic SATRACK configuration.

"static" missile test was conducted in support of each missile flight test. The static test, which is equivalent to an actual SATRACK missile test with the "missile signal translator" stationary on the roof of a building at the APL facility, measures directly the errors experienced at a known location.

Another way to evaluate the relative quality of the GPS ephemeris estimates is to compare SATRACK missile trajectories derived using various sources of ephemeris estimates with the estimate determined from radar data and from telemetry Doppler metric measurement subsystem (TDMMS) data obtained from TRIDENT test flights (these tracking systems augment the SATRACK measurements).

A third way is to compare estimates provided by different processing facilities, i.e., the GPS Master Control Station, the Aerospace Corp., and the Naval Surface Weapons Center/Dahlgren.

A careful analysis of all the data collected by the three methods has led to the conclusion that the

current GPS ephemeris errors are approximately three to four times larger than expected.

Signal Propagation Errors. Three major propagation effects that can corrupt SATRACK measurements are missile plume, tropospheric, and ionospheric. Avoiding plumes by carefully selecting tracking sites has been the basic design philosophy of SATRACK. Tropospheric models have been shown to be accurate enough for SATRACK if elevation angles of less than 4° are not used.

Single-frequency satellite-to-missile links are corrected by means of a historic ionospheric model that is adjusted in response to measurement data collected for this purpose. As the program has evolved, ionospheric data have been collected from Transit satellites close to the time of missile flight using equipment located at APL. Sounder data from the particular missile flight have also been collected. These data, provided by the dual-frequency transmission between the surface station and the missile,

measure electron content and electron content differences (from range and Doppler data) as the missile transits the ionosphere. The data are unique in that they provide local vertical profiles.

The error was small for C4X-18 because it was a nighttime flight. C4X-19 provided useful data for evaluating the ionospheric corrections and the calibration of the sounder hardware. C4X-21 provided additional data for evaluating the ionospheric corrections.

The ionospheric errors have been larger than anticipated in the 20 to 50 second region following the peak effect, which typically occurs 200 to 250 seconds into flight. The errors are a larger percent of the predicted value than is assumed for the current model, but their absolute values (less than 0.05 ft/s) are not large. Except for the small region indicated, the ionospheric model corrections appear to be adequate.

Hardware Error Characteristics. The primary hardware concerns identified at the beginning of the SATRACK development program resulted from the very low signal levels at the missile, the stability characteristics of the translator, and the configuration of the missile antenna. Figure 1 illustrates the basic hardware configuration. When signals from GPS satellites arrive at the missile input antenna from different directions, they are affected differently because of missile dynamics. Beyond the input antenna, all signal effects before separation of the independent GPS signals in the Post Flight Receiver are common to all signals. Separate tests have shown that the delay characteristics of the translator/receiver (channel 2; 1574 MHz) are independent of signal frequency over the expected Doppler range and are also independent of signal level over the expected level change. Therefore, when the GPS signals are differentiated in the processing system, only the input antenna errors and the channel-to-channel hardware errors of the Post Flight Receiver remain.

The missile antenna causes a large variation in signal level at the translator as its aspect angle changes with respect to the signal source. The peak signal levels in the C4X-18 test were 2 dB above the expected value, indicating that both the GPS signal levels and the translator noise figure were nominal. The composite specification for the GPS signal level and the missile antenna requires a level greater than -144 dBm over 90% of the spherical region surrounding the missile. For evaluation purposes, this has been interpreted to mean over 90% of the available tracking span. This condition has been exceeded for all three C4X flight tests.

Phase errors resulting from the antenna system are more difficult to evaluate. For each antenna pair,

a theoretical interferometer correction is made to the data, based on the nominal positions of the antenna elements on the missile body. Since two pairs are available, signals are selected so that corrections made near an antenna pattern null are not included in the final tracking data; i.e., the interferometer correction is not considered accurate in the null region where a very precise match to the theoretical model is required. The data for the three flights show that the interferometer errors, after correction, are consistent with the expected performance.

Two primary concerns with the translator hardware are that the added phase instability and/or noise would degrade tracking performance and that the channel 1 characteristics could not be calibrated sufficiently to allow dual-frequency ionospheric range measurement. The total system phase jitter has been evaluated for each flight. In each case, overall performance has been within the specification levels established for the translator. The delay calibration issue is not resolved but dual-frequency Doppler data have provided adequate information on the ionospheric model.

Based on the three flight tests and on other tests conducted throughout the development program, it has been determined that tracking errors of the Post Flight Receiver are represented properly by the jitter characteristics dictated by the signal-to-noise levels in the system. Interchannel delay bias effects are below 5 ns. The only other error characteristics are the truncation effects in the hardware counters. Specifically, a single delay measurement has a 2 ns quantization, and a single integrated Doppler measurement has a 0.01 cycle quantization. However, these errors are small relative to the signal-to-noise jitter.

Based on experience to date, the hardware system is performing exactly as expected and the projected error budget values are being realized.

EVALUATION RESULTS

In spite of the limited GPS support for the three flight tests (two GPS satellites for C4X-18, three for C4X-19, and four for C4X-21 as compared with the planned six), SATRACK has estimated trajectories quite well. One way to evaluate performance is to extrapolate the reentry bodies to impact using the SATRACK estimates of the deployment state vector plus the Lockheed Missiles and Space Co. deployment and reentry estimates and compare the result with an independent result from the Missile Impact Location System. When these comparisons are made, the agreement is very good.

The following conclusions can be drawn from the SATRACK C4X flight test evaluation:

1. The real-time data collection hardware is meeting its requirements fully,
2. The Post Flight Receiver is tracking the GPS signals with the expected precision,
3. GPS ephemeris errors are larger than were anticipated,
4. The tests demonstrate dramatically how the tracking results improve when more satellites support a flight,
5. SATRACK estimates of missile trajectory and guidance system performance compare very well with radar/TDMMS results,
6. Guidance uncertainties giving rise to cross-track velocity errors were more observable in SATRACK data than in radar/ TDMMS data,

7. The ionospheric correction technique for SATRACK data has been very successful for satellite links at elevation angles greater than 15°, and
8. Current experience indicates that SATRACK will meet or exceed all of its performance goals when GPS support reaches its expected level.

REFERENCE

1. *Satellite Missile Tracking Program*, SSPO Report 2200.3, Dec 1975.

*Authors: R. J. Anderson, L. J. Levy,
T. Thompson, and R. B. Hester*

Support: Strategic Systems Project Office, SP-25

SATRACK POST FLIGHT RECEIVER

Narrowband (10 Hz) Doppler and range tracking of low-level Global Positioning System (GPS) satellite signals translated through a Trident missile has been demonstrated by APL. Wideband (2 MHz) predetection analog signals are digitized (1 bit) and recorded for post-flight processing.

BACKGROUND

As part of the Trident Improved Accuracy Program (IAP), SATRACK was developed to provide a precision tracking system for determining a missile's trajectory during powered flight. In order to minimize changes to missile hardware, a simple frequency translator is placed in each test missile. The GPS satellite signals at 1575 MHz are received at the missile, translated to 2200 MHz, and transmitted to ground-based receiving stations. There, the signals are

heterodyned down to base band (less than 1 MHz), digitized (1 bit quantized), and recorded on magnetic tape. The required precision tracking of the translated GPS signals necessitated the development of the SATRACK Post Flight Receiver.

Development began with a hardware bread-board implementation of a digital phase lock loop receiver that could accept input data with 1-bit quantizing (zero crossing point on analog signal). Extensive tests were conducted at various input signal-to-noise ratios and tracking bandwidths to verify the operation of the design concept. The results of those tests showed that the loss in performance (output phase-tracking jitter) relative to a perfect theoretical analog loop was less than 1.5 dB. Tracking resolution goals of 0.01 cycle (3.6°) for Doppler and 2 ns for range were established to meet the overall SATRACK requirements.

The final implementation of the SATRACK Post Flight Receiver System consists of 16 digital hardware receivers controlled and serviced by a central high-speed computer. The system design goal of being able to process the recorded raw data in "real time" (no slowdown during playback) was achieved. Critical parameters (i.e., bandwidths and thresholds) associated with signal acquisition and tracking are completely under software control. The complicated process for determining the proper phase error (in the presence of rapidly changing signal levels) for each loop is also implemented in computer software. Tracked range and Doppler data from each receiver are transferred to the computer and are saved on magnetic tape.

DISCUSSION

In order to achieve the desired tracking performance at the low signal levels of the GPS satellites, very narrow tracking bandwidths (10 Hz or less) are required. During the early stages of powered flight, the relative range vector between the missile and the GPS satellite and/or ground stations is changing rapidly. The resulting rate of the translated GPS Doppler signals requires a tracking bandwidth greater than 300 Hz simply to maintain phase lock. Narrow-band tracking is achieved by aiding each loop extensively, based on precomputed data derived from the missile guidance system. The critical problem of aligning the time of the aiding data with the real-time playback of the raw data has been solved.

During the past year, recorded raw data from four live missile tests have been processed successfully through the SATRACK Post Flight Receiver System. The following discussion is on the performance achieved relative to the high signal dynamics for a brief period of one flight.

Figure 1 is a plot of the tracked received frequency versus time from one GPS satellite. It shows the rapid Doppler rate that must be tracked. The maximum rate of approximately 1400 Hz/s is achieved at the end of the interval. As mentioned previously, extensive aiding corrects for most of the dynamics; however, the loop by itself must track differences between the predicted and actual dynamics.

Figure 2 gives a good example of this capability. The receiving antenna (at the input to the missile translator) consists of four individual omnidirectional antennas mounted at 90° intervals around the diameter of the missile. Each antenna feed is summed with the antenna directly across from it, resulting in two pairs of antennas mounted orthogonally. An R1

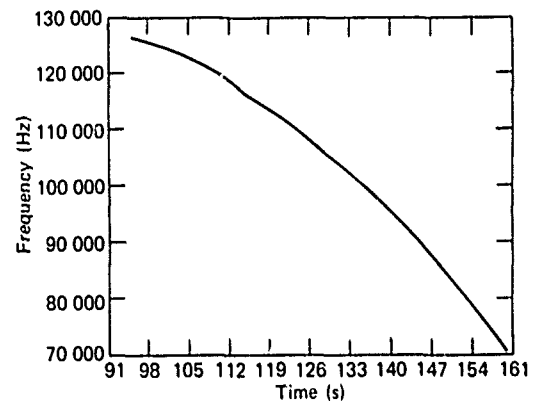


Fig. 1 Received frequency versus time from a GPS satellite translated through a Trident test missile.

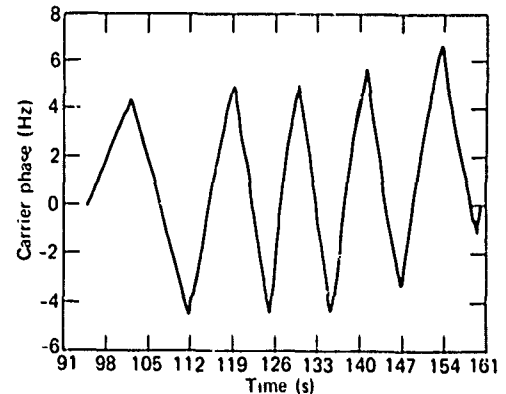


Fig. 2 Accumulated phase difference of signals received through missile antenna pairs.

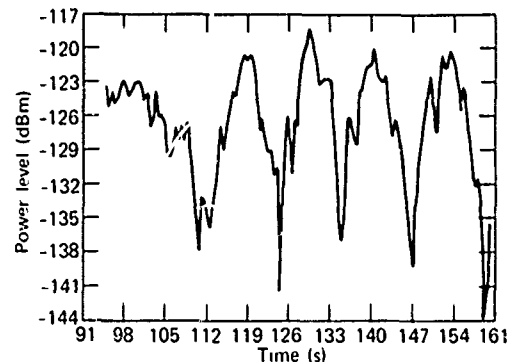


Fig. 3 Received signal power level at missile translator from GPS satellite.

switch determines which pair of antennas is feeding the translator at any given instant. The frequency of the antenna switch clock is 434 Hz. Proper reconstruction of the clock, after the fact, permits the signals received from each pair of antennas to be tracked independently.

Figure 2 is a plot of the accumulated Doppler difference resulting from independently tracking one GPS signal from each pair of antennas. The data are derived by differencing measured Doppler cycles from each track over the same interval (0.2 s) and then summing or integrating the differences over the entire time span. It is essentially the instantaneous phase difference between the two signals starting from an assumed in-phase condition. The cyclic phenomenon is a result of the phase interference from the two pairs of antennas as the missile rotates about its own body axis. Several cycles of phase are accumulated because the received wavelength (0.2 m at 1575 MHz) is small compared with the diameter of the missile. Since Fig. 2 is a phase plot, abrupt changes in its slope represent small steps in frequency. For instance,

at 126 s the phase slope changes from -1.5 to $+1.5$ Hz, indicating a frequency shift of 3 Hz. Since no aids are available for this phenomenon, the tracking loop itself must follow the steps. It is important to note that this relatively small effect is in addition to the total dynamics observed in Fig. 1. The noise on the instantaneous phase difference is a measure of the output tracking jitter and is less than 0.1 cycle.

Figure 3 is a plot of absolute signal power level from one pair of missile antennas as seen at the translator input. The 15 dB nulls are due to poor antenna gain when the line between the antennas is perpendicular to the line-of-sight vector to the satellite. Obviously, at that time, reception is very good from the other pair. The tracking loop can maintain phase lock, at a constant bandwidth, under the difficult conditions of rapidly changing signal levels.

Author: L. L. Warnke

Support: Strategic Systems Project Office, SP-25

COMPUTER TECHNOLOGY APPLICATIONS

INTRODUCTION

Extensive computational facilities are maintained by APL to support the work of its scientists and engineers. The central digital computer facility consists of an IBM 3033 Multiprocessor (MP) with high-speed large-scale dual processors. The 3033 is highly failure resistant, has a basic machine cycle time of 58 ns with overlapped (parallel) instruction execution, and has an advanced virtual memory operating system. Its main memories contain 16 million bytes and it has a virtual memory capability of 32 million bytes. This capability is supplemented by auxiliary direct access storage totaling 44.3 billion bytes (disk and mass storage). The facility serves a wide variety of tasks including large-scale simulations, complex analysis, and data processing and reduction. Extensive use is made of interactive processing for the real-time solution of problems; about 250 remote terminals are available.

APL also supports two analog/hybrid computer laboratories. Analog and hybrid computations are essential to the solution of complex problems, particularly when large numbers of simultaneous differential equations must be solved. Hybrid facilities can simulate economically large physical systems composed of continuous and discrete processes as well as real-time simulations that include hardware in the loop.

APL's two hybrid computer laboratories are the Interactive Simulation Laboratory (ISL) and the Guidance System Evaluation Laboratory (GSEL). The EAI 680 analog computers in the ISL are interfaced with an IBM 3033 digital machine that is part of the MP configuration. The other hybrid system, consisting of an EAI PACER 600 system interface to missile hardware and a radio

frequency test chamber darkroom, is used primarily to test missile guidance hardware. The physical facilities of both laboratories are being upgraded.

Data reduction, tape decoding, and reformatting of field-generated data are activities required to support the many test programs conducted by APL. A separate data reduction facility performs complex wave analysis, reformats analog and digital data for direct entry into the computer, and digitizes and plots data on paper and on microfilm.

Software development, minicomputer systems, and microcomputer development are supported by special facilities described in the 1976 *Developments in Science and Technology* (JHU/APL DST-4, pp. 52-57).

The articles in this section, a sample of computer-related projects at the Laboratory, cover the following areas:

1. A low-cost, computer-based system for measuring and displaying antenna patterns;
2. A software development and documentation system based on user interaction with computer-based software tools; and
3. A handbook that provides guidance and trade-offs to assist the designer of a distributed computer system.
4. Tactical speech synthesis by means of computers, studied as an aid to personnel who are required to perform complex coordination duties.

AN AUTOMATIC SYSTEM FOR MEASURING ANTENNA PATTERNS

A conventional antenna range receiver and manually operated antenna positioning system have been integrated with a small computer to form an automatic system for measuring antenna patterns. The expandable system, assembled and programmed for the NASA Goddard Space Flight Center, automatically measures and processes antenna pattern data at a cost that is substantially less than commercially available automated measurement systems.

BACKGROUND

NASA expressed the need for an automatic antenna pattern measurement system that was low cost, would use their existing range instrumentation, and would allow future expansion. It was desired to have the measurements formatted into a contour plot of antenna gain and also to be able to transfer the automatically collected data to a central computer facility for more advanced processing and analysis. The Antenna Pattern Data System (APDS) (Fig. 1) was developed to meet these needs. It provides portability and also compatibility between two antenna test ranges at Goddard.

The APDS is an outgrowth of an automatic data acquisition system developed at APL (Ref. 1) to satisfy the need for thorough and repeatable measurements of antenna patterns. It has been used for such tasks as collecting and processing radome error data.

The automatic data acquisition system was made possible by the standardization of an instrumentation bus (IEEE 488, Ref. 2) and by the availability of low-cost small computers. Necessary instrumentation can be connected over a single bus and controlled by the computer. Even instrumentation not having bus capability can be interfaced through other bus-compatible instruments such as analog-to-digital (A/D) converters and relay actuators.

DISCUSSION

Figure 2 is a block diagram of the APDS. The system controller, a Hewlett-Packard 9825A Desktop Computer, positions the antenna pedestal and measures the antenna data. The commands for direction and axis of antenna pedestal motion are directed over the general-purpose interface bus (GP-IB, IEEE 488) to a relay actuator. The relay actuator is interfaced with the pedestal interface control, which provides direct control of the antenna pedestal functions as

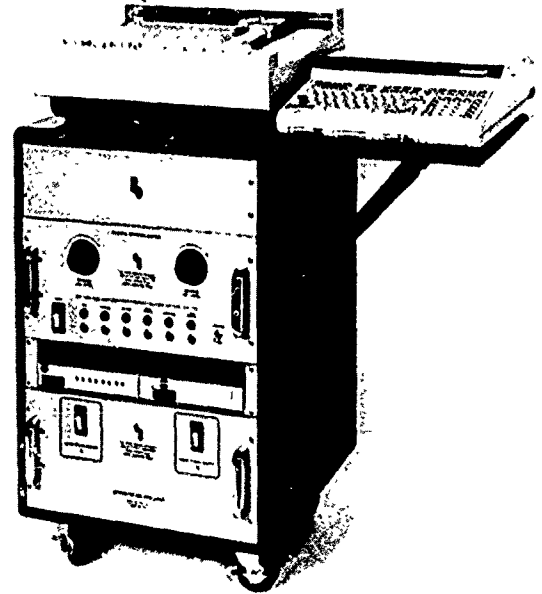


Fig. 1 Antenna Pattern Data System.

well as the manual selection of pedestal movement speeds. A three-phase synchronous waveform from the antenna pedestal, indicating the current position, is sent through a synchro distribution panel to the pattern recorder, console display, and pedestal interface control. The synchro-to-digital converter converts the synchronous position signal to a 16 bit digital word. The computer inputs the digital position information through a 16 bit input/output port and, after interpreting the input as angular position in degrees, determines if the antenna pedestal has arrived at the desired position. If so, the antenna pedestal is commanded to stop and the next axis of interest is positioned.

Antenna data are taken after the pedestal has been positioned properly. The π signal from the test antenna is directed into a phase/amplitude receiver along with a reference signal. The receiver outputs the measured phase as a DC voltage and the amplitude of the two π signals as a 1 kHz signal. The amplitude channels are fed through separate 1 kHz precision detectors to yield DC voltages proportional to the π signal amplitudes. The phase and amplitude channels are directed to an A/D converter that is controlled through the interface bus by the computer. The digital value corresponding to each A/D converter input is then read by the computer.

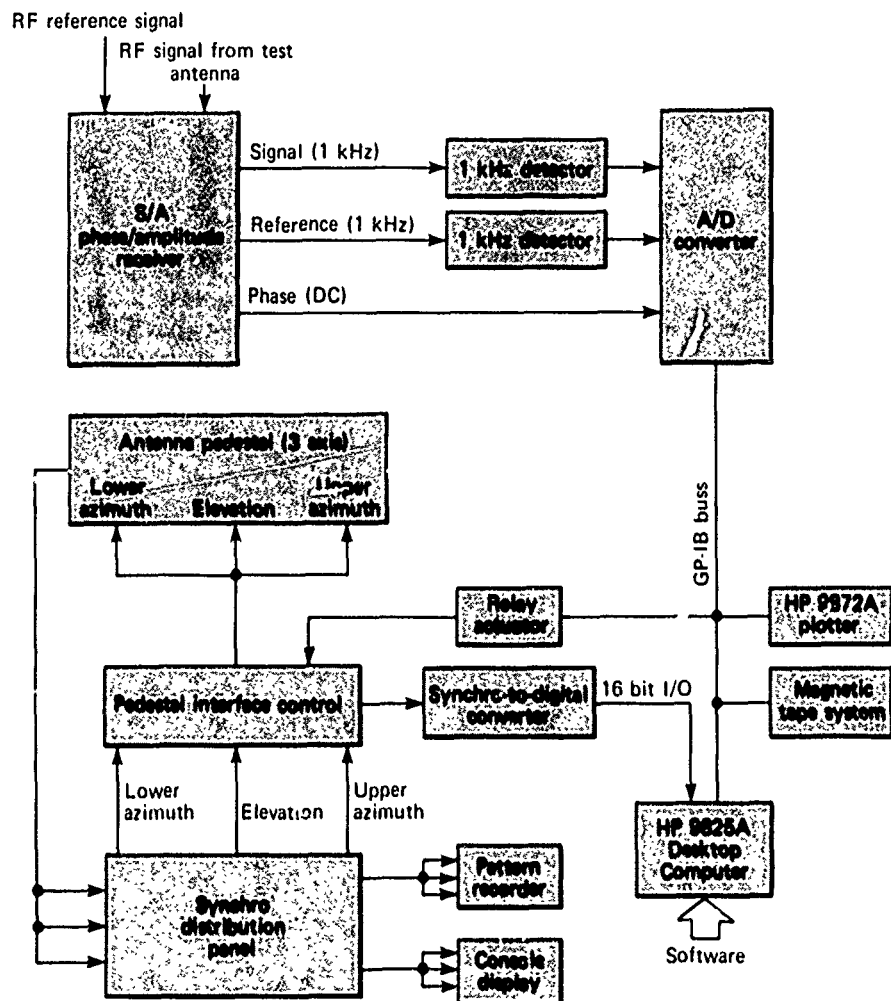


Fig. 2 Block diagram of APDS.

An automated test is performed when the computer, under software control, commands a programmed series of antenna pedestal movements and measurements previously selected by the operator. A magnetic tape system provides for permanent storage of the collected antenna data and allows data to be transferred to a central computer complex for further processing. A plotter displays the results of the test in a "readable" form.

The operation of the APDS revolves around three primary tasks: positioning the antenna pedestal, collecting the antenna data, and communicating the test results in an acceptable format. The antenna data collection program automatically positions the antenna pedestal to all of the desired azimuth and elevation angles and measures the signal characteristics through the antenna at each position. The resulting amplitude

and phase data are recorded on magnetic tape. A four-color radiation distribution plot is generated (shown without color in Fig. 3) while the measurements proceed, so that the progress of the test can be followed and to give a rough indication of the antenna gain characteristics. The antenna data collection program positions the antenna over a complete sphere with a discrete angular step size of 0.5° or larger. Smaller angular step sizes can be achieved by making minor changes to the program and reducing the speed of the pedestal movement.

The antenna radiation contour program retrieves the data previously recorded on magnetic tape by the antenna data collection program and generates a four-color radiation contour plot (shown without color in Fig. 4) of the tested antenna. This program can merge multiple files of data representing

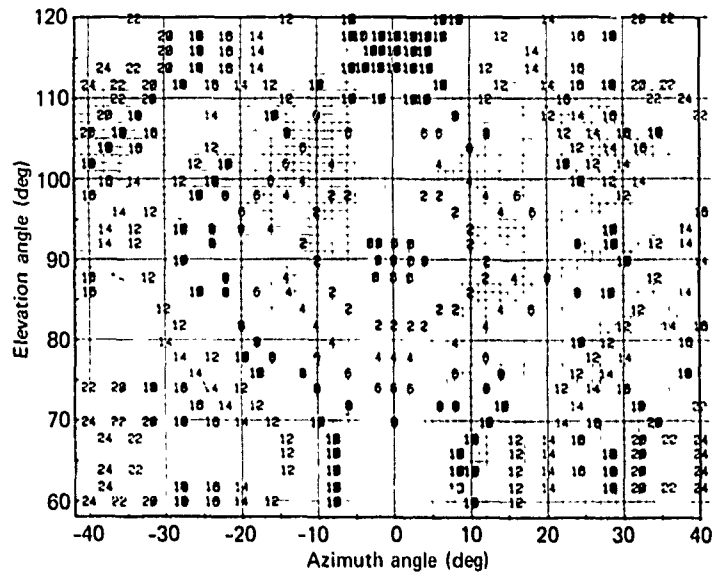


Fig. 3 Radiation distribution plot for a standard gain horn.

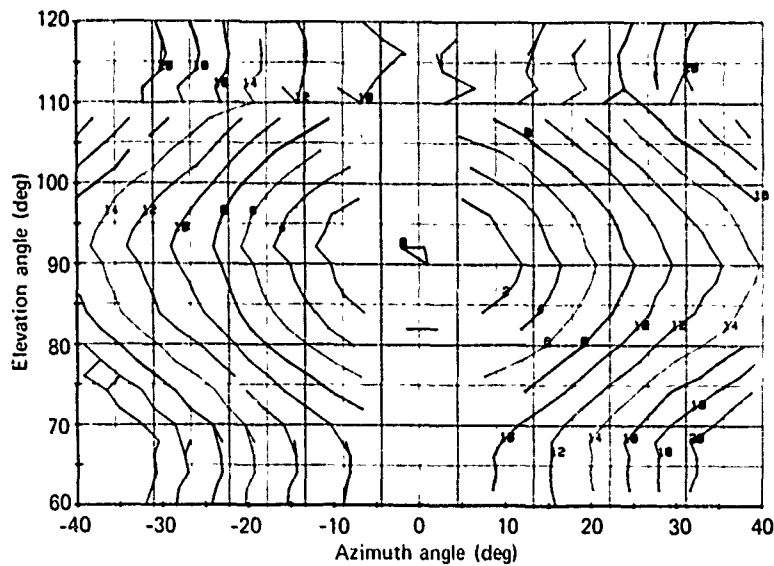


Fig. 4 Radiation contour plot for a standard gain horn.

separate tests of a single antenna into a single radiation contour plot. Incomplete data files resulting from an aborted test can also be accepted as data for a contour plot if desired. The characteristics of the plot, such as contour levels and dynamic range, can be chosen by the operator.

REFERENCES

- 1 C. H. Ronnenburg, *Evaluation of Interferometer Antenna Systems Using an Automatic Data Acquisition System*, APL JHU F1B 78U-042, 18 Apr 1978

- 2 *IEEE Standard Digital Interface for Programmable Instrumentation*, Institute of Electrical and Electronics Engineers Std 488-1975

- 3 C. H. Ronnenburg and R. L. Trapp, *Antenna Pattern Data System*, APL JHU F 579 001, Feb 1979

Authors: R. L. Trapp and C. H. Ronnenburg

Support: NASA Goddard Space Flight Center

THE COMPUTER ASSISTED SOFTWARE ENGINEERING SYSTEM

The Computer Assisted Software Engineering (CASE) System provides a comprehensive software development tool for engineers, designers, programmers, and managers. It guides its users through the tasks of documentation, design, coding, testing, configuration control, and status analysis.

BACKGROUND

Software engineering teams often find the development of a software system to be a harrowing experience. Let us trace a typical software system development cycle as depicted in block diagram form in Fig. 1.

The cycle begins with the definition of a requirement. A software system is designed to fulfill that requirement and a definition of "what" each system component must provide is formulated. The "what" is mapped into the "how" at the computer program design stage. This stage is also marked by the identification and design of the program units that comprise the computer program. Various levels of test plans and procedures are constructed, based on the system and program design specifications. Next, the program units are coded, individually tested, and integrated in an orderly fashion. At this point, hardware and software are combined and a formal certification test is conducted. Following approval of the software system, performance and design documents, data base descriptions, and user manuals are drafted, edited, and delivered. Modifications may be introduced at any stage in the development cycle.

Traditionally, the only steps of the software system development cycle that are performed with the aid of a computer are the coding of program units, their integration, and the certification testing. The remaining steps have to be performed manually. Thus, the following typical software-development problems arise:

1. Coding is started before the design has been completed;
2. Program documentation is done last, ergo poorly;
3. Managers have inadequate status information;
4. There is a lack of support facilities;
5. There is low programmer/designer productivity; and
6. The result is expensive, unreliable software.

DISCUSSION

A team of engineers and systems analysts in the Fleet Systems Department of APL conducted a study of the problems associated with the development of a software system and drafted requirements for a standard system software development tool. Thus, the CASE system was initiated.

The CASE system is precisely that—a system. It is an integration of various pieces of hardware with special CASE software and a unique operating system, PWB/UNIX, developed by Bell Laboratories. Figure 2 is a block diagram of the CASE environment.

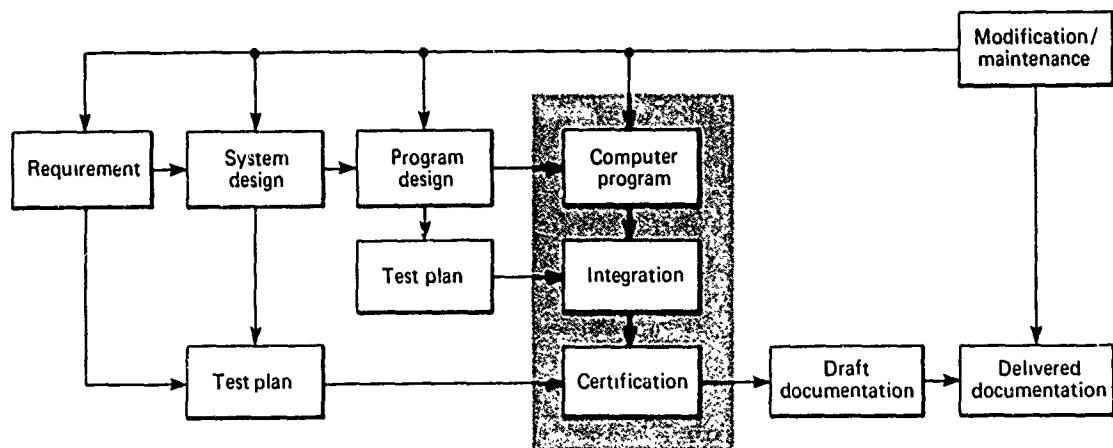


Fig. 1 Typical software development cycle.

The most important interface is with the application computers (hosts of the software system once it is developed and tested). A desirable environment calls for at least one application computer serving as a batch job processor for compilations, assemblies, and links and another reserved for interactive program unit testing.

The system offers its users a comprehensive set of functions on document production, design and code production, module testing, configuration management, and management reports production.

DOCUMENT PRODUCTION

The steps involved in document production using the CASE system follow.

Step 1: Creation of the Document Profile. The CASE data base includes "canned" document outlines for many documents whose outlines have been standardized. Starting with one of the canned outlines or a new one, the Project Administrator upgrades the document outline to a document "profile" by appending certain information to each section's title, including a description of what the Project Administrator wants the section to contain, the assigned authors of the section, and keywords to

be associated with the contents of the section (used later for retrieval purposes).

The Project Administrator may also include general document formatting decisions (single or double spacing, right column justification, etc.) within the profile.

Step 2: Creation of a First Draft of the Document. The author then issues a "document creation" command at a terminal, making sure to identify the profile upon which the document is based. The CASE system retrieves the document profile, isolates the entries pertaining to the first section, and prompts the user with information resembling the following:

1. INTRODUCTION
 Author = Linda Smith
 Keyword = CASE
 This section should briefly describe the name and purpose of this document.

The CASE system is now waiting for the author to enter the contents of the first section. He has a choice of five ways to enter the contents (Refs. 1 and 2). He also may enter a .MORE keyword to signal that the contents are incomplete and will be revised later.

Step 3: Modification of the Document. The author may incorporate suggested modifications to

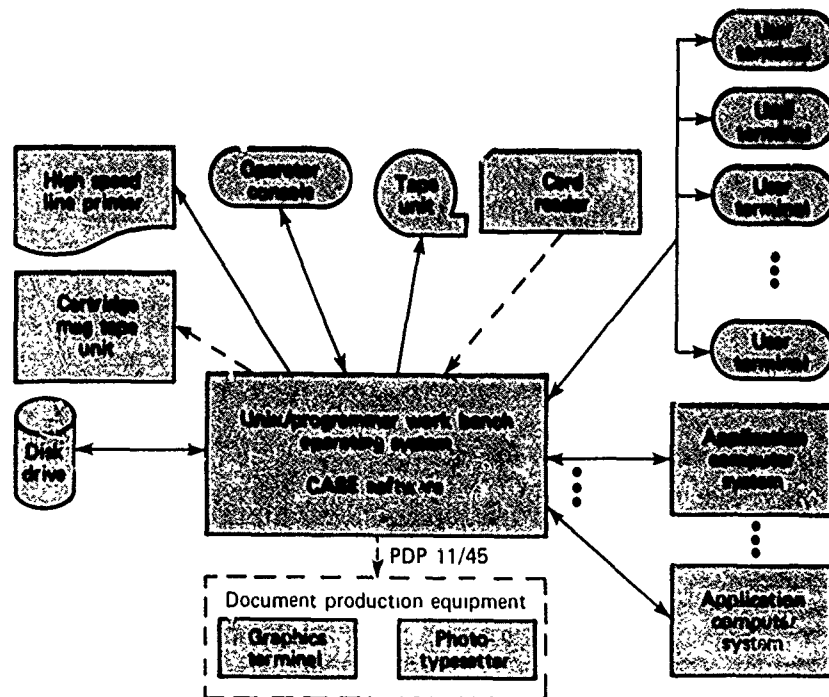


Fig. 2 Block diagram of the CASE environment.

the document file by issuing the "modify document" command and executing the procedures described in Refs. 1 and 2.

Step 4: Document Publication. When the Project Administrator decides that a document has reached the point where it is acceptable for general publication, he issues a "publish" command. The output of this processing may be routed to one of the documentation devices that interfaces with the CASE system to produce a high-quality report.

DESIGN AND CODE PRODUCTION

Once an individual or a group has been assigned responsibility for the design and coding of a particular module, the following tasks are undertaken:

Design Tasks.

1. Creation of a description of the module in text form,
2. Creation of a flowchart of the module,
3. Definition of the module's subroutine control flow and data interaction, and
4. Definition of the module's key data elements.

Coding Tasks.

1. Creation of source code that compiles or assembles without error, and
2. Creation of object code that links with other modules' object code without error.

The CASE functions that assist users in the completion of these tasks are listed and described in Refs. 1 and 2.

MODULE TESTING

The CASE module testing facility is a versatile testing, debugging, and integration tool that aids greatly in the production of high-quality, reliable software. It enables the test engineer to describe module inputs and outputs in engineering terms using a special-purpose high-level language designed specifically to describe real-time test procedures. The CASE system supports its users in all phases of module testing, including creating and verifying test description files, executing and storing module tests, producing test results, and analyzing module performance. The CASE functions that aid users in the completion of these tasks are described in Refs. 1 and 2.

CONFIGURATION MANAGEMENT

During the entire development cycle of a software system, the Project Administrator is faced with

the problem of configuration control. Documentation, source code, object code, design data, and test information must all be kept under configuration control. Working versions of each category of data must be kept separate from certified versions. Access privileges to certified versions must be monitored closely. The project data base must be protected but not to the extent that progress is impaired.

The CASE system is designed to offer considerable aid to the Project Administrator's role as configuration manager. It provides a user file (where the user can create, modify, or destroy the file, as desired) and a configuration control system (CCS) file (where certain access restrictions have been imposed). The restrictions on CCS files are given in Ref. 1.

MANAGEMENT REPORTS PRODUCTION

Throughout the development cycle, the Project Administrator requires system status information that can be retrieved quickly in order to make sound judgment about the course to be followed to complete the software system. The CASE system provides the following management reports:

1. Documentation status, including sections to be supplied/completed;
2. Code status, including total number of lines, number of lines changed, and number of reassemblies;
3. Configuration management, including update summaries, outstanding discrepancies, and a discrepancy-update map;
4. Schedules and milestones;
5. Memory usage, and
6. Time usage.

The CASE system is presently being used by three organizations on a half-dozen projects that involve the development of a software system.

REFERENCES

- 1 W. A. Amey, "The Computer Assisted Software Engineering (CASE) System," *Proc. 4th Software Engineering Conf.*, Sep 1979, pp 111-115.
- 2 W. S. Amey, D. J. Buscher, R. G. Greenberg, and M. H. Gates, *CISE User's Guide*, JHU API 15-79 070, Oct 1979.

Authors: M. H. Gates and W. S. Amey

Support: NAVSEASYSKOM, SEA-62X

A DISTRIBUTED PROCESSING HANDBOOK

There are many ways to distribute processing power among various computers, computer peripherals, and systems. A handbook written at APL discusses and categorizes many of the distributed approaches.

BACKGROUND

The term "distributed processing" has been used in recent years to describe a wide variety of computer architectures that display various degrees of processing parallelism. Distributed processing is recognized as being advantageous for several reasons. First, computational performance is improved if tasks are shared by several computing elements. Second, the resulting system is more reliable than if a conventional approach is used because if one computer fails, its work load can be shared by the remaining processors. Third, the system is readily expandable — more computers may be added to improve performance. The problem is that the designer of a system that might potentially use distributed architecture is faced with many possibilities. Whatever system is being designed, there must be some means to determine if a distributed processing approach is advantageous and, if so, what type of system should be used.

In response to this need, the *Distributed Processing Handbook* was written (Ref. 1). Various topics in the field are treated, and many examples from the literature are presented. A checklist enables one to narrow the search to appropriate systems, and an extensive bibliography lists sources for further reading. In this article, several important issues in the field of distributed processing are discussed. The specific chapters of the handbook where these topics may be found are noted.

DISCUSSION

The computers, computer peripherals, terminals, and other elements in a distributed system may be located in the same room, on the same aircraft or ship, or thousands of miles apart. The pockets of distributed system elements are called "nodes." A somewhat arbitrary but useful division of distributed processing systems based on the geographical distribution of the nodes has been made in Section 3.1 of the handbook. This division separates the systems into three major categories: dispersed networks, local networks, and localized systems. The

systems in which nodes are distributed across the country, called "dispersed networks," include nationwide and worldwide configurations such as the ARPA network (a resource sharing and message passing system) and the Aloha network in Hawaii. In the ARPA network as well as in other geographically dispersed systems, the links between nodes tend to be expensive. Therefore, great care must be taken to route packets of information efficiently from the source to the destination node.

At the other extreme is the localized system. A number of distributed processing and parallel computer architectures fit into this category, including multiprocessors that consist of several computers located in the same room, working on the same problem in parallel. If the system is programmed correctly, a substantial increase in throughput over that of a single computer should be realized.

Between the dispersed network and the localized system falls the local network. It consists of a number of terminals, computers, and computer devices (such as controllers or interfaces to sensors or actuators) located within an office building, laboratory, or ship. Messages are passed between the nodes. There has been much interest in the concept of a "paperless city" in which mail, personal banking information, news, and so on would be transferred between a personal terminal and the bank, news center, or mail service, over a common network. A few of the developing local networks are already experimenting with these ideas.

Section 3.2 of the handbook is concerned with the coupling between nodes, i.e., the rate at which information can be transferred. Many geographically dispersed systems are loosely coupled. For example, a typical link in a computer network developed by Texas Instruments runs at about 50 000 bits of information per second. In moderately coupled systems (e.g., many local networks), a typical data transfer rate is 1 to 5 million bits per second, whereas data are transferred even faster in closely coupled systems.

A very important issue in the design of a distributed processing system is its topology, i.e., how the nodes are physically interconnected. Different network topologies are described in Section 3.3. There are several possibilities for local and dispersed networks (Fig. 1). Most geographically dispersed networks are irregularly connected, whereas a popular local network topology is the shared line over which all devices communicate (the shared line might be a

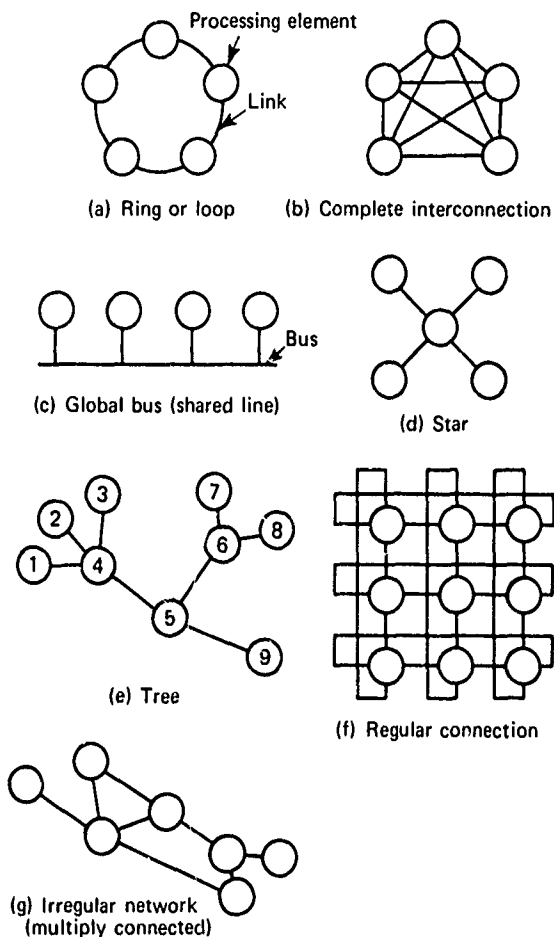


Fig. 1 Network topologies.

coaxial cable, for example). In a geographically dispersed system, the link between nodes could be a leased telephone line or microwave circuit. The topology of the localized system is quite different from that of the networks because information must be transferred between computers with much greater speed. In a multiprocessor, there are a number of ways in which the various central processing units pass data through a common memory. One example, the C.mmp multiprocessor of Carnegie-Mellon University, is shown in Fig. 2.

Once the physical architecture is defined, a distributed processing system is only useful if there is a well-defined protocol whereby data are transferred reliably and efficiently. The protocol must assure that data are transferred error-free between nodes in networks. This issue is treated in the handbook in Section 3.4. Other issues involved are control of the network's operation, the security of messages, the

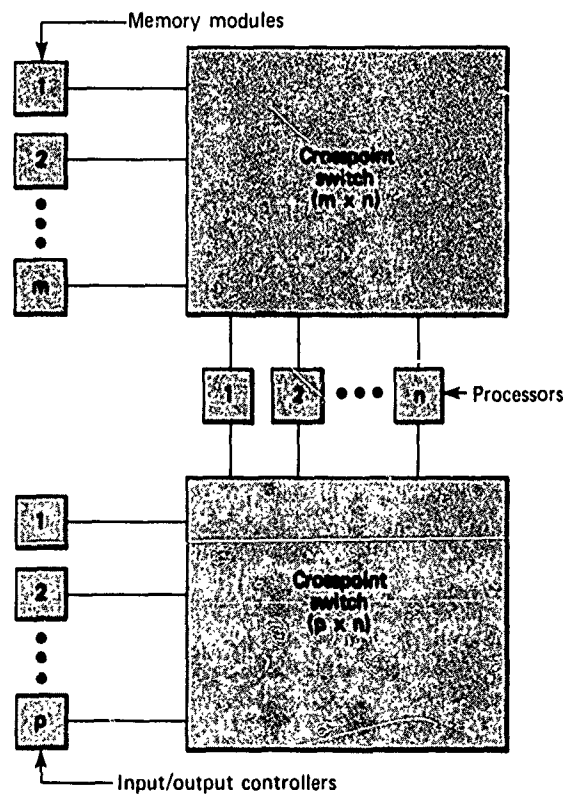


Fig. 2 C.mmp multiprocessor.

routing of packets through intermediate nodes, the detection of element failures within a distributed system, and network testing. Even if a protocol exists and messages can be transferred reliably from node to node, the applications software must be written to use this distributed environment effectively. This is true if several nodes are cooperating to solve one problem (fixed application) or if users at certain nodes require the resources at other nodes (resource sharing). Because software considerations for localized systems are often quite different from those of networks, this issue is treated in a separate section of the handbook.

In addition to the previously mentioned topics, the handbook covers networks that are built from other networks and brings up the issue of a "gateway" between systems. Section 3.9 provides a brief overview of conventional, as well as exotic, computer systems, some of which can be considered to be examples of distributed processing systems.

The handbook and the bibliography are good places to begin the study of distributed processing. For those interested in a bibliography on localized systems, Ref. 2 may be helpful. Reference 3 is a good

introduction to the growing field of network protocols.

REFERENCES

1 S. A. Kahn, *Distributed Processing Handbook*, API/JHU 15-79-080, Jul 1979.

2 R. A. Mosier, *A Multiprocessor Compendium*, Institute for Defense Analyses Research Paper P-433, Jun 1968.

3 J. M. McQuillan and V. G. Cerf, *Tutorial: A Practical View of Computer Communications Protocols*, IEEE Computer Society, 1978.

Author: S. A. Kahn

Support: Indirectly Funded R&D

TACTICAL SPEECH SYNTHESIS

A low-cost speech generation system has been interfaced to a standard Navy computer system in the Combat Information Center (CIC) of the APL Combat Systems Evaluation Laboratory. It automatically generates auditory alerts and status reports during simulated battle scenarios. The configuration will permit investigations into the utility of synthesized speech in improving operator efficiency in a CIC.

BACKGROUND

The Navy's Aegis Ship Combat System, a highly automated integrated system of computers, weapons, and radar, is in production and will be installed in a new class of cruiser in the 1980's. The Aegis New Computer Technology Program has been established to investigate new computer-related technological developments whose application to the Aegis Combat System may reduce costs or improve system performance (Ref. 1). Computer-generated speech has been identified as a maturing technology offering the potential benefit of improved operator efficiency in a CIC. To assess the potential benefit realistically, an experimental low-cost speech generation system has been interfaced to a standard tactical computer system in the CIC. The configuration enables the tactical computer system to issue auditory alerts and status reports automatically in response to changes in a simulated tactical environment.

DESCRIPTION

The tactical computer system consists of a Univac Q20 computer and a Univac 1230 computer (Fig. 1). The Q20 simulates friendly and hostile forces in the combat environment according to one of many battle scenarios. The 1230 simulates the Aegis Combat System operating within and interacting with the combat environment. The standard 1230 software has been enhanced to review the progress of the simulated battle periodically and to request appropriate synthesized announcements. Requests are communicated to the speech generation system through an APL-designed hybrid communications link.

The speech generation system (Figs. 1 and 2) consists of a Cromemco Z-2 microcomputer and two low-cost synthesizers: a Computalker CT 1 and a Speech Technology M188. The microcomputer decodes communications from the 1230 and sends back the required acknowledgments. It assembles appropriate synthesizer control parameters and sends them to one of the speech synthesizers, causing an announcement to be articulated. Currently only the Computalker is used.

A communications protocol has been designed and implemented to ensure that the receiving system is ready to accept data before the data are sent from the transmitting system. In general, communications are initiated by the 1230 system. However, a user may

request a status report by pressing a remote pushbutton connected to the speech system; this causes the Z-2 to initiate a communication, forwarding the request to the 1230.

A communications stream consists of control codes and speech codes. Control codes provide communications protocol and convey speech processing options. The options include selection of the specific synthesizer to be used and specification of announcement priorities; a high priority announcement (e.g., a threat alert) will immediately interrupt any announcement in progress. Speech codes consist of an utterance code identifying a word or phrase to be spoken and a post-utterance delay code. Utterance code

values of 0 to 69 have been assigned arbitrarily to the words and phrases needed to form a preliminary set of announcements. Delay codes specify the length of the pause that should separate the requested utterance from the one that follows. Delays may range from 0 to 1.5 seconds in increments of 0.1 second.

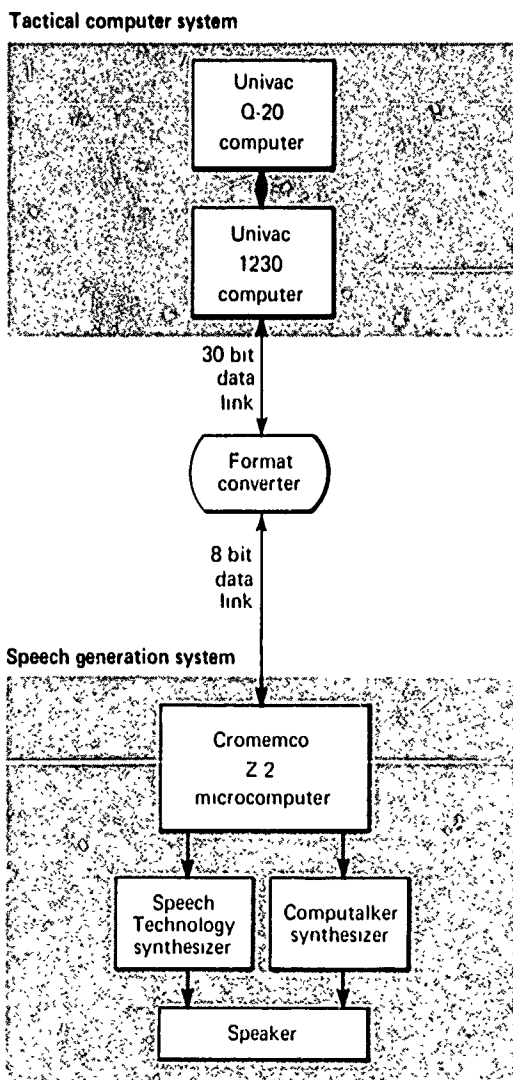


Fig. 1 Block diagram of tactical speech synthesis system.

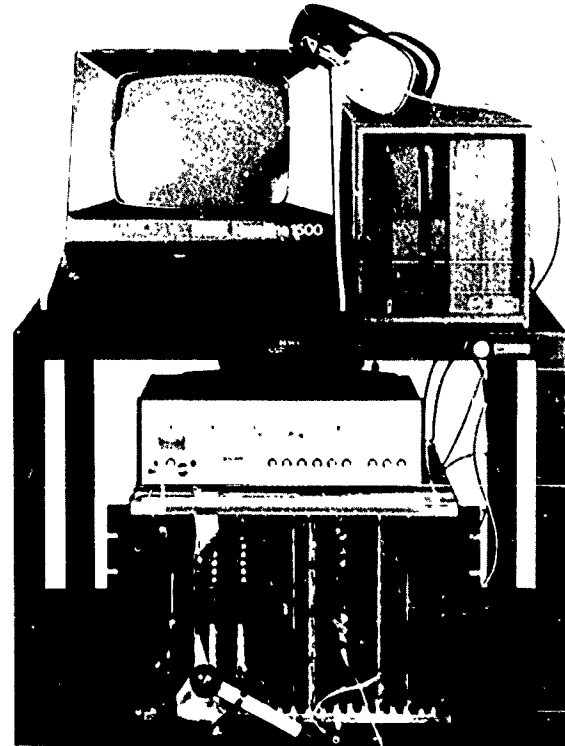


Fig. 2 Speech generation system.

In the current phase of the investigation, the Computalker is being used to evaluate and develop effective tactical announcements. Table 1 lists three preliminary candidate announcements currently implemented and the conditions under which each is generated. Despite its modest speech quality, the Computalker synthesizer was chosen for this phase because its speaking vocabulary can be changed to accommodate new announcements. The vocabulary consists of a list of phonetically spelled words stored in the microcomputer's memory. A new word to be added is translated into a sequence of phonetic symbols, which are added to the list.

The system described above constitutes a tool for experimenting with and evaluating computer-generated speech in the dynamic tactical environment

TABLE 1
PRELIMINARY CANDIDATE ANNOUNCEMENTS

Type	When Presented	Example
Periodic status report	Every 10 minutes during periods of no hostile activity	"Time: Twenty-three, thirty. No hostile contacts. Response plan bravo set. Auto fire not set."
Initial threat alert	First penetration of a threat into preset range	"Threat alert! Contact at: Thirty-three miles. Decision time: Forty-one seconds."
On-demand status report	Operator requested, typically used during attack	"Status: Sixteen threats. Twelve engaged. Highest unengaged threat: twenty-three seconds to go." (Track number and additional unengaged threats given if time to go is less than a preset values.)

of a CIC. Since the effectiveness of this speech depends on the intelligibility of the announcements, selected messages may be implemented in the future on a synthesizer with better fidelity. The Speech Technology synthesizer incorporated in the speech generation system is a possible candidate. Although its speaking vocabulary (consisting of custom-ordered digital recordings of human speech) is inconvenient to change, the clearer, more natural articulation makes it well-suited for final evaluation once a tactical announcement set has been chosen.

REFERENCE

1. A. E. Davidoff, *Aegis Ship Combat System New Computer Technology Applications Technical Plan*, APL/JHU FS-78-058, Jul 1978.

Author: D. F. Sterne

Support: NAVSEASYSKOM, PMS-400

ENERGY RESEARCH AND DEVELOPMENT

INTRODUCTION

APL began studying the environmental and social impact of energy facilities in 1971 in collaboration with The Johns Hopkins University Department of Geography and Environmental Engineering and with the Chesapeake Bay Institute. It has since evaluated for the State of Maryland all proposed power-generating facilities in the state. The work has led to projects and contributions in a wide variety of technical areas related to the location of energy facilities and the mitigation of damaging effects. One project reported in this section — an assessment of the environmental effect of saline water "drift" emitted from a cooling tower — is intended to quantify the emission and deposition of salt and the effects on crops, soils, and vegetation from the operation of a large natural draft cooling tower using brackish water.

APL is also contributing to the development of new energy systems. By 1973, it had analyzed energy technologies and concluded that the use of low-grade heat (solar thermal, geothermal, and waste) will provide increasingly important alternatives to scarce fossil fuels. Programs were initiated in-house to study ocean thermal energy (solar energy stored in tropical oceans), geothermal applications, and systems such as the Community Annual Storage Energy System that save summer heat for winter use. A common requirement of these applications is more efficient heat exchange at small temperature differences, but reliable engineering design data were not available. The Ocean Thermal Energy Conversion (OTEC) heat transfer experiments conducted by APL over the past several years provided the first firm basis for the design of economical evaporators and condensers for large OTEC plants.

The Laboratory has become a leader in developing the concept of using ocean thermal gradients to produce ammonia. Domestic ammonia for nitrogen fertilizers is now made from natural gas. The APL version of OTEC could have a substantial effect on the consumption of natural gas in the United States. Our efforts have included the design and evaluation of heat exchangers as well as the design of an OTEC pilot plant that will produce 5 to 10 MW of electrical energy. During the past year, a model of a proposed heat exchanger (designed by APL to satisfy cost effectiveness objectives) was tested as an evaporator, with excellent results; this effort is reported here.

APL is responsible for studies of geothermal resources in Region 5 of the Department of Energy/Division of Geothermal Energy (DOE/DGE). Scenarios outline the potential magnitude of identified resources, present development and use schedules, and indicate problems that must be surmounted before the resource can be used. Institutional impediments to the development of low-head hydroelectric power are being studied. Work has begun on techniques for extracting methane from landfills and continues on the active acoustic detection of leaks in underground natural-gas lines.

DOE recently completed an extensive drilling program, including a deep well (4500 feet) at Crisfield, Maryland, which resulted in the discovery of 133°F water — temperatures of up to 200°F are expected at other locations. In order to determine the potential effect of the development of geothermal resources in this region, APL has undertaken a geothermal energy market study for DOE. The Laboratory will survey current requirements for thermal energy at temperatures below 250°F, perform generic engineering studies to ensure that geothermal energy is feasible for satisfying these requirements, analyze the economics of supplying geothermal energy for those applications, and develop a methodology to assess market penetration. Three articles report on this work. One addresses the survey results and engineering studies, another presents a more detailed engineering study of the Crisfield well data, and the third discusses economic modeling of potential geothermal resource applications.

Other energy-related programs are under way. Pioneering work has been done in developing efficient flywheels from filamentary materials, and a feasibility study has been completed in which the operation of a complete, low-cost flywheel energy storage system was demonstrated.

APL is also making advances in energy conservation. Over the last several years, reductions have been made in the energy required for its own facilities. One technique uses the waste heat from the computer system and from air conditioning systems together with a heat pump to augment the heating and hot water systems for several buildings. The Laboratory is now helping the State of Maryland to review the energy efficiency of several state buildings.

ENVIRONMENTAL ASSESSMENT OF SALINE DRIFT FROM THE CHALK POINT NATURAL DRAFT COOLING TOWER

The environmental impact of saline water "drift" (an aerosol formed directly from a tower's cooling water and emitted from the cooling towers) can be an important consideration in the siting of electrical power generating plants. The Chalk Point Cooling Tower Project is an experimental and analytical program to quantify salt emission, salt deposition, and the effects of salt on crops, soils, and native vegetation resulting from the operation of a large natural-draft cooling tower that uses brackish water. APL has had a major role in this unique project including conducting field experiments, creating mathematical models, and performing systems analysis.

BACKGROUND

Historically, plants that use steam to generate electricity have used once-through cooling as the preferred form of heat removal. During the 1960's, however, electric generation equipment increased in size, and there was growing concern about the environmental effects of dispersing heat into natural waters. Moreover, many desirable sites for large generating stations do not have enough water to allow once-through cooling.

A proposed solution to the problem is to use large evaporative cooling towers. However, the emissions from cooling towers also have environmental effects. Heat and moisture emitted into the atmosphere as a warm, moist, buoyant plume can alter the meteorological conditions in the vicinity of the tower (e.g., by enhancing fogging and icing). Drift is carried up with the plume and subsequently deposited on the surrounding terrain. Mineral salts in the drift droplets can be harmful to vegetation and to man-made structures if deposited in sufficient concentrations. Cooling tower manufacturers responded with improved drift eliminators, which reduced drift emissions by an order of magnitude without seriously degrading cooling performance.

The 600 MWe Unit No. 3 of the Potomac Electric Power Company (PEPCO) generating station at Chalk Point, Maryland, was a prime candidate for study in 1970. Environmental concerns were raised at the legislative and regulatory level because the proposed natural draft cooling tower would be located in a choice agricultural setting and would use brackish water from the Patuxent River as makeup. Special

concern was expressed about the effect on crops important to Maryland's economy, such as tobacco (tobacco's burning rate is sensitive to chloride concentration). The effect on other crops (e.g., corn and soybeans) and on native vegetation was also of concern.

Hence the Chalk Point Cooling Tower Project was initiated in 1971 by a Maryland Public Service Commission action that required a research and monitoring program to determine the effect of salt drift at Chalk Point. The project has been jointly sponsored by the State of Maryland Power Plant Siting Office, the Electric Power Research Institute, the U.S. Department of Energy, the U.S. Environmental Protection Agency, and PEPCO. It has been implemented by the University of Maryland, Environmental Systems Corp. (ESC), Meteorological Research, Inc. (MRI), Bendix Environmental Science (BES), and APL.

DISCUSSION

The project has involved several phases of data collection, data reduction, and modeling analysis. In 1973, the Agronomy and Botany Departments of the University of Maryland implemented a program of vegetation and soil monitoring at several sites near the plant. Research was undertaken to establish the tolerance of crops, plants, and soils to saltwater aerosol spray. These field programs have continued into 1979 with excellent data recovery. Later in 1973, the program was expanded to develop and validate ways to estimate salt drift deposition from cooling towers by using data on tower emissions and ambient meteorology.

To support this effort, a program was begun to acquire the necessary data. ESC designed, constructed, and operated an instrumentation package to measure plume thermodynamics and drift parameters within the tower and to sample salt deposition on the terrain. BES instrumented a 100 m meteorological tower at three levels. During critical test periods, APL provided radiosonde measurements, and MRI instrumented an aircraft to measure external plume meteorology (including the drift aerosol). In 1975, baseline measurements were made of internal plume and drift parameters. Then in December 1975 and June 1976, full-scale intensive tests were conducted to

provide data on the internal and external plume and on salt deposition over a wide range of ambient meteorological conditions.

Since the flue gas scrubber on the boiler stack is also a source of saline drift droplets, the drift dye tracer experiment was conducted in June 1977 to identify cooling tower drift. The data collected by a dense array of samplers were used to validate a saline drift deposition model developed by APL. The model and the Chalk Point data base were then used to predict the effects of the full operation of several plant configurations. Reference 1 is an overview of the entire project.

Drift Dye Tracer Experiment. The Drift Dye Tracer Experiment (Ref. 2) was designed to separate and identify individual aerosol sources contributing to the total downwind drift at the Chalk Point site. The tracer in the circulating water of the cooling tower was 1 ppm rhodamine WT dye. The experiment provided a complete set of data to validate the deposition models, including the simultaneous measurements of tower emissions, ambient meteorology, and ground deposition. Preliminary to the field test, laboratory tests established proof of principle, environmental safety, and chemical controls for the use of the dye. Rhodamine WT was selected because it is inexpensive, safe, and controllable. The only limitation noted was its chemical decomposition in the presence of ultraviolet radiation, so the test had to be conducted at night.

Two sampling arrays subtending an arc of 35° were deployed 0.5 and 1.0 km downwind of the cooling tower. Each station had three funnel samplers for data on total deposition and three filter papers for data on droplet size distribution. Background sampling stations were upwind of the cooling tower. All sampling stations were within 40 m of each other in order to resolve the variation in deposition across the drift plume.

Chemical and fluorescent analyses of the funnel samplers were used to separate the total tower drift deposition from that caused by other sources. Both water and fluorescent droplet stains on the filter papers were read manually to determine the droplet size distributions from the two sources. Figure 1 is an example of the mass-fraction size distributions that were obtained. Examining the distributions provided an alternate measurement of the total deposition at each sampling location. Subtracting the total deposition determined by fluorescent analysis from the total determined by chemical analysis provided separate measurements of drift deposition from the cooling tower and from other sources (the boiler stack). Figures 2 and 3 show the rates of sodium deposition 0.5 and 1.0 km from the cooling tower using the

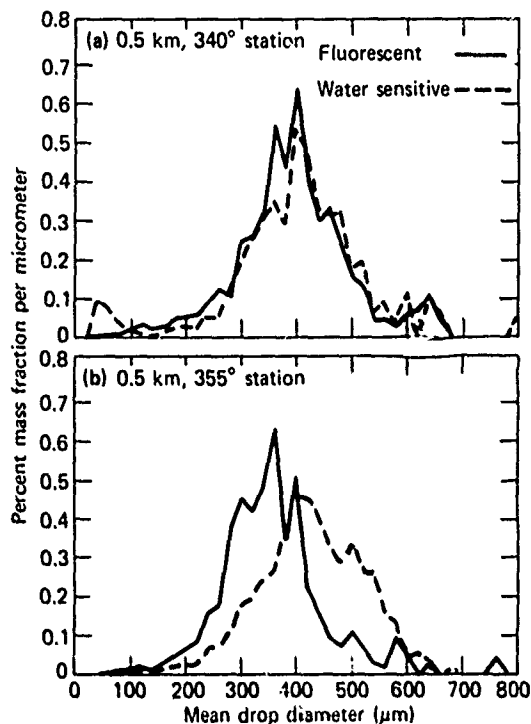


Fig. 1 Comparison of percent mass fraction distribution curves for fluorescent and water-sensitive filter paper droplet distributions at 0.5 km, showing little or no stack effect at 340° station and considerable stack effect at 355° station.

separation technique. Since some of the droplet distribution data have not been reduced, a complete comparison cannot be made, but the available results show that the total sampling and the droplet methods are in good agreement. Both sets of data show that the tower plume was centered over the sampling arrays during the experiment, allowing an accurate accounting of all tower drift deposited at those distances. The data together with the droplet size spectra are essential for model validation.

Modeling and Analysis. APL has developed a model (Fig. 4) to predict where the drift goes after it leaves the tower. The saline drift deposition model (Ref. 3) is a time-increment simulation that tracks the trajectories of various sizes of drift droplets. Using the tower characterization data and the meteorological tower data taken over several years, the model predicts the carryover of drift with the buoyant plume and the droplet breakaway, fall, and deposition for each three hour period. The effects of evaporation and turbulent dispersion on droplet trajectories are considered in the estimates.

The model's features and physical basis are comparable to those of several being used. However,

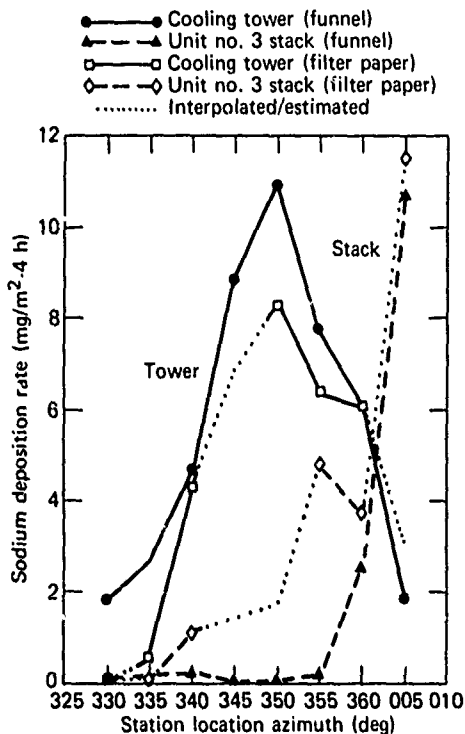


Fig. 2 Sodium deposition rates from major Chalk Point sources at 0.5 km from tower, by two independent measurement techniques.

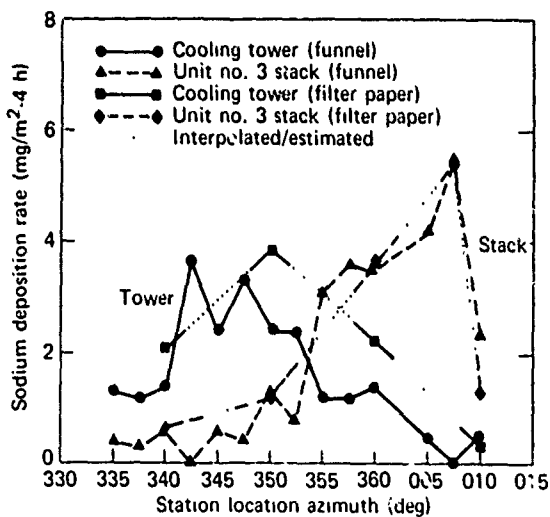


Fig. 3 Sodium deposition rates from Chalk Point sources at 1.0 km from tower, by two independent techniques.

the differences in models can result in predictions that disagree by a factor of two or more, hence the need for validation against a good set of field data such as that obtained in the tracer experiment. The APL model has been validated with these data and its predictions compared with those of several other models.

The data from the intensive test periods have been analyzed and reduced to model inputs that define the tower emission characteristics under varying atmospheric conditions. ESC measured the salt emission with an isokinetic sampler. This measurement, together with the basin water salinity, indicates that the tower drift rate is about 0.001% of the circulating water flow or about 2.2 gal/min, a value that is about one-half the design value of 5.2 gal/min. The instrumentation package used by ESC also measured temperature, relative humidity, and velocity at the tower. Size distributions of the drift droplets at the tower exit were measured by instrumentation using laser light scattering and by sensitive paper samplers. Although the emphasis was on the cooling tower, a limited amount of data was collected on the boiler stack.

The APL model has been used to estimate monthly, seasonal, and annual salt deposition for various operating configurations of both cooling towers and stacks (Ref. 3), and isopleths have been prepared. Figure 5 shows the annual isopleth for cooling tower deposition. The model predictions indicate that with full-time, full-load operation of two 600 MWe units, significant levels of salt deposition

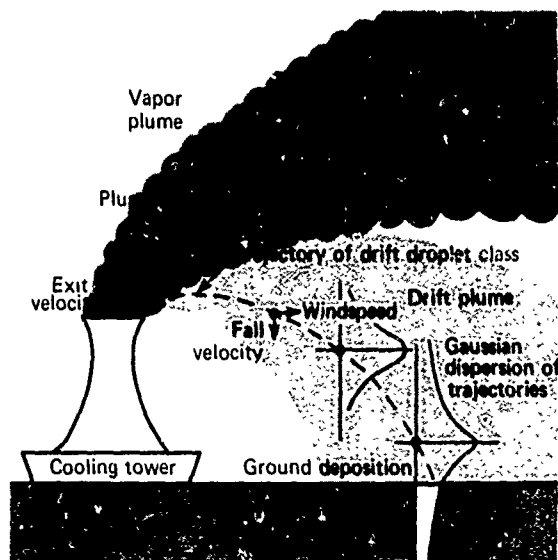


Fig. 4 Essential features of APL saline drift model.

Conditions:

Unit no. 3 cooling tower
Plant load 590 MWe
Operating 24 h/day

* Point of maximum deposition

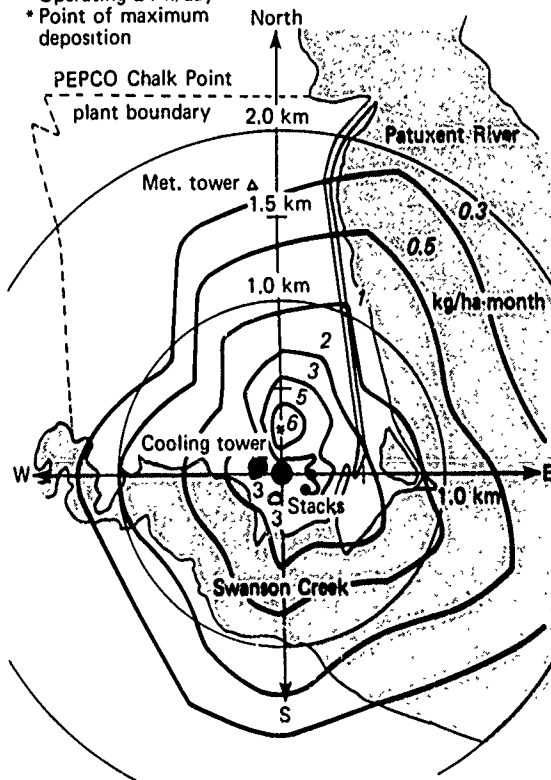


Fig. 5 Isopleths of estimated annual salt loading (kg/ha-month).

occur only on the plant site within 0.5 km of the source. The maximum deposition rates are predicted to be 13 kg/ha-month (12 lb/acre-month) from the cooling tower and 23 kg/ha-month from the stack. If two units are operational, the estimated maximum seasonal rate on site is 58 kg/ha-month during the summer months. In all cases, the off-site deposition is of the same order as the ambient salt background, approximately 1 kg/ha-month.

The effects on crops, soils, and native vegetation have been predicted (Ref. 3) by comparing the predicted salt deposition rates with measurements of vegetation sensitivity reported by the University of Maryland (Refs. 4 and 5). The data from three years

TABLE I
MAXIMUM EFFECT OF OFF-SITE SALT DEPOSITION ON CROPS*

	Maximum Deposition of Salt†	Reduction in Yield of Corn (%)	Reduction in Yield of Soybeans (%)	Reduction in Tobacco Burn Time (%)
No. 3 tower	2.0	1	0	0
No. 3 tower and stack	3.2	1	0	0
Nos. 3 and 4 cooling towers and stacks	5.4	2	0	0

*The data in this table apply at a distance of 1 km from the plant. Effects decrease at greater distances.

†In units of kg/ha-month, which is approximately 1 lb/acre-month.

of spray experiments have been reduced to regression equations (Ref. 4) that relate reductions in crop yields (and the reduction in burn time for tobacco) to salt deposition. The results indicate that the highest off-site deposition rates are well below significant levels established for corn, soybeans, and tobacco. Table 1, which summarizes the effects on crops at approximately 1 km, shows that the off-site effects are extremely small. Similar analyses for native vegetation and soils predict very small effects at off-site locations.

REFERENCES

1. M. I. Moon, *Overview of the Chalk Point Cooling Tower Project, 1972-1979*, JHU/API PPS-CPCIP-27, Mar 1979
2. J. H. Meyer and W. D. Stanbro, *Cooling Tower Drift Dye Tracer Experiment June 16 and 17, 1977*, JHU API PPS-CPCIP-16, Vol. 2, Aug 1977
3. E. A. Davis, *Environmental Assessment of Chalk Point Cooling Tower Drift and Vapor Emissions*, JHU API PPS-CPCIP-28, Mar 1979
4. C. I. Mukhi, D. C. Wolt, and J. A. Armbruster, *Cooling Tower Effects on Crops and Soils*, University of Maryland PPS-CPCIP-23, Jul 1978
5. G. W. Patterson, C. R. Curtis, I. I. Lauver, and G. Hosokawa, *Native Vegetation Study*, University of Maryland WRR-CPCIP-24, Jul 1978

Authors: E. A. Davis and J. H. Meyer

Support: State of Maryland, Electric Power Research Institute, Department of Energy, and Environmental Protection Agency

TESTING OF THE APL OTEC HEAT EXCHANGER AS AN EVAPORATOR

The main objective of the APL Ocean Thermal Energy Conversion (OTEC) Program is to demonstrate the feasibility of producing usable energy on a large scale from the temperature differences of tropical oceans, at minimum overall cost. A heat exchanger concept using large-diameter folded aluminum tubes and meeting the cost objective has been under study at APL. In the past year, a full-scale model of the proposed heat exchanger was tested as an evaporator at the Argonne National Laboratory (ANL) in order to obtain experimental data on its novel design and to validate or provide a basis for modifications of the computer code that will be used to estimate performance of an operational unit. The results of the experiment indicate that the unit works very well as an evaporator and that it presents a viable option for an OTEC heat exchanger.

BACKGROUND

A heat exchanger that meets the overall cost objective for OTEC plantships may not necessarily provide the greatest transfer of heat but should be low-cost, cleanable, and maintainable, in addition to offering modularity. The design conceived by APL (Ref. 1) offers advantages in these areas. The use of tubes with relatively large diameters reduces the number of tube joints, thereby reducing fabrication and assembly costs. No heat exchanger shells *per se* are required, and there is a good possibility for economical *in situ* cleaning of the heat exchanger without interrupting operations (Refs. 2 and 3). Its modularity (20 to 40 modules per plantship) will permit regularly scheduled inspection and maintenance, one module at a time, with no significant reduction in total output.

In an OTEC plant, warm seawater will flow vertically downward over the banks of tubes; ammonia flowing inside the tubes will vaporize, drive a power turbine, and then be condensed in a similar heat exchanger that uses cold seawater drawn from a depth of 2500 ft. The resultant electric power will be used to manufacture ammonia, aluminum, or other energy-intensive products aboard the ship.

Although prior performance analyses (Ref. 4) and tests on sections of the heat exchanger to measure the internal and external heat transfer coefficients have been encouraging (Refs. 5 through 8), tests of a full-scale model were clearly needed to demonstrate the overall performance and to evaluate possible problems with flow instability under simulated ocean conditions.

The results of the tests of the model as an evaporator (described herein) were used to modify the correlations that were used in the system studies.

DISCUSSION

Figure 1 is a simplified drawing of the model, which consists of three parallel-folded, 3-in.-OD aluminum tubes in a water box. Each tube has 43 passes, 14.3 ft long. The diameter and length of each folded tube are full scale to simulate a complete full-scale heat exchanger module as nearly as possible within the sizing and testing constraints imposed by the ANL facility. The three active tubes (with ammonia flowing inside) are contained within an inner water box through which water flows vertically downward by gravity from a head pond. A row of dummy (inactive) half-tubes is mounted on each inner wall of this box to provide the proper water-flow geometry. An outer box supports the hydrostatic head. In the plantship, the tubes will be contained in a volume formed by the concrete compartments of the ship, so the heat exchanger is considered to be shell-less. The outer box in the present experiment allows suitable fabrication tolerances to be maintained for the walls and tubes of the inner box.

To test the unit as an evaporator, subcooled liquid ammonia was fed into the three tubes at the bottom, and a two-phase mixture issued from the top. Warm water (78 to 82°F) was pumped into the head pond (which had a free surface) and was exhausted through a 12 in. pipe at the bottom. During May and June 1979, 56 test runs were made; 41 more were made during August and September. The most important test variables are shown in Table 1.

Changes in the entrance and exit manifolding for the ammonia were explored in order to determine their effects on performance; no significant differences were found. In addition, the first 38 tests were made with swirler elements in the first pass of each tube. Although these swirlers were used to enhance the transfer of liquid heat flow, to promote the onset of boiling in the unit, and to preclude flow instabilities, subsequent testing without the swirlers (all remaining tests) showed no significant difference in performance.

The system, which also included a condenser, pumps, a steam heater, and connecting pipes, demonstrated remarkable stability in operation, reaching

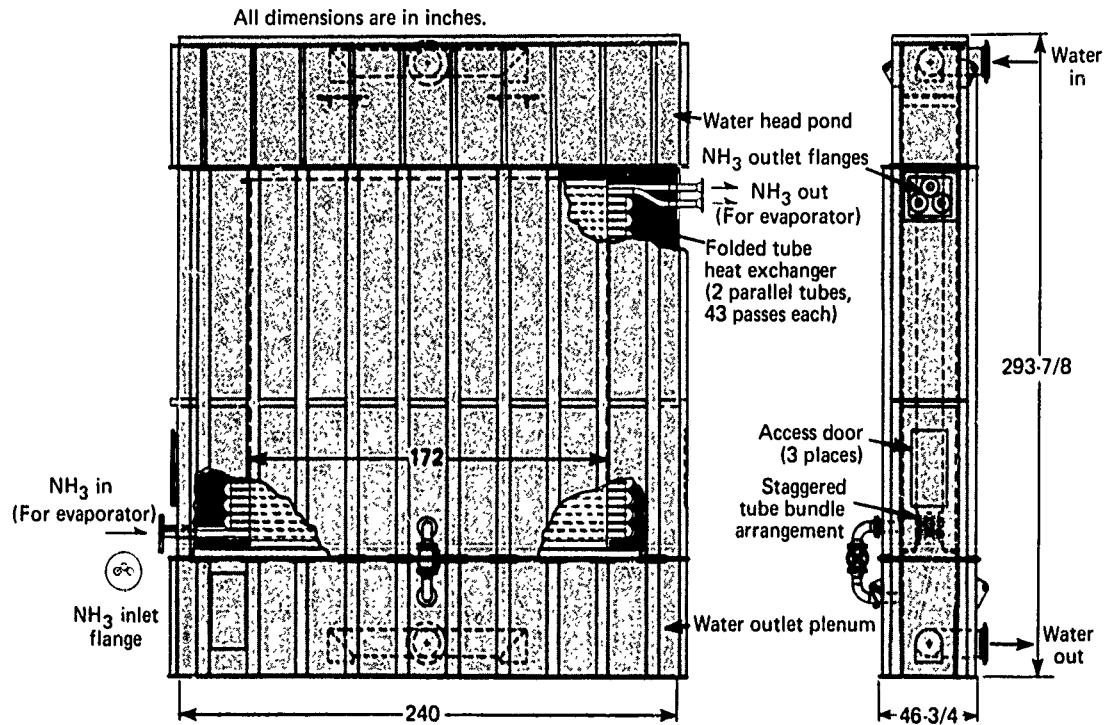


Fig. 1 Model of APL OTEC heat exchanger.

TABLE 1
TEST VARIABLES

Variable	Nominal	Variation
Heat duty	3.2×10^6 Btu/h	$(2.8 \text{ to } 4.6) \times 10^6$
Water flow rate	3200 gal/min	1500 to 4700
Water inlet temperature	80°F	78 to 82°
Ammonia flow rate	1.0 lbm/s/tube	0.7 to 2.0
Ammonia inlet temperature	72°F	55 to 72°
Ammonia inlet valve pressure drop	2 psid	0 to 4
Demister	Individual for each tube	Single common
Swirl element	Installed in first pass of each tube	Removed

equilibrium 1 to 2 hours after start-up or after changes in flow rates and heat duties. The test evaporator ran quietly and was free of significant vibration, and the ammonia flow divided equally (within 2%) among the tubes.

The thermal performance of the test evaporator was characterized by an overall heat transfer coefficient, U , the calculation of which was based on the heat duty, the areas involved in the heat exchange, the temperatures of the water at the top and bottom of the box, and the ammonia saturation temperatures at the inlet and outlet. The data from the first 56 tests gave the correlation shown in Fig. 2, in which U^* (U minus the effect of the tube wall) is plotted against a parameter involving the Reynolds number of the ammonia (Re_{NH_3}) and the water (Re_w).

Also shown is the predicted performance of the original analytical simulation. As the combined Reynolds number parameter increases, the original analytical simulation underpredicts the thermal performance by an increasing amount. Data from the remainder of the tests (not shown) also fall onto the correlation produced by the tests. With these data, modifications can be made to the analytical simulation to bring it in line with the observed results (the modifications are discussed in detail in Ref. 9).

Other important performance parameters measured by the experiments were the two-phase ammonia pressure drop and the water pressure drop. The ammonia pressure drop was less than was

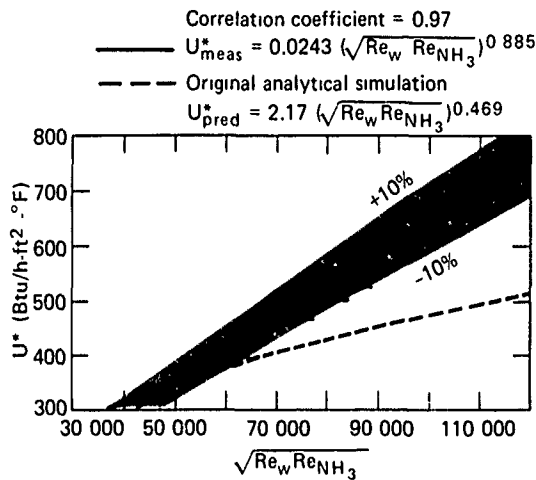


Fig. 2 Correlation of data.

predicted by the analytical simulation. The water pressure drop agreed with existing correlations for banks of smaller diameter tubes. Reference 9 gives details of the modifications to the analytical simulation for the ammonia pressure drop.

The results of the performance tests and the subsequent modifications to the analytical simulation with respect to the thermal performance and the ammonia pressure drop led to a prediction of about 13% more net power for the baseline pilot-plant design. (Reference 1 gives the baseline predictions.) Gains in net power of up to 22% have been estimated for higher flows of ammonia (increased Re_{NH_3}). The

APL heat exchanger model is the only evaporator tested that is directly scalable to a full-size ocean-going unit. Its demonstrated feasibility encourages support for its continuing development. Plans are now being made to test the model as a condenser and to test a similar evaporator model at sea.

REFERENCES

1. J. F. George, D. Richards, and L. L. Perini, "A Baseline Design of an OTEC Pilot Plantship," APL/JHU SR 78-3, May 1979.
2. P. P. Pandolfini, "Biotfouling and Cleaning Experiments for OTEC Heat Exchangers," *APL Developments in Science and Technology*, APL/JHU DST-5, Fiscal Year 1977, p. 88.
3. P. P. Pandolfini, W. H. Avery, and I. K. Hill, "Experiments in Cleaning of API/OTEC Heat Exchanger Biotfouling with an Ultrasonic Device," *Proc. 6th OTEC Conference*, Washington, 19-22 Jun 1979.
4. H. I. Olsen and P. P. Pandolfini, "Analytical Study of Two-Phase-Flow Heat Exchangers for OTEC Systems," API/JHU AEO-75-37, Nov 1975.
5. H. I. Olsen, P. P. Pandolfini, and J. I. Rice, "Internal Heat Transfer Experiments in a Simulated OTEC Evaporator Tube," API/JHU AEO-76-066, Nov 1976.
6. P. P. Pandolfini and J. I. Keirsey, "Internal Heat Transfer Experiments for OTEC Evaporator Tubes," *APL Developments in Science and Technology*, API/JHU DST-4, Fiscal Year 1976, p. 42.
7. P. P. Pandolfini and R. A. Makotski, "Circumferential Heat Transfer and Pressure Drop in Tube Arrays with a Low-Lateral-Pitch Ratio in Crossflow," APL/JHU CP 066, Jun 1978.
8. P. P. Pandolfini, J. I. Keirsey, and J. I. Rice, "An Experimental Investigation of the Onset of Nucleate Boiling Inside Large-Diameter Smooth Aluminum Tubes," API/JHU BBP-78-28, Mar 1978.
9. J. I. Keirsey, J. A. Funk, P. P. Pandolfini, and R. I. Cusick, "Core Unit Testing of the API/JHU Shell-less Folded Tube Heat Exchanger," *Proc. 6th OTEC Conference*, Washington, 19-22 Jun 1979.

Authors: P. P. Pandolfini, J. L. Keirsey, and J. A. Funk

Support: U.S. Department of Energy

GEOHERMAL ENERGY MARKET STUDY ON THE ATLANTIC COASTAL PLAIN

A Geothermal Energy Market Study (GEMS) has been performed for the Department of Energy/Division of Geothermal Resource Management (DOE/DGRM) in four potential geothermal resource areas on the Atlantic Coastal Plain. Information on the nature and size of current markets for thermal energy and estimates of the cost of supplying those markets with geothermal energy are useful to

DOE in formulating plans to explore, develop, and commercialize the resources.

BACKGROUND

Except for a few warm springs, geothermal resources generally have been considered to be a

phenomenon found in the western United States. Only in the past few years has the work of John Costain et al. (Ref. 1) at Virginia Polytechnic Institute and State University (VPI&SU) brought significant attention to the exploration for geothermal resources in the eastern United States. His basic tenet is that ancient (200 million year old) implantations of molten magma in the upper granitic crust in the east are richer in radioactive elements (U, Th, and K) than are the crustal rocks. When these igneous intrusions, or plutons, are covered with sufficient thicknesses of sediments (which act as thermal insulators or, more properly, heat sinks), the heat from the decay of the radioactive elements can be trapped, adding to the heat conducted from the earth's core and thereby providing a potentially attractive source of geothermal energy (even though all of the original sensible heat in the pluton was probably lost before and during sedimentation). DOE has funded VPI&SU to continue work on targeting such resources. Last year an extensive drilling program — 40 shallow (1000 to 1800 ft) wells and one deep (4500 ft) well at various locations — culminated in the discovery of 133°F water at Crisfield, Maryland. Temperatures up to 200°F are expected at other locations.

In order to help justify such exploration and to determine the effect of the development of the resources on the national energy situation, DOE requested that APL perform a study to (a) survey current requirements for thermal energy at temperatures below 250°F in the areas of potential geothermal resources (Fig. 1), (b) perform generic engineering studies to ensure that geothermal energy is a feasible source for satisfying the requirements, (c) perform analyses to determine the economic feasibility of supplying geothermal energy for these applications, and (d) develop a methodology to estimate the extent to which the resources could penetrate existing markets for thermal energy.

In the first phase of the GEMS effort, the first two tasks were completed for the four northern resource areas (Fig. 1); some of the results are given here. The economic analysis (Refs. 2 and 3) is discussed in another article in this volume. The market penetration study has been started for the residential sector (Ref. 4) and will begin shortly for the other sectors. In the second phase, the two most southern resource areas will be examined for potential geothermal energy markets.

DISCUSSION

The greatest requirements for thermal energy at temperatures below 250°F are in space and water heating for the residential and commercial sectors,

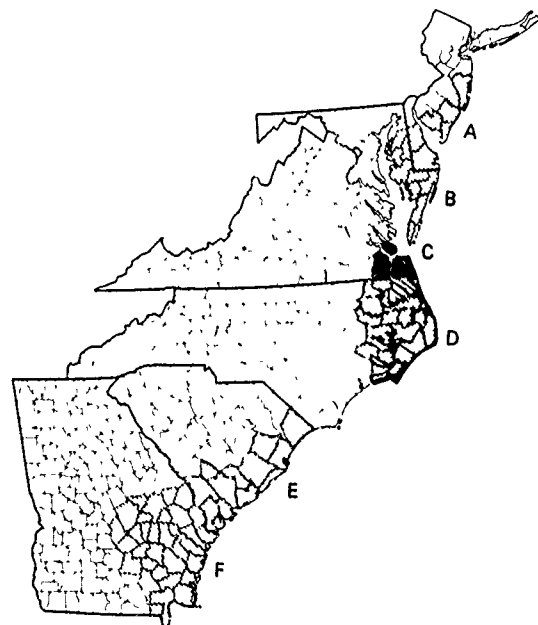


Fig. 1 Six geothermal resource areas on the Atlantic Coastal Plain.

however, because of the diffuseness of those requirements, expensive community distribution networks must be provided to satisfy many small individual loads. Moreover, the seasonal and hourly variations in loads place additional constraints on a community distribution system. All these factors are manifested in higher costs for delivered energy. Therefore, it is necessary to identify areas with high population densities so that distribution systems can be limited in size and cost.

It is not practical to obtain space and water heating data for the residential and commercial sectors on a local (door-to-door) basis. Individual building loads can vary drastically, even for identical buildings, because the occupants may have different schedules and activities. A survey to obtain such data, even if limited to very high density areas, would be prohibitively expensive and time consuming. However, useful data can be obtained on a more aggregated census tract or minor civil division level, where large numbers of buildings are included, because averages for space and water heating are fairly accurate for large populations.

A model developed by J. Karkheck et al. (Ref. 5) was selected for estimating the space and water heating loads. With this model, space heating is given on a per capita basis as a function of the number of annual heating degree-days and of building type, i.e.,

single-family or multifamily residences or commercial buildings. Annual water heating demands for the residential and commercial sectors are estimated on a average per capita basis. Heating degree-day information for selected cities was obtained from the National Climatic Center; interpolated values were developed on a county basis. Census Bureau population and housing data were obtained, and water and space heating demands were calculated. The results of the calculations were mapped to display the spatial distribution of the energy loads. Table 1 summarizes the residential and commercial heat loads for the four areas.

Data on space and water heating for military installations were obtained from the DoD Defense Energy Information System (DEIS) I and II reports. The data, also summarized in Table 1, represent actual energy consumption. The heat load for the NASA facility at Wallops Island, Virginia, was obtained independently and is included in the total for the Delmarva Peninsula.

The principal agricultural requirements for heat are in space heating and in crop drying. On the Delmarva Peninsula, most of this usage is connected with the very large poultry industry. Since only 13 companies were involved, each was contacted, and actual heat requirements for broiler house heating, egg hatching, and crop drying were obtained. The net results are shown in Table 1. Nearly 70% of the total is for broiler house heating.

Sources of such information for the remaining three resource areas were more numerous and diffuse; therefore, data on crop drying were obtained from the Bureau of the Census and the Department of Agriculture. These are included in the table. The large requirement in North Carolina is mostly for drying tobacco.

Estimates of energy consumption for process heat and space and water heating in the industrial sec-

tor are usually obtained from data on the average energy consumption per employee for a particular industry and the number of employees at each plant. In the past this approach has provided qualitative estimates for county totals. However, on a single plant basis the estimates can be grossly inaccurate; e.g., a warehouse and a factory with equal numbers of employees will appear to have the same energy requirements, whereas they actually are markedly different. Therefore, a detailed industrial survey was undertaken in the four areas to provide accurate estimates of energy demands.

Because the potential resources were not expected to exceed 250°F, not all of the two-digit SIC (Standard Industrial Classification) industries were likely prospects for geothermal energy applications. An initial screening identified six that had significant requirements for process heat at temperatures below 250°F, including foods and kindred products, textiles, tobacco products, lumber and wood products, pulp and paper, and chemicals. As the survey progressed, the largest and best suited industries were found to be food and lumber. Within the food industry, poultry processing, vegetable canning, and crab processing consume the most heat. The first two often are performed by large companies that could use nearly the entire thermal output of one or more geothermal wells and thus are attractive candidates for the early commercialization of geothermal resources. On the other hand, crab processing plants often are small concerns that require steam at 250 to 260°F, are scattered in sparsely populated areas, and thus are not attractive candidates.

More than 600 companies were included in the survey and more than 500 were contacted individually. At least 300 were found to have energy requirements that were compatible with expected geothermal resources, either directly or through the use of heat pumps. In terms of heat load, only 100 require more than 1×10^{10} Btu per year. (If a geothermal well could

TABLE 1
CURRENT POTENTIAL MARKETS FOR GEOTHERMAL ENERGY
IN THE FOUR NORTHERN ATLANTIC COASTAL PLAIN
RESOURCE AREAS

Resource Area	Sector			
	Residential and Commercial	Military	Agricultural	Industrial
S.E. New Jersey	290*	25	0.2	9.3
Delmarva	125	8	14.5	23.2
Norfolk area	200	97	0.5	9.1
E. North Carolina	78	15	9.5	13.7

* Values are given in 10^{11} Btu per year.

produce 200 gal/min of hot water and its temperature were lowered 50°F to supply process heat, the total heat available would be a little more than 4×10^{10} Btu per year.) Thus, two-thirds of the companies have energy requirements that may be too small to justify drilling their own geothermal wells.

The totals for all 300 companies in the four resource areas are shown in Table 1. Figure 2 shows the locations and sizes of the 146 companies (nearly half of the total) that are located on the Delmarva Peninsula. As Table 1 shows, the largest total market areas are Norfolk, Virginia, and Southeastern New Jersey; however, the residential/commercial markets, which are the major markets in the two areas, are the most difficult to serve in the short term. Likewise, most agricultural markets are quite diffuse and probably are best served by incorporating them into dual-purpose community systems. Military markets are the most attractive in the short term because (a) they are "captive" markets, (b) they are large, high-density consumers who would need many geothermal wells to satisfy their energy demands, (c) they currently use hot water or steam distribution systems that may minimize conversion costs and time, and (d) they are under directives to reduce energy consumption and therefore are exploring alternate energy sources.

A definite commitment by the federal government to develop such resources on such a large scale would encourage private concerns to become involved in the commercialization of geothermal resources. Unfortunately, there is reluctance in some quarters to do this. Therefore, the greatest short term potential for geothermal energy application is in the industrial sector, which has been investigated in the greatest detail.

The Delmarva Peninsula has the largest industrial market. Most of the market is made up of the poultry industry, which is extremely well suited to direct-use applications of geothermal energy. Grain drying facilities often are collocated with processing plants, further increasing the potential short term market.

The GEMS work is finished in four areas. Some additional work might be needed to extend the survey if resource locations or the awareness of other applications so warrants. Current plans are to study the South Carolina and Georgia resource areas beginning in the spring of 1980.

REFERENCES

- 1 J. K. Costain, I. Glover III, and A. K. Sinha, *Evaluation and Targeting of Geothermal Energy Resources in the Southern United States — Progress Report*, VPI&SU-5103-3, Mar 1977

Thermal requirements below 250°F

Estimated	Actual usage	Btu/yr
●	■	$0.5 - 1.0 \times 10^{11}$
◐	◑	$1 - 5 \times 10^{10}$
○	□	$1 - 10 \times 10^9$
•	▪	$< 10^9$

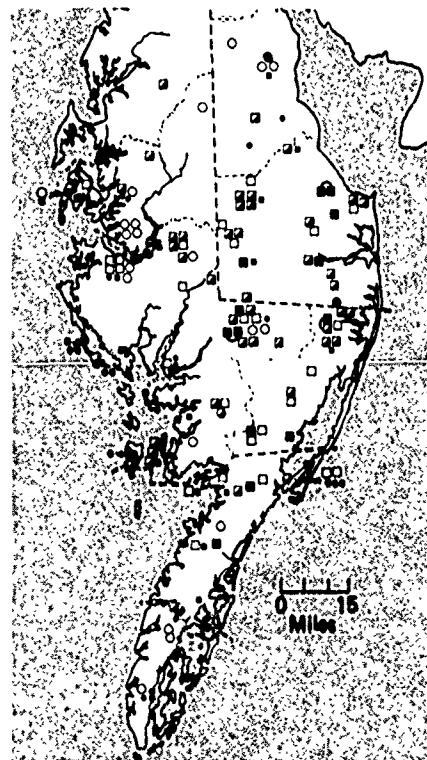


Fig. 2 Industrial markets for geothermal energy on the Delmarva Peninsula.

- 2 R. Weissbrod, W. F. Barron, P. Kroll, and W. J. Toth, *Economic Evaluation Model for Direct Uses of Moderate Temperature (up to 250°F) Geothermal Resources in the Northern Atlantic Coastal Plain*, APL/JHU GEMS-003, Jun 1979.
- 3 R. Weissbrod and W. F. Barron, *A Review of Recent Energy Price Projections for Traditional Space Heating Fuel, 1985-2000*, APL/JHU GEMS-005, Mar 1979.
- 4 A. C. Goodman, *Geothermal Energy Market Penetration for the Residential Sector*, APL/JHU GEMS-006, Sep 1979.
- 5 J. Karkheck, E. Beardsworth, and J. R. Powell, "Technical and Economic Aspects of Potential U.S. District Heating Systems," *Proc. 11th Intersociety Energy Conversion Engineering Conf. (IECEC)*, 1976, pp. 1669-1674.

Author: W. J. Toth

Support: U.S. Department of Energy/Division of Geothermal Resource Management

GEOHERMAL RESERVOIR ANALYSIS

In the Eastern United States, hot water is found in deep sedimentary deposits under the Atlantic and Gulf Coastal Plains and in inland sedimentary basins. These hydrothermal resources may be an effective source of energy for space heating and for industrial, agricultural, and maricultural process heat—displacing scarce and expensive fossil fuels.

BACKGROUND

The cost of developing geothermal reservoirs depends on the water temperature, the physico-chemical properties of the water and the surrounding rocks, and the productivity and life of the wells from which the hot water is withdrawn and into which the cooled water is reinjected.

Much is known about geothermal resources in the Western United States because of associated natural geysers. However, very little is known about geothermal resources in the East, where most of the United States population lives. Therefore, a resource exploration program was initiated under the auspices of the Department of Energy. The program culminated in the drilling of the first deep test well in the Eastern United States, at Crisfield, Maryland.

The chemical properties of geothermal waters are determined by withdrawing samples for analysis. The temperature is measured by inserting a thermometer in the well at the location of a productive aquifer. The hydraulic properties of the aquifer are determined by measuring the pressure of the water column in the well as water is withdrawn. The accuracy of the determination depends on how long each aquifer is tested. The tests are complex and expensive; accordingly, compromises are always required. It is also demanding and costly to determine the extent of the reservoir and the constancy of its characteristics. Conventional analysis usually selects only a portion of the test data.

The results of the initial Crisfield data analysis showed lower water temperature and well productivity than had been expected. The well productivity estimates varied, depending on which data set was used. The Crisfield well data are very significant because they define the geothermal resource under the Delmarva Peninsula. Therefore, APL analyzed well productivity using all of the test data for the most productive aquifer in order to find a best-fit measure of productivity. The extensive analysis led to a new set of reservoir properties. The magnitude of the most

critical parameter, transmissivity, increased by nearly 50%. Estimated (economic, useful) well life is greater than hundreds of years instead of a few days. This aquifer is not ideal but it has many potential applications, and it has sparked renewed interest in geothermal energy in the East.

This article presents a summary of the test well data and the unique analysis of the pump test data set.

DISCUSSION

The Crisfield test well was cased and cemented, and perforations were made through the cement and casing into three zones of permeable sand:

Test Zone	Depth (ft)	Net Permeable Region (ft)	Water Temperature (°F)
1	4148-4223	62	135
2	3901-4032	89	133
3	3698-3849	44	128

There were four perforations per foot for zones 1 and 2 and two per foot for zone 3.

After a brief review of the entire test data set, the data from zone 2 were selected because that zone was the most productive and those data were the most complete and the most reliable.

Zone 2 had been developed by means of several irregular sequences of pumping and pausing, as is done when developing oil wells. The pumping phase continued for about two days, followed by a two-day recovery period. The rate was varied considerably throughout the pumping phase, including a 23-minute shutdown because of equipment malfunction. Sand was produced throughout the pumping period. The pressure-time history is shown in Figs. 1 and 2.

Several features merit comment. The pressure drop near 8 a.m. (see Fig. 1) does not involve pumping head loss. Although there is no notation in the pump-test record, it was inferred that the pressure drop was caused by the pressure sensor being pulled up from its initial depth of 3966.5 ft (listed at the beginning of the pump test record) to its final depth of 3890 ft (stated at the end of the record). The least-square-fit parameters to the calibration of the pressure sensor, performed at the end of the test, give an apparent pressure drop of 34.28 psi for this depth change. The supposition that the pressure sensor was pulled up 76.5 ft is further supported by the fact that,

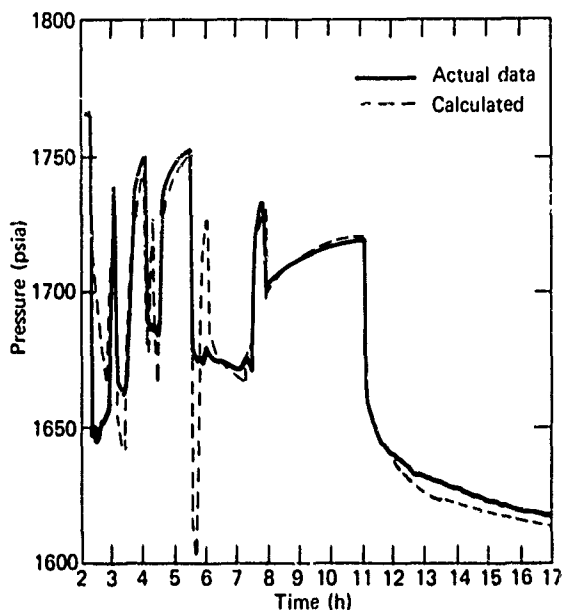


Fig. 1 Calculated and actual pump-test data from Crisfield test well, zone 2, well development and early test phases.

with the associated pressure correction, the apparent drop in pressure disappears and the corrected test data give rise to a continuous derivative of pressure recovery data (see Fig. 1, near 8 a.m.).

When the pump-test phase began, the pressure head was still actively recovering. This introduced transients into the early data. In addition, there were numerous perturbations throughout the test.

Applicability of Conventional Evaluation Methods

If a well's water level lowers as water is withdrawn, the flow is "unsteady" (i.e., nonsteady state). However, the three conventional ways to determine the characteristics of an aquifer are based on a data set with a constant water pumping rate and an absence of transients.

To determine leakage and delayed yield, it is useful to examine the Theis plot, i.e., a log-log plot of pressure loss (drawdown) versus pumping time (Refs. 1 and 2). For pressure loss, we may reference the static level of 1732 psia. However, since the pumping was initiated while the head was actively recovering, there is no convenient reference point for the time axis. We have therefore used the actual pumping time in Fig. 3. The curvature is minimal, so we cannot reliably determine the transmissivity and

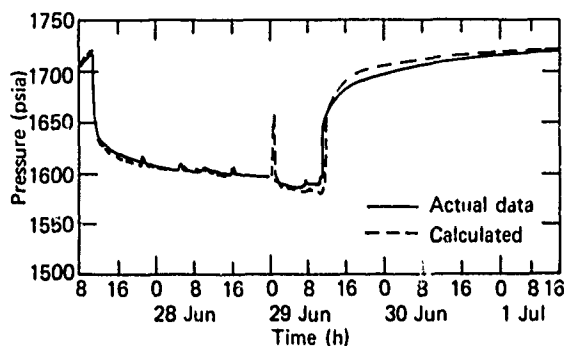


Fig. 2 Calculated and actual pump-test data from Crisfield test well, zone 2, pump test and recovery phases.

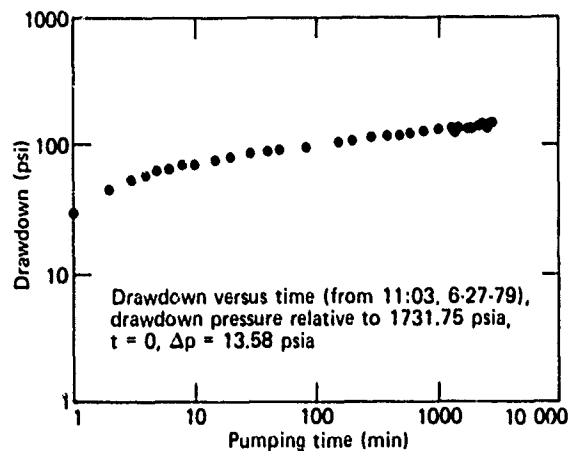


Fig. 3 Data from Crisfield test well, zone 2.

the storage coefficient by matching this curve with the theoretical Theis curve. Assuming that the changes in the pumping rate can be neglected, Fig. 3 shows that there is no evidence of recharge into zone 2 for the duration of the pump tests. Similarly, there is no evidence of leakage or delayed yield for that zone. After studying the well log, we concluded that zone 2 may be considered a confined aquifer. Thus, aside from this qualitative indication, the Theis curve method fails to give reliable estimates of the formation's characteristics.

Another method is to examine pumping time versus drawdown in a semi-log plot (Fig. 4), but this involves the same difficulty of not having a true time reference. According to elementary theory, the curve is supposed to be a straight line (provided the pumping rate has been held constant), but this curve bends

at about the sixth minute of pumping. Since the pressure was actively recovering when the pump-test phase was initiated, the early part of the data cannot be separated from the pre-existing transient effects. After the bend, the apparent transmissivity is approximately $0.70 \text{ cm}^2/\text{s}$ (≈ 487 gallons per day per foot, in hydrological units). In view of the pumping rate variations and the unrecovered drawdown condition, this value is uncertain. In addition, the uncertainty about the time reference prevents us from inferring the storage coefficient.

To overcome the "noise" problem in the pumping phase data, the ratio of the time since pumping started to the time since recovery started is plotted in a semi-log plot versus pressure (head) recovery—the Horner plot. This, too, is supposed to yield a straight line according to elementary theory. Figure 5 is the Horner plot of the recovery data. The curve bends very noticeably because of transient and "real-well" effects. Therefore, the Horner plot yields an unreliable result.

Thus, the conventional methods of data analysis are inapplicable to zone 2 data.

Theoretical Calculations

Zone 2 behaved as a confined aquifer during the pump tests. Because there were no observation wells, there is no reason to introduce anisotropy. Therefore, we have chosen the model to be an isotropic and homogenous confined aquifer. We have further assumed that the parameters of the aquifer remained constant.

Head loss was calculated, using all 85 variations in the pumping rate, for a fixed set of permeability and storage coefficients. The approximate ranges are 10 to $10^3 \text{ cm}^2/\text{s}$ for the transmissivity (which corresponds in permeability to 2 darcys to 0.2 millidarcy) and 10 to 10^5 for the storage coefficient.

The best fit to the pumping data was obtained for a transmissivity of $0.50 \text{ cm}^2/\text{s}$ (about 107 millidarcys) and a storage coefficient of 0.20. (From the well log, a better value of 3.9×10^3 was inferred. The large value here is due to the radius extension effect resulting from the extensive production of sand.) Theoretical results are compared with experimental results in Figs. 1 and 2.

The more interesting comparison is in Fig. 2. For the most part, the agreement is better than ± 1 psi (during the pumping phase). In the recovery phase, the experimental data lagged the theoretical recovery during the early hours. This difference (ap-

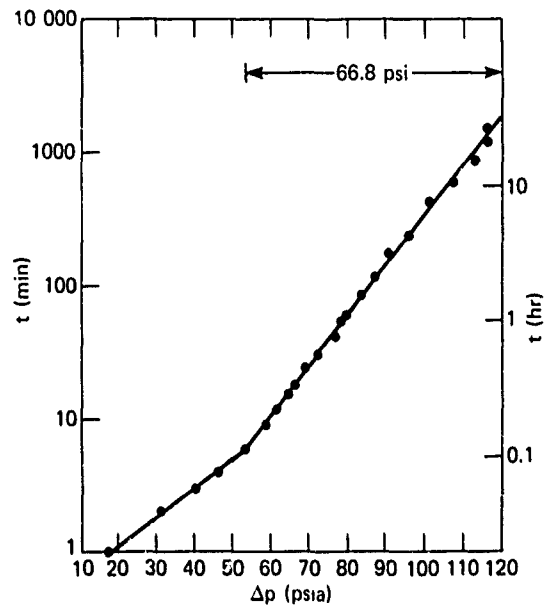


Fig. 4 Data from pumping phase of Crisfield test well, zone 2.

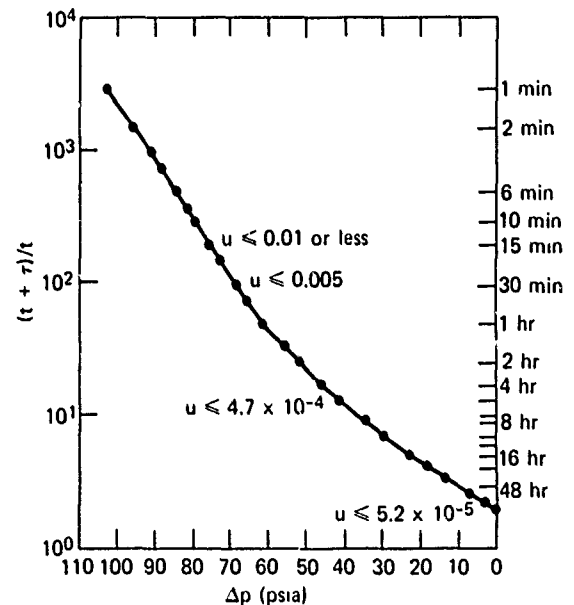


Fig. 5 Data from recovery phase of Crisfield test well, zone 2, Horner plot.

proximately 10 psi) can be explained on the basis of the real-well (or well-bore) effect.

Unlike the "mathematical" well, which is infinitely thin, the real well has a finite radius within

which the water content is 100%, in contrast to a 25% porosity in the theoretical case. This gives rise to an integral equation for which we have obtained an approximate first-order perturbation solution. Evaluating the first-order correction in the appropriate range gives about a 10 psi lag in the recovery, which eliminates the apparent disagreement between theory and experiment. (The first-order correction term is proportional to T^2 , where T is transmissivity. Thus, the real-well effect is more pronounced for a well with low transmissivity, such as the one under consideration. This causes a noticeable bend in the Horner plot.)

Reference 3 is a detailed analysis of the Crisfield well data.

REFERENCES

1. D. K. Todd, *Ground Water Hydrology*, John Wiley, New York, 1959.
2. S. N. Davis and R. J. M. DeWiest, *Hydrogeology*, John Wiley, New York, 1966.
3. K. Yu, *Crisfield, Maryland Well Characteristics Determined Using All Test Data*, JHU/API QM-80-056, 20 Mar 1980.

Authors: K. Yu and F. C. Paddison

Support: U.S. Department of Energy/Resource Applications

ECONOMIC MODELING OF GEOTHERMAL ENERGY IN THE EASTERN UNITED STATES

The characteristics of geothermal resources, their market, and the economic conditions under which they are developed may vary considerably from site to site and over the life of a particular project. APL and the Center for Metropolitan Planning and Research of The Johns Hopkins University (Metro Center) have developed computer models that estimate the effect of these variations on the delivered cost of geothermal energy for direct-use applications.

BACKGROUND

The eventual development and widespread use of geothermal energy will depend on its cost competitiveness with other alternate, as well as conventional, sources of energy. The resource conditions that exist elsewhere in the United States where geothermal energy has been used directly for space, water, and process heating generally are more favorable than those in the eastern United States; therefore, the costs incurred in those applications are not very useful for estimating the costs in the east. Some countries have developed resources similar to those of the eastern United States, but the lack of good economic data prohibits a direct comparison of

costs. Thus, the only way to determine expected costs is to analyze systematically the costs of various system components through the use of computer models.

Because there is considerable uncertainty and variability in resource conditions, in user requirements, and in the financial conditions likely to be encountered in developing moderate temperature (less than 250°F) geothermal resources, a comprehensive economic analysis must be made for a wide range of conditions. Existing economic models either have not been sufficiently flexible or have failed to include such important considerations as the cost of the pumping energy required for deep nonartesian wells and the influence of the rate of market penetration, while they have overemphasized the engineering optimization of the distribution system. Thus, it was necessary to develop a computer model that included engineering details of production and distribution systems in an economic accounting framework, and the framework had to be flexible to reflect the various conditions in which geothermal energy is likely to be encountered. Such a development naturally proceeded in stages and resulted in four computer programs.

DISCUSSION

The first two computer programs, developed in late 1978, were designed to calculate the average cost over a project's lifetime. GTCOST calculates the average delivered cost of geothermal energy for three types of residential users, where the resource temperature and the mix of fossil peaking plant and geothermal system are variables, while the costs of wells, central heat exchangers, etc. are held constant.

The use of a peaking plant to augment a geothermal system to satisfy short-term peak loads during the coldest days of the year gives the system designer a means of optimizing the system design temperature for a given resource and user combination by changing the proportion of the annual heat load supplied by geothermal water and by fossil fuel. As the proportion changes, the designer can decrease the output of the geothermal well proportionally or can keep it constant and supply a larger community. In the latter case, there are more residences to amortize the system's capital costs, and the cost of energy for each is reduced. Figure 1 shows energy costs as a function of the system design temperature, i.e., the ambient temperature at which the peaking plant begins to augment the geothermal system, the number of residences supplied, and the proportion of the annual heat load supplied by geothermal energy.

The Geothermal Resource Economic Evaluation System (GREES) (Ref. 2) was developed as an interactive computer program that internally sizes and costs all system components, amortizes each over its expected lifetime, calculates all operating costs, and determines the average cost for the delivered geothermal energy.

In 1979, the GREES model was expanded to the Geothermal Resource Interactive Temporal Simulation (GRITS) model to evaluate cost and revenue streams over a variable evaluation period (e.g., 20 years). GRITS uses GREES as its basic computational framework and iterates each year on the basis of user-specified rates of change for a potentially wide range of variables. The model provides two economic accounting measures: the discounted average cost (the price that equates the discounted cost and revenue streams) and the net present value (the sum of the discounted net revenue stream). The first measure indicates the value of the resources required to bring a unit of geothermal energy to the user; the second indicates the potential attractiveness of a resource investment to developers.

The user of the GRITS model defines a particular project by specifying values of resource conditions (well depth, temperature, pumping energy requirements, flow rate, number of wells), demand con-

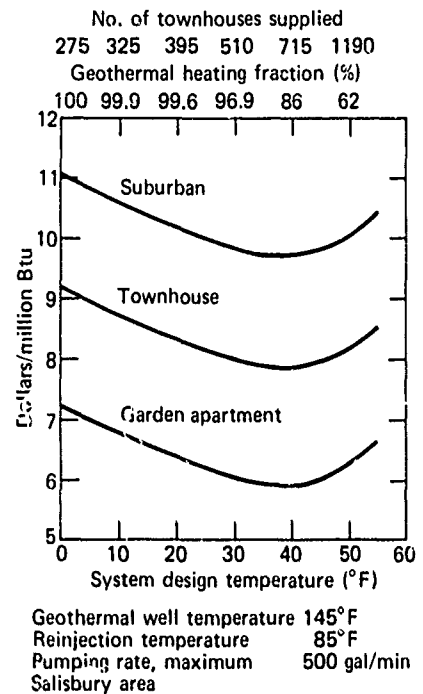


Fig. 1 Cost of geothermal energy versus system design temperature.

ditions (user type, density of users, rate of market penetration, climate), and financial conditions (length of evaluation period, interest rate, inflation rate, selling price of energy). The user may determine the relative size of the geothermal base plant and the nongeothermal peaking plant by changing the design temperature. GRITS includes relatively detailed modeling of such equipment costs as submersible pumps, heat exchangers, and storage tanks because those costs will change drastically in actual systems as resources and economic conditions change.

The size of a community heating system (Fig. 2) is determined internally by GRITS on the basis of user-specified variables such as building type, desired rejection temperature, design temperature, and local climate. GRITS can also estimate costs for commercial and industrial users. Its most attractive feature is its ability to model changes in resource, user, and economic conditions as they occur on a year-to-year basis. Figure 3 shows the effect on net revenues of two rates of market penetration in a residential district heating system. The area between the two curves represents the monetary value of the higher rate of market penetration over the lower; it is extremely useful to prospective geothermal utilities in evaluating market strategies.

One minor drawback of GRITS is its tendency to overestimate the pumping energy costs in a real

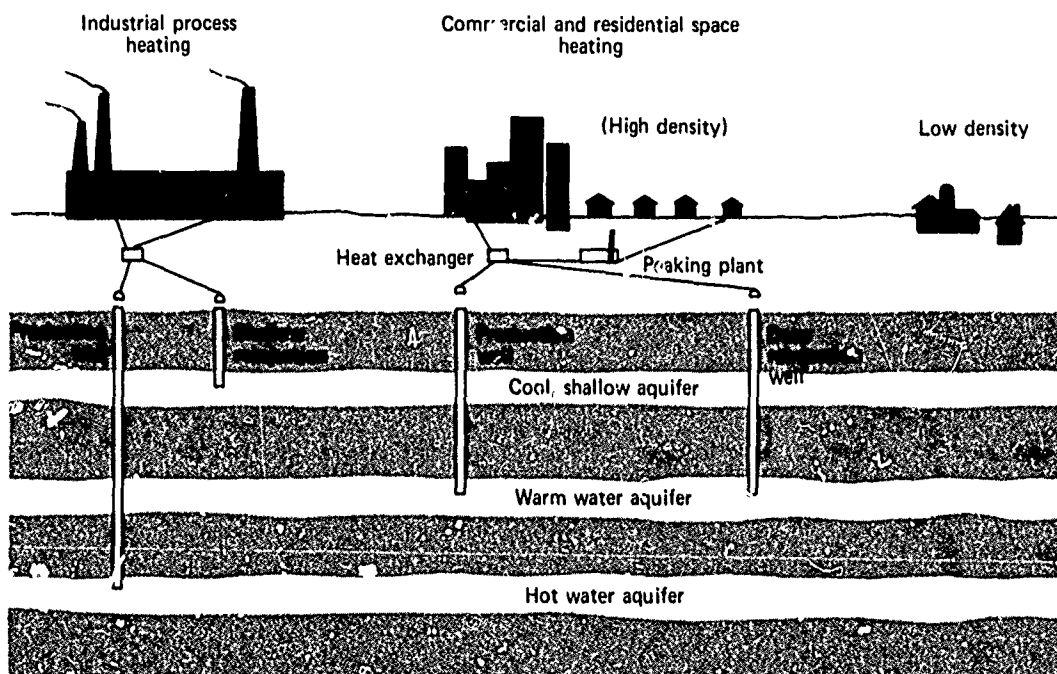


Fig. 2 Direct applications of moderate temperature geothermal energy.

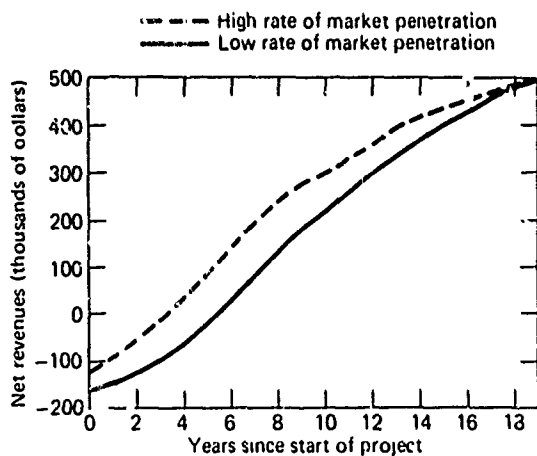


Fig. 3 Net revenue curves for relatively high and relatively low rates of market penetration.

aquifer where the drawdown (the lowering of the water table as a result of pumping) at a particular time and pumping rate change with the withdrawal rate. The GTWELL computer program models the hydrologic behavior of an aquifer where specific resource parameters (i.e., transmissivity and storage

coefficient) are known. Given a pumping schedule based on ambient temperatures (for space heating) or on variations in industrial process demands, GTWELL can calculate the drawdown associated with the varying pumping rate. For example, Fig 4 illustrates the expected well drawdown of a geothermal aquifer at Crisfield, Maryland, where the aquifer transmissivity is 348 gal/day/ft and the storage coefficient is 3.9×10^{-3} . The pumping rate follows the heating degree-day requirement for the Crisfield High School (Refs. 3 and 4) and reaches a maximum of 98 gal/min. Pumping energy requirements and costs are then calculated. GTWELL is extremely useful in evaluating pumping strategies (e.g., cyclic pumping at high rates versus low pumping rates for longer periods with surface storage). The pumping costs obtained from GTWELL can be entered into the GRITS model to evaluate the total system costs.

GRITS is far more flexible than other models and is much better suited for preliminary economic evaluations. It represents a productive collaboration between economists and engineers, an important but often elusive goal of "resource economics." The models have proven useful for the study of potential eastern geothermal resources and probably will be applied to other regions and resources in the near future.

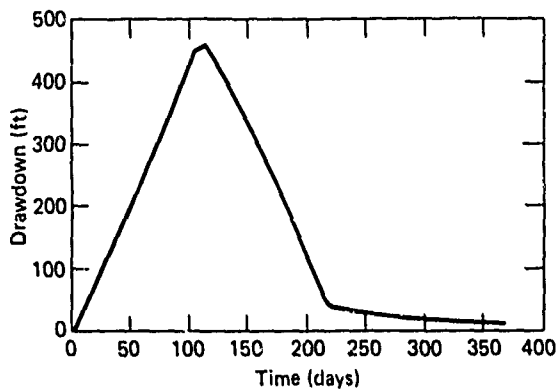


Fig. 4 Calculated well drawdown versus time (first year) for proposed space heating at High School, Crisfield, Maryland.

REFERENCES

1. I. C. Paddison, C. S. Lefel, W. J. Toth, and R. S. Weisbrod, *Direct Applications of Geothermal Energy in the Eastern United States and Estimates of Life Cycle Costs*, APL/JHU QM-78-232, 30 Oct 1978.
2. R. Weisbrod, W. Barron, and P. Kroll (Metro Center) and W. J. Toth (APL), *Economic Evaluation Model for Direct Use of Moderate Temperature (up to 250°F) Geothermal Resources in the Northern Atlantic Coastal Plan*, APL/JHU GEMS-003, Jun 1979.
3. K. Yu, *Head Loss and Pumping Cost of Geothermal Well, with Space Heating Application to Crisfield, MD*, APL/JHU QM-79-220, 31 Oct 1979.
4. I. C. Paddison, "The Crisfield, Maryland, Well and Energy," APL/JHU Lett. CQO-2544, 2 Nov 1979.

Authors: W. F. Barron (Metro Center) and W. J. Toth, F. C. Paddison, and K. Yu (APL)

Support: U.S. Department of Energy/Division of Geothermal Resource Management

BIOMEDICAL SCIENCE AND ENGINEERING

INTRODUCTION

The Johns Hopkins Medical Institutions (JHMI) and APL have collaborated in biomedical research and development since 1965. An important objective of the program has been the application of current engineering, physical science, and systems approaches to solve problems in medical research and health care delivery. The program has included collaboration with nearly all of the clinical departments and with many of the basic science departments of the medical divisions in areas of biophysics, ophthalmology, neurophysiology, radiology and radiation therapy, cardiovascular systems, rehabilitation engineering, patient monitoring, computer support and clinical information systems, and clinical engineering.

The application of state-of-the-art technology has contributed to many areas of basic medical research and to clinical diagnosis and therapy by improving instrumentation, techniques, and knowledge. Systems engineering techniques, focused in the Department of Biomedical Engineering, have helped solve problems of health care delivery. In addition, a new educational program developed in collaboration with the Department of Biomedical Engineering of JHMI and leading to a master's degree in clinical engineering was established in September 1973 at the School of Medicine.

The results of the research and development are reported in the open literature, principally in biomedical, biological, and medical journals. During the program's relatively short life, more than 190 papers and book chapters have been published and many instruments for research and clinical application have been developed. APL staff members have assumed line responsibility for JHMI in areas where technology can make specific contributions to patient care and to health care delivery, including radiation physics, clinical information systems, and clinical engineering.

The first article in this section describes an economical device that allows handicapped persons to use simple voice commands to control electrical devices. The next article describes a device that measures esophageal acidity and maintains a history of acidity in ambulatory outpatients. The third article explains the use of an intracranial pressure device, developed at APL, to monitor hydrostatic pressure on the brains of experimental monkeys during normal sleep. A laser device that can measure three-dimensional fluid velocities without mechanical contact is discussed in the fourth article. The next article discusses how studies using histochemistry, X-ray spectral analysis, and scanning electron microscopy demonstrated a microcrystalline manifestation of tuberculosis. The last article describes space electronics technology that is used to record electrical activity of the human heart at the time of fibrillation and defibrillation.

Further details of this and other work are reported in the *Biomedical Research, Development, and Engineering Annual Report* (JHU/APL MQR), which is published in November of each year.

LOW-COST VOICE-ACTUATED CONTROLLER FOR THE HANDICAPPED

A low-cost voice-actuated controller for the handicapped has been developed by APL. This versatile controller uses a low-cost microprocessor, simplified speech input requirements, and visual timing cues and could be made available to the handicapped at a significantly lower cost than for present controllers.

BACKGROUND

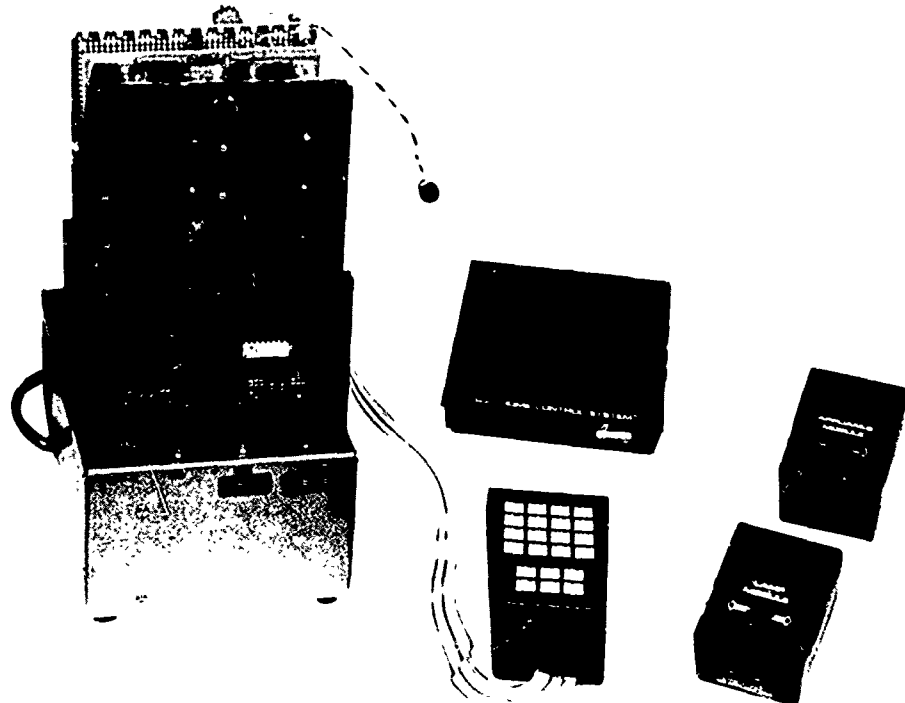
There is a need for devices that permit a handicapped user, such as a spinal column injury victim, to control his environment by means of his voice. At present, typical environment controllers for the handicapped cost more than \$1000 and are cumbersome.

DISCUSSION

The voice-actuated controller (Fig. 1) consists of a microprocessor circuit, a microphone input circuit, a menu display with visual cues that permits the user to

select from a variety of functions, and a wireless interface to a \$40 commercial master environment controller. The visual cues are cycled every 15 seconds through the available performance functions (up to seven remote devices (\$15 each) in the current design, plugged into common electric power outlets). Actuation depends on timing an utterance to the visual cues on the display board (Fig. 2). The display board consists of eight red display modules, numbered 1 to 8, each corresponding to a particular function. A title beside the display module describes the actual functions. A green light-emitting diode (LED) to the right of each display module indicates whether the function is active.

Since control is performed without physical connections, the device is suitable for attachment to a mobile conveyance such as a wheelchair. To operate in a wheelchair situation, the user points his wheelchair in the general direction of the stationary master controller. A separate master controller could be placed in each room to permit unique room-to-room control.



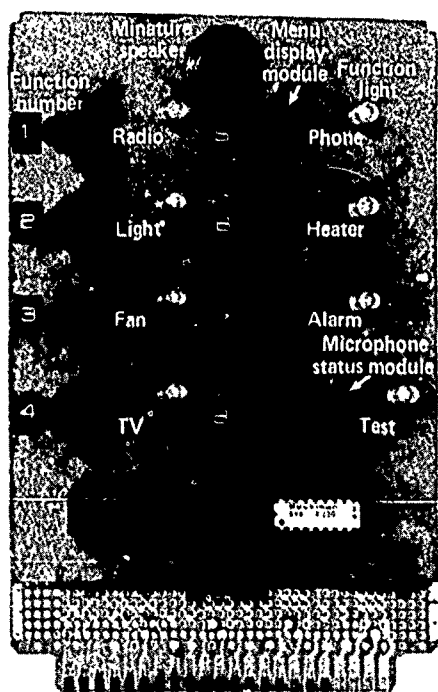


Fig. 2 Menu display board.

An example will help illustrate how the voice-actuated controller works (Fig. 3). Suppose that one of the commercial receiver modules is set to function code 3 and that a fan is plugged into its AC outlet. The menu display board of the controller continuously cycles through the eight red display modules, lighting up the bottom bar of one module at a time. The user waits for the lower bar of the third menu display module to light up. When the cue bar on that display module moves to the high position, he slowly says "con" holding this utterance until the cue bar again appears below. He then quickly says "tact" to complete the process. If the connection is successful, warning beeps are issued from a miniature speaker. He remains quiet during the ensuing four seconds, and a change in the state of activity of the fan occurs. If the corresponding green function light is off, indicating that the fan is off, the fan will turn on and the green light will light up (and vice versa). There are special provisions for situations where the user is very close to a correct response and also for selecting function 8 to assist the user in training himself.

The voice-actuated controller uses a simple-to-implement, user-independent algorithm (Fig. 4). Basically, the microphone circuit sends a "0" to a microcontroller circuit when no sound is present and a

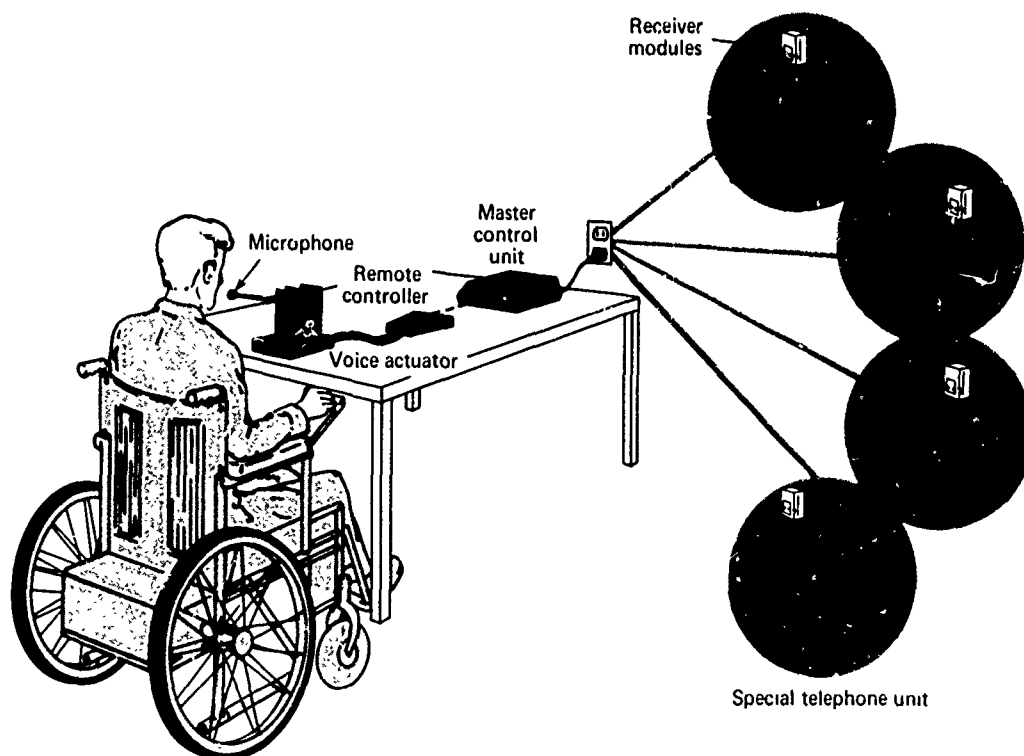
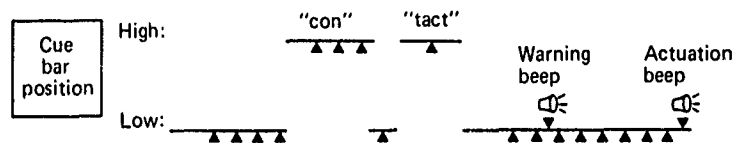


Fig. 3 Representative control environment for voice-actuated controller.



▲ = Series of microphone output checks
(user should be silent if cue bar is low
and vocally active if cue bar is up)

Fig. 4 Voice-actuated algorithm.

"1" when sound is present. It will remain "1" for the duration of the sound. At appropriate times the microcontroller circuit checks to see that the microphone output is the same as the state of the selected function cue bar. A low bar is considered "0" and a high bar, "1." If the states of the microphone and cue bar are not in agreement, the microcontroller advances to the next function and tries again. If, on the other hand, all checks are successful, the wireless controller communicates with the master environment controller and the state of the selected function changes.

The performance of this controller has been evaluated informally on a number of occasions. Most

users have been able to operate the device readily after a five-minute demonstration and coaching session. Two paraplegics also have had brief opportunities to operate it; both were successful. In order to obtain a more definitive evaluation under operational conditions, it is planned that one of the paraplegics will use the controller in his home.

Author: A. E. Davidoff

Support: Veterans Administration

PORTABLE pH DATA COLLECTOR

In collaboration with the Johns Hopkins School of Medicine's Department of Biomedical Engineering, APL has designed and built a portable pH data collection system. The system facilitates the monitoring of gastric acid reflux into the esophagus in ambulatory patients by providing a flexible mode of data collection and instant strip-chart playback.

BACKGROUND

Various stomach problems can be related to the reflux of gastric acid in the esophagus of patients.

Previous devices required that the patient be hospitalized and therefore could not monitor everyday situations. It is preferable that such a device be used by outpatients in order to reflect the normal stress of physical activity or emotional conflict. Furthermore, it should be flexible enough to ignore long periods of unimportant data.

DISCUSSION

The system consists of a portable pH data collector and a support unit that interfaces with an

esophageal probe and a strip-chart recorder. The collector is in a small metallic container that may be carried in a shirt pocket or on a belt (Fig. 1). It is connected to the esophageal pH probe and provides analog buffering and filtering for the probe. Internal rechargeable batteries power the unit for 15 hours of operation. An event switch at the top of the collector records gastric events sensed by the patient for correlation with actual pH changes. A status light shows that the system is operating.

The collector can be connected to the top of the support unit (Fig. 2) to recharge the batteries, enter commands, and display collected data on the strip-chart recorder (which is connected to the front of the support unit).

Two modes of data collection are available. In the first, the pH is sampled once or twice per minute and is recorded to an accuracy of 1/8 pH. In the second, the pH is sampled every 1, 5, or 10 s and is recorded whenever the change is greater than 1 or 2 pH. Data may be displayed on the strip-chart recorder in slow or fast mode, allowing playback rates of from 10 to 1800 times real time, depending on the data collection mode. This permits a quick or a detailed review of the data.

The required flexibility of the system was provided by a design based on an 1802 CMOS microprocessor. Data are stored in 760 eight-bit words of CMOS memory. The software requires 500 words of program storage. The power consumption of the remote unit is 25 mW. The support unit interfaces to the microprocessor in the data collector for command key decoding and digital-to-analog converter loading.

A typical operating procedure starts with the remote unit attached to the support unit and the probe connected. The probe is calibrated by immersing it in pH 4 and 7 solutions and entering the appropriate commands. Each step requires approximately two seconds. If the unit has been calibrated previously, the procedure need not be repeated. All commands require one or two buttons on the support unit to be pressed and a "go" signal to be issued by pressing the event button on the remote unit. Commands to select the data collection mode are entered, the remote unit is disconnected from the support unit and connected to the patient's pH probe (which has been inserted into the esophagus through a nostril), and the go signal is given.

During the collection period, the patient may "mark" the data by pressing the event button. At the end of the collection period, the remote unit is disconnected from the probe, reconnected to the support unit, and commanded for data playback. The data are displayed with event marks appearing as -1 pH levels.

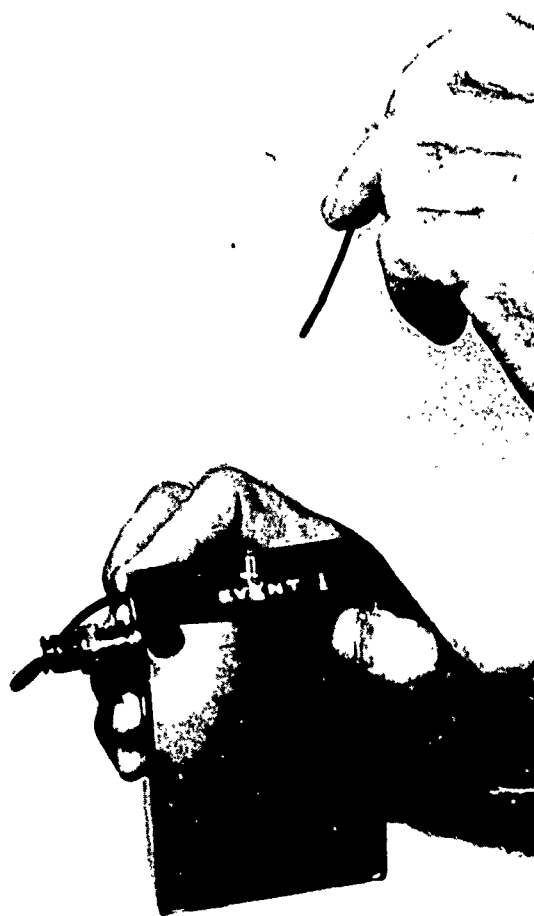


Fig. 1 Portable pH data collector and probe.

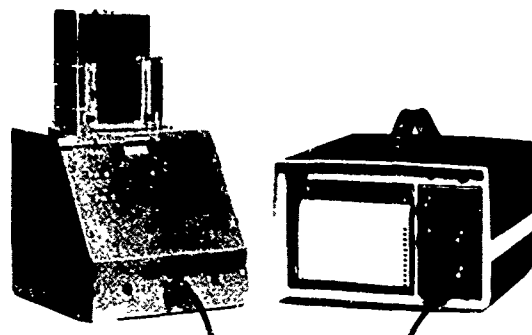


Fig. 2 Support unit with pH data collector connected to top and strip-chart recorder connected to front.

The portable pH data collector is an example of sophisticated, low-power, compact instrumentation that is made possible by standard, off-the-shelf, large-scale integrated circuits. This particular design may be expanded easily to a multichannel data collection unit.

Authors: W. Schneider and D. B. Klein

Support: Johns Hopkins Medical Institutions

INTRACRANIAL PRESSURE DURING WAKEFULNESS AND SLEEP

Because improved instrumentation is now available, continuous 24 hour monitoring of intracranial pressure (ICP) is being used to an increasing extent for the management of neurological patients. The telemetry procedures for making the recordings are comparatively new, and there is considerable interest in determining the significance of the observed ICP wave phenomena. Since there is insufficient information on the temporal behavior of ICP in the normal mammal, we have undertaken to study the ICP profile in normal undrugged monkeys during sleep and wakefulness.

BACKGROUND

The monitoring procedure is used in selected patients to warn of excess pressure, to provide diagnostic information, and to evaluate treatments for controlling ICP. Because pressure wave phenomena observed in the continuous recordings of ICP are used for patient evaluation, it is important to understand the nature and cause of the waves. They may arise from normal cardiogenic or neural mechanisms and may have typical patterns in well individuals. The patterns may change in patients with hydrocephalus, brain tumor, or head trauma. The frequency, amplitude, and duration of ICP waves for patients with those conditions as well as for normal persons must be described and classified in order to make the best use of continuous ICP recording as a supplement to other methods of managing neurosurgical patients.

DISCUSSION

Seven monkeys from the primate colony were acclimated to a primate chair for approximately one

week. An ICP sensing device (Ref. 1) was implanted epidurally in the burr hole. At the same time electroencephalography (EEG) and electromyography (EMG) electrodes were implanted in the skull and neck muscles, respectively. Throughout the night, EEG, EMG, and ICP recordings were made as the monkey passed through his normal sleep cycles. Each monkey had two days of baseline ICP recording in addition to EEG and EMG recordings.

Indwelling arterial catheters were placed in the brachial arteries of four monkeys. The catheter was connected to a Statham pressure transducer to record systemic blood pressure continuously. The recordings were made with a Grass Model 6 EEG machine operating at a chart speed of 1.5 mm/s.

The ICP in all seven monkeys was steady during wakefulness except for transient changes caused by movements, heartbeat, and respiration (see Fig. 1). It showed no significant variation during slow wave sleep except for small pressure changes secondary to heart pulsation and respiration (see Fig. 2). However, it rose during all episodes of desynchronized (REM) sleep above the levels found in other sleep states. This rise in pressure averaged 169 \pm 4.6 mm H₂O (number of samples, *N*, is 168) above the normal levels. At the end of the REM sleep period, the ICP returned abruptly to its original level (see Fig. 3).

Desynchronized sleep episodes were defined as periods in the sleep cycle during which the amplitude of the EEG potentials was low and EMG activity decreased markedly. During the onset of REM sleep, the ICP rose gradually over a period of 0.5 to 1 minute, then reached a more or less constant level of pressure that lasted between 2 and 12 minutes. The cessation of the ICP wave was abrupt. The pressure returned to the original ICP in 5 to 10 seconds, coin-

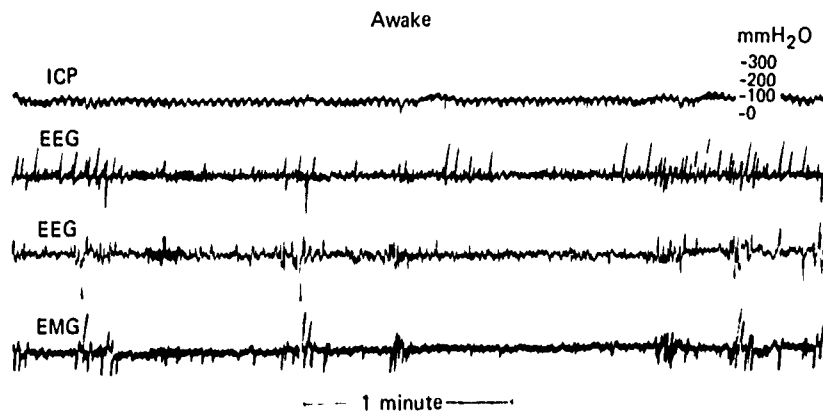


Fig. 1 Recordings of ICP, frontal EEG activity, occipital EEG activity, and temporalis electromyogram in the awake undrugged monkey. The ICP is at 90 mm H₂O; small variations are due to heartbeat and respiration.

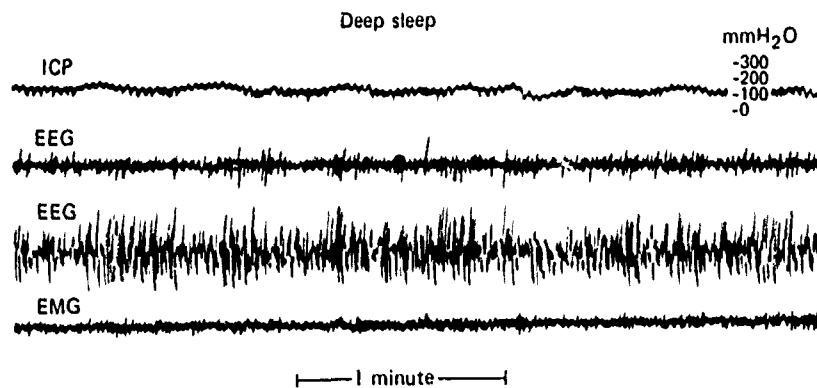


Fig. 2 Recordings of the same parameters from the same monkey during sleep. No movement artifacts appear in the EMG, and the EEGs show large amplitude waves characteristic of deep sleep. The ICP shows small variations about the level of 100 mm H₂O.

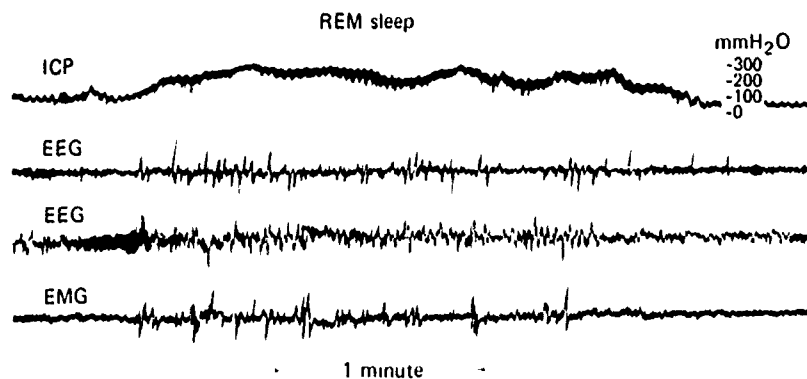


Fig. 3 Recordings of the same parameters from the same monkey during REM sleep. The EEGs show desynchronized activity with pantogeniculate occipital waves. The EMG shows REM artifacts. Note the 3 minute plateau wave on the ICP rise to a level of 300 mm H₂O. The pulse pressure from the heartbeat becomes about three times larger than that observed in other sleep states. The downgoing pulses on the ICP record are artifacts.

ending with the end of the REM sleep epoch (see Fig. 3). The ICP wave and REM sleep lasted an average of 7 ± 0.8 minutes ($N = 170$) during which time the systemic blood pressure decreased by an average of 17 ± 1.2 mmHg ($N = 37$). The ICP waves and the concurrent REM sleep states occurred an average of 9 ± 1.2 times per night ($N = 37$). Bilateral sympathectomy in four monkeys had no significant effect on the properties of REM sleep or the ICP wave phenomenon.

The results of our study support the belief that elevated ICP during REM sleep is a normal physiological occurrence. The elevated ICP is in the form of a pressure wave having the shape and characteristics of the A-wave described by Lundberg (Ref. 2) but it differs in magnitude. The rapid pressure changes in the ICP wave that occur during REM sleep suggest that the effect is a result of vascular changes. In a number of neurological disease states the ICP is initially high, using up much of the reserve intracranial space. Therefore, a small increase in blood volume when the reserve space is exhausted causes a large rise in the ICP. Under those circumstances, during REM sleep the patient who has little ICP reserve could have, rather than a doubling of ICP, an ICP in the region of 500 to 1000 mm H₂O — the classical plateau wave described by Lundberg. In such cases, the conditions exist for cerebrovascular decompression (Ref. 3) in which these dangerously high levels of ICP could depress nervous function.

The results of our studies (Ref. 4) indicate that, in a neurological patient, continuous recordings during the sleep state may be useful for assessing the patient's ICP reserve. A rise in ICP should be expected during REM sleep; its magnitude will be a measure of the patient's intracranial compensatory reserve. More studies are needed to determine what levels of ICP waves in REM sleep are normal and what levels indicate pathology.

REFERENCES

1. A. E. Walker, I. J. Viernstein, and J. G. Chubbuck, "Intracranial Pressure Monitoring in Neurosurgery," *Indwelling and Implantable Pressure Transducers*, D.G. Fleming, W. H. Ko, and M. R. Neuman (Eds.), CRC Press, Cleveland, 1977, pp. 69-77.
2. N. Lundberg, "Continuous Recording and Control of Ventricular Fluid Pressure in Neurosurgical Practice," *Acta Psychiatr. Scand* 36, Suppl. 149, 1960, pp. 1-193.
3. T. W. Langitt, N. I. Kassell, and J. D. Weinstein, "Cerebral Blood Flow with Intracranial Hypertension," *Neurology* 15, 1965, pp. 761-773.
4. G. Gucer and I. Viernstein, "Intracranial Pressure in the Normal Monkey while Awake and Asleep," *J. Neurosurg* 51, 1979, pp. 206-210.

Authors: L. J. Viernstein (APL) and
G. Gucer (JHMI)

Support: National Institutes of Health Contract
NS-5-2332

THREE-DIMENSIONAL LASER DOPPLER VELOCIMETER

A laser Doppler velocimeter that can measure flow velocities in three dimensions was designed and built to measure velocity fields in casts of human arteries. An important part of the velocimeter is a rotating diffraction grating that is used both to split the laser beam and to facilitate the measurement of bidirectional flow along a particular path. A United States patent has been granted to us for this instrument (Ref. 1).

BACKGROUND

The art of measuring fluid flow is now relatively sophisticated and requires comparatively

complex instruments. Devices to make flow measurements include pitot tubes, vanes, hot-wire and hot-film anemometers, and heat-flux transducers. They all have the disadvantage that they must be physically located in the flow at the point to be measured. Consequently, local flow is distorted at the point of interest. Another disadvantage is that they are subject to adverse environmental factors such as excessive pressure and temperature, which may cause damage.

On the other hand, a laser Doppler velocimeter can measure flow velocities without disturbing the flow noticeably and without being subject to environmental effects. Its principle of operation is that the frequency of light scattered from a moving particle is

Doppler shifted. This principle is the same one that police use to measure automobile velocities. The difference between the two systems is a matter of scale.

Several optical configurations are possible in laser Doppler velocimetry. One common type is the reference beam velocimeter. An unscattered reference beam and light scattered from the point of interest are brought to the same point on a photomultiplier. The nonlinear nature of the photomultiplier tube causes heterodyning, which produces an electrical signal whose frequency is the difference between the frequencies of the two light sources.

Another common optical configuration is the differential mode velocimeter. Scattered light from the intersection of two beams is focused on a photomultiplier. Again, the resultant signal has a frequency that is the difference between the frequencies of the two scattered light sources.

Our velocimeter uses the differential mode. To understand this mode, consider the following. When two beams from the same laser cross, a fringe pattern is formed in the intersection volume. A particle passing through this volume scatters or does not scatter light, according to whether it is passing through a bright or a dark fringe. Thus, the frequency of the photomultiplier output depends on how fast a particle passes through the volume and also its direction or angle relative to the fringe pattern. However, a particle moving in the exact opposite direction will produce an identical frequency in the photomultiplier output.

In many instances, it is important to know the direction of a particle along a path without ambiguity. Ambiguity arises because zero velocity ($v = 0$) normally corresponds to zero frequency, and $+v$ and $-v$ both correspond to the same output signal frequency, f . To avoid ambiguity, Bragg cells, Pockels cells, or rotating diffraction gratings can be used to shift the frequency of the velocimeter beams relative to one another.

Our device uses a rotating diffraction grating (Refs. 2 and 3). A laser beam passing through a rotating grating is diffracted in the usual fashion (Fig. 1). However, the various orders ($n = 0, 1, 2, \dots$) of diffracted light are shifted in frequency. Thus, the frequency of the n th order is $f_n = f_0 \pm n\Delta f$, where the sign is determined by the direction of rotation and Δf depends on the speed of rotation and the spacing between lines on the grating. If one mixes the light from the first-order lines on either side of the zero-order line on a photomultiplier, a signal frequency of $2\Delta f$ results. If the beams intersect at a point in the fluid flow and the light scattered from both beams is focused on a photomultiplier, then zero velocity cor-

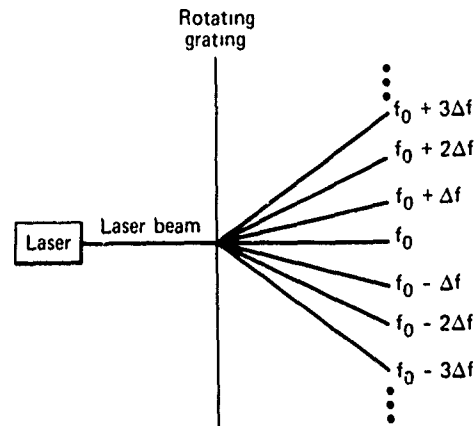


Fig. 1 Diffraction of laser beam by rotating grating.

responds to a signal frequency of $2\Delta f$. Frequencies greater than $2\Delta f$ can be defined as flow in the positive direction; frequencies less than $2\Delta f$ correspond to flow in the negative direction. These effects can also be explained in terms of the fringe pattern, which was stationary when the intersecting beams were of the same frequency but now propagates continuously through the intersection volume in a direction perpendicular to the lines of the pattern. Thus, a stationary particle in the volume produces a frequency at the photomultiplier output of $2\Delta f$ because the fringes now move relative to the particle. If the particle moves, the rate at which the fringes are encountered will depend on the relative motion of the fringe pattern and the particle.

DISCUSSION

Four beams are needed to make a three-dimensional velocimeter. The device should be reasonably easy to align. Ideally, self-aligning features should be incorporated into the design so that the four beams will intersect at the point at which the velocity is to be determined. This can be done by using the rotating diffraction grating as a beam splitter and as a frequency shifter.

Figure 2 shows schematically a laser Doppler velocimeter that measures velocity in three dimensions and incorporates a large measure of self-alignment. The laser (2) emits a beam (4) that passes through a rotating diffraction grating (6). The rotating grating converts the beam into a number of beams having different frequencies. A mask (7) is mounted in the path of the beams emerging from the grating. The mask has an aperture suitably dimensioned to block all diffracted beams except the center one (4) and the

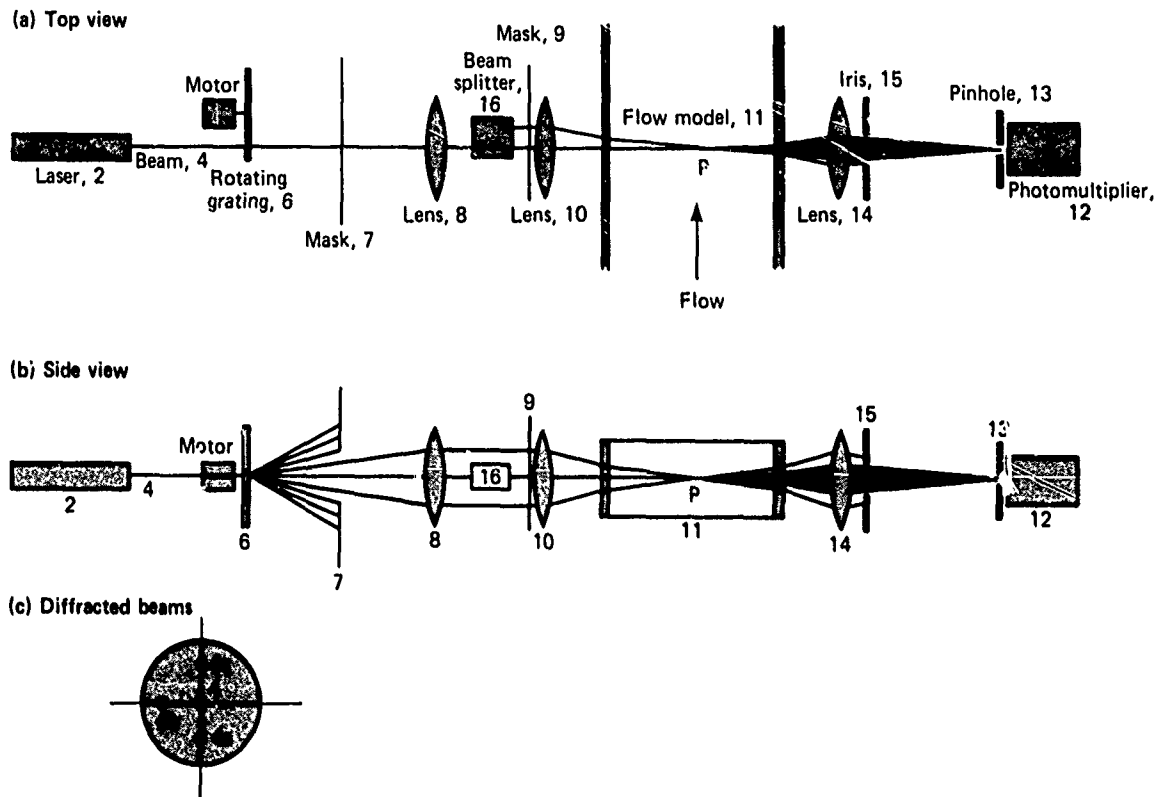


Fig. 2 Schematic of laser Doppler velocimeter.

first-order diffracted beams (4a and 4c) in Fig. 2c, which are made parallel to the center beam (4) by being passed through a lens (8). The center beam then passes through a conventional beam splitter (16) that splits the beam in two, thereby providing an additional beam (4b) of the same frequency as, and traveling parallel to, the center beam (4).

The measurement of fluid velocity is made at P , the point of intersection of the four beams. P can be varied by moving the optical system rigidly with respect to the flow model channel (11) without having to realign the beams or change lenses. The optical system is mounted on a precision machining table with one rotational and three translational degrees of freedom.

Each pair of beams intersecting at P forms a fringe pattern. The scattered light from P is focused by a lens (14) onto the cathode of a photomultiplier tube (12) via a pinhole (13). The photomultiplier tube is shown aligned with the optical axis, which is convenient but not necessary. An iris (15) blocks the unscattered light in any pair of the original beams (4, 4a, 4b, or 4c). The frequency of the intensity-modulated light is easily measured by conventional techniques, such as spectrum analysis or correlation

analysis, applied to the output of the photomultiplier tube.

Figure 2c shows the spatial arrangements of the four parallel beams (4, 4a, 4b, and 4c) as they reach the beam mask (9). Three beams (4, 4a, and 4c) can be selected in pairs by blocking the remaining beams with suitable masks. If the measurements from any two of the three pairs are combined, the two orthogonal components of velocity in the vertical plane can be derived. Similarly, if a mask that selects pair 4b and 4c or pair 4b and 4a is used and these measurements are combined with the orthogonal velocity components in the vertical plane, the three mutually orthogonal velocity components can be derived.

REFERENCES

1. C. B. Barger and O. J. Deters, "Three-Dimensional Laser Doppler Velocimeter," United States Patent 4,148,585, 10 Apr 1979.
2. W. H. Stevenson, "Optical Frequency Shifting by Means of a Rotating Diffraction Grating," *Appl Opt* 9, No. 3, 1970, p. 649.
3. F. F. Mark, C. B. Barger, O. J. Deters, and M. H. Friedman, "Experimental Investigations of Steady and Pulsatile Laminar Flow in a 90° Branch," *J Appl Mech* 44, No. 3, 1977, p. 372.

Authors: O. J. Deters and C. B. Barger
Support: National Institutes of Health

OCCURRENCE AND IDENTIFICATION OF INTRACELLULAR CALCIUM CRYSTALS IN PULMONARY SPECIMENS

Scanning electron microscopy, X-ray analyses, and histochemical techniques have identified unusual birefringent, intracellular, calcium carbonate crystals in the sputum specimens of a 68-year-old man with cavitory pulmonary lesions. He was clinically diagnosed and treated for pulmonary tuberculosis. Although other etiologies are possible, we contend that the calcium salt crystals identified in his sputum represent a peripheral manifestation of tuberculosis that is rarely noticed in sputum specimens.

BACKGROUND

Although calcium deposition occurs in the lungs in a number of systemic and local disorders, it is less often observed in sputum specimens. Calcium compounds occur most frequently in sputum as structureless, acellular, flaky debris, as extracellular rounded bodies, or (uncommonly) as laminated bodies in association with tumor cells. By contrast, the finding of intracellular calcium crystals in the sputum specimen is distinctly unusual. The presence of intracellular calcified crystals has been documented in a patient clinically diagnosed and treated for pulmonary tuberculosis (Ref. 1). Histochemical, X-ray, and scanning electron microscopy studies of the crystals were undertaken in order to establish their nature.

The patient was a 68-year-old factory worker who came to the Johns Hopkins Hospital with fever and cough. A former cigarette smoker with known chronic bronchitis, he had lost 13 pounds over a one-year period. He had worked until the age of 65 in an aluminum factory. Initial chest radiographs showed several left upper-lung cavitory lesions. The clinical course was marked by spiking temperature to 103.8°F and mild leukocytosis (12 800/mm³) with 11% monocytes. The working diagnosis was tuberculosis. The patient was begun on drug therapy and was discharged from the hospital two weeks after entry. Four months later, chest radiographs showed persistent but smaller cavities in the left upper lung. The patient appeared clinically improved and has remained so 10 months later.

Satisfactory smears and filter preparations of spontaneous sputum specimens were examined from 11 different days over a four-month period. Selected sputum smears showing intracellular crystals were stained and subjected to scanning electron microscopy and X-ray analysis. Sample crystals were identified in

the light microscope and reidentified in the scanning electron microscope. An electron beam was directed at a particular spot on the crystals. Excited X-rays indicated the elements involved. In addition, sputum from a normal, healthy, male adult was analyzed as a control.

DISCUSSION

Intracellular, birefringent, needle-shaped crystals were present in all of the patient's sputum specimens, although to a lesser extent after therapy was initiated. The crystals were present both in multinucleated giant cells and in the single, mononucleated histiocytic cells. They did occur extracellularly, but rarely. In the cells, the crystal usually fanned out from a small narrow base. The needle-shaped spicules varied in number from 6 to more than 50. At times, true rosette formations and lamination were seen. Most of the crystals were glassy and colorless with a faint brownish-gray hue. Some were flat, wide, blunt-tipped, and elliptical. They measured up to 20 μ m in size. Under polarized light, they were brilliantly birefringent with faint rainbow colors. In one instance, a Curschmann's spiral was completely surrounded by multinucleated cells containing calcium crystals. These crystals stained specifically with Von Kossa's stain.

The X-ray spectra from six spots on an isolated field incorporating an intracellular crystal were recorded (S_1 to S_6 , Fig. 1). The presence of calcium was established in the crystal exclusively (spots S_1 , S_2 , S_4 , and S_6). The X-ray spectra of the control sputum were identical to those of extracellular areas (spots S_3 and S_5). In both specimens, artifactual amounts of gold (used to coat the specimens to prevent charging) and of tungsten (from the stain) were present, as well as a possible trace of silicon, which probably represented the glass slide (Fig. 2).

Intracellular calcium deposition in the lungs is seen in a wide variety of diseases. In addition, occupational diseases are commonly associated with calcium deposits in the lungs as well as with foreign bodies such as talc. Of interest in this case was the finding in sputum of unusual intracellular crystals that eluded specific classification and prompted further investigation. Since the limitations of X-ray techniques preclude the identification of elements below fluo me in atomic number, the exact consti-



Fig. 1 Scanning electron micrograph of sputum specimen showing intracellular crystal. Spots analyzed by X-ray procedures are marked S_1 to S_6 ($\times 2200$).

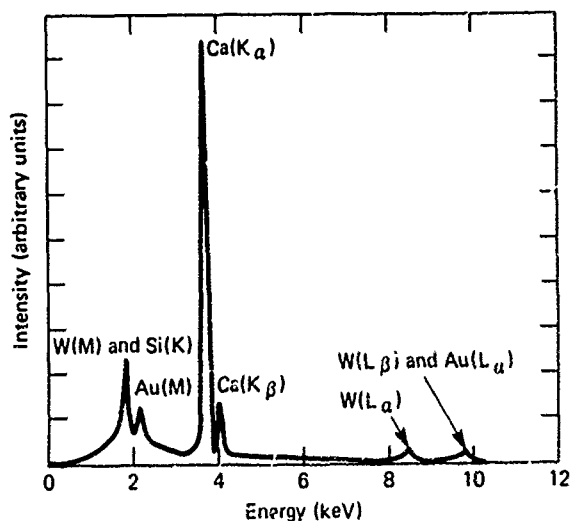


Fig. 2 X-ray analysis of typical spot (S_1) on the crystal.

tments of the compounds in the crystals could not be established unequivocally. Nevertheless, the predominant element was found to be calcium, and there was no indication of aluminum or aluminum products—the only significant occupational exposure documented in this case.

In the absence of systemic disorder, the intracellular calcium particles in the sputum are presumed to be related to the cavitary pulmonary pathologic process. Besides pulmonary tuberculosis, aspergillosis may cause cavitary lesions that have been associated with calcium oxalate deposits. Since the Von Kossa reaction is nonspecific and stains a wide variety of calcium salts including carbonates, phosphates, and oxalates, aspergillosis remains a possible etiologic factor. However, no fungi (which are associated with aspergillosis) were identified in this case, and the specific therapeutic response in the patient makes a fungal lesion unlikely. A diagnosis of calcium salts such as phosphates was not supported by X-ray analysis. However, in a large group of tuberculosis cases only 3% of the patients were reported to have isolated crystals. Small calcific concretions may be seen in specimens of sputum obtained from patients with tuberculosis; however, to our knowledge intracytoplasmic crystals have not been previously described. A review of sputum specimens from pulmonary tuberculosis patients failed to reveal any intracellular calcium crystals.

The rare occurrence of intracytoplasmic calcium carbonate crystals in this case of pulmonary tuberculosis probably represents a cytologic manifestation of an unusual interplay of infection and the host, altered by the environment or other unknown factors.

REFERENCE

1. V. J. Vigorita, P. K. Gupta, C. B. Bergeron, and J. K. Frost, "Occurrence and Identification of Intracellular Calcium Crystals in Pulmonary Specimens," *Acta Cytol.* 23, No. 1, 1979, pp. 49-52.

Authors: V. J. Vigorita, P. K. Gupta, and J. K. Frost (JHMI) and C. B. Bergeron (APL)

Support: William Penn Foundation

EXTERNAL ECG RECORDER SYSTEM FOR USE WITH THE AUTOMATIC IMPLANTABLE DEFIBRILLATOR

A portable, external electrocardiogram (ECG) recorder has been developed by APL to monitor and evaluate an automatic implantable defibrillator (AID). The small solid-state device records heart activity during a fibrillation/defibrillation event plus other data of interest, all of which may be read out later on a special doctor's console.

BACKGROUND

The recently developed AID senses the occurrence of ventricular fibrillation in an ambulatory patient and automatically applies an electric shock to the heart to effect a return to normal rhythm (Refs. 1 and 2). APL was asked to review the design of the present AID system from the standpoint of component selection and reliability. A second task involved the addition of a data recording and readout capability to provide recoverable information concerning the operation of the AID circuitry during an actual fibrillation episode. Accordingly, while the AID circuit design was being finalized and clinical animal tests were being performed, the design was begun of a small recording and telemetry subsystem that could fit into the AID. It soon became clear that completion of the miniaturized recording and telemetry circuitry would probably delay the availability of the im-

planted system for human trials. It was decided to use the design of the implantable recorder for a small, external ECG recorder that could be worn by a patient who had an implanted AID. In addition to small size, other necessary design constraints included low power consumption in order to use a small battery and the use of readily available components to satisfy the short time schedule. In addition, a special doctor's console was designed to read out and make a permanent record of data from the recorder.

DISCUSSION

The primary function of the external ECG recorder is that of a "demand" recording device; that is, in the event of a fibrillation/defibrillation episode, a detailed record of heart electrical activity is made and preserved. If such an event occurs, the patient is prompted by the recorder to visit his doctor and have the data read out for analysis. In addition to ECG information, other data are maintained in the recorder circuitry to provide the doctor with a complete picture of defibrillator and recorder operation since the previous readout.

Figure 1 is a functional diagram of the external ECG recorder. Heart signals are picked up by a set of

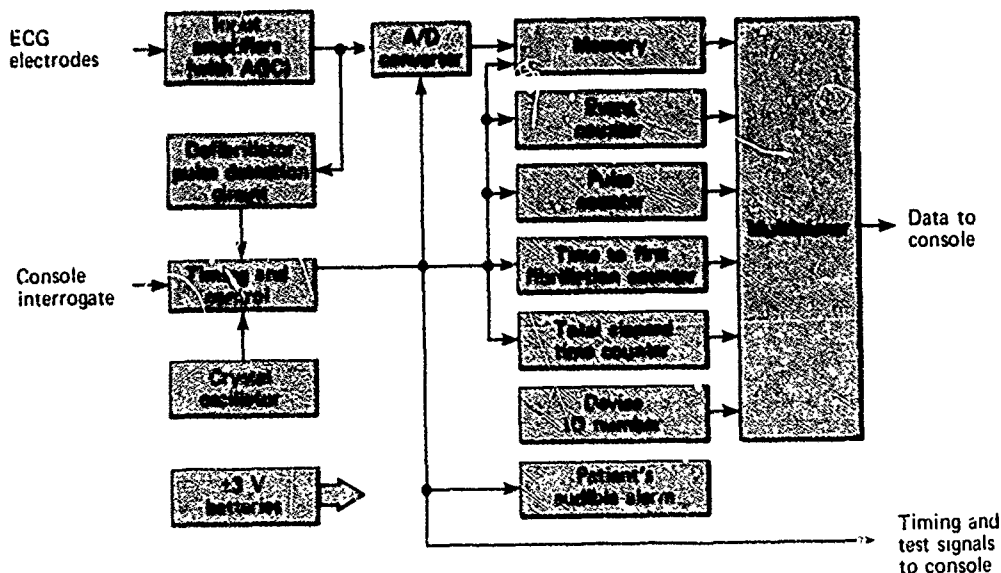


Fig. 1 Functional diagram of the external ECG recorder.

electrodes held in proper position on the chest by an elastic harness. These weak signals are amplified in a preamplifier that includes automatic gain control (AGC) to ensure proper amplitude for the analog-to-digital converter. The ECG waveforms are sampled and digitized by the converter continuously; at the proper time they are stored in a solid-state memory, which has a capacity of 4096 six-bit words. If the patient has not experienced a fibrillation episode since his last visit to the doctor, the recorder remains in the monitor mode while the current ECG input is written continuously into a dedicated "precursor" portion of memory (one-fourth of the capacity) that requires 22.5 s to fill. If nothing has occurred when the memory sector is filled, new data are stored at the beginning of the sector, overwriting the previous data. Therefore, at any time, the precursor memory contains the latest 22.5 s of ECG information.

The input circuits of the recorder detect the coupled high-energy pulse generated by the AID device as it defibrillates the heart, not the fibrillation activity itself. When the initial pulse occurs, the recorder leaves the monitor state and stores the next 67.5 s of ECG data in the remaining memory space (three-fourths of the capacity). This recording time covers the maximum possible period of defibrillator action, which can include up to four shocks to restore natural rhythm. At this point, the entire 90 s memory holds the data stored before, during, and after the defibrillation event. No more recording is allowed, and a periodic audible alarm sounds to tell the patient to visit his doctor. If additional fibrillation episodes occur in the interim, no ECG data are recorded but a record is kept of the total number of events and the number of defibrillator pulses delivered. A crystal

oscillator allows the recorder circuits to maintain an accurate record of elapsed time between readouts as well as the time at which the initial fibrillation episode occurred.

When the patient visits the doctor, the recorder is connected to the console. An interrogate command from the console switches the recorder to the read mode, and all stored data from memory and from the various counters are transferred to the console for storage. Recorder data are read out a second time and compared with the data stored in the console, for verification. All non-ECG data are displayed on the front panel, and the operator obtains a hard-copy strip-chart printout of the 90 s recording.

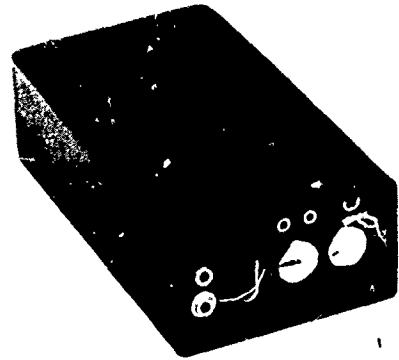


Fig. 2 The external ECG recorder.

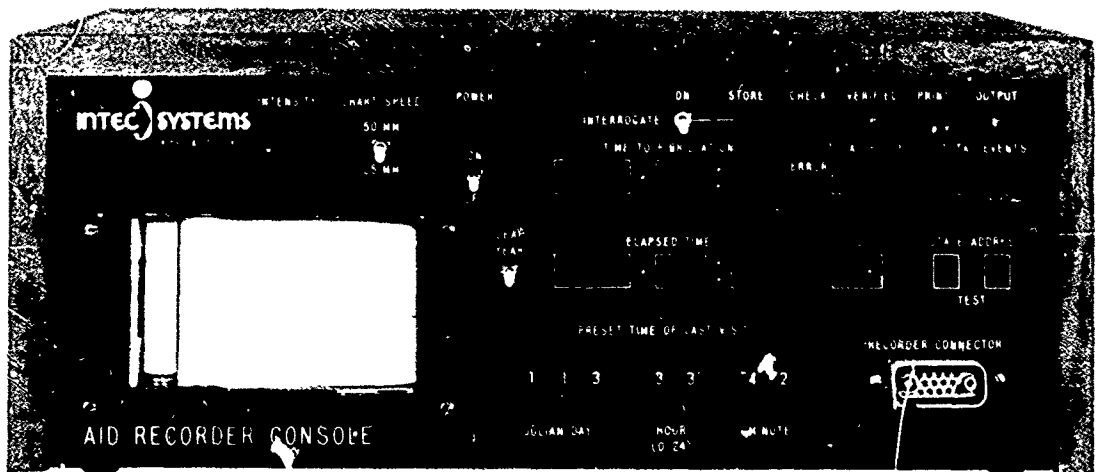


Fig. 3 Doctor's console for readout, display, and recording of recorder data.

If the doctor is satisfied with the data output, the interrogate command is turned off; the recorder returns to its monitor state and may be disconnected from the console. The operation of the recorder may be checked during a routine office visit even if no fibrillation episode has occurred. In that case, 67.5 s of current, normal ECG data can be recorded in a manner similar to data of an actual episode. When the memory is filled, readout proceeds as before.

Five external ECG recorders are being fabricated for initial human trials. Two have been completed and tested, and three are in various stages of fabrication. Figure 2 is a photograph of the recorder. It weighs approximately 12 ounces (340 grams) and is powered by four watch-type silver oxide batteries, which provide enough power for about three months of operation. All digital circuits, including the memory, are CMOS (complementary metal oxide semiconductor) integrated circuits.

The first of three consoles has been fabricated and is being checked (Fig. 3). A recorder has been tested successfully on a dog with an implanted defibrillator. The AID has been approved for limited clinical trials with human patients in the near future.

REFERENCES

1. A. Langer et al., "Considerations in the Development of the Automatic Implantable Defibrillator," *Med. Instrum.* 10, No. 3, May Jun 1976, pp. 163-167.
2. M. Mirowski et al., "Chronic Animal and Bench Testing of the Implantable Automatic Defibrillator," presented at the Vth World Symposium on Cardiac Pacing, Montreal, Canada, 2-5 Oct 1979.

Authors: R. E. Fischell, C. A. Blackburn,
and S. F. Oden

Support: NASA Goddard Space Flight Center

OCEAN SCIENCE AND TECHNOLOGY

INTRODUCTION

APL must understand the physics of the ocean environment to perform its mission in support of the Fleet. This area of physics includes the propagation of electromagnetic and acoustic radiation; absorption and scattering both within and at the surface of the ocean; hydrodynamic phenomena such as surface waves, internal waves, and currents; and the effects of such physical variables as water temperature, pressure, salinity, and density on ocean dynamic phenomena. Central to APL's effort is the development of sensing and data-processing systems to detect and characterize signals propagated through or at the surface of the ocean. Analysis, simulation, and laboratory research are extremely useful, but many phenomena of interest must be studied at sea. Accordingly, APL has developed the ability to conduct large-scale scientific studies in the open ocean.

Although much ocean research is not reported here for security reasons, the selected sample will illustrate the areas of interest. Theoretical studies are exemplified by the first article, which presents an analytical model of specular reflection from a single facet on the mean ocean surface. The model aids in interpreting measured sun glitter data and shows promise of representing spatially averaged glitter radiance.

The second article describes work related to the NASA-sponsored SEASAT-A satellite — the first dedicated to oceanographic research. Analysis of the SEASAT Synthetic Aperture Radar data demonstrates its ability to detect low energy swell systems and to measure ocean wavelength and direction accurately. To provide a better understanding of the worldwide oceanographic and atmospheric background, airborne research flights in Antarctica and Greenland were undertaken to perform experiments in meteorology, air sampling/chemistry, infrared spectroscopy, magnetometry, ice thickness measurements, and aerial photography of glacier movements. They are discussed in the third article.

The last article describes the development of a low-power laser radar to measure the seal position on the Navy's experimental 100-ton surface effect ship. This measurement capability provides both a real-time seal position monitor for use by the ship's control team and highly accurate measurement data for use in evaluating the test ship and the concept.

Although APL's increasing expertise in ocean physics to date has been applied to Navy problems, it will be available in the future to enhance the specific understanding of the ocean environment and to assist in its peaceful exploitation. The determination of optimum locations for OTEC plantships by site surveys is one example of many possible applications.

ANALYTICAL INVESTIGATION OF A SIMPLIFIED MODEL TO STUDY TEMPORAL FLUCTUATIONS OF SUN GLITTER

The term "sun glitter" describes the optical radiance from individual areas or facets of the ocean surface that are inclined so that they specularly reflect solar radiation to the point of observation. This glitter is often the major source of sea-surface radiance. A simplified analytical model of specular reflection from a single facet on the mean surface has been developed and investigated. The insight gained from this model aids the interpretation of measured sun glitter data. An extension of the methods used shows promise of representing spatially averaged glitter radiance.

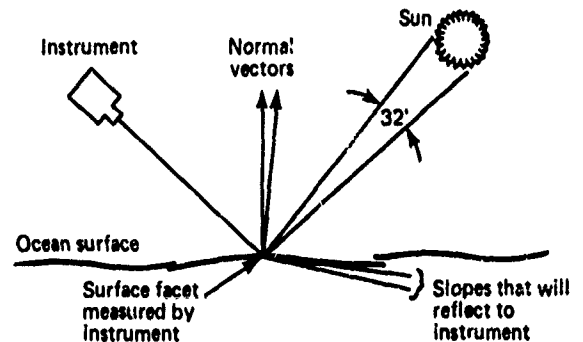


Fig. 1 Geometry of sun glitter reflection.

BACKGROUND

The reflection of the sun's rays from the ocean surface has been studied for several decades. In the 1950's, Cox and Munk (Ref. 1) performed a classical experiment using defocused cameras to measure the average intensity of the reflected radiation. From these data they were able to deduce the probability density function of the surface slopes. In order to obtain a more fundamental understanding of the reflection process, which includes space-time fluctuations, a simplified model has been analyzed. The model represents the reflection of solar radiation from a single facet on the mean ocean surface and considers reflections in only one dimension. The input and output power spectra have been compared. Numerical results indicate that spectral peaks may be observed in the output at frequencies where there are no peaks in the input. The reverse is also true; i.e., input spectral peaks may not be observed at the output. A series expansion has been used to explain these numerical results analytically.

DISCUSSION

The geometry of the reflection process is illustrated in Fig. 1. The instrument is measuring the reflection from a small area or facet on the surface. Ray optics is assumed to be applicable, and both the incoming and reflected rays lie in the plane of the figure. Since the sun has finite extent, a range of surface slopes will reflect radiation specularly to the instrument. The slopes and their normal vectors are illustrated.

Figure 2 shows the nonlinear filter used to model sun glitter reflection. The input, $x(t)$, is the slope of the facet measured by the instrument and is

assumed to be a Gaussian stochastic process. If the slope of the facet lies within the range required for reflection to the instrument (i.e., if $s_1 < x(t) \leq s_2$, where s_1 and s_2 define the boundary of the slope region that reflects to the instruments), then unit output is received at the instrument; otherwise the output is zero. Using this model, the temporal autocorrelation function of the glitter, $R_{yy}(\tau)$, can be related to the temporal autocorrelation function of the slopes, $R_{xx}(\tau)$. The appropriate expression is

$$R_{yy}(\tau) = \begin{cases} \int_{s_1}^{s_2} \frac{1}{\sigma_x \sqrt{2\pi}} \exp\left[-\frac{x^2}{2\sigma_x^2}\right] \left[\operatorname{erf}\left(\frac{s_2 - r x}{\sigma_x \sqrt{1 - r^2}}\right) - \operatorname{erf}\left(\frac{s_1 - r x}{\sigma_x \sqrt{1 - r^2}}\right) \right] dx & \text{for } \tau \neq 0 \\ \operatorname{erf}\left(\frac{s_2}{\sigma_x}\right) - \operatorname{erf}\left(\frac{s_1}{\sigma_x}\right) & \text{for } \tau = 0 \end{cases}$$

where

$$r = r(\tau) = \frac{R_{xx}(\tau)}{\sigma_x^2}$$

$$\operatorname{erf}(z) = \frac{1}{\sqrt{2\pi}} \int_0^z \exp[-w^2/2] dw$$

In this equation, σ_x^2 is the variance of the input slopes.

Since the autocorrelation function and power spectrum constitute a Fourier transform pair, the equation expresses a relationship between the slope

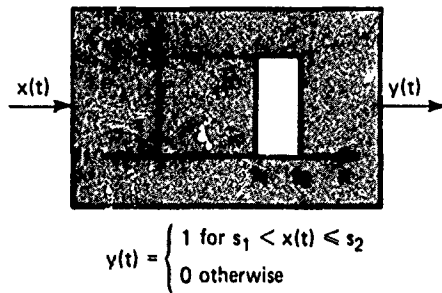


Fig. 2 Nonlinear filter to model sun reflections from a surface facet.

and the glitter power spectra. However, the integral in the equation cannot be evaluated analytically. It has been evaluated numerically using both the Romberg technique and a Gaussian quadrature method. Results have been verified by simulation using analytical forms for the slope autocorrelation function.

Figure 3 shows a slope power spectrum computed from the wave elevation spectral model proposed in Ref. 2. The wind friction velocity for this case was $u_* = 48$ cm/s. Features to note on this slope spectrum are the low and high frequency dropoffs, the peak, and the high frequency shoulder. The corresponding glitter spectrum, computed using the above model, is shown in Fig. 4. (This figure is shown in decibels because it would appear as a straight line on even one cycle of log paper.) Notice that the main peak of the input is still visible on the output spectrum, as is the high frequency shoulder. However, the features have been greatly attenuated. Also note that there is power in the output at low frequencies where there was none in the input. The higher frequencies also are whitened.

By expanding the Gaussian density in terms of Hermite polynomials, the integral in the autocorrelation equation can be written as an infinite series. Although the series converges very slowly for values of $r(\tau)$ not significantly smaller than unity, it can be used to interpret some of the numerical results. In particular, various terms in the series explain the low and high frequency whitening and also the appearance of peaks in the glitter spectrum at frequencies where there were no peaks in the slope spectrum. (This last phenomenon was observed in results not discussed here.)

CONCLUSIONS

The numerical results and analyses provide insight into the glitter process and explain why measured glitter spectra tend to be whitened. However, several important effects have not been included in

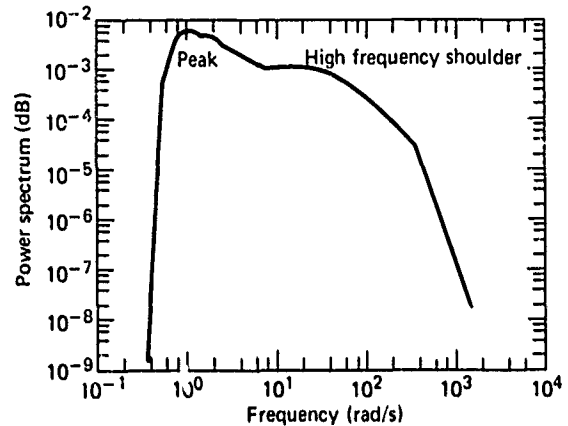


Fig. 3 Slope power spectrum, $u_* = 48$ cm/s.

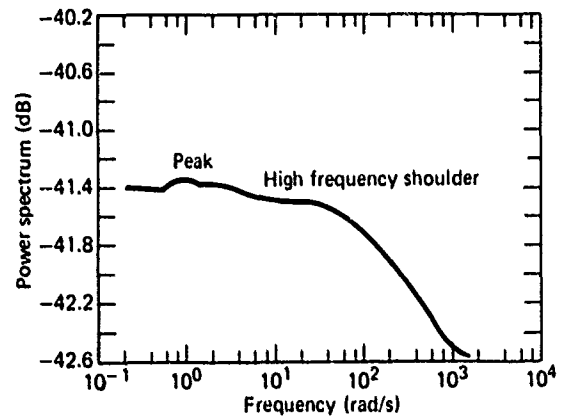


Fig. 4 Glitter power spectrum, $u_* = 48$ cm/s.

the investigation. First, reflection really occurs in two dimensions, not just one. Second, in practice the instrument views a finite area of the sea surface, not just a single point or facet. Thus the effects of spatial averaging must be included in the mathematical model of the process. Current investigations are directed toward including these complexities in the analysis.

REFERENCES

- 1 C. Cox and W. Munk, "Slopes of the Sea Surface Deduced from Photographs of Sun Glitter," *Bull. Scripps Inst. Oceanogr.* 6, No. 9, 1956, pp. 401-488.
- 2 A. W. Bjerkaas and I. W. Riedel, *Proposed Model for the Elevation Spectrum of a Wind Roughened Sea Surface*, APL JHU STD-041, 1978.
- 3 G. B. Irami et al., *Ocean Sun Glitter Fluctuations, Part I. Data Acquisition and Processing*, APL JHU POR-3158 (Revised), 25 Jul 1978.

Author: F. W. Riedel

Support: Strategic Systems Project Office

DETECTION OF LOW-ENERGY SWELL SYSTEMS WITH THE SEASAT SAR

SEASAT approached the east coast of the United States at 1520 GMT on 28 September 1978. The 100 km swath of its synthetic aperture radar (SAR) ran approximately parallel to the coast but displaced eastward by about 20 km. On the basis of the present analysis of that pass, several major conclusions were reached: (a) the SAR can successfully detect low-energy swell systems with significant wave heights, H_s , of well under 1 m (actually 0.65 ± 0.25 m); (b) the refraction of low-energy but well-organized swell resulting from changes in the local depth of the ocean is clearly detectable in both wavelength and direction; and (c) the complexity of the ocean spectrum (e.g., whether it is composed of more than one system or is spread in direction and wave number) seems to have little bearing on the threshold detection limits.

BACKGROUND

Studies made with aircraft in the past few years indicate that ocean swell can be imaged with a SAR, at least for some wind velocities, when there is a substantial component of the swell traveling along the radar's line of sight. However, the bounds on wind, wave, and geometric conditions for which the detection of ocean waves is reliable remain elusive for want of an extensive experimental data base. SEASAT provided a unique, although limited, opportunity to reexamine the wave detection problem with few of the artificial constraints of aircraft measurements. Reference 1 gives a concise summary of the SEASAT SAR design parameters; Ref. 2 gives a more general description of the system and of its fundamental limitations. Preliminary assessments of its ocean wave detection capabilities have been compiled in Refs. 3, 4, and 5.

During the 100 day lifetime of the SEASAT SAR, nearly 500 passes of 1 to 15 min duration were collected at three domestic and two foreign receiving stations. Twenty-three passes provided acceptable SAR imagery within 70 km of a well-instrumented "sea truth" pier operated by the U.S. Army Corps of Engineers, Coastal Engineering Research Center (CERC) at Duck, North Carolina. APL and several government agencies collected wind and wave measurements from 12 August to 9 October 1978.

DISCUSSION

Figure 1 shows the areas for which estimates or measurements were collected on 28 September. For

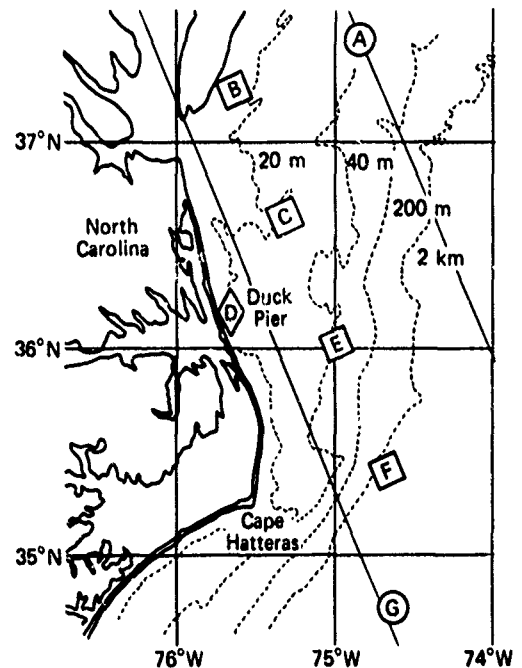


Fig. 1 Locations of surface, aircraft, and spacecraft measurements of the low-energy swell systems present on 28 September 1978.

reference, the boundaries of the 100 km SAR swath are shown by the solid lines inclined approximately 25° with respect to north at this latitude. The locations are keyed alphabetically from north to south. The Navy Fleet Numerical Weather Center (FNWC) grid point 271 is indicated by A. B, C, E, and F are 15 km^2 areas over which the SEASAT SAR imagery was Fourier transformed optically. The appreciable changes in local ocean depth (dotted contours in Fig. 1) at B, C, and E would cause spreading of a single frequency deep-water wave in both wavelength and direction. Deep-water dispersion prevails only at F for wavelengths greater than 70 m. Local depth changes at B are especially severe, ranging from less than 10 to at least 20 m. The laser profilometer spectrum in Fig. 2 was collected at C by a National Oceanic and Atmospheric Administration/Sea Air Interaction Laboratory (NOAA/SAIL) aircraft. *In-situ* one-dimensional spectral measurements were collected at the CERC pier (D). The FNWC grid point 260 (G) provides a convenient reference spectrum for the SAR

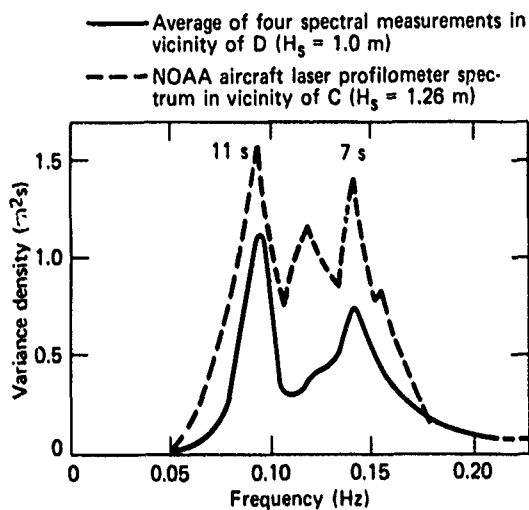


Fig. 2 A comparison of surface and air measurements of the wave height spectra near Duck, North Carolina.

imagery data collected at *F*. *F* and *G* are the only deep-water locations of Fig. 1.

Time histories of the long (greater than 1 s) waves were recorded by five instruments in the vicinity of the research pier for a 20 min interval spanning the satellite overpass time. The one-dimensional long-wave spectrum was measured near the pier with two Baylor gauges, two wave-rider buoys, and one capacitive wave staff. Spectra from each instrument show varying amounts of 11 and 7 s systems. The average of the two gauges and the two buoys (Fig. 2) clearly identifies each wave system. The significant wave height derived from the averaged spectrum is 1.0 m, which of course includes the combined energy from both the 11 and the 7 s systems. The significant wave height for each separate system (roughly equal in energy at the pier) is closer to 0.7 m. By comparison, the FNWC grid point closest to the pier (*G*) yields estimates of 0.4 and 0.6 m for the long-wave and the short-wave systems, respectively.

Flying about 50 km to the east of the pier, the NOAA aircraft was equipped with a laser profilometer to measure the one-dimensional ocean height spectrum in the flight direction of the aircraft. For a typical "swell-run," the aircraft heading is chosen to correspond (within a few degrees) to the vector direction of the swell. The resulting spectrum accurately measures the total energy on the surface if the spectrum contains little energy orthogonal to the flight vector, because that energy is effectively excluded. The laser spectrum plotted against the averaged pier spectrum in Fig. 2 verifies a double wave system with predominant periods at 11 and 7 s, and a total

significant wave height of 1.26 m, or approximately 0.9 m for each system. The energy of the 7 s system is probably underestimated because of the directional sensitivity of the laser profilometer. However, the energy of the 11 s system should be accurate and probably represents an effective upper bound to the significant wave height in the transformed areas.

The SAR was activated for approximately four minutes on 28 September as it approached the U.S. east coast. The radar interaction wavelength is about 30 cm, and the image intensity (or reflected power) is generally proportional to the amplitude of Bragg scatterers of the 30 cm wavelength on the ocean surface (Ref. 6). The amplitude of the scatterers may, in turn, be strongly (but not solely) correlated with surface wind at the boundary layer. In general, brighter regions in an image correspond to higher winds and darker regions to lower winds.

The imagery from the SAR pass on 28 September was optically Fourier transformed, digitally scanned at the equivalent of 6 m ground resolution, and spatially averaged using a 7×7 element sliding window. The contrast was enhanced by means of a three-segment, piecewise, linear-level transformation with a very high gain in the center segment. Each set of break points was optimized individually to compensate for the variations in average intensity.

Figure 3 shows a progression of enhanced optical Fourier transforms representing the image spectra at *F*, *E*, *C*, and *B* as the wave trains approach shore. The sequence shows quite clearly the refraction effects of the variations in ocean depth on the long-wave component. A 210 m wave in deep water at *F* shortens to 170 m at *E*, to 160 m at *C*, and finally to 120 m at *B*, in shallow water. Furthermore, the deep-water spectrum of *F* correlates well with the FNWC estimate made at *G* (grid point 260) of spectral peaks in both wave number and direction. The presence of a short-wave system is also evident on the transforms. At least in part, this short-wave energy correlation may be an artifact of the ground processor. Recent digitally processed and transformed imagery of the same area shows much weaker correlations in the short-wave (7 s) portions of the spectrum.

It should be emphasized that no correlation between spectral energy density and image transform density has been attempted. A proper treatment of that question would require careful accounting of the many system nonlinearities, some deliberately introduced for enhancement and some unknown. A better understanding of ocean backscatter models is also a prerequisite for further progress here.

The quantitative shallow-water dispersion relationship (Ref. 7) is shown by the curves in Fig. 4, on

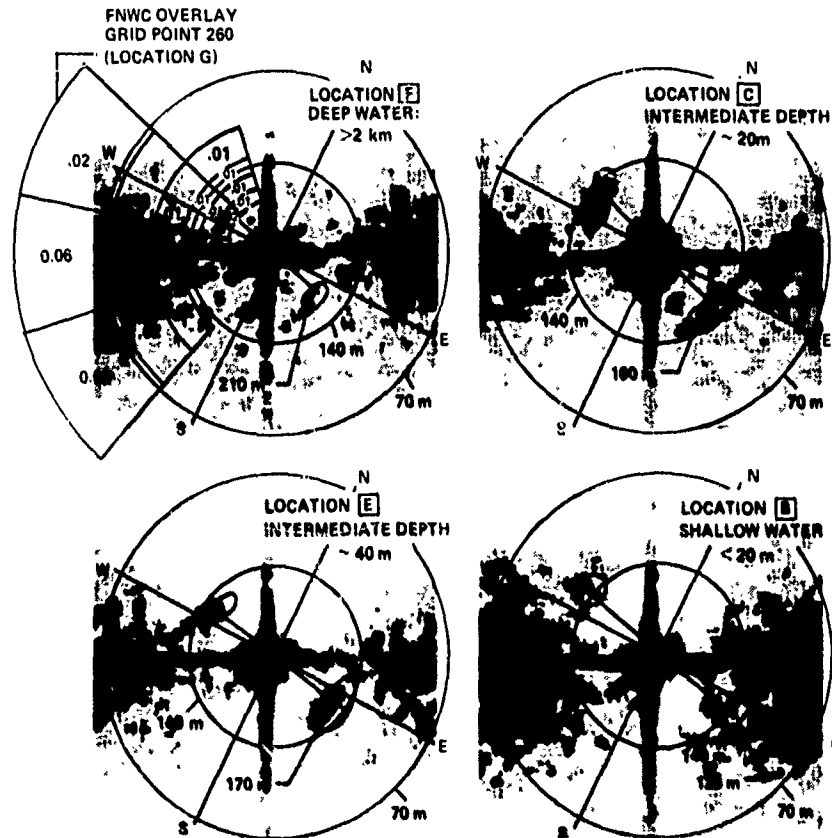


Fig. 3 Optically processed, optically transformed, and digitally enhanced SAR wave spectra from each of the four locations F, E, C, and B. The sequence moves from deep to shallow water and illustrates both wavelength and direction change as the 11 s swell system approaches shore. The overlap of the FNWC spectra for grid point 260 (G) on the SAR image spectrum at F shows the remarkable correlation of the 11 s swell system present on 28 September 1978. Overlay units are expressed in relative energy units per cell.

which are also plotted the results of Fig. 3. Each of the four center wavelengths from the optical transforms is entered on the horizontal axis of the dispersion relationship and is transferred according to the variation in depth for its particular location. The location of peaks from the optical transforms is judged to be accurate to $\pm 5\%$. These two uncertainties combine to produce the areas of uncertainty shown in Fig. 4. The data set is seen to be most consistent with the assumption of an 11.7 s swell system.

In summary, a well-organized, very-low-energy swell system off the east coast has been tracked with the SEASAT SAR from deep water, across the continental shelf, and into shallow water. The results indicate that a spaceborne imaging radar can measure ocean wavelength and direction accurately, even in coastal areas and in the presence of a mixed ocean. For separating swell systems in a mixed ocean, its ac-

curacy may exceed that of any other known technique.

ACKNOWLEDGMENTS

This work was jointly supported by NOAA and the National Aeronautics and Space Administration as a portion of the SEASAT Announcement of Opportunity Program under Contract MO-A01-78-00-4330. The laser spectrum of Fig. 2 was provided by D. Ross of NOAA. The gauge spectrum of Fig. 2 was provided by D. Lichy of CERC. J. Jenkins of APL enhanced the images shown in Fig. 3.

REFERENCES

1. R. Jordan, "The SEASAT-A Synthetic Aperture Radar Design and Implementation," *Proc. Synthetic Aperture Radar Technicians Conference*, Las Cruces, N.M., 1978.

Note: Uncertainty areas are due to changes in bathymetry over transform area of 15 km² and to peak wavelength error of $\pm 5\%$ of nominal.

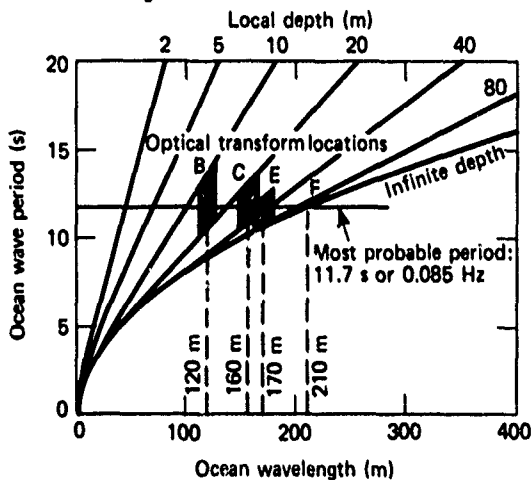


Fig. 4 The results of Fig. 3 plotted on the shallow-water dispersion relationship.

2. R. C. Beal, "Useful Spaceborne Synthetic Aperture Radars," *Proc. XXIXth International Astronautical Federation Congress, Dubrovnik, Yugoslavia, 1978*.
3. F. I. Gonzalez et al., "SEASAT Synthetic Aperture Radar: Ocean Wave Detection Capabilities," *Science* **204**, 1979, pp. 1418-1421.
4. R. C. Beal, *The SEASAT SAR Wind and Ocean Wave Monitoring Capabilities*, APL/JHUSIR-79-U-019, Aug 1979.
5. R. C. Beal, "Spaceborne Imaging Radar: Monitoring of Ocean Waves," *Science* **200**, 1980, pp. 1373-1375.
6. J. W. Wright, "A New Model for Sea Clutter," *IEEE Trans. Antennas and Propagation* **AP-16**, No. 2, 1968, pp. 217-223.
7. B. Kinsman, *Wind Waves*, Prentice Hall, 1965, pp. 126-133.

Author: R. C. Beal

Support: National Oceanic and Atmospheric Administration and National Aeronautics and Space Administration

AIRBORNE RESEARCH FLIGHTS IN ANTARCTICA AND GREENLAND

APL personnel participated in airborne research flights in Antarctica and Greenland to conduct experiments in meteorology, air sampling, air chemistry, infrared spectroscopy, magnetometry, ice thickness measurements, and aerial photography of glacier movements.

BACKGROUND

The polar research aircraft is an LC-130R, specially equipped and operated for the Division of Polar Programs (DPP) of the National Science Foundation by Navy Antarctic Development Squadron Six (VXE-6). Figure 1 shows the polar research aircraft at Williams Field, McMurdo Station. APL provided the Airborne Research Data System (ARDS) and the tail-mounted scalar magnetometer. APL supported the principal investigators by assisting in installing and checking equipment, recording and disseminating the scientific data, and coordinating flight operations with DPP and VXE-6 personnel. APL also assists

DPP and the principal investigators in planning future airborne experiments.

DISCUSSION

The air-sampling/air-chemistry sensors, infrared spectrometer, magnetometer, and ARDS were installed aboard the aircraft at the Naval Weapons Center, China Lake, California, during the first week of November 1978. The principal investigators and their projects were: W. Zoller (University of Maryland), atmospheric trace elements; A. Hogan (SUNY/Albany), aerosols; E. Robinson (Washington State University), air chemistry; A. Mason (University of Miami), tritium; R. Rasmussen (Oregon Graduate Center), halocarbons and N₂O; R. Renard (Naval Postgraduate School), mesoscale meteorology; D. Murcray (University of Denver), infrared atmospheric measurement; and R. Hickerson (APL), magnetometer studies.

The aircraft left Pt. Mugu, California, on 9 November 1978 and arrived in Christchurch, New



Fig. 1 Polar research aircraft LC-130R #159131, at Williams Field, McMurdo Station, Antarctica. The van at left supports airborne research experiments.

Zealand, on 13 November with stops in Hawaii and Pago Pago. Experiments were conducted during transpacific deployment to collect data at different latitudes and to check the equipment before Antarctic operations.

In Christchurch, the magnetometer and electronics were removed from the aircraft to reduce its gross weight, and provisions were made to mount the aerial camera. The aircraft departed from McMurdo Station, Antarctica, on 17 November to begin the air-sampling/air-chemistry series of flights.

On 27 November, the aircraft returned to Christchurch for repair of a leaking fuel tank. All of the long-range air-sampling/air-chemistry missions had been completed, and the magnetometer was reinstalled so that some checkout runs could be made. During the return to Antarctica on 1 December, the southern jetstream was transited. This was fortunate because previous attempts to penetrate the jetstream from McMurdo had been unsuccessful. When the rest of the air-sampling/air-chemistry flights had been completed, the aircraft returned to Christchurch on 7 December.

Initially, the air-sampling/air-chemistry experiments and magnetometry were not performed on the same flights as aerial photography. However, APL personnel volunteered to operate the ARDS and the magnetometer during aerial photography missions. Consequently, atmospheric waves were recorded on the Ellsworth Mountains mapping flights, and the scalar magnetic field of the Byrd Glacier was mapped.

Equipment for the atmospheric science experiments was removed on 8 December but the magnetometer remained aboard the aircraft. The radio echo-sounding radar, furnished by the Technical University of Denmark, was installed. The magnetometer housing and radio echo-sounding antennas are shown in Fig. 2. The radar transmits pulses into the ice at 60 and 300 MHz that are reflected from the bedrock and from discontinuities in the ice to form a picture of ice structure. The principal investigators were D. Drewry (Cambridge University, England) and J. Behrendt (U.S. Geological Survey). The aircraft left Christchurch on 13 December and returned on 29 December after completing the radio echo-sounding magnetometer flights. The ARDS, magnetometer, spares, test equipment, and data tapes were returned to APL.

The ARDS, magnetometer, and radio echo-sounding radar were again installed aboard the LC-130R at the Patuxent River Naval Air Station, Patuxent River, Maryland. The aircraft left for Sondrestrom Air Base, Greenland, on 5 May. The Greenland missions were similar to the radio echo-sounding missions in Antarctica. The principal investigators were P. Gudmandsen (Technical University of Denmark) and L. Thorning (the Geological Survey of Greenland). Twelve of the 13 flights were surveys of the Greenland Ice Sheet and various fjords; the other was a survey of the Penny Ice Cap of Baffin Island, Canada. The aircraft returned to the Patuxent Air Station on 15 May.

At the start of the program, APL was expected to operate and maintain the ARDS and to send the



Fig. 2 Polar research aircraft at Christchurch International Airport, Harewood, New Zealand. The radio echo-sounding antennas are mounted under the right wing. The airborne proton precession magnetometer is housed in the tail boom.

data to the World Data Center in Boulder, Colorado, for distribution. However, APL's role expanded as scientific and military personnel requested assistance in other areas. For example, APL assisted in planning the test flights, repaired the aerial camera and a recorder used by the radio echo-sounding radar, and even assisted in repairing the aircraft's inertial navigation system. At the Patuxent Air Station, APL coordinated installation and preparation, which involved obtaining clearance for Danish nationals. Finally, APL developed new procedures that eliminated a two-year backlog in processing the ARDS data tapes at the World Data Center. Investigators now obtain their data in a reasonable time.

Because of the success of the first full season, DPP is expanding APL's role. A new method of aircraft magnetic compensation is being developed, and significant improvements are being made in the

ARDS. Also, APL probably will build a new radio echo-sounding pulsed Doppler radar. DPP has given APL personnel considerable freedom in conducting operations because of their demonstrated ability to function with minimum direction.

The APL field personnel on the Antarctic team were R. L. Hickerson, R. A. Hutchins, and H. P. VonGunten. The personnel on the Greenland team were R. L. Hickerson, R. A. Hutchins, and J. A. Ford.

REFERENCE

1. R. L. Hickerson, "LC-130 Research Flights 1978-79," *Antarct. J. U.S.*, Oct 1979.

Author: R. L. Hickerson

Support: National Science Foundation,
Division of Polar Programs

LASAR RADAR INSTRUMENT FOR MEASURING SEAL DYNAMICS IN THE SURFACE EFFECT SHIP

A very-low-power CW laser radar ($0.9 \mu\text{m}$) has been developed by APL to measure the position (in three coordinates) of a point on the planing bow seal of a surface effect ship (SES). This noninvasive measuring instrument provides seal position to the ship's cockpit for real-time seal control and provides accurate (0.1 in. resolution) wide-bandwidth (100 Hz) measurements for seal dynamic studies and drag calculations. The successful development of this electro-optical radar instrument is a major milestone in the development of a laser altimeter for use in an existing wave profiling system.

BACKGROUND

An air cushion vehicle uses a pressurized bubble of air, confined within a flexible skirt, for lift. Because there is little contact friction, it can move at speeds greater than 40 kt over calm water when propelled by air screws. A variant of this technology is the SES, which captures an air bubble between two rigid sidewalls and two flexible skirts or seals, located at the bow and stern. The SES is constrained to operate only on water. However, because of its efficient propulsion systems (such as water propellers and water jets) and the improved sidewall sealing, it can achieve very high speeds (over 90 kt by a 100-ton test ship).

The flexible bow and stern seals present severe materials and maintenance problems when the vehicles are operated at high speeds. The seals also have typically slow dynamic response to impact by waves, which reduces their efficiency in high sea states. A planing seal designed by the Rohr Corporation has been installed on a 100-ton SES test ship (SES-100A) for evaluation (Fig. 1). It is expected that the planing seal will have an extended life while providing a lightweight system with individual elements that allow rapid differential responses to fluctuating wave forces. The seals are constructed from rigid planer elements, 2 ft wide, which are held together by heavy rubberized joints. The position and attitude of the seal are controlled by an inflatable bag, seal geometry, and retract straps (Fig. 2). Each element deflects as it encounters waves while maintaining an effective seal against the air. The rubberized joints allow the seal to conform to three-dimensional waves by allowing a small degree of lateral motion.

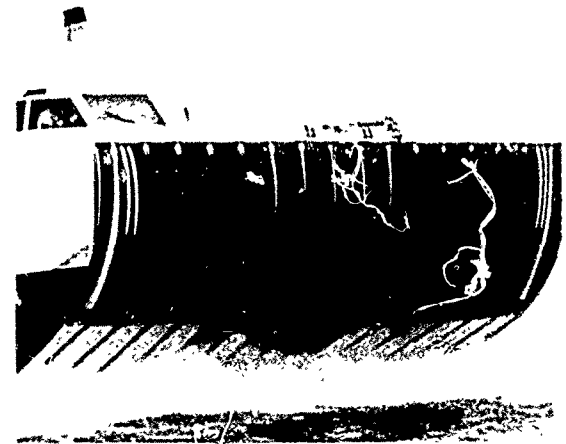


Fig. 1 Planing bow seal on the surface effect ship.

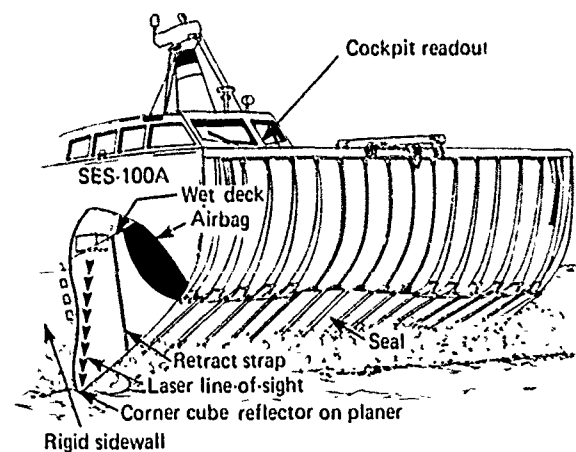


Fig. 2 Bow seal height instrumentation on SES-100A.

To analyze SES performance, the dynamics of the seal must be known as a function of ship speed, encountered sea state, and wave spectrum. In addition, a real-time measurement of seal height helps the ship's commander to achieve optimum ship performance.

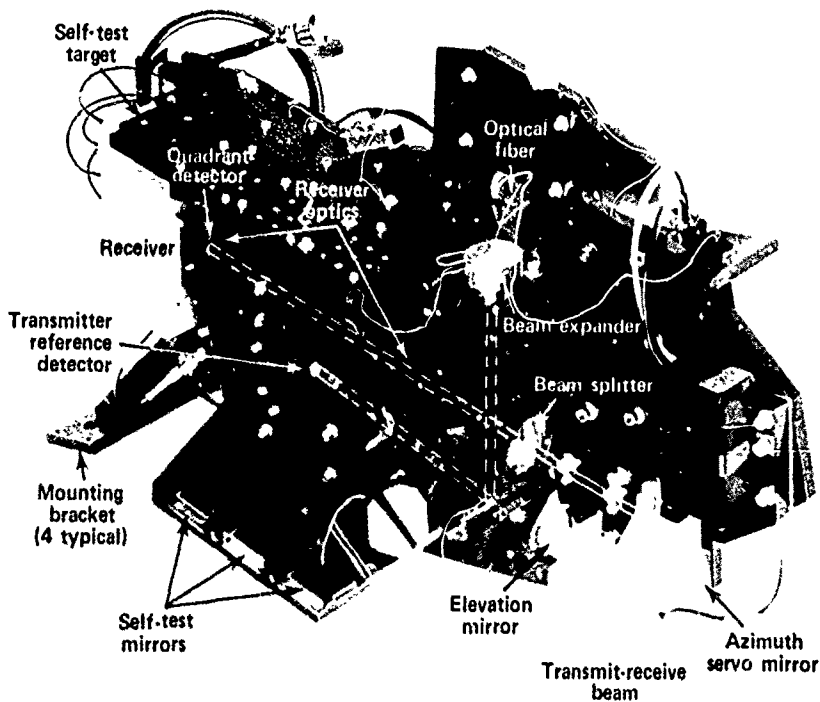


Fig. 3 Optical bench assembly.

The laser radar instrument can provide the dynamic position measurements needed to evaluate the seal. The instrument is a variant of an ongoing development (Refs. 1 and 2), i.e., the design of a laser radar for accurate, on-board, real-time measurement of the wave profile in front of a high-speed ship. The Electro-Optic Seal Height Instrument (Figs. 3 and 4) has successfully completed performance testing in the laboratory, including water spray, temperature, and vibration environments, and was installed on the SES-100A in December 1979.

DISCUSSION

The block diagram (Fig. 5) illustrates the operation of the instrumentation. The system consists of a laser ranging device that measures the distance to a corner cube reflector mounted on one of the planers and a two-axis tracking device that provides azimuth and elevation angles to the same point. The basic range measurement is achieved by measuring the actual phase difference between the 30 MHz cw modulation of the transmitted beam and that of the received beam returning from the retro-reflector target. The phase sensitivity to change in range at 30 MHz is $1.828^\circ/\text{in.}$; for a 0.1 in. resolution this requires resolving 0.2° of phase. The unambiguous

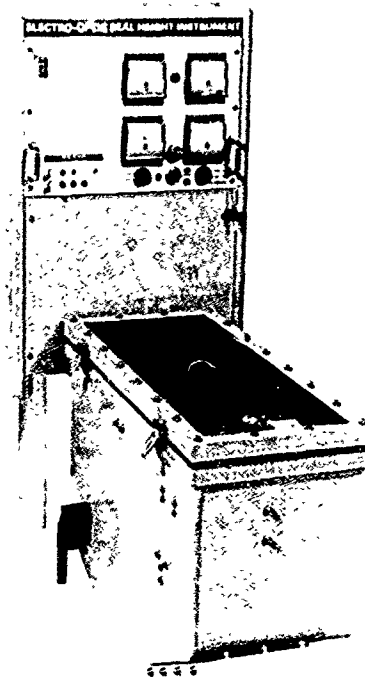


Fig. 4 Electro-Optic Seal Height Instrument.

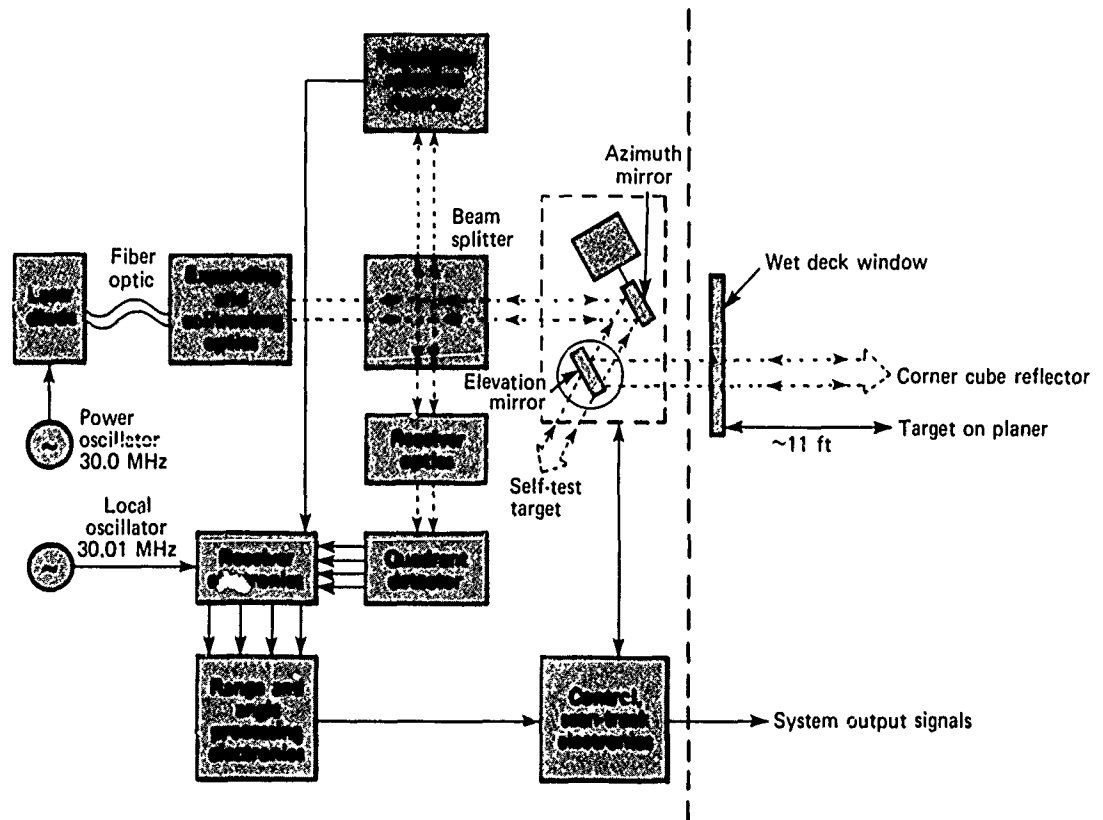


Fig. 5 Block diagram of the electro-optical seal height instrumentation.

range is 98.5 in. A collimated beam 0.6 in. in diameter is held centered on the target (corner reflector) by the angle tracking system. Target tracking is achieved using a quadrant photodetector, the angle processing electronics, and the elevation and azimuth beam steering mirrors.

The output of the 30 MHz crystal oscillator/power amplifier and a 100 mA DC bias current are applied to a solid-state laser source (laser diode) to modulate the output beam optically. The laser energy from the diode source is spatially collected and reshaped using an optical fiber. The beam exiting from the fiber is expanded by refractive optics to a 0.6 in. diameter "collimated" beam and is directed through the beam splitter whose primary function is to make the transmitter beam coaxial with the receiver's field of view. The output beam is directed toward the target by the steering mirrors. The modulation of the transmitter's output beam is detected by a photodetector to provide a reference signal for the range processing electronics. The beam returning from the target passes through the beam splitter and is focused on the quadrant detector by the receiver optics.

The 30.01 MHz output of a second crystal oscillator amplifier is mixed with the 30 MHz signals

(one reference and four received) to provide a receiver IF frequency of 10 kHz. The five 10 kHz signals are processed to provide the range measurement and angle error signals. The received collimated beam is optically reduced by the receiver optics to be 0.8 times the diameter of the quadrant detector. The four quadrant signals are synchronously detected, summed, and differenced to yield the azimuth and elevation angle error signals. The two angle error signals are normalized by the output dividers to yield the angle tracking error signals for input to the angle tracking electronics. The sum signal, designated automatic gain control (AGC), is used to evaluate system performance and to assess the spray environment in the SES plenum. A comparison of the AGC signal with a preset threshold generates a discrete output signal (called the acquisition signal) for search-track control.

The design of the angle track loop is identical for both the elevation and the azimuth steering mirrors. For small lateral planar motions, the corner cube reflector sends the collimated beam back toward the receiver, parallel to the incident beam but translated. An error signal is derived by means of the quadrant processing electronics from the translational error as was described previously. The range AGC is

included in the loop to cancel variations in loop gain and dynamics as the range changes. The error signal is integrated twice and passed through a lead compensation network before driving the steering galvanometer. The galvanometer has a capacitive angle transducer whose output indicates angular position. This output is fed back within the minor loop of the galvanometer to increase its bandwidth greatly; it also indicates the angular position of the corner cube with the required accuracy.

The accuracy of the angle output signal is limited not by the angle transducer but by the dynamic tracking error of the track loop. Calculations of the tracking error in response to expected motions of the planer show that the maximum expected target position error resulting from angle tracking in either axis is less than 0.1 in. The bandwidth of the closed angle track loop is approximately 100 Hz.

The system is designed to self-test the laser source, the optical system, and 95% of its electronics and to provide a go/no-go signal to indicate operation. The self-test is implemented by closing the optical path on a built-in corner cube target. Since the target is at a known range and the self-test range gate is set very narrow, the automatic self-test at turn-on provides a system operational check and also a verification of range calibration.

The system has an adaptive scanning and acquisition circuit whereby the system, upon loss of track, automatically begins a high-frequency, low-amplitude scan pattern about the last track point. If the target is not immediately reacquired, the pattern slowly opens up into a sawtooth scan pattern covering all possible locations of the target ($\pm 20^\circ$ elevation and $\pm 5^\circ$ azimuth). To minimize transients on the output signals during track loss, the last valid output signals are held by memory circuits until reacquisition.

The operating parameters of the system are listed in Table 1.

TABLE 1
SYSTEM OPERATING PARAMETERS

Laser beam	
Output power	480 μ W
Diameter	0.6 in.
Power density	0.7 mW/cm ²
Collimated	< 2 mrad divergence
Receiver	
S/N ratio	86 dB
Dynamic range	50 dB
Scan angle	$\pm 20^\circ$ elevation, $\pm 5^\circ$ azimuth
Range resolution	< 0.1 in.
Accuracy	1 in. (0 to 8 ft)
Output signals	
Range	50.0 mV/in.
Elevation angle	0.2 V/deg
Azimuth angle	1 V/deg
Seal height	0.8333 V/ft
Acquisition discrete	+ 5 V (track), 0 V (scan)
AGC	0 to 10 V

ACKNOWLEDGMENT

The following people contributed to the development of the instrument: T. M. Rankin (Project Engineer); B. G. Boone, R. E. Phelps, and S. H. Gordon (optics); R. H. Lapp, R. R. Gardner, and F. Jurgens (mechanical design); M. J. Mayr (control system); P. R. Gilchrist, T. G. Constable, and F. Mucino (receiver and processor); and G. R. Seylar (error studies).

REFERENCES

1. *Feasibility Demonstration of a Short Range CW Laser Altimeter System*, JHU/APL FID(3)78-U-083, 27 Apr 1978.
2. *Documentation of Design Performance and Qualification of the SES Wave Profiling System*, JHU/APL SES-025, Dec 1978.

Authors: T. M. Rankin and M. J. Mayr

Support: NAVSEASYS COM, PMS-304

FUNDAMENTAL RESEARCH

INTRODUCTION

In recognition of the fact that fundamental research will play a vital role in future technological achievements, APL has consistently encouraged basic investigations in physics, chemistry, biology, and mathematics. Their focus has been to provide fundamental support of technological programs aimed at solving the nation's military and civilian problems.

The basic science programs have also provided a link between APL and the academic and medical divisions of The Johns Hopkins University as well as the international academic community. The Laboratory's competence in these areas acts as a reserve for technical innovation and a resource when current technology and engineering methods are inadequate. APL has earned an outstanding reputation for its achievements in basic research. Some accomplishments of the past year are summarized in the articles in this section.

The first article describes a new *ab initio* calculation of the transport properties of hydrogen by means of an accurate determination of the intermolecular potential between two hydrogen molecules. The approach could be a significant advance in theoretical chemistry by permitting the prediction of macroscopic properties from fundamental principles.

An important program for several years has been the detection of leaks in underground gas distribution lines. With the active acoustic technique, a sound signal is excited in the gas within a pipe, and the component of the earth's surface displacement caused by radiation of the leak is measured. The article presents a theoretical basis for differentiating between coherent wall radiation of the nonleaking pipe and the signal produced by the leak.

In the third article, the hyperfine interactions of Kr_2F and the F_3^- defect in LiF have been calculated using a semiempirical valence bond approach. The results have provided structural information concerning these species and have given new insight into bonding and stability. In a related article, a theory of chemically induced magnetic polarization in free radical reactions has been advanced, using integral equation techniques. It was found that magnetic hyperfine structure interactions can greatly influence the reactivity of radicals by affecting singlet-triplet mixing in the system.

The next article describes an Ising model of phase transitions that has been used to investigate the influence of the interaction potential on the phase diagram for higher-neighbor Ising systems. The model has been surprisingly successful in describing behavior near the critical point.

The final article presents in mathematical form a comprehensive theory of vision. The theory furnished a rigorous mathematical basis for analyzing visual sensation.

These articles describe only a few of the ongoing research projects at APL. Programs in the areas of quantum electronics, chemical kinetics, fluid dynamics, and applied mathematics have been reported in previous issues of *Developments in Science and Technology*.

AB INITIO CALCULATION OF THE TRANSPORT PROPERTIES OF HYDROGEN

The differences between the viscosities of ortho and para hydrogen are reproduced satisfactorily by a new, elaborate, ab initio calculation of the forces between two hydrogen molecules. This accomplishes the double objective of verifying this molecular property — which is important in astrophysics — and offering the possibility of calculating macroscopic parameters.

BACKGROUND

The nature of the forces between hydrogen molecules is of interest for several reasons. Hydrogen is the major constituent of interstellar space, it is a potential energy source in either a combustion or a fusion reactor, and, because it is the simplest of all diatomic molecules, it offers the possibility that its properties may be predicted from fundamental principles.

Since hydrogen is the major constituent of interstellar clouds, the intermolecular forces between hydrogen molecules determine macroscopic astrophysical properties such as the transport coefficients entering the hydrodynamic equations of change. The properties are determined principally by the average overall orientations of the hydrogen molecules. Other properties (such as rotational energy and angular momentum relaxation, line shapes and pressure broadening, and depolarization of spectral lines) that determine the energy balance and the spectral characteristics of astrophysical observations are determined by the anisotropic part of these forces.

An accurate determination of the intermolecular potential of two hydrogen molecules would be important to the ultimate goal of theoretical chemistry: (a) given the molecular interaction between molecules, calculate their macroscopic properties; or (b) more ambitiously, predict intermolecular properties completely from fundamental principles and use them to predict macroscopic properties.

DISCUSSION

Although gas transport properties such as diffusion, viscosity, or heat conduction are insensitive (to within 2 to 4%) to the anisotropy of intermolecular forces, within that error margin they characterize the orientational average of the forces

quite well. This has been substantiated by indirect experimental evidence and by several recent calculations. It has also been possible to carry out rather clever experiments on transport properties that directly measure the anisotropic part of intermolecular interactions.

One such experiment (Refs. 1 and 2) measures the differences between the viscosities of ortho and para hydrogen at low temperature. Para hydrogen at low temperature is almost entirely in the $j = 0$ rotational state and is spherically symmetric; ortho hydrogen is effectively restricted to the $j = 1$ rotational state. This gives rise to three distinct ways in which the interactions between hydrogen molecules can differ:

1. Because para hydrogen in the $j = 0$ state is spherically symmetric, only the orientational average of the intermolecular forces determines the viscosity of para hydrogen at low temperatures. On the other hand, for ortho hydrogen there are 25 possible types of molecular interaction, depending on the relative orientation of the molecules.
2. Para hydrogen acts as a Bose system of spin 0; ortho hydrogen acts as a Bose system of spin 1. Consequently, certain collision trajectories that are allowed for ortho hydrogen are not allowed for para hydrogen because of the Pauli exclusion principle.
3. Finally, ortho hydrogen is slightly larger than para hydrogen because of centrifugal forces. Therefore, the spherical as well as the anisotropic components of the molecular force field are affected.

Recently, elaborate calculations of the intermolecular forces between hydrogen molecules have been carried out by solving the Schrödinger equation (Ref. 3) numerically. In an attempt to assess the accuracy of the potential energy surface, scattering calculations have been made (Ref. 4) and the results were inserted into the relevant kinetic theory expressions for transport coefficients (Ref. 5).

The resultant viscosity differences are shown in Fig. 1. Almost perfect agreement is observed with one set of experimental results (Ref. 2), i.e., for a normal ortho-para hydrogen mixture (75% ortho). Because this concentration is probably the most accurate, the

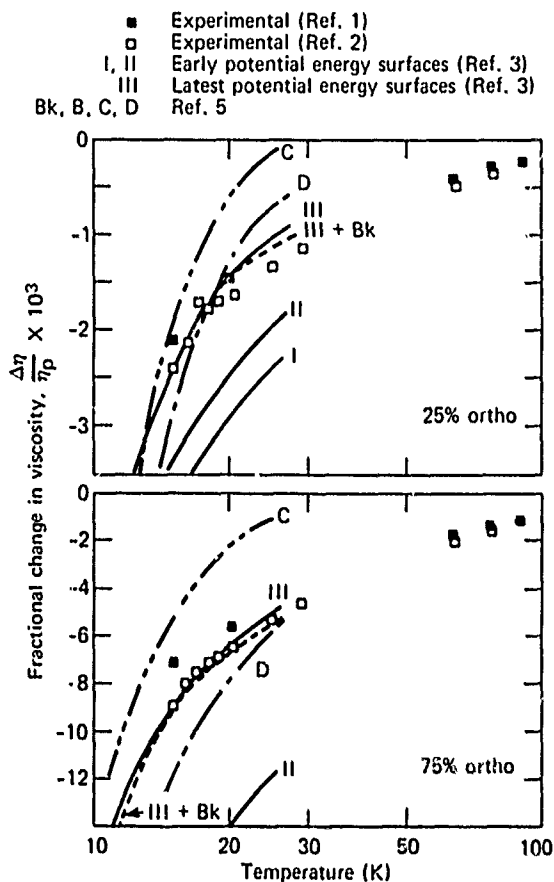


Fig. 1 Fractional change in viscosity with amount of ortho hydrogen.

agreement with experiment is quite satisfactory, and one may conclude that the new H_2 - H_2 potential energy surface is quite accurate. Also shown are the results of an earlier calculation (Ref. 5) that used a semi-empirical potential energy surface. One may conclude from these results that each of the effects enumerated above — quantum symmetry differences, anisotropy, and centrifugal stretching — contributes equally to the observed quantum differences.

REFERENCES

1. E. Becker and E. Stehle, "Ein Zähigkeitsunterschied von Ortho- und Para-Wasserstoff bei tiefen Temperaturen," *Z. Phys.* **133**, 1952, pp. 615-628.
2. M. Camani, "Wirkungsquerschnitte in Ortho-Para-Wasserstoffgemischen" *Helv. Phys. Acta* **44**, 1971, pp. 437-450.
3. W. Meyer, University of Kaiserslautern, personal communication.
4. L. Monchick and J. Schäfer "Ab Initio Calculations of the Transport Cross Sections of H_2 ," *Abstracts, VII International Symposium on Molecular Beams*, 28 May-1 Jun 1979, p. 55.
5. L. Monchick, "Multipole Interactions and Macroscopic Differences in Ortho and Para Hydrogen," *Chem. Phys. Lett.* **24**, No. 1, 1974, pp. 91-95.

Authors: L. Monchick (APL) and J. Schäfer
(Max-Planck Institute)

Support: Indirectly Funded R&D and Max-Planck
Institute

EXCITATION OF AN ELASTIC HALF-SPACE BY A BURIED LINE SOURCE OF CONICAL WAVES

A formal solution has been obtained to the problem of displacement produced by radiation from a buried line source of conical waves propagating at a constant phase velocity, c , in an isotropic elastic half-space. The determination of the properties of surface displacements is essential to any program evaluating the integrity of buried pipe lines.

BACKGROUND

To detect leaks in underground gas distribution lines with the active acoustic method, a sound signal is excited in the gas within a pipe, and the component of earth surface displacement caused by elastic disturbances associated with the leak is measured. An

obstacle to this method of leak detection is the coherent wall radiation of an intact pipe. Thus, the characteristics of such radiation must be known if one is to differentiate successfully between signals caused by a leak and those caused by the wall. An earlier theory (Ref. 1) to determine surface displacements resulting from elastic waves excited by a nonleaking pipe was confined to surface positions directly over the pipe axis (epicenter). That theory showed that epicenter surface displacements are accounted for by radiated compressional and shear waves and that the displacements exhibit a series of maxima and minima with frequency because of the markedly different propagation velocities of these types of waves. Theoretical predictions were confirmed by experiment (Ref. 1).

The general theory of disturbances excited in an isotropic elastic half-space by axisymmetric pipe wall vibrations is described in this article. As in the earlier theory, the pipe excites both shear and compressional conical waves that are reflected from the surface. Unlike the previous theory, which resorted to a plane wave approximation for conical waves valid at the epicenter, this theory holds for a general position on the surface of, or within, the half-space. It takes into account curved wave fronts and diffraction phenomena associated with their interaction with a planar surface. Expressions for surface displacements are derived in the form of integrals that must be evaluated approximately. Using the method of steepest descents, the integrals are evaluated for small perpendicular distances from the epicenter. At the epicenter, this theory coincides with the earlier one.

DISCUSSION

Pressure variations, p , accompanying the propagation of an acoustic plane wave within a pipe result in axisymmetric displacements of the pipe wall. An exaggerated view of this phenomena is shown in Fig. 1, where arrows in the external medium indicate pipe wall displacement. The vibrating wall generates elastic waves in the earth characterized by the compressional and shear potentials ϕ and ψ , respectively, which satisfy $\nabla^2 \phi = (1/\alpha^2) \partial^2 \phi / \partial t^2$ and $\nabla^2 \psi = (1/\beta^2) \partial^2 \psi / \partial t^2$. The compressional wave velocity, α , and shear wave velocity, β , are determined by the elastic constants of the earth. Solutions to these wave equations representing conical waves radiating outward from the pipe are as follows:

$$\phi = AH_0^{(2)}(k_c r) \exp [i(\omega t - k_0 y)]$$

and

$$\psi = BH_0^{(2)}(k_s r) \exp [i(\omega t - k_0 y)] ,$$

where k_c and k_s are wave vectors and

$$k_c = \sqrt{k_\alpha^2 - k_0^2}$$

and

$$k_s = \sqrt{k_\beta^2 - k_0^2} .$$

In these equations, $k_\alpha = \omega/\alpha$, $k_\beta = \omega/\beta$, and $k_0 = \omega/c$ with ω being the angular frequency. The radial coordinate is $r = \sqrt{x^2 + z^2}$, and $H_0^{(2)}(x)$ is the zero-order Hankel function of the second kind. The condition for radiation is that arguments of the Hankel functions must be real, requiring c to be greater than α or β . This condition holds for pipes filled with air or methane, buried in clay or in sandy soils (Ref. 1). The constants A and B are determined by boundary conditions at the pipe/earth interface (continuity of radial and longitudinal displacements).

The difficulty with this problem arises when conical waves in cylindrical coordinates interact with a planar surface. At the stress-free surface, normal (P_{zz}) and tangential (P_{zy} and P_{zx}) stresses must vanish. These stresses are functions of the compressional and shear potentials; e.g.,

$$P_{zz} = \lambda \nabla^2 \phi + 2\mu (\partial^2 \phi / \partial z^2 + \partial^2 w_y / \partial x \partial y - \partial^2 \psi_x / \partial y \partial z) ,$$

where λ and μ are the Lamé constants for the half-space. The Hankel functions in the potentials describing the radiation field are decomposed into their Cartesian components using an integral representation before they are substituted in the stress equations.

The solution proceeds by introducing an image source located a distance above the surface equal to the depth of the pipe. For an incident compressional wave, the image source ensures that normal stress

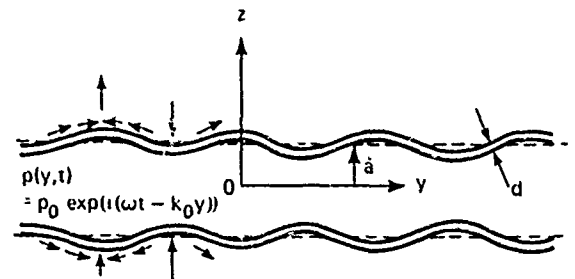


Fig. 1 Pipe section showing radial and longitudinal wall displacements produced by internal acoustic pressure variations.

vanishes at the surface but not the tangential components. Similarly, for an incident shear wave, the image source ensures that tangential stresses vanish at the surface but not the normal component. In order for stresses to vanish at the surface, an additional compressional component and two shear components must be added to both cases of incident compression and shear waves and their respective image sources.

For example, for a compressional wave incident on a planar surface, the complete solution is given in terms of the compressional potential, $\phi = \phi_{image} + \phi_s$, and the shear potential, $\psi = \psi_1 + \psi_2$. The displacement, $s(u, v, w)$, is $s = \nabla \phi + \nabla \times \psi$. This represents the formal solution to the problem in the sense that the potentials are expressed in the form of integrals that can only be evaluated approximately. For instance, the vertical displacement of the earth's surface resulting from an incident compressional wave is

$$w(x, y) = -\frac{2iA}{\pi} \int_{-\infty}^{\infty} \frac{k_\beta^2 [2(k^2 + k_0^2) - k_\beta^2]}{F(k^2 + k_0^2)} \exp [i(\omega t - k_0 y + ih\nu_\alpha - \kappa x)] dk \quad (1)$$

where h is the pipe depth, $\nu_\alpha = \sqrt{k^2 - k_c^2}$ where $R(\nu_\alpha) \geq 0$, and $F(k^2 + k_0^2)$ is the Rayleigh function:

$$F(k^2 + k_0^2) = [2(k^2 + k_0^2) - k_\beta^2]^2 - 4(k^2 + k_0^2)\nu_\alpha \nu_\beta \quad (2)$$

Similarly, $\nu_\beta = \sqrt{k^2 - k_s^2}$ where $R(\nu_\beta) \geq 0$. Equation 1 is evaluated in the complex k plane (Fig. 2).

The integration path must avoid singularities of the integrand. These singularities constitute a branch cut along the negative imaginary axis from $-i\infty$ to the origin and along the real axis from 0 through the branch point k_c to the branch point k_s . The Rayleigh function has a simple pole when $k = k_r = \sqrt{k_s^2 - k_0^2}$, where $k_s = \omega/\gamma$ and γ equals the velocity of the Rayleigh surface wave. The integral, Eq. 1, is in a form suitable for evaluation by the method of steepest descents (Ref. 2).

The steepest descent path is roughly a parabola (Fig. 2a) beginning in the third quadrant and ending in the fourth quadrant with a maximum in the first quadrant. The path passes through the saddle point, k_m , which is on the real axis and varies from 0 for $x = 0$ to k_c when $x \rightarrow \infty$. As x increases, the latus rectum of the parabola decreases until the steepest descent path encounters the singularities, where it must be distorted to avoid them (Figs. 2b and 2c). When x increases to the point where the path recuts the real axis to the left of the Rayleigh pole, the contribution

from this singularity must be included, and similarly for the branch points at k_c and k_s . This suggests that there is a minimum distance, x , before diffraction effects (such as surface "head" waves associated approximately with k_c and k_s , and the surface Rayleigh wave) begin to form. The ratio of the minimum epicenter distance to the pipe depth, x_r/h , for Rayleigh wave formation is plotted in Fig. 3 as a function of phase velocity, c . The dashed line corresponds to the two-dimensional limit, $c \rightarrow \infty$.

The vertical surface displacement at $x = 0$ evaluated by the method of steepest descents is equal to that found using the plane wave approximation of Ref. 1, since the two approximations are equivalent at the epicenter. The theory for an incident axisymmetric shear wave is almost the same. The total displacement is found by summing displacements for incident shear and compression.

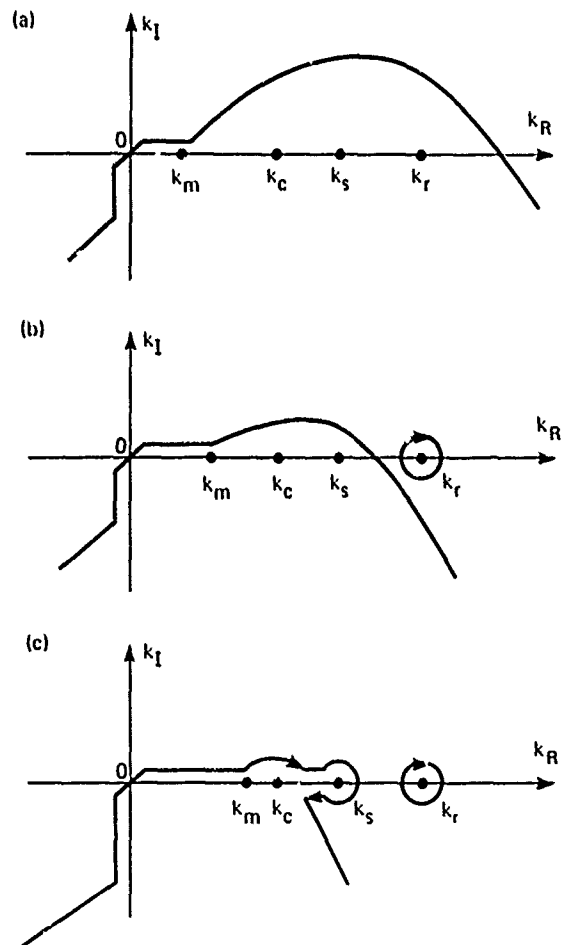


Fig. 2 Steepest descent paths.

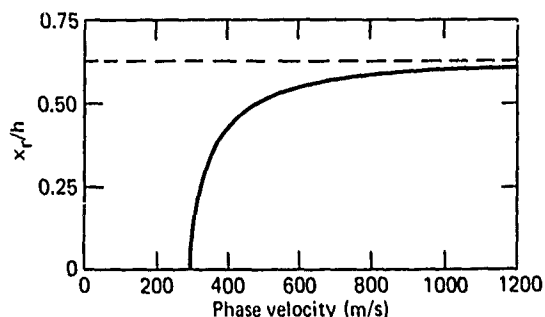


Fig. 3 Ratio of lateral distance to source depth for Rayleigh wave formation as a function of phase velocity.

Theory predicts that displacement perpendicular to the pipe axis, $u(x,y)$, is zero when $x = 0$, which also follows from the symmetry of the pipe-

planar surface system. This suggests that monitoring horizontal displacement, u , instead of vertical displacement, w would minimize interference from the wall radiation and thus maximize detectability of leak-related signals. A significant reduction of u at $x = 0$ has been confirmed experimentally at the APL pipe line facility.

REFERENCES

1. A. N. Jette, M. S. Morris, J. C. Murphy, and J. G. Parker, "Active Acoustic Detection of Leaks in Underground Natural Gas Distribution Lines," *Mater. Eval. (Res. Suppl.)* 35, No. 10 197, pp. 90-97.
2. M. W. Ewing, W. S. Jardetsky, and F. Press, *Elastic Waves in Layered Media*, McGraw-Hill, New York, 1957.

Authors: A. N. Jette and J. G. Parker

Support: Gas Research Institute

VALENCE BOND STUDY OF HYPERFINE INTERACTIONS AND STRUCTURE OF Kr_2F AND THE F_3^- DEFECT IN LiF

A semiempirical valence bond (VB) wave function that includes correlation between electrons of opposite spin has been used to calculate the electron-nuclear, magnetic, hyperfine interaction constants (hfc) in the triatomic radical $Kr-F-Kr$ (Ref. 1) and in the radical dianion F_3^- (Ref. 2). The latter species exists as a radiation-induced defect in LiF. Comparison of calculated and experimental hfc has confirmed the electronic ground state as ${}^2\Sigma_u$ and has determined the bond distances and electron charge distribution in these molecular species, which are of special interest because their existence violates classical chemical bonding theory. Furthermore, the molecular parameters of the F_3^- center in LiF show that it is the long-sought, but hitherto unidentified, interstitial halogen atom interacting with two lattice F anions.

BACKGROUND

Modern spectroscopic techniques such as electron spin resonance (ESR) spectroscopy combined with

the cryogenic stabilization of weakly bound species, laser-based spectroscopic methods, etc. are resulting in the discovery of increasing numbers of weakly bound molecular species that should not exist according to classical bonding theory. In addition to the fundamental scientific interest in these so-called hypervalent radicals, their tendency to have strongly emitting states gives them practical importance in laser applications. The foremost example is high-power ultraviolet lasers using the noble gas monohalides.

The recent ESR identification of the paramagnetic molecule Kr_2F as a reaction product of photolytically generated F atoms with a Kr matrix at 10 K (Ref. 3) is especially interesting because Kr_2F violates the two bonding precepts that Kr forms no bonds and that F is monovalent. The ESR work determined all components of the anisotropic hfc tensors of the Kr and F atoms. It showed that the Kr atoms are equivalent and that the molecule has the nondegenerate ${}^2\Sigma_u$ electronic ground state. This

motivated the extension of our semiempirical VB model of hfc in diatomic hypervalent radicals (such as the noble gas monohalides and diatomic halogen anions) to include the triatomic species Kr_2F so as to check the ESR results and estimate the molecular parameters of Kr_2F .

The work recalled that some years ago Cohen et al. (Ref. 4) had observed a paramagnetic center based on the F_3^- dianion in X-irradiated LiF (V_f center). Their ESR data indicated a large isotropic hfc for the central F atom, implying a large unpaired electron density in the 2s orbital of this atom. Since this disagreed with molecular orbital (MO) theory predicting for a nondegenerate $^2\Sigma_u$ ground state, F_3^- was assigned the degenerate $^2\Pi$ ground state. The assignment was questionable in view of the finding that Kr_2F has a $^2\Sigma_u$ ground state. Moreover, MO theory is unable to deal with electron correlation interactions, which are especially important in hypervalent radicals. A VB investigation of whether the F_3^- hfc could in fact be accounted for by the more reasonable $^2\Sigma_u$ ground state followed.

DISCUSSION

The magnetic hyperfine interactions between the unpaired electron and a given nucleus of a paramagnetic molecule are described by an isotropic and an anisotropic hfc, denoted a and B_1 , respectively (Refs. 1 and 2). The value of a is determined by the unpaired electron density in the spherically symmetrical s orbitals of the atom to which the nucleus belongs; B_1 is determined by unpaired electron density in the nonspherically symmetric atomic orbitals, in this case the p orbitals. These constants are computed with the VB wave function as outlined below for Kr_2F . The computation proceeds in much the same way for F_3^- .

The VB wave function for Kr_2F is a linear combination of neutral and ionic VB structures, i.e.,

$$\Psi(^2\Sigma_u) = \lambda \Psi(\text{Kr}^+ \text{F}^- \text{Kr}) + \sqrt{\frac{1-\lambda^2}{2}} \{ \Psi(\text{Kr}^+ \cdot \text{F}^- \text{Kr}) + \Psi(\text{Kr} \text{F}^- \text{Kr}^+ \cdot) \} \quad (1)$$

where $\lambda \approx 1$ is the charge distribution parameter and the dot denotes the location of the unpaired electron in a given VB structure. Electron correlation is included in this wave function by using different atomic orbitals for a neutral atom and the corresponding ion and by considering polarization effects.

Calculation of B_1 is relatively straightforward because the unpaired electron is primarily located in valence p orbitals of the noble gas cation Kr^+ and the halogen atom F^- . Accordingly, $B_{1,\text{Kr}}$ is approximately proportional to $(1 - \lambda^2)/2$, which is the weight factor of the ionic structure in Eq. 1, whereas $B_{1,\text{F}}$ is approximately proportional to λ^2 , which is the weight factor of the neutral VB structure ($\text{Kr} \text{F}^- \text{Kr}$). However, there is an additional contribution to both $B_{1,\text{Kr}}$ and $B_{1,\text{F}}$ from a cross term involving the neutral and ionic VB structures. This term, whose weight factor is

$$\sqrt{\frac{1-\lambda^2}{2}} S$$

(where S is an overlap integral with an order of magnitude of 0.1 to 0.2), is especially important to $B_{1,\text{Kr}}$ because the direct term proportional to $(1 - \lambda^2)/2$ is unusually small. Thus, λ can be determined from the experimental anisotropic hfc.

The origin of the isotropic hfc is more subtle since none of the VB structures in Eq. 1 provides unpaired electron density in the atomic s orbitals. The s-orbital density, and consequently the isotropic hfc, results from the following refinements:

1. *Overlap.* In the VB structure ($\text{Kr} \text{F}^- \text{Kr}$), a small amount of the unpaired electron density in the F pz orbital (i.e., a p directed along the molecular bond) is transferred to the terminal Kr s orbitals via the overlap of the F_{p_z} and Kr_s orbitals. However, since the F atom is at the inversion symmetry center of the $^2\Sigma_u$ molecule, the overlap contribution to the isotropic F hfc from the structures ($\text{Kr}^+ \cdot \text{F}^- \text{Kr}$) and ($\text{Kr} \text{F}^- \text{Kr}^+ \cdot$) must be zero.
2. *Polarization.* In the ionic VB structures ($\text{Kr}^+ \cdot \text{F}^- \text{Kr}$) and ($\text{Kr} \text{F}^- \text{Kr}^+ \cdot$), a spin-selective polarization of the open shell Kr^+ ion by the F^- anion contributes to the Kr isotropic hfc. This occurs because the polarization-induced distortion of those Kr s orbitals with the same spin as the Kr 4pz orbital must not give them any 4pz character (Pauli exclusion principle), whereas the polarization of the other Kr s orbitals is unrestricted, resulting in a partial unpairing of the Kr s orbitals. There are no polarizing coulomb interactions in the neutral VB

structure ($\text{Kr F} \cdot \text{Kr}$); however, the van der Waals interactions, which here are the polarization of the F atoms by the instantaneous dipole moments of the Kr atoms, have a similar effect, resulting in a contribution to the F isotropic hfc. In fact, even if there were coulomb polarizations in this structure as there are for the corresponding F_3^- VB structure ($\text{F}^- \cdot \text{F} \cdot \text{F}^-$), these one-electron interactions could not produce unpaired electron density in the s orbitals of an atom at the symmetry center of a ${}^2\Sigma_u$ molecule. The van der Waals interactions, being two-electron interactions between electrons on different atoms, do not suffer from this symmetry restriction. MO methods, even those refined by including configuration interaction, cannot account for the van der Waals type of electron correlations and, hence, erroneously predict very small isotropic hfc for atoms at the symmetry center of Σ_u and other highly symmetrical radicals.

3. *Overlap-Polarization* is a contribution to the isotropic hfc from a combination of the aforementioned overlap effect and the polarization of the closed shell s orbitals.
4. *Atomic hfc* is the isotropic hfc of the isolated $\text{Kr}^+ \cdot$ ion and the $\text{F} \cdot$ atom. The term results from spin-dependent two-electron interactions between the closed shell s orbitals and the unpaired electron in the valence p_z orbital. The atomic hfc is known from experiment for the halogen atoms, and the constant for $\text{Kr}^+ \cdot$ was extrapolated from the halogen values.

The results for both Kr_2F and F_3^- are given in Table 1 where they are compared with experimen-

tal results at values of bond distance, R , and charge parameter, χ , that give the closest fit. It is apparent that the theoretical values agree very well with experiment. Clearly, the ESR spectra for both Kr_2F and F_3^- are consistent with a ${}^2\Sigma_u$ ground electronic state if the wave function includes electron correlation.

The internuclear distance and charge distribution parameter for F_3^- suggest that this center is an interstitial atom, B , interacting with two lattice halogen ions, A and C , as depicted in Fig. 1. The dependencies of $a(A) = a(C)$ and $a(B)$ on R and χ are illustrated in Fig. 2. As expected, the isotropic hfc decreases rapidly with R . The conclusion that F_3^- is primarily an interstitial atom in LiF is of significance since it has long been sought as the natural partner of the F-center (electron at a negative ion vacancy).

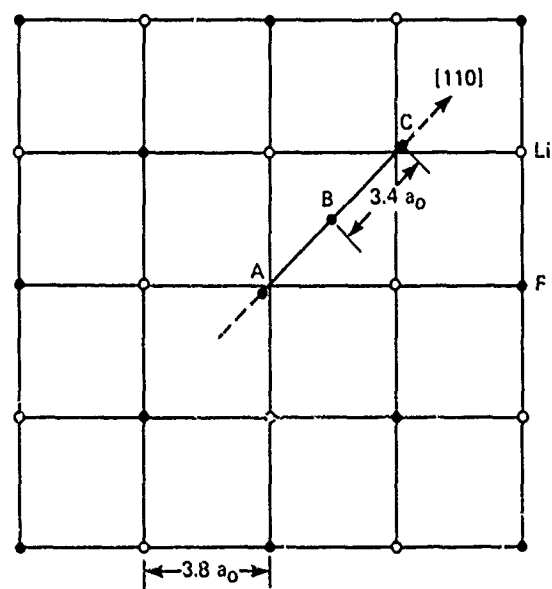


Fig. 1 Plane of the LiF lattice containing the interstitial halogen atom.

TABLE I
COMPARISON OF COMPUTED HYPERFINE CONSTANTS (MHz)
OF Kr_2F AND F_3^- WITH EXPERIMENTAL VALUES

Molecule	$R(a_0)$	χ	Nucleus	$a^{(\text{Th})}$	$a^{(\text{Exp})}$	$B_{\text{H}}^{(\text{Th})}$	$B_{\text{H}}^{(\text{Exp})}$
Kr_2F	4.88	0.96	${}^{81}\text{Kr}$	20.9	20.3	25.1	26.8
			F	407.0	472.7	2816.0	2927.5
F_3^-	3.40	0.91	$\text{F}_{\text{lattice}}$	530	560	506	498
			$\text{F}_{\text{interstitial}}$	612	599	2599	2543

Note: Th = theory, Exp = experimental

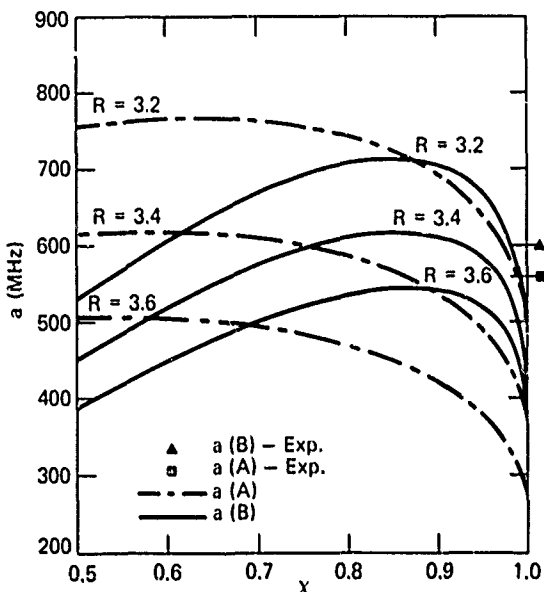


Fig. 2 Isotropic hyperfine constants for F_3^+ in LiF (A is lattice ion, B is interstitial atom).

REFERENCES

1. F. J. Adrian and A. N. Jette, "Valence Bond Study of Hyperfine Interactions and Structure of Kr_2F^+ ," *Chem. Phys. Lett.* **64**, No. 3, 1979, pp. 555-559.
2. A. N. Jette and F. J. Adrian, "Identification of the V_1 -Center (F_3^+) in LiF as an Interstitial F Atom," *Phys. Rev. Lett.* **43**, No. 15, 1979, pp. 1119-1123.
3. A. R. Boate, J. R. Morton, and K. I. Preston, "ESR Spectrum of Kr_2F^+ ," *Chem. Phys. Lett.* **54**, No. 3, 1978, pp. 579-581.
4. M. H. Cohen, W. Kanzig, and T. O. Woodruff, "The Hyperfine Structure of the V_1 -Center," *J. Phys. Chem. Solids* **11**, 1959, pp.120-130.

Authors: F. J. Adrian and A. N. Jette

Support: Indirectly Funded R&D

THEORY OF CHEMICALLY INDUCED MAGNETIC POLARIZATION: EFFECT OF S - T₋ MIXING IN STRONG MAGNETIC FIELDS

Free radical reactions in liquids often yield magnetically polarized products and reactants. Detailed knowledge of the polarization mechanisms enables important mechanistic information to be extracted from the observed nuclear and electron spin polarizations. (Qualitatively, intramolecular magnetic interactions promote reactions of a radical pair by aligning their electron spins in the antiparallel configuration required for bond formation.)

Recently an integral equation method has been used to investigate the mixing of the reactive singlet state, S, of a radical pair with the lowest sublevel of their unreactive triplet state, T₋, as the diffusion of the molecules carries them through the separation where the levels cross (Ref. 1). It is found that this process contributes to the nuclear spin polarization of the radical pair reaction products and to the electron spin polarization of the unreacted radicals in two cases. (a) when at least one component of the pair has a large electron-nuclear magnetic hyperfine in-

teraction, which provides rapid S-T₋ mixing; and (b) in reactions involving large radicals and or viscous solutions where slow diffusion through the level crossing region provides a long S-T₋ mixing interval.

BACKGROUND

The essence of the radical pair mechanism of chemically induced magnetic polarization is that the magnetic hyperfine structure (hfs) interactions between the nuclei and the unpaired electron of each radical can convert a radical pair initially in an unreactive triplet electron spin state to a reactive singlet state, and vice versa (Ref. 2). Nuclear spin states that are most efficient in effecting this conversion are favored in the reaction products, in an external magnetic field, this results in a nuclear spin polar-

ization that is readily observed by nuclear magnetic resonance spectroscopy. The process also yields electron spin polarization of the unreacted radicals, the two phenomena being known as chemically induced nuclear/electron polarization, or CIDNP/CIDEP.

As shown in Fig. 1, the valence interaction, $J(r)$, that is responsible for the respective bonding and antibonding natures of the singlet and triplet states of the pair is a short-range function of the inter-radical separation, r . The triplet state is split into three components by the external magnetic field. Most CIDNP/CIDEP results from mixing of the singlet and the center (nonmagnetic) triplet sublevel, T_0 , because those levels are degenerate over a range of r beginning at a few molecular diameters and extending to infinite separation. $S-T_0$ mixing can occur over this entire range, whereas $S-T_{\pm}$ mixing is restricted to the level crossing region (Ref. 2). Nevertheless, an investigation of CIDNP/CIDEP contributions from $S-T_{\pm}$ mixing was deemed desirable, partly because of the intrinsic interest and importance of level crossing processes in chemical dynamics, but especially because experimental work done elsewhere indicated that $S-T_{\pm}$ mixing could contribute to the observed polarizations in cases involving either a large hfs interaction and consequent rapid $S-T_{\pm}$ mixing (this is realized in the important case where one component of the radical pair is a hydrogen atom) or slow diffusion through the level crossing region.

DISCUSSION

The interactions involved in the radical pair mechanism are described in the following Hamiltonian (Ref. 2):

$$\begin{aligned} \mathcal{H}(r) = & -J(r) (\frac{1}{2} + 2S_1 \cdot S_2) \\ & + \mu_B (g_1 S_1 \cdot H + g_2 S_2 \cdot H) \\ & + A_1 I_1 \cdot S_1 + A_2 I_2 \cdot S_2 \end{aligned} \quad (1)$$

The first term is the spin-dependent valence interaction, where S_1 and S_2 are the spins of the two radicals. The remaining terms are (a) the Zeeman interaction of the electron magnetic moments, $\mu_B g_1 S_1$ and $\mu_B g_2 S_2$, with the external magnetic field, H , and (b) the electron-nuclear hyperfine interactions where I_1 and I_2 are nuclear spins on radicals 1 and 2 and A_1 and A_2 are the corresponding hyperfine constants. The hfs interactions are weak compared with the exchange and Zeeman interactions and thus can mix the electron spin states only at separations where the latter interactions are zero, as in the $S-T_0$ case, or cancel each other, as in the $S-T_{\pm}$ level crossing case depicted in Fig. 1.

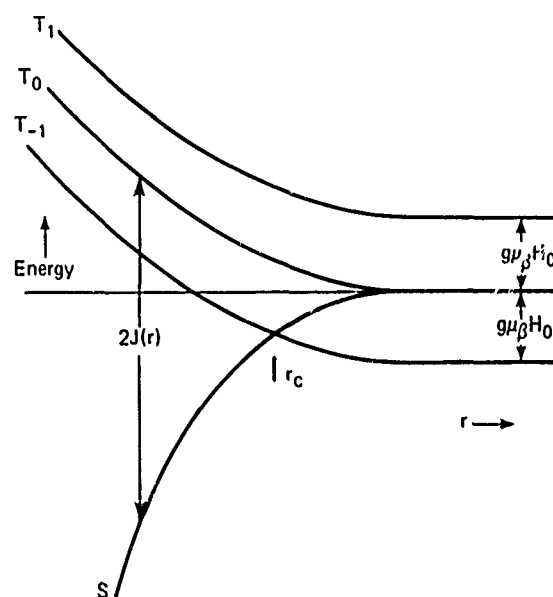


Fig. 1 Singlet and triplet energy levels of a radical pair in an external magnetic field as a function of separation.

Diffusion of the radicals in the liquid phase reaction mixture obviously plays an important role in the radical pair mechanism. The quantitative treatment of diffusion is difficult because it requires solving the time-dependent Schrödinger equation for the radical-pair spin function, with $J(r)$ a random function of time because of the diffusive motion. Previous treatments of the $S-T_{\pm}$ mixing case have either been highly approximate or required numerical solution and, except for one extremely limited calculation, have been restricted to the weak magnetic field case.

The time-dependent Schrödinger equation for $S-T_{\pm}$ mixing is $\mathcal{H}(r(t))\psi_{RP} = i\partial\psi_{RP}/\partial t$, where \mathcal{H} is given by Eq. 1 and where $\psi_{RP} = C_S(t)|S\rangle + C_{T_{\pm}}(t)|T_{\pm}\rangle$. Instead of dealing directly with the wave function coefficients C_S and $C_{T_{\pm}}$, which are complex quantities, it is convenient to consider the 2×2 density matrix ρ formed from the Hermitian product of the coefficients as follows: $\rho_{ij}(t) = C_i C_j^*$. The Schrödinger equation for ρ is $\mathcal{H}\rho - \rho\mathcal{H} = i\partial\rho/\partial t$.

$$\begin{aligned} \frac{d\rho_i}{dt} &= \Omega(r) \times \rho_i; \\ \rho_i &= \begin{pmatrix} \rho_1 \\ \rho_2 \end{pmatrix}; \\ \Omega(r) &= \begin{pmatrix} a = A_1/\sqrt{2} \text{ or } A_2/\sqrt{2} \\ 0 \\ J(r) - \frac{1}{2}\mu_B(g_1 + g_2)H \end{pmatrix}. \end{aligned} \quad (2)$$

This equation is simplified and its physical significance revealed by transforming ρ as follows: $\rho_0 = \rho_{SS} + \rho_{T-T}$, $\rho_z = \rho_{SS} - \rho_{T-T}$, $\rho_x = \rho_{ST} + \rho_{TS}$, and $\rho_y = -i(\rho_{ST} - \rho_{TS})$, where the transformed components of ρ are all real (Refs. 1 and 3). Because the radical pair is always a singlet, a triplet, or some combination of these states, $\rho_0 = 1$. The relative amounts of singlet and triplet character are given by ρ_z ; in particular, if the state was initially a pure singlet [$\rho_z(0) = 1$], then $\rho_z(0) - \rho_z(t)$ gives the amount of triplet mixing that has occurred by time t . In the absence of diffusion, the time evolution of the transformed density matrix is given by the simple vector equation:

According to Eq. 2, the rate of change of ρ_i at any time is a rotation of magnitude Ω about an axis in the direction of Ω . For an initial singlet-state radical pair, the development of polarization via $S-T$ mixing corresponds to rotation of the vector ρ_i away from its initial state: $\rho_z(0) = 1$, $\rho_x(0) = 0$, $\rho_y(0) = 0$. (Similar considerations apply to the initial triplet case when $\rho_z(0) = -1$.) However, when the radicals are close together (as they are initially), $J(r) \gg \frac{1}{2}\mu_B(g_1 + g_2)H \gg a$. When they are far apart, $J(r) = 0$ and $\frac{1}{2}\mu_B(g_1 + g_2)H \gg a$ for the large H case. In each case depicted in Figs. 2a and 2c, respectively, Ω is nearly parallel or antiparallel to the z axis, and the rotation of ρ_i about Ω does not change ρ_z . However, in the level crossing region, $J(r) \approx \frac{1}{2}\mu_B(g_1 + g_2)H$ and $\Omega = a$ is directed along the negative x axis. Then, rotation of ρ_i about Ω changes ρ_z from its initial value of unity, leading to $S-T$ mixing and magnetic polarization. Unless the hfs interaction is very large or the radicals diffuse very slowly, the $S-T$ mixing and polarization will be small, because the rapid variation of $J(r)$ with r severely limits the extent of the crossing region, making it unlikely that the radicals will remain in the crossing region for the time of order $1/a = 10^8$ to 10^9 s as is required for an appreciable rotation of ρ_i about the x axis. This level crossing case is depicted in Fig. 2b.

The problem is treated quantitatively by adding a diffusion term to Eq. 2, obtaining

$$\frac{\partial \rho_i(r,t)}{\partial t} = D \frac{\partial^2 \rho_i(r,t)}{\partial r^2} + \Omega(r) \times \rho_i(r,t). \quad (3)$$

Since we are interested in the polarization in the long time limit ($t \rightarrow \infty$), the time dependence can be eliminated from Eq. 3 by taking the Laplace transform and using the theorem $\lim_{s \rightarrow 0} s \rho'_i(s) = \lim_{t \rightarrow \infty} \rho_i(t)$,

where ρ'_i is the Laplace transform of ρ_i . The system of three coupled differential equations described by Eq. 3 can be transformed, using Green functions, into a single integral equation for the polarization ρ_z (Refs. 1 and 3). For the case of an exponentially decaying valence interaction (i.e., $J(r) = J_0 e^{-\lambda r}$), the required Green functions can be expressed as Bessel functions of complex order and argument (Ref. 1). Since the deviation of $|\rho_z|$ from its original value of unity is small, the integral equation can be solved by expansion in a Neumann series. In the original paper (Ref. 1) the resulting expression for the polarization was a complicated series that had to be evaluated numerically, but very recently this series has been evaluated analytically to obtain a simple expression for the polarization.

$$P = \frac{\pi A^2}{2\mu_B(g_1 + g_2)H} \frac{r_c}{\lambda D}, \quad (4)$$

where r_c is the level crossing separation and all other quantities have been defined previously.

Clearly, the $S-T$ mixing occurs in the level crossing region and is favored by rapid singlet-triplet mixing (large A) and slow diffusion through the level crossing (large $r_c/\lambda D$). The theory agrees well with experiment if the range of the exponentially decaying exchange interaction (given by $1/\lambda$) is of the order of two to eight molecular diameters, thus providing a crude but useful estimate of this chemically important quantity.

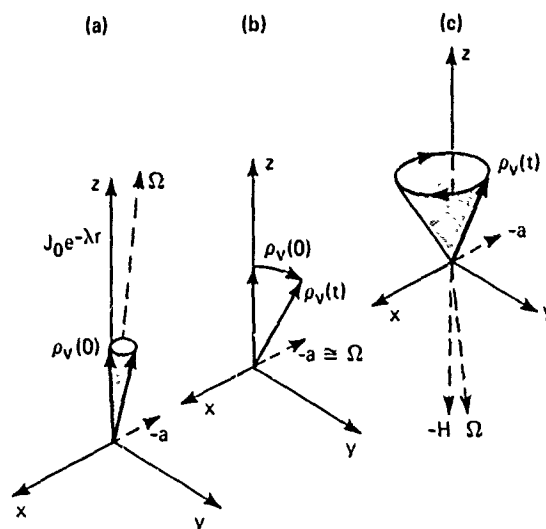


Fig. 2 Vector model of $S-T$ mixing. (a) Large valence interaction when radicals are close together inhibits singlet-triplet mixing. (b) Valence and Zeeman interactions cancel in the $S-T$ level crossing region, enabling singlet-triplet mixing. (c) Large Zeeman interaction when radicals are widely separated inhibits singlet-triplet mixing. Here $J(r) = J_0 e^{-\lambda r}$ and $H = \frac{1}{2}\mu_B(g_1 + g_2)H$.

REFERENCES

1. F. J. Adrian and L. Monchick, "Theory of Chemically Induced Magnetic Polarization. Effects of $S, T_{\pm 1}$ Mixing in Strong Magnetic Fields," *J. Chem. Phys.*, 15 Sep 1979, p. 2600.
2. F. J. Adrian, "Radical Pair Mechanism of Chemically Induced Magnetic Polarization," *Chemically Induced Magnetic Polarization - Theory, Technique and Applications*, L. T. Muys et al. (eds.), Ch. 5, D. Reidel, Boston, 1977.
3. L. Monchick and F. J. Adrian, "On the Theory of Chemically

Induced Electron Polarization (CIDEP): Vector Model and an Asymptotic Solution," *J. Chem. Phys.*, 15 May 1978, p. 4376.

Authors: F. J. Adrian and L. Monchick

Support: Indirectly Funded R&D

ISING MODEL OF PHASE TRANSITIONS

Study of the nearest-neighbor Ising model has been particularly rewarding for deducing the behavior of phase transitions in the immediate vicinity of their critical points. Although certain universality principles show that such critical point behavior is insensitive to possible higher-neighbor interactions, there are no general principles that can be used to deduce behavior away from the critical points. In a collaborative program with Professor Paul Meijer of the Catholic University of America, we have examined the influence of the interaction potential on the phase diagram for higher-neighbor Ising systems.

BACKGROUND

Phase transitions are some of the most common and obvious phenomena in nature. They occur in such diverse systems as ferromagnets, binary alloys, gases, and polymeric solutions. At absolute zero temperature, these systems exist in a perfectly ordered state (e.g., the spin axes of the ferromagnet are aligned parallel to one another); above a critical temperature they exist in a disordered state (e.g., the axes are oriented randomly). The thermodynamic behavior of the systems near their critical points is remarkably similar, and this fact has stimulated theoretical studies of the Ising model in which the systems are equivalent.

The simple nearest-neighbor Ising model of a spin-one-half ferromagnet considers a crystalline lattice that is occupied by magnetic molecules whose energy of interaction is $-JS_i^{(i)}S_j^{(j)}$ if i and j are nearest neighbors and is zero otherwise. Here, $-J$ is the strength of interaction; $S_i^{(i)}$ is the normalized

z -component of spin in the i th lattice site and takes the values ± 1 . The model has been surprisingly successful in describing behavior near the critical point, but obvious deviations are observed away from the critical region.

Certain universality principles predict that critical point behavior should be insensitive to possible higher-neighbor interactions; however, there are no general principles to predict the influence of the interaction potential on behavior outside this critical region. Since the three-dimensional Ising model has not been solved, we developed 'trial-like series expansions (Ref. 1) for higher-neighbor Ising models (i.e., allowing interactions among more distant neighbor molecules) on the face-centered-cubic lattice. Analysis of these series shows that for a given interatomic potential, thermodynamic behavior is determined primarily by the effective number of neighbors of the potential and is more or less independent of the detailed shape of the potential.

DISCUSSION

Diagrammatic techniques have proven extremely beneficial in developing series expansions for the thermodynamic properties of Ising models. A convenient expression for the Helmholtz free energy of the Ising model of the gas-liquid transition is given in Fig. 1 to terms exact through sixth order in inverse temperature. There, β is the usual temperature factor $(k_B T)^{-1}$, L is the number of lattice sites, and ρ is the density of the lattice gas (fraction of lattice sites that are occupied). We have evaluated the diagrams for a

selected so as to mimic various model potentials. The specific models are: Sutherland inverse-cubic (S3) and inverse-sixth-power (S6) potentials, a modified equal-strength (MVW) potential, and a modified Sutherland inverse-sixth-power (MS6) potential. The values of J_i for the models are given in Fig. 2. The modified potentials attempt to account for the fact that the number of i th-neighbor sites on the face-centered-cubic lattice is not proportional to the square of the i th-neighbor separation distance, as it would be in continuum models.

Setting the largest J equal to unity allows us to interpret $q \equiv \sum_i Z_i J_i$ as an effective number of nearest neighbors. The transition line curves in Fig. 2 can be ordered according to the effective number of nearest neighbors, which is infinite for the molecular field (MF)

model and is ≈ 13.8 for S6. We have examined many other model potentials. In all but one, the transition curve is determined primarily by the value of q and is more or less independent of the shape of the potential.

REFERENCE

1. R. A. Farrell, S. Favin, J. T. Sullivan, S. Vimolvanich, and P. H. E. Meijer, "Coexistence Curves for Four-Neighbor Ising Models on the Face-Centered-Cubic Lattice," *Phys. Rev. B* **19**, 1979, p. 4703.

Authors: R. A. Farrell and S. Favin (APL)
and J. T. Sullivan, S. Vimolvanich, and P.
H. E. Meijer (Catholic University)

Support: NAVSEASYSOCOM and Office of Naval
Research

THEORY OF VISION

A comprehensive theory of visual sensation was developed from accepted basic principles of human vision into a mathematical form suitable for quantitative investigations. The theory was then elaborated by vector-functional analysis of a variety of visual phenomena, yielding interpretations of old experiments and predictions of new observations.

BACKGROUND

Human vision is built up from elemental sensations (viz., color and brightness variations in time and space), which thus lie at the base of all visual experience. There has been extensive study of achromatic brightness variations and of essentially invariant color sensations. But little attention has been devoted to full chromatic spatial-temporal variations. Toward a unified analysis of the various aspects of vision, we have formulated a comprehensive theory of visual sensation based on the Helmholtz and Hering principles of vision.

The theory is in mathematical form, in which the brightness-color sensation elements constitute a

vector space-time function. Thus, existing achromatic brightness and invariant color studies are seen as the special cases of scalar field and constant vector aspects of the theory, respectively. The visual sensation vector was related through a physiological visual system operator back to photoreceptor quantum absorptions. A vector functional analysis of the light-to-sensation transmutation then provided a unified quantitative theory for application to a variety of visual experiments. The theory elucidates existing brightness-contrast studies and standard color models, provides color vision generalizations of classic space-time brightness laws, analyzes wavelength-pulse and color-flicker experiments, and yields an understanding of heterochromatic luminance additivity for flicker and border observations.

DISCUSSION

Briefly, the theory separates visual sensation into components of color and brightness as functions of space and time. Brightness refers to the magnitude of the visual sensation, while color may be reduced to

the Hering color-opponent pairs, "red" versus "green" and "blue" versus "yellow," and the relative proportion of "white" in a sensation. Thus, we describe visual sensation by a three-dimensional space (Fig. 1): a tritanopic (T) axis represents redness versus greenness, a deuteranopic (D) axis represents blueness versus yellowness, and an achromatic (A) semiaxis represents whiteness (with black located at the origin). In this geometry, the visual sensation is represented by the vector \bar{V} ; components V_A, V_T, V_D completely describe the color and brightness attributes of sensation. Each vector component is a function of sensory time and space:

$$V_s(t', x', y') \quad (s = A, T, D) \quad (1)$$

Ultimately, these functions underlie sensations of location, form, movement, and change.

To study the space-time sensory field function (1), we consider a varying light stimulation of spectral distribution $P\lambda(t, x, y)$ at retinal position x, y at time t . By Helmholtzian photoabsorption in cones (R, G, B) and rods (S), this illumination is transformed into a four-vector of effective quantum absorptions.

$$Q_a(t, x, y) = \int_0^\infty d\lambda P_\lambda(t, x, y) a_\lambda(t, x, y) \quad (a = R, G, B, S) \quad (2)$$

where a_λ represents the R, G, B, S spectral sensitivities. The quantum absorptions, Q_a , initiate the subsequent physiological operations of the visual system (denoted generically as the spatio-temporal vector operator, $\Phi\{\dots\}$) that transmute the Helmholtzian vector, \mathbf{Q} , into the Heringian sensory vector, \mathbf{V} . Thus, the sensation-light field relationship is written in component form as

$$V_s(t', x', y') = \Phi_s\{Q_a(t, x, y)\} \quad (s = A, T, D; a = R, G, B, S) \quad (3)$$

Among other operations in the Helmholtz-Hering transmutation, the $\Phi_s\{Q_a\}$ represent the space-time dynamics with which this theory is largely concerned.

As an example of the application of the theory, consider minimally distinct border (MDB) observations. The MDB technique requires the observer to minimize the "distinctness" of the border separating differently colored half-fields by adjusting the intensities of one or both halves. To the extent that the MDB judgment is independent of the color differences between the two half-fields, and from evidence that has been adduced, we assume that the MDB depends mainly on the achromatic sensation component, V_A . The stimulus field in the MDB ex-

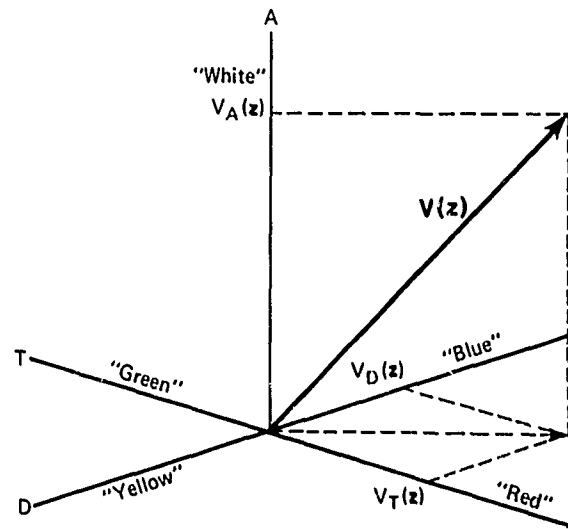


Fig. 1 Geometric representation of visual sensation, \bar{V} , in the three orthogonal dimensions (A, T, D). Brightness is given by the magnitude, \bar{V} , and color by the relative components V_A, V_T, V_D . All are functions of the sensory space-time coordinates $\bar{z} \equiv t', x', y'$.

periment may be regarded as a step function in x . The observer presumably attends to a neighborhood about the border. Consequently, the high-frequency portion of the Fourier expansion of the stimulus step determines the distinctness of the border. We can linearize $V_A(x')$ in the latter fine-scale variation in the form $V_A(x') = V_A^0(x') + \Delta V_A(x')$, where $V_A^0(x')$ is the nonlinear result of low spatial frequency components and $\Delta V_A(x')$ is the linear high-frequency part of the sensation. $V_A^0(x')$ can be thought of as a blurred approximation to the step response $V_A(x')$, shown schematically in Fig. 2a, and $\Delta V_A(x')$ is the difference between $V_A(x')$ and $V_A^0(x')$ (see Fig. 2B). Border distinctness then may be defined as the change in $\Delta V_A(x')$ across the border, i.e., $\partial \Delta V_A(x') / \partial x'$ in Fig. 2c.

From Eq. 3 we can write

$$\Delta V_A(x') = \sum_a \left[\int_{-\infty}^{\infty} dx \mathcal{F}_{Aa}(x', x) H(x) \right] \Delta Q_a \quad (4)$$

in terms of the Green's function matrix \mathcal{F}_{sa} representing the linearized operator in Eq. 3 (viz., $\delta \Phi_s / \delta Q_a$), where $H(x)$ denotes the high frequency part of the Fourier expansion of the unit step function and ΔQ_a is the difference between photoreceptor absorptions resulting from test and from comparison stimuli. This leads to a set of equations for luminance matches for which the MDB operation may be represented as $\partial \Delta V_A(x') / \partial x' = 0$. Since ΔQ_a enters

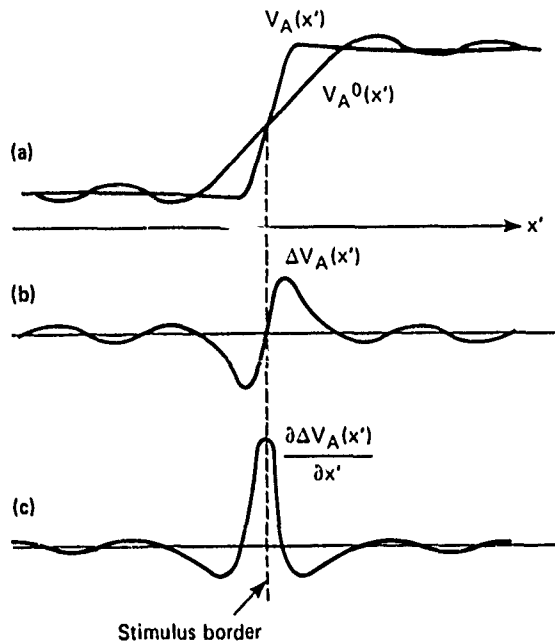


Fig. 2 Schematic of achromatic sensation component, V_A , versus sensory coordinate, x' , in minimal border experiments.

only as multiplicative factors in Eq. 4, this yields Abney's law of scalar additivity for heterochromatic MDB observations, which is in agreement with experiment.

As illustrated by a number of other applications in Ref. 1, the theory furnishes a rigorous mathematical base for unified analysis of experimental approaches to varied aspects of visual sensation. Thus the theory contributes to a quantitative comprehension of the sensory elements underlying human visual experience — a comprehension that is essential in many research and practical contexts.

REFERENCES

1. J. I. Bird and R. W. Massot, "A General Zone Theory of Color and Brightness Vision. II. The Space-Time Field," *J. Opt. Soc. Am.*, 68, No. 11, 1978, pp. 1471-1481.
2. R. W. Massot and J. I. Bird, "A General Zone Theory of Color and Brightness Vision. I. Basic Formulation," *J. Opt. Soc. Am.*, 68, No. 11, 1978, pp. 1465-1471.

Author: J. F. Bird

Support: Indirectly Funded R&D

URBAN TECHNOLOGY

INTRODUCTION

The recognition that great cities continue to play a key role in maintaining the nation's vitality has spurred renewed interest in the institutional structures that support urban life. Through a variety of special projects, APL has participated in and contributed to programs for developing and applying modern technology to a variety of civilian problems directly relevant to current urban issues. The programs have included transportation, fire research, flight aircraft safety studies, the siting of power plant facilities near urban centers, health care delivery systems, and, more recently, the location of leaks in buried natural-gas distribution lines. While not all of these program areas are included here, several are brought together in an effort to provide a unifying perspective on their scope and their relationship to urban life.

Public transportation facilities in the United States have become severely limited in recent decades as a result of the dispersed travel patterns characteristic of our urban areas, the inability of public transportation to compete with the automobile in convenience and travel time, and sharply rising labor costs. However, because of the need to provide an alternative to the automobile, there has been increasing interest in the development of fully automated transit systems that eventually may be able to provide a high level of service to an entire metropolitan region.

Since 1969, APL has conducted major programs to improve transportation in our urban centers. The efforts have included research and development directed at determining the requirements and constraints of an automated control system, various approaches to solving the control problem, and technical assistance to public agencies in the conduct of their automated transit system programs. The Laboratory has been investigating the requirements imposed on an automated control system as the headway (i.e., the spacing between vehicles) is reduced. The first article discusses the hardware requirements and the control law pertinent to the implementation of a vehicle-follower system.

The APL Fire Program deals with four major areas related to fire: combustion research, fire casualties analysis, fire operations assessment, and technical information transfer both within the fire community and between the fire community and the public. The effort is interdisciplinary and includes collaboration with the School of Hygiene and Public Health of The Johns Hopkins University and with fire and health agencies of the State of Maryland. The program addresses four questions: (1) What are the physical causes and medical consequences of fires that lead to fatalities or injuries? (2) What useful devices or practices can be designed for the fire service or the population at large? (3) What are the information needs of the fire field, and how can they be strengthened? (4) What chemical factors control the ignition and extinction of flames?

The second article in this section reports on efforts to relate the demographic data on fire victims with the causes of fire starts and their medical consequences and thus to arrive at conclusions about more effective preventive measures. The next article reports on measurements of flammable gases evolving from a burning, char-forming plastic. Better understanding of the chemistry involved in the ignition, fire spread, and extinction behavior of plastics may lead to better chemical means to inhibit and extinguish unwanted fires.

The last article in this section discusses the development of a unique remote sensing technique for studying air motion and diffusion. Using environmentally safe microscopic fluorescent particles as tracers and a lidar system as the remote sensor, it permits the detection of atmospheric tracers in much smaller quantities than was previously possible. The technique should aid future studies of stack plumes, especially near urban centers where the environmental background limits study to the immediate vicinity of the stack when more conventional techniques are used.

IMPLEMENTATION OF A VEHICLE-FOLLOWER CONTROL LAW FOR SHORT-HEADWAY AGT SYSTEMS

The implementation of a vehicle-follower control law for short-headway Automated Guideway Transit (AGT) Systems has been examined in terms of required sensor accuracy, controller structure, and data transmission requirements. For the first time in any automated transit study, an analysis has been performed to select data rate, allowable time delay, and controller gain to assure string stability and acceptable dynamic response.

BACKGROUND

AGT systems represent a new class of urban transport in which automatically controlled vehicles operate on dedicated guideway networks. At the short headways necessary for adequate capacity, intervehicle spacings and velocities must be regulated accurately to assure safe and reliable operation. For this purpose, two basic approaches have been suggested for the longitudinal control of vehicles. One, point following, assigns each vehicle to a moving cell, the cells being propagated along the guideway network at predetermined velocities and spacings. The other, vehicle following, which is specifically considered in this task, allows communication between successive vehicles so that the motion of a vehicle is controlled in accordance with the motion of its immediate predecessor.

The stringent requirements for short-headway systems are a challenging problem in the application of modern control system engineering. Previous analyses and simulations have shown that the approach discussed in Ref. 1 satisfies the requirements imposed on the controller. The current task is directed at evaluating practical considerations for the required computation and communications hardware.

DISCUSSION

Four fundamental elements constitute the implementation of a vehicle-following or a point-following strategy:

1. Design of a basic control law,
2. Design of the controller structure,
3. Determination of sensor accuracy requirements, and
4. Selection of system parameters.

These elements are discussed below, in turn, with emphasis on the vehicle-follower approach.

The coupling of vehicles under the vehicle-following strategy can cause abrupt maneuvers unless

provision is made for anticipating sudden motions (Ref. 2). In addition, a "kinematic constraint," imposed by ride quality limits on vehicle acceleration and jerk, must be satisfied. The difficulties encountered in controlling a vehicle subject to the kinematic constraint have been resolved by a controller that is a nonlinear function of states (Ref. 1). The controller thus provides a baseline system that can be used in a study of implementation techniques.

The design of the controller structure involves questions concerning the distribution of control computation between on-board and wayside devices, the type of information exchanged between the wayside and the vehicle, and the rate of information exchange. Many implementations lead to a hierarchical control structure under which a wayside control device has jurisdiction over a string of vehicles on a section of guideway. As a result, the question of control distribution is whether control loops should be closed on board the vehicle or through the wayside computer. In general, the former approach may be loosely classified as providing a "smart" vehicle, while the latter approach yields a "dumb" vehicle, although many intermediates exist.

Time lags, computation rates, noise resulting from digital/analog interfaces, and word lengths are practical problems that also affect system performance. Thus a fundamental consideration in implementing a control law is the trade-off between hardware requirements and system response. In particular, at short headways communication costs may be significant because of the large number of vehicles that must be closely regulated on a section of guideway. Consequently, it is beneficial to minimize the data rate to each vehicle without impairing the ride quality as specified by jerk and acceleration limits.

Preliminary studies (Ref. 3) of the implementation of a nonlinear vehicle follower control law (Ref. 1) for short-headway operation demonstrated the advantages of a smart vehicle in terms of the data sample rate from wayside to vehicle and the resulting system response. Furthermore, the number of bits required for information transmission and on-board computation were determined in conjunction with the corresponding sample rates. However, that study did not consider alternative controller configurations that may reduce the required data rates. That is, certain information may be combined at wayside rather than on the vehicle, resulting in fewer bits being needed to represent the transmitted information. Using this ap-

proach, the four configurations investigated by computer simulation have been shown to reduce the required data rate between vehicle and wayside.

Another aspect of implementation that affects overall system cost is the sensor accuracy requirements. There are many techniques for measuring vehicle states directly or indirectly. In a vehicle-following strategy, it seems most appropriate for each vehicle to measure directly the states of the immediately preceding vehicle (by microwave, laser, and acoustic methods). However, such schemes have not been successful technically and create operating problems in the event of failure. Thus, the simplest system would be one in which vehicle position is determined by markers in the guideway. As a vehicle passes over each marker, the event is recorded by the vehicle itself or by the wayside. Because of failure considerations, wayside monitoring of vehicle position probably will be the more attractive. This study investigated the accuracy of position and velocity estimates using a position measurement that is sampled and corrupted by additive noise. No further constraining assumptions are made; therefore, the results should be applicable to any system that uses a position measurement scheme.

The specification of system parameters combines the three aspects of system implementation previously described. Data rates, computation rates, quantization levels, and allowable time delays must be determined for a given control law, controller configuration, and sensor accuracy so that satisfactory vehicle performance is assured. Moreover, the overriding factor in specifying system parameters, particularly uplink rate and delay, is string stability. Analyses and simulations are used to select controller gains to maximize the overall allowable delay while maintaining acceptable dynamic response.

The general system configuration considered in this study is illustrated in Fig. 1. It is assumed that the vehicle position is known with some accuracy at intervals of T_D seconds. For example, as is shown in the figure, the vehicle is known to be between two guideway position markers at any time. A dynamic estimator uses these position measurements to estimate vehicle velocity and position. A wayside control computation is then performed and an uplink command is transmitted to the vehicle at intervals of T_U seconds. The on-board control logic uses the uplink command to transmit the velocity command, v_c , to the vehicle propulsion system.

RESULTS OF INVESTIGATION

The problem of determining sensor accuracy requirements at headways of 0.5 and 3.0 s was approached analytically via a suboptimal Kalman filter

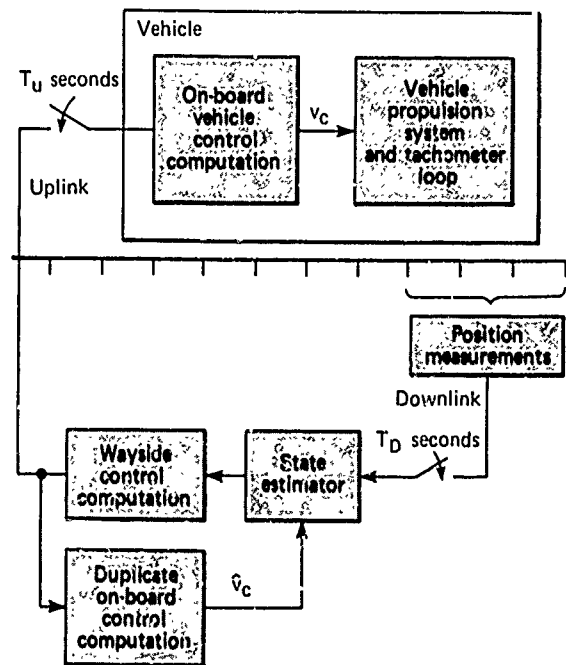


Fig. 1 General system control structure.

design, in which it is assumed that vehicle velocity and position are estimated using sampled position measurements corrupted by noise. The results of this work are summarized in Ref. 4; details are given in Ref. 5.

Continuing studies have been made of the performance of this estimator in the presence of a force disturbance such as wind gusts or a grade. The controller response is essentially unaffected when estimator states rather than actual states are used. However, the estimator is sensitive to a mismatch between an on-board velocity command and the velocity command calculated at wayside as an input to the estimator.

To alleviate estimator errors resulting from mismatch and to improve transient response, several designs were considered. The analytic approach is to locate estimator poles on the basis of noise sources but constrain the poles to be within a certain region of the z -plane (for the discrete filter). This significantly reduces estimator errors resulting from mismatch although more accurate position measurements are still required (Ref. 5).

The other area of investigation was the selection of controller configurations for headways of 0.5 and 3.0 s. The basic control law (Refs. 1 and 5) requires the calculation of the error between vehicle spacing and a kinematically required spacing. The error is given by

$$\epsilon = S + (5.3 - h)(v_p - v_t) + 0.33v_t(v_p - v_t)$$

where S is vehicle spacing, h is the desired headway, and v_p and v_t are the preceding and trailing vehicle velocities, respectively. The 5.3 and 0.33 gains are determined from an assumed jerk limit of 2.0 m/s^3 and an acceleration limit of 1.5 m/s^2 . A feed-forward derivative, $u = (1/k)\dot{\epsilon}$ is used for control, where k is controller gain.

The configuration recommended for implementation at a 3.0 s headway is one where ϵ is calculated by the wayside computer and uplinked at 0.5 s intervals, using 8 bits to represent the information. At a headway of 0.5 s, the wayside forms the sum of u and ϵ and uplinks this sum at 0.1 s intervals, using 8 bits. On board the vehicle, the sum is separated into u and ϵ by passing through a first-order filter. Finally the basic control law (Ref. 1) is modified to incorporate either constant headway or constant k -factor with a corresponding reduction in velocity-error gain.

This modification reduces the control bandwidth, thereby relaxing the data rate and time delay requirements. In addition, the vehicle is allowed to operate closer to the preceding vehicle without violating the kinematic constraint.

REFERENCES

1. A. J. Pue, "A State-Constrained Approach to Vehicle-Follower Control for Short Headway Automated Transit System," *J. Dyn. Syst. Meas. Control* **100**, No. 4, Dec 1978, pp. 291-297.
2. H. Y. Chiu, G. B. Stupp, and S. J. Brown, "Vehicle Follower Control with Variable Gains for Short Headway Automated Gueway Systems," *J. Dyn. Syst. Meas. Control* **99**, No. 3, Sep 1977, pp. 183-189.
3. A. J. Pue, "Implementation Trade-offs for a Short Headway Vehicle-Follower Automated Transit System," *IEEE Trans Veh Technol.* **VF-28**, No. 1, Feb 1979, pp. 46-55.
4. A. J. Pue, "Sensor Accuracy Requirements for a Short-Headway Automated Transit System," *Developments in Science and Technology*, JHU/APL DST-6, Fiscal Year 1978.
5. A. J. Pue, *Control Law Implementation for Short Headway Vehicle-Follower AGT Systems*, JHU APL CP 075, TPR 045 (in press).

Author: A. J. Pue

Support: DOT, Urban Mass Transit Administration

HUMAN FATALITIES FROM UNWANTED FIRES

To reduce fire fatalities substantially requires that the causes of the fatalities be understood and that the links in the chain of events that leads to death be established.

Few previous investigations have gone beyond the limited information contained in "vital statistics." The purpose of this study was to tie together more closely the demographic data on fire victims with the medical consequences and with the causes of fires, and to draw conclusions about preventive measures and better medical treatment for survivors. The study is based on data from the State of Maryland for "rapid" fire fatalities — i.e., deaths that occurred within six hours after exposure to the fires. The rapid fire fatalities represent approximately 80% of all fire fatalities; the remaining 20% (attributable to burn injuries and pulmonary lesions), with survival time of several weeks or months, are difficult to study.

shows a substantial predisposition to being fire casualties (approximately twice what might be expected according to the census data for age group distributions), whereas the age group 10 to 40 is well below the expectation.

At all ages, the absolute number of male fire deaths exceeds that of females, but this is particularly so in the 30 to 60 age group. The fraction of casualties with blood alcohol levels greater than 0.1% (the legal limit for drunkenness) rises rapidly to approximately 70% of all fatalities in the 30 to 60 age group. The pattern of a very substantial ingestion of alcohol prior to becoming a fire fatality, particularly for men, parallels the substantially higher alcoholism rate of men in this age group. Fifty percent of all fire fatalities above the age of 20 show an alcohol level above 0.1%.

DEMOGRAPHIC RESULTS

Fire fatality data are available from urban, suburban, and rural locations (Baltimore City, four large counties, and 19 small counties). In all three locations, casualties as a function of the ages of the fire victims show a similar trend. The age group 50 to 60 +

PHYSICAL CAUSES OF FIRE AND HUMAN RESPONSES

Fully 85% of fires that result in fatalities are caused by human misjudgment or by deliberate actions. By far the most damaging single cause is fire resulting from carelessly handled cigarettes (44%). More than

80% of the fatalities occur in residences, with four-fifths of those in living rooms or bedrooms. With rare exceptions (such as very young children and invalids), fire victims generally have been alerted to the fires and have made unsuccessful efforts to escape. Most victims were overcome while trying to escape from the room where the fire originated.

MEDICAL CONSEQUENCES OF FIRES

Figure 1 summarizes the medical findings. Apparent is the primacy of toxic gases as the cause of fire deaths (more than 70%). The largest fraction of those fatalities have carboxyhemoglobin (COHb) levels greater than 50%, the level considered to be the margin for survival. Measurements have shown that many fire victims with high carbon monoxide (CO) intakes have also been exposed to substantial amounts of hydrogen cyanide (HCN). The significance of the cyanide intake is difficult to assess because the sequence of inhalation of the two gases is unknown.

A number of the fire victims with COHb levels below 50% were found to have ingested substantial, but sublethal, doses of hydrogen cyanide. Animal experiments show that the two gases act additively, so that a combined exposure to sublethal concentrations of each may prove fatal. A second cause of death from sublethal levels of carbon monoxide can be tied to the observation that persons with impaired circulatory systems tend to succumb at carbon monoxide levels below 50%. This is unlikely to be a contributor in cases where there was a high alcohol intake because such intake significantly relaxes the circulatory system.

CONCLUSIONS

Preventive measures should concentrate on sources that contribute most significantly to the number of fatal fire incidents. The study suggests that

1. Materials, especially in bedrooms and living rooms, should be modified to withstand ignition by cigarettes (or the igniting power of cigarettes should be reduced);
2. The public should be educated to the risks of careless smoking, particularly when accompanied by excessive drinking; and
3. Early alerting devices such as smoke detectors should be used.

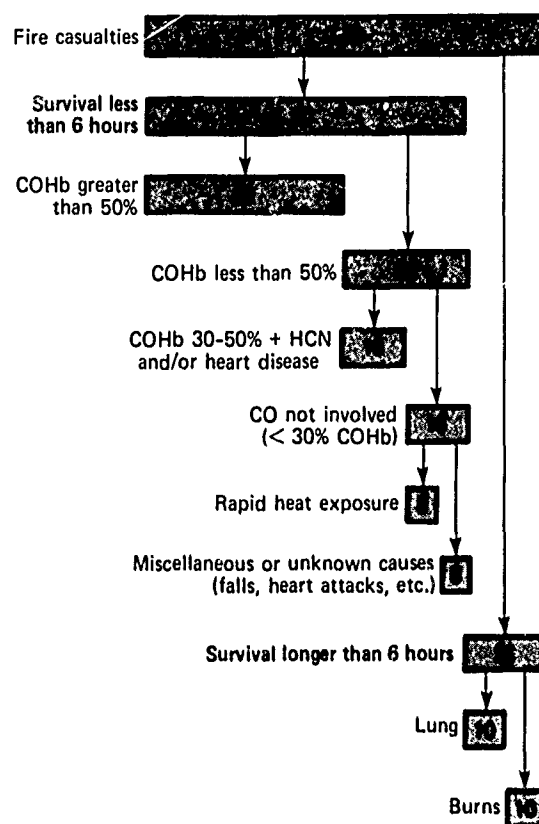


Fig. 1 Overall assessment of fire fatalities, showing the medical causes of death. The numbers in shaded boxes indicate the percentages of major events that resulted in fatalities.

Better medical treatment for survivors may depend to some extent on the ability to identify the specific causative agents in each fire situation. Especially in view of the large number of new synthetic materials used for construction, furnishings, and fire inhibitors, methods need to be developed to rapidly detect toxic substances (such as halogen acids, hydrogen cyanide, and carbon monoxide) in order to institute the most effective treatment as quickly as possible.

Authors: W. G. Bert and B. M. Halpin

Support: National Bureau of Standards
Grant G7-9016

DETERMINATION OF THE FLAMMABLE GASES EVOLVING FROM A BURNING PLASTIC

When a plastic burns, it decomposes to produce hot flammable gases that react quickly with air in a zone very near the surface. We have made the first detailed measurements of the flammable gases evolving from a burning, char-forming plastic.

BACKGROUND

Many unwanted domestic fires are initiated or fueled by plastics. The ignition, fire spread, and extinction behavior of plastics is strongly affected by the chemistry involved, which we are only beginning to understand. A better understanding of the chemistry could lead to better chemical means to inhibit and extinguish unwanted fires.

DISCUSSION

For a long time, indirect evidence has pointed to a qualitative picture of plastic combustion in which the heat-releasing chemical reactions take place in the gas phase (Fig. 1). The reaction zone is supplied on one side by flammable gases evolving from the solid and on the other by oxygen diffusing inward from the air. Some of the heat feeds back to the solid to sustain the decomposition reactions that produce the flammable gases. The consumption of oxygen in the reaction zone causes a gradient to be maintained in its

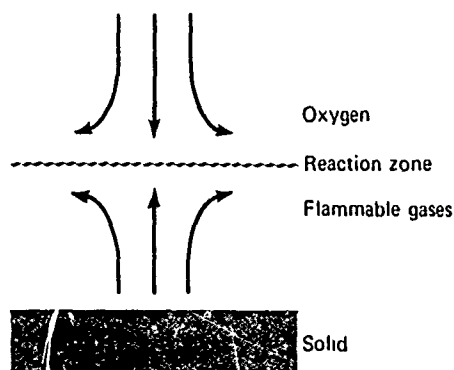


Fig. 1 A qualitative picture of the combustion of plastics. The plastic degrades thermally with production of flammable gases that react with oxygen in the gas phase. The reaction zone is only a fraction of a millimeter from the solid at normal pressures, but the distances increase at reduced pressure.

concentration that allows the diffusion of oxygen to continue.

The flammable gases evolving from burning plastic are attacked by oxygen within 0.1 mm of the surface. The gases had never been isolated and identified until recently, when two techniques were developed to achieve the steady-state combustion of plastics. One technique (Ref. 1), developed at the University of California (La Jolla), is appropriate for clean-burning plastics. However, most plastics of practical importance leave a char residue. The other technique, developed at APL (Ref. 2), works well with any plastic that can be coated on thin fiberglass yarn.

The coated yarn is pulled lengthwise through a cross flow of hot oxygen produced by a burner (Fig. 2). Each particle of plastic moving with the yarn is heated from room temperature to the ignition point. Then flammable gases begin to evolve and burn with the hot oxygen. As the particle continues its motion, its temperature rises, resulting in greater combustion intensities. The flame on the plastic is quenched by an exit thermal shield. Burned plastic (i.e. char) is continually replaced.

Gas samples can be withdrawn through a quartz needle (orifice of 0.05 mm diameter) and analyzed on a mass spectrometer. Heat transfer to the yarn can be measured (Ref. 3) and surface

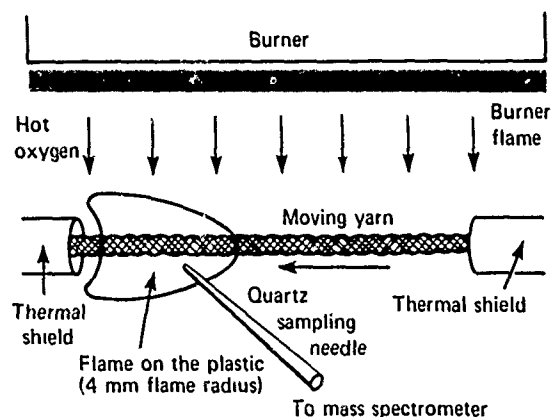


Fig. 2 Experimental apparatus for studying the combustion of plastics in steady state.

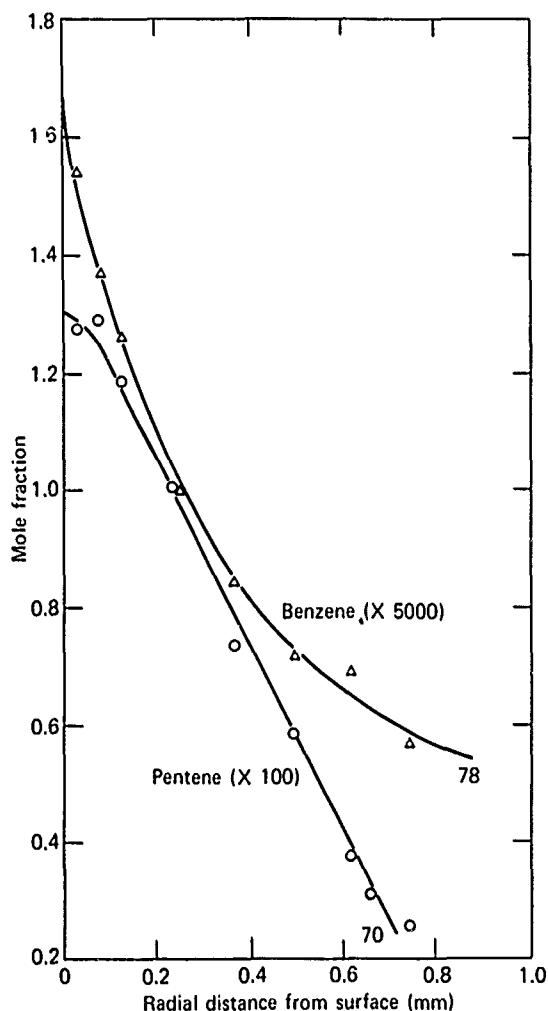


Fig. 3 Radial concentration profiles of two flammable gases evolving from burning polyvinyl chloride. The measurements shown were made at 0.1 atm pressure. At normal pressures (1 atm), the oxidation takes place much closer to the surface.

temperatures calculated (Ref. 4). The mass flux from the plastic is determined from the mass loss of the yarn and the speed.

We obtained a fiberglass yarn commercially coated with polyvinyl chloride (PVC), a char-forming plastic. The flammable gases of higher molecular weight that evolve from the PVC include benzene, pentene, and butene. Hydrocarbons of lower molecular weight make up the remaining flammable gases. Two concentration profiles (Fig. 3) show that thermal degradation of the gases takes place soon after they evolve. The fragments rather than the whole molecules react with the oxygen. The reactions of the fragments take place much farther from the surface (4 mm). The measurements shown were made at 0.1 atm pressure to expand the flame on the plastic. At normal pressure (1 atm), the oxidation takes place too close to the surface to permit detection of the flammable gases.

Our results confirm the picture of plastic combustion shown in Fig. 1 and point the way to analyses that may further elucidate the chemistry.

REFERENCES

1. K. Seshadri and F. A. Williams, "Structure and Extinction of Counterflow Diffusion Flames above Condensed Fuels: Comparison between PMMA and Its Liquid Monomer, Both Burning in Nitrogen-Air Mixtures," *J. Polymer Sci.* 16, 1978, p. 1755.
2. L. W. Hunter, C. Grunfelder, C. H. Hoshall, and R. M. Fristrom, "Combustion of Polyvinyl Chloride Studied by a Low-Pressure Moving Wire Technique," *Combust. Flame* 35, 1979, pp. 169-177.
3. L. W. Hunter and C. Grunfelder, "Heat Transfer Measurements in the Moving Wire Technique for Studying Polymer Flammability," *Combust. Flame* 34, 1979, pp. 265-274.
4. L. W. Hunter and S. Javin, "Steady State Temperature Distribution in a Solid Cylinder Moving in the Direction of Its Axis through a Cross-Flow of Hot Gas," *J. Heat Transfer* 99, 1977, pp. 668-674.

Author: L. W. Hunter

Support: National Bureau of Standards Grant G7-9016

A NEW LIDAR/FLUORESCENT TRACER TECHNIQUE FOR ATMOSPHERIC RESEARCH

A new remote-sensing technique developed by APL for the study of air motion and diffusion uses microscopic fluorescent particles as tracers and a light detection and ranging (lidar) system as the remote sensor. It permits much smaller quantities of atmospheric tracers to be detected than was previously possible.

BACKGROUND

Lidar has been used in meteorological studies and air pollution applications for well over a decade (see Ref. 1 for a survey). In particular, it found early application in the study of stack plumes (Ref. 2). Particulates emanating from power plant stacks are

readily detected by lidar. However, as the distance from the stack increases, the plume becomes progressively more diffuse and tenuous until it is finally obscured by the natural aerosol background, or it becomes unrecognizable after mixing with plumes from other sources.

The background aerosol concentration represents the "noise" in which the laser returns from particulates of interest (from stacks) must be resolved. With the advent of stack water scrubbers and particle precipitators, the concentration of particulates from stacks has been reduced considerably. In turn, the range at which the stack particles merge into the background has also been reduced. In general, the study of plume rise and behavior using conventional lidar techniques becomes restricted to the immediate vicinity of the stack (Ref. 3) or to extremely dirty plumes in a very clear environment (Ref. 4).

DISCUSSION

A technique has been developed that virtually eliminates the background aerosol limitation and allows plume behavior to be studied at extended ranges and in the presence of a complex "clutter" background. Microscopic fluorescent particles are injected into the plume and are excited by means of pulsed laser light (i.e., a lidar). The backscatter signal is composed of the return at the laser frequency from the background aerosols and from the fluorescent particles themselves and the return from the fluorescent particles at the shifted frequency. By filtering out the laser (or fundamental) frequency and selectively detecting only the shifted fluorescent frequency, the return from the background aerosols is eliminated.

The fluorescent plume can also be identified in the presence of background noise or clutter environ-

ments — clouds, stable layers, multiple sources of particulates, the ground, and buildings. Returns from these targets usually are at the laser frequency and do not contribute to the return at the shifted fluorescent frequency.

Because the returns from the dye and from the environment appear at different frequencies, each can be mapped selectively by proper filtering at the detector. The fluorescent plume can be mapped by filtering out the laser frequency. Conversely, the background can be mapped by centering the detector filter at the laser frequency. This can be done by using two detectors or by switching the filters of a single detector.

Finely powdered fluorescent aerosols that are environmentally safe and suitable for use as atmospheric tracers are produced as pigments for fluorescent paints. The characteristics of many such pigments produced by one manufacturer, the DAY-GLO Color Corp., were evaluated in the laboratory for use as atmospheric tracers. The fluorescence and excitation spectra were measured with a fluorometer developed by Benson and Kues (Ref. 5). Figure 1 summarizes the measurements of the fluorescence spectra. All of the pigments are approximated by one of these spectra. The excitation spectra of four representative materials are shown in Fig. 2.

The lidar system was assembled from equipment available within APL to test the concepts of the fluorescent tracer technique. The lidar contains a frequency-doubled Nd-YAG laser with a variable pulse rate of up to 200 Hz, an output wavelength of 532 nm, and a pulse length of 12 ns. This laser wavelength lies close to the peak of the excitation spectrum of the Fire Orange A-14 pigment (Fig. 2). The complete lidar consists of the narrow-beamwidth pulsed laser mounted on a plate along with a Cassegrainian telescope and a photomultiplier detector, with intervening optical filters that pass either the

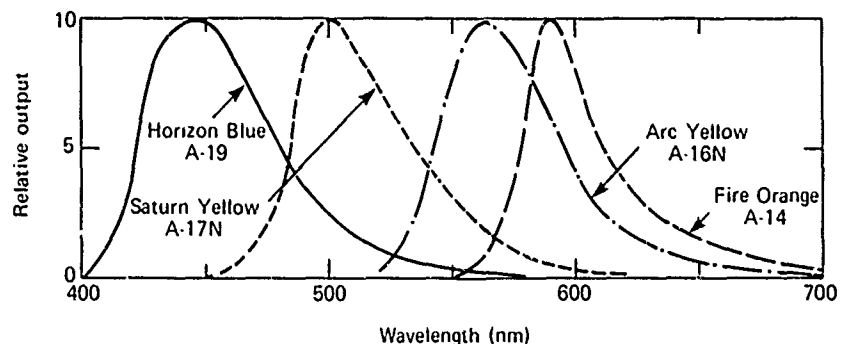


Fig. 1 Fluorescence spectra of selected fluorescent tracers.

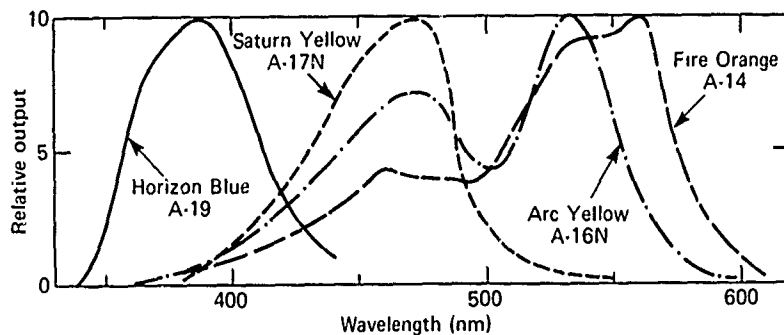


Fig. 2 Excitation spectra of selected fluorescent tracers.

laser frequency or the fluorescent frequency, depending on the experiment. The plate assembly is bolted to a mount that is electrically driven in azimuth and elevation. Controls for the mount and electrical read-outs of azimuth and elevation may be located remotely. The lidar and data recording equipment are mounted in a truck to ensure a flexible mobile system. The results of preliminary field experiments performed in the fall of 1978 are discussed in Ref. 6.

A full-scale field test was conducted in June 1979 with the cooperation of NASA at Wallops Island, Virginia. A motorized instrument, placed at the 150 ft level of an instrumented meteorological tower, dispensed the Fire Orange aerosol at a known constant rate. The tracer diffused as it drifted with the wind, forming a well defined plume that was invisible to the eye. The lidar scanned the plume and produced cross-sectional views of it on an intensity-modulated oscilloscope.

Figure 3 shows a horizontal cut through one portion of the plume; the only return is from the tracer. Figure 4 shows a vertical cut through the plume at one azimuth; returns from vegetation as well as from the tracer are observed. It is believed that these returns are due to the fluorescence of organic chemicals in the vegetation and to the inability of the filters to reject the laser wavelength.

The average concentration of fluorescent tracer in the plume, approximately $10 \mu\text{g}/\text{m}^3$, was determined from the dispensing rate of the tracer, from the wind speed, and from lidar measurements of the cross-sectional area of the plume. Later measurements were made with concentrations as low as $0.5 \mu\text{g}/\text{m}^3$. Measurements of the low natural-background fluorescence indicate that tracer concentrations as low as $0.006 \mu\text{g}/\text{m}^3$ may be detectable. For comparison,

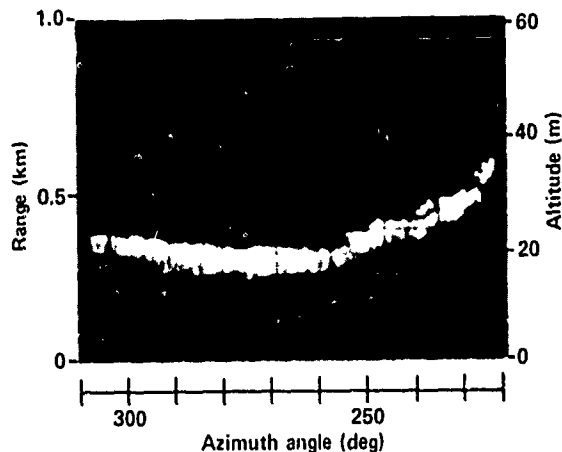


Fig. 3 Horizontal section of the fluorescent plume.

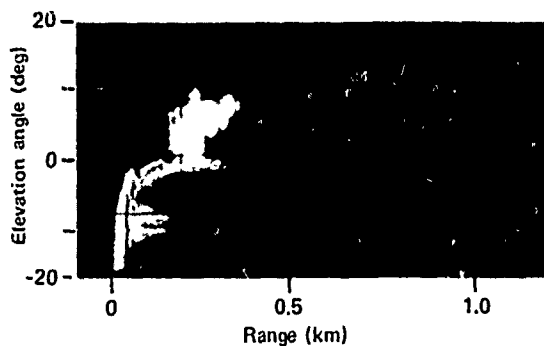


Fig. 4 Vertical section of the fluorescent plume. R^* is the range downwind of the dispenser.

the average natural-background concentration of aerosols in a clean outdoor environment is $50 \mu\text{g}/\text{m}^3$.

REFERENCES

1. R. Collis and P. Russell, "Laser Applications in Remote Sensing," *Remote Sensing for Environmental Science*, E. Schanda (Ed.), Springer-Verlag, 1976.
2. P. M. Hamilton, K. W. James, and D. J. Moore, "Observations of Power Station Plumes Using a Pulsed Ruby Laser Range Finder," *Nature* **210**, 1966.
3. G. Northam, I. Mills, W. Hunt, J. Weil, C. White, and F. Yelmek, "Validation of Plume Models for Tall Stacks Using Lidar Data," *Abstracts 8th International Laser Radar Conf.*, Drexel University, 1977.
4. E. E. Utte, "Results Obtained on Three Recent Mobile Lidar Studies of Smoke Plume Behavior and Density," *Abstracts 8th International Laser Radar Conf.*, Drexel University, 1977.
5. R. C. Benson and H. A. Kues, "Absorption and Fluorescence Properties of Cyanine Dyes" *J. Chem. Eng. Data* **22**, 1977, pp. 378-383.
6. J. R. Rowland and T. G. Konrad, "A New Lidar Technique Using Fluorescent Aerosols as Tracers of Air Motion and Diffusion," *Abstracts 9th International Laser Radar Conf.*, Munich, 1979.

Authors: J. R. Rowland and T. G. Konrad

Support: Indirectly Funded R&D

PATENTS

PATENTS ACTIVITIES

The APL Patents Office is responsible for ensuring compliance with contract and grant requirements relative to patent and data rights, as imposed by the various governmental agencies that sponsor work at the Laboratory. In addition to preparing formal disclosures of inventions for the appropriate sponsors, the Patents Office prepares and prosecutes patent applications on behalf of both the University and the Department of the Navy.

The following lists indicate the invention disclosures submitted to sponsors, the patent applications prepared and filed in the United States Patent Office, and the previously filed applications that were successfully prosecuted to issuance as patents, during Fiscal Year 1979.

INVENTION DISCLOSURES

- J. L. Abita—*Process for Extending the Life of Boron Nitride Crucible*
- J. L. Abita—*Surface Acoustic Wave (SAW) Attenuator*
- G. S. Bitings—*Circuitry for Generating a Present Number of Cycles, Represented by Two Out-of-Phase Pulses, Following a Start Pulse*
- G. S. Bitings—*Circuitry for Programmably Controlling the Power of a Sonar Pinger*
- G. S. Bitings—*Circuitry for Providing Improved High Power Output from a Transformer by Connecting Each Transformer Input to a Corresponding Driver Net*
- G. S. Bitings—*Method for Using Corrosible Electrical Apparatus in a Water Environment*
- B. G. Boone and T. Rankin—*Short Range CW Laser Apparatus for Wave Profiling*
- J. J. Breivogel—*Door Hinge Lock*
- H. K. Charles, Jr.—*Acoustic Thermometer Utilizing Surface Acoustic Waves*
- C. Feldman, H. K. Charles, Jr., and F. G. Satkiewicz—*Thin Film Solar Cell Employing a Metal Boride as One Electrode*
- R. E. Fischell and V. L. Piscane—*A Drag Free Lo-Lo Satellite System for Improved Gravity Field Measurements*
- R. B. Givens and B. H. Nall—*Horizon Indicator Employing Thermistors*
- J. T. Glover—*Cable Jig for Efficient Cable Handling*
- P. J. Grunberger, S. C. Jones, and H. D. Zink—*Method and Apparatus for Processing Synthetic Aperture Radar (SAR) Signals in Real-Time*
- J. F. Gulick—*Capacitive Pickoff for a Gyroscope*
- L. L. Hanson—*Panel Slide/Hinge*
- L. W. Hart and K. Reintz—*Permeable Spherical Shell Magnetometer*
- J. Herzog—*Interface Control Between an Antenna Pedestal and a Desk-Top Calculator*
- M. L. Hill, T. White, and J. Rowland—*Remote Detection of Chimney Plumes by Means of Atmospheric Electric Fields*
- E. J. Hoffman and W. P. Birmingham—*Global Positioning System Package (GPSPAC) Spaceborne Navigation Apparatus*
- E. C. Jarrell, D. R. Marlow, P. H. Gilbert, and J. F. Gulick—*RF Guidance System Design for Block I RAM Missile*
- E. C. Jarrell, D. R. Marlow, H. B. Tetens, and J. F. Gulick—*Target Seeker Simulator*
- C. A. Keller—*Fluid Layer Thickness Measuring Device*
- C. A. Keller—*Fluid Level Sensor with Digital Output*
- C. A. Keller—*Infra-red Fluid Level Detection System*
- C. A. Keller—*Measurement of Biofouling by Detecting Optical Attenuation*
- C. A. Keller—*Photon Energy Conversion Fluid Level Detector*
- C. A. Keller and M. S. Block—*Optical Water Pollutant Identification System*
- C. A. Keller and M. S. Block—*Self Cleaning Ultra-violet Fluid Level Measurement Device*
- B. E. Kuehne—*Six-Degree of Freedom (DOF) Missile Simulation Using Trim Aerodynamic Data*
- H. A. Kues, Jr. and R. H. Brown—*Current Profiling Dye Bomb*
- J. H. Loveless—*Motorized Wheel Chair*
- J. H. Loveless and W. Seamone—*Chin Controller with Optical Sensors for Electric Wheelchair Control*
- B. H. Nall—*Horizon Indicator Employing Heated Wires on an Acoustical Field*
- P. P. Pandolfini—*Heat Transfer Coefficient Measuring Instrument*
- T. O. Poehler, R. Potember, and D. O. Cowan—*Organic Memory or Threshold Switch Composed of Copper or Silver Complexed with TNAP or TCNQ Electron Acceptors*
- W. R. Powell, S. Ciarrocca, D. Thayer, and C. Williams—*Cases Software (CASES)*
- T. Rankin and R. L. Konigsterg—*Apparatus for Transforming the Vertical Acceleration from Body Coordinates into Inertial Coordinates*
- K. Reintz and L. W. Hart—*Solid State Magnetometer*
- C. H. Ronnenburg and R. L. Trapp—*Antenna Pattern Data System*
- S. L. Sachs and F. K. Hill—*Ultrasonic Cleaning Apparatus*
- S. B. Springer, E. L. True, A. W. Currano, and A. E. Dixon—*Microcomputer-Controlled Cartridge Tape Module*
- R. R. Talbott and R. R. Boss—*Frequency Synthesizer Control Apparatus*
- R. Talbott, G. Smoot, D. Prengaman, G. Starken, J. Doza, and A. Pruitt—*Digital Side-Look Sonar Scan Converter Device*
- R. E. Walker, B. F. Hochheimer, A. B. Fraser, and L. Mastracci—*Lidar System for Measuring Internal Waves in the Ocean Thermocline*
- J. J. Wozniak—*Towed Underwater Launch Platform*

PATENT APPLICATIONS

- R. E. Fischell—*Charge Control Switch Responsive to Cell Casing Deflection*
- R. E. Fischell—*Implantable Programmable Medication Infusion System*
- E. C. Jarrell, D. R. Marlow, H. B. Tetens, and J. F. Gulick—*Target Seeker Simulator*
- C. A. Keller—*Linear Response Capacitance Wave Height Measuring System*
- J. C. Murphy and R. C. Cole—*Laser Interferometry Detection Method/Apparatus for Buried Structure*
- J. R. Norton—*Radio Frequency Receiver for Satellite Navigation System*
- S. R. Osborne—*Planned View Display Raster Scan Generator*
- T. R. Small—*Superflywheel Energy Storage Device*
- L. E. Stillman and T. B. Coughlin—*Solar Panel Deployment Mechanism*

PATENTS ISSUED

- C. B. Bargeron—*Three Dimensional Laser Doppler Velocimeter*, No. 4,148,585
- R. E. Fischell—*Human Tissue Stimulation Electrode Structure*, No. 4,125,116
- R. E. Fischell and W. R. Powell—*Epidural Lead Electrode and Insertion Needle*, No. 4,141,365
- M. L. Hill and T. R. Whyte—*Ionic Air Speed Indicator*, No. 4,131,013
- R. P. Hockensmith, E. E. Skelton, and D. L. Thomas—*Process for Making a Plastic Antenna Reflector*, No. 4,154,788
- R. H. Lapp and J. D. Schneider—*Radar Sector Scan Reversal Apparatus*, No. 4,123,757
- W. Seamone—*Low Axial Force Servo Valve Spool*, No. 4,155,535

PUBLICATIONS AND PRESENTATIONS

PUBLICATIONS

- F. J. Adrian and A. N. Jette, "Valence Bond Study of Hyperfine Interactions and Structure of Kr_2F ," *Chem. Phys. Lett.* **64**, No. 3, 1979, pp. 555-559.
- F. J. Adrian and L. Monchick, "Theory of Chemically Induced Magnetic Polarization. Effects of S-T_{1/2} Mixing in Strong Magnetic Fields," *J. Chem. Phys.* **71**, No. 6, 1979, pp. 2600-2610.
- W. S. Amey, "The Computer Assisted Software Engineering (CASE) System," *Proc. 4th Software Engineering Conf.*, 1979, pp. 111-115.
- M. J. Amir and W. B. Newman, "Information: Unlimited Demands—Limited Funds (Testing the Viability of a Scientific Journal Collection in Light of Economic Realities)," *Collect. Manage.* **3**, No. 1, 1979, pp. 111-119.
- T. P. Armstrong (Univ. Kansas), S. M. Krimigis (APL), and R. P. Lepping (NASA/Goddard), "Magnetosheath Bursts of Predominantly Medium Nuclei Observed with Imp 8 on February 16, 1974," *J. Geophys. Res.* **83**, No. A11 1978, pp. 5198-5206.
- R. H. Bauer, "A Wind-Effects Model and Ocean Current Determination for a Satellite Updated Dead Reckoning System," *Proc. Annual Meeting, Institute of Navigation*, 1979.
- R. C. Benson and R. A. Meyer (APL) and M. E. Zaruba and G. M. McKinnon (JHMI), "Cellular Autofluorescence—Is it due to Flavins?" *J. Histochem. Cytochem.* **27**, No. 1, 1979, pp. 44-48.
- A. E. Berger, M. Ciment, and J. C. W. Rogers, "The Alternating Phase Truncation Method for Numerical Solution of a Stefan Problem," *J. Numer. Anal.* **16**, 1979, pp. 563-587.
- W. G. Berl and B. M. Halpin, "Human Fatalities from Unwanted Fires," *Fire J.* **73**, 1979, pp. 105-123.
- F. S. Billig, L. J. Crawford, and C. J. Gundersdorf, "Advanced Oceanographic Instrumentation Systems and Measurements at St. Croix, U.S.V.I.," *J. Hydronaut.* **13**, No. 3, 1979, pp. 77-84.
- J. F. Bird, "Hydromagnetic Perturbations Due to Localized Flows: An Eddy Theorem," *Phys. Fluids* **22**, No. 3, 1979, pp. 585-586.
- J. F. Bird (APL) and R. W. Massof (JHMI), "A General Zone Theory of Color and Brightness Vision. II. The Space-Time Field," *J. Opt. Soc. Am.* **68**, No. 11, 1978, pp. 1471-1481.
- B. I. Blum (APL) and R. E. Lenhard, Jr. (JHMI), "Privacy and Security in an Oncology Information System," *Proc. Second Annual Symposium on Computer Applications in Medical Care*, Nov 1978, pp. 500-508.
- J. Bohandy and B. F. Kim, "Conventional and Dye Laser Optical Spectra of Zinc Porphin in Anthracene," *Spectrochim. Acta* **35A**, 1979, pp. 415-420.
- H. Bouver (APL) and R. E. Bargmann (Univ. Georgia), "Numerical Solutions of the Beta Distribution," *Proc. Computer Science and Statistics: Annual Symposium on the Interface*, Institute of Statistics, 1978.
- H. Bouver (APL) and R. E. Bargmann (Univ. Georgia), "Optimizing the Karl Pearson Coefficients β_1 and β_2 in Statistical Curve Fitting when Using the Method of Moments," *Proc. ASA 1978 Statistical Computing Section*.
- P. R. Briggs and T. P. Armstrong (Univ. Kansas) and S. M. Krimigis (APL), "Hydrogen over Helium Enhancement in Successive Solar Flare Particle Events from the Same Active Region," *Astrophys. J.* **228**, 1979, pp. L83-L87.
- N. J. Brown, K. H. Eberius, R. M. Fristrom, K. H. Hoyerman, and H. G. Wagner, "Low Pressure Hydrogen/Oxygen Flame Studies," *Combust. Flame* **33**, 1978, pp. 151-160.
- N. J. Brown and R. M. Fristrom, "A Two Zone Model of Flame Propagation Applied to H₂-Air and HCl Inhibited Flames," *Fire Mater.* **2**, No. 3, 1978, p. 117.
- J. N. Campbell (JHMI), R. A. Meyer (APL), and R. H. LaMotte (JHMI), "Sensitization of Myelinated Nociceptive Afferents that Innervate Monkey Hand," *J. Neurophys.* **42**, No. 6, 1979, pp. 1669-1679.
- F. R. Castella, "Heading and Speed Errors for x,y Tracking Filters," *IEEE Trans. Aerosp. Electron. Syst.* **AES-15**, No. 2, 1979, pp. 284-287.
- H. Y. Chiu, "A State-Constrained Vehicle-Follower Approach to the Station-Egress Problem," *IEEE Trans. Veh. Technol.* **VT-28**, No. 1, 1979, pp. 70-79.
- H. Y. Chiu, R. M. Somers, and R. C. Benson, "Decomposition of Solid NaN₃ by CO₂ Laser Radiation," *Chem. Phys. Lett.* **61**, No. 1, 1979, pp. 203-208.
- L. L. Cronvich, "Aerodynamic Development of Fleet Guided Missiles in Navy's Bumblebee Program," *Proc. AIAA Aerospace Sciences Meeting*, Jan 1979.
- W. M. Cronyn, S. D. Shawhan, J. J. Rieckard, and D. G. Mitchell (Univ. Iowa) and E. C. Roelof and B. L. Gotwols (APL), "IPS Activity Observed as a Precursor of Solar Induced Terrestrial Activity," *AGARD Proc. No. 238* (Conf. on Operational Modeling of the Aerospace Propagation Environment), 1979, pp. 30-1 to 30-17.
- E. P. Cunningham, "Probability of Crashing from Monte Carlo Simulation," *J. Spacecr. Rockets* **16**, No. 5, 1979, pp. 348-350.
- A. J. Dessler (APL) and V. M. Vasyliunas (Max-Planck Inst. für Aeronomie), "The Magnetic Anomaly Model of the Jovian Magnetosphere: Predictions for Voyager," *Geophys. Res. Lett.* **6**, No. 1, 1979, pp. 37-40.
- G. L. Dugger, "Is There a Chance for OFEC?" *Astronaut. Aeronaut.* Nov 1979, pp. 36-42.
- T. W. Eagles and T. S. Margulies (APL) and J. Cohon and C. ReVelle (JHMI), "Multiobjective Regional Energy Location Model. Cost Versus Population Proximity Trade-Offs," *Trans. Am. Nucl. Soc.* **37**, 1979, pp. 613-615.
- P. B. Edwards, S. Favin, and J. L. Teesdale, "Evaluation of Educational Programs: Why? How? By Whom?" *Proc. 1979 Conf. on Frontiers in Education*, pp. 323-330.
- L. W. Ehrlich, "A Marching Technique for Nonseparable Equations," *Math. Computation* **33**, No. 147, 1979, pp. 881-890.
- L. W. Ehrlich, "The Numerical Solution of a Navier-Stokes Problem in a Stenosed Tube: A Danger in Boundary Approximations of Implicit Marching Schemes," *Comput. Fluids* **7**, 1979, pp. 247-256.

- L. W. Ehrlich, "Solving the Biharmonic Equation on Irregular Regions," *ACM Trans. Math. Software* 5, No. 3, 1979, pp. 251-258.
- L. W. Ehrlich, "On Some Iterative Methods for Solving Coupled Equations of Fluid Flow," *Proc. IMACS Conf.* 3, 1979, pp. 304-312.
- A. R. Elcrat (Wichita State Univ.) and V. G. Sigillito (APL), "A Spatial Decay Estimate for the Navier-Stokes Equations," *ZAMP* 30, 1979, pp. 449-455.
- R. A. Farrell and S. Favin (APL) and J. T. Sullivan, S. Vimolvanich, and P. H. E. Meijer (The Catholic Univ. America), "Coexistence Curves for Fourth-Neighbor Ising Models on the Face-Centered-Cubic Lattice," *Phys. Rev. B* 19, No. 9, 1979, pp. 4703-4710.
- M. R. Feinstein, J. W. Halley, and P. Scholfield, "Dynamics of Molten Salts," *J. Phys. Chem.* 12, No. 20, 1979, p. 4185.
- D. W. Fox, "An Initial Value Problem for Slow Flow in Stratified Fluids," *Developments in Mechanics* 10 (Proc. 16th Midwestern Mechanics Conf.), 1979, pp. 179-182.
- D. W. Fox, "Lower Bounds for Energies of Atoms," *Proc. 1978 Workshop on Mathematical Properties of Schrödinger Operators and Wave Functions*, 1979, pp. 73-84.
- D. W. Fox, "A Method for Lower Bounds for Frequencies of Thin Skew Plates," *Developments in Mechanics* 10 (Proc. 16th Midwestern Mechanics Conf.), 1979, pp. 127-130.
- R. M. Fristrom, "The Problems, Language and Scientific Basis of Flammability Testing," *IEEE Trans. Electr. Insul.* EI-132, No. 5, 1978, pp. 367-375.
- R. M. Fristrom (APL) and P. Van Tiggelen (Univ. Louvain, France), "An Interpretation of the Inhibition of C-H-O Flames by C-H-X Compounds," *Proc. 17th Combustion Institute Symp.*, 1979.
- J. Goldhirsh, "Cumulative Slant Path Rain Attenuation Statistics Associated with the Comstar Beacon at 28.56 GHz for Wallops Island, VA," *IEEE Trans. Antennas Propag.* AP-27, No. 6, pp. 752-758.
- J. Goldhirsh, "Predictive Methods for Rain Attenuation Using Radar and In-Situ Measurements Tested Against the 28 GHz Comstar Beacon Signal," *IEEE Trans. Antennas Propag.* AP-27, No. 3, 1979, pp. 398-406.
- J. Goldhirsh and I. Katz, "Useful Experimental Results for Earth-Satellite Rain Attenuation Modeling," *IEEE Trans. Antennas Propag.* AP-27, No. 3, 1979, pp. 413-415.
- G. Gücer (JHMI) and I. J. Viernstein (APL), "Long Term Intracranial Pressure Recording in the Management of Pseudotumor Cerebri," *J. Neurosurg.* 49, 1978, pp. 256-263.
- B. F. Hochheimer, "A Dye for Experimental Choroidal Angiography," *Exp. Eye Res.* 29, 1979, pp. 141-143.
- E. J. Hoffman (APL) and W. P. Birmingham (Naval Surface Weapons Center, Dahlgren), "GPSPAC: A Spaceborne GPS Navigation Set," *Proc. IEEE Position Location and Navigation Symp.*, Nov 1978, pp. 13-20.
- L. W. Hunter, "Models of Cable Tray Fires," *Trans. Am. Nucl. Soc.* 30, 1978, p. 673.
- L. W. Hunter, "Models of Horizontal Electric Cables and Cable Trays Exposed to a Fire Plume," *Combust. Flame* 35, 1979, pp. 311-329.
- L. W. Hunter and C. Grunfelder, "Heat-Transfer Measurements in the Moving-Wire Technique for Studying Polymer Flammability," *Combust. Flame* 34, 1979, pp. 265-274.
- L. W. Hunter, C. Grunfelder, C. H. Hoshall, and R. M. Fristrom, "Combustion of Polyvinyl Chloride Studied by a Low-Pressure Moving-Wire Technique," *Combust. Flame* 35, 1979, pp. 169-177.
- L. W. Hunter, C. H. Hoshall, C. Grunfelder, and R. M. Fristrom, "Moving Thermocouple Measurements of Heat Transfer in Hot Gases," *Proc. Materials Research Symp.*, 1978.
- T. Iijima and R. Fujii (Univ. Tokyo) and T. A. Potemra and N. A. Saffekos (APL), "Field-Aligned Currents in the South Polar Cusp and Their Relationship to the Interplanetary Magnetic Field," *J. Geophys. Res.* 83, No. A12, 1978, pp. 5595-5603.
- A. N. Jette and F. J. Adrian, "Identification of the V_i Center (F_3^{2-}) in LiF as an Interstitial F Atom," *Phys. Rev. Lett.* 43, No. 15, 1979, pp. 1119-1123.
- Y. Kamide (Kyoto Sangyo Industrial Univ., Japan) J. S. Murphree, C. D. Anger, and F. T. Berkey (Univ. Calgary), and T. A. Potemra (APL), "Nearly Simultaneous Observations of Field-Aligned Currents and Visible Auroras by the TRIAD and Isis 2 Satellites," *J. Geophys. Res.* 84, No. A8, 1979, pp. 4425-4431.
- B. F. Kim and J. Bohandy, "Site Selective Optical Spectra of Free Base Porphin in Anthracene," *J. Mol. Spectrosc.* 73, 1978, pp. 332-343.
- L. G. Kohlenstein, "On the Proportion of the Chesapeake Bay Stock of Striped Bass that Migrates into the Coastal Fishery," *Proc. Annual Meeting, American Fisheries Society*, Aug 1978.
- S. Koslov, "Radio-Frequency Radiation: The Buildup of Knowledge against the Background of Concern," *IEEE International Conf. on Communications*, Jun 1979, pp. 31.2.1-31.2.8.
- S. M. Krimigis (APL), T. P. Armstrong (Univ. Kansas), W. I. Axford (Max-Planck Inst. Aeronomy), C. O. Bostrom (APL), C. Y. Fan (Univ. Arizona), G. Gloeckler (Univ. Maryland), L. J. Lanzerotti (Bell Labs.), E. P. Keath, R. D. Zwickl, and J. F. Carbary (APL), and D. C. Hamilton (Univ. Maryland), "Hot Plasma Environment at Jupiter: Voyager 2 Results," *Science* 204, 23 Nov 1979, pp. 977-984.
- S. M. Krimigis (APL), T. P. Armstrong (Univ. Kansas), W. I. Axford (Max-Planck Inst. Aeronomy), C. O. Bostrom (APL), C. Y. Fan (Univ. Arizona), G. Gloeckler (Univ. Maryland), L. J. Lanzerotti (Bell Labs.), E. P. Keath, R. D. Zwickl, and J. F. Carbary (APL), and D. C. Hamilton (Univ. Maryland), "Low-Energy Charged Particle Environment at Jupiter: A First Look," *Science* 204, 1979, pp. 998-1003.
- S. M. Krimigis (APL), D. Venkatesan (Univ. Calgary), and J. C. Barichello and E. T. Saris (Democritus Univ. Thrace), "Simultaneous Measurements of Energetic Protons and Electrons in the Distant Magnetosheath, Magnetotail, and Upstream in the Solar Wind," *Geophys. Res. Lett.* 5, No. 11, 1978, pp. 961-964.
- J. R. Kuttler, "Dirichlet Eigenvalues," *SIAM J. Numer. Anal.* 16, No. 2, 1979, pp. 332-338.
- L. J. Lanzerotti (Bell Labs.), S. M. Krimigis and C. O. Bostrom (APL), W. I. Axford (Max-Planck Inst. Aeronomy), and R. P. Lepping and N. F. Ness (NASA/GSFC), "Measurements of Plasma Flow at the Dawn Magnetopause by Voyager 1," *J. Geophys. Res.* 84, No. A11, 1979, pp. 6483-6488.
- A. T. Y. Lui and C.-I. Meng, "Relevance of Southward Magnetic Fields in the Neutral Sheet to Anisotropic Distribution of Energetic Electrons and Substorm Ac-

- tivity," *J. Geophys. Res.* **84**, No. A10, 1979, pp. 5817-5827.
- J. H. Manley, "Implementing Change in Very Large Organizations," *TIMS Studies in the Management Sciences* **13**, 1979, pp. 189-203.
- T. S. Margulies, "Evaluation and Comparison of High Population Density Sites," *Trans. Am. Nucl. Soc.* **33**, 1979, pp. 615-617.
- C.-I. Meng, "Conjugate Low Energy Electron Observations Made by ATS-6 and DMSP-32 Satellites," *Geophys. Monogr.* **21**, 1979, pp. 96-109.
- C.-I. Meng, "Diurnal Variation of the Auroral Oval Size," *J. Geophys. Res.* **84**, No. A9, 1979, pp. 5319-5324.
- R. A. Meyer, "Light Scattering from Biological Cells: Dependence of Backscatter Radiation on Membrane Thickness and Refractive Index," *Appl. Opt.* **18**, No. 5, 1979, pp. 585-588.
- G. E. Mitzel (APL) and S. J. Clancy and W. J. Rugh (The Johns Hopkins Univ.), "On Transfer Function Representations for Homogeneous Nonlinear Systems," *IEEE Trans. Autom. Control* **AC-24**, No. 2, 1979, pp. 242-249.
- L. Monchick, "Differential Scattering of Polarized Molecules: Computations for He+CO," *J. Chem. Phys.* **71**, No. 2, 1979, pp. 578-581.
- L. Monchick, "On the Theory of Chemically Induced Electron Polarization (CIDEP). II. Potential Forced Diffusion," *J. Chem. Phys.* **70**, No. 11, 1979, pp. 4887-4892.
- L. Monchick (APL) and D. J. Kouri (Univ. Houston), "Magnetic Transitions in the Initial-1 Labeled Interpretation of the CS Approximation. Computations for He+HCl," *J. Chem. Phys.* **69**, No. 7, 1978, pp. 3262-3267.
- J. R. Morton, K. F. Preston, and S. J. Strach (National Research Council of Canada) and F. J. Adrian and A. N. Jette (APL), "Anisotropic Hyperfine Interactions of Rare-Gas Nuclei near Trapped Hydrogen Atoms," *J. Chem. Phys.* **70**, No. 6, 1979, pp. 2889-2893.
- W. B. Newman and M. J. Amir, "Report Literature: Selecting versus Collecting," *Special Libraries* **69**, No. 11, 1978, pp. 415-424.
- R. R. Newton, *The Moon's Acceleration and Its Physical Origins. Vol 1: As Deduced from Solar Eclipses*, The Johns Hopkins Univ. Press, Baltimore, 1979.
- R. R. Newton, "The Orientation of the Earth's Axis Two Millennia Ago," *Mon. Not. R. Astron. Soc.* **186**, 1979, p. 231.
- V. O'Brien and L. W. Ehrlich, "Variation of Wall Stress with Arterial Geometry," *Proc. 32nd Annual Conference, Alliance for Engineering in Medicine and Biology*, 1979, p. 145.
- D. E. Olsen, "A Confidence Interval for the Barlow-Scheuer Reliability Growth Model," *IEEE Trans. Rehab.* **R-27**, No. 5, 1978, pp. 308-310.
- V. L. Patel, R. J. Greaves, and S. A. Wahab (Univ. Denver) and T. A. Potemra (APL), "Dodge Satellite Observations of Pc3 and Pc4 Magnetic Pulsations and Correlated Effects in the Ground Observations," *J. Geophys. Res.* **84**, No. A8, 1979, pp. 4257-4266.
- V. L. Pisacane, "Filtering of Satellite-to-Satellite Observations," *Acta Astronaut.* **6**, 1979, pp. 685-696.
- V. L. Pisacane, A. Eisner, S. M. Yonoulis, R. J. McConahy, H. D. Black, and L. L. Pryor, "A Geos 3 Orbit Determination Experiment," *J. Geophys. Res.* **84**, No. B8, 1979, pp. 3926-3932.
- R. S. Potember and T. O. Poehler (APL) and D. O. Cowan (The Johns Hopkins Univ.), "Electrical Switching and Memory Phenomena in Cu-TCNQ Thin Films," *Appl. Phys. Lett.* **34**, No. 6, pp. 405-407.
- T. A. Potemra, "Observation of the Birkeland Currents with the TRIAD Satellite," *Astrophys. Space Sci.* **58**, 1978, pp. 207-226.
- T. A. Potemra and C. O. Bostrom (APL) and J. P. Doering and J. S. Lee (The Johns Hopkins Univ.), "Observations of Low-Energy Electrons from AE-C in the South Polar Cusp during the Geomagnetic Storm of September 21, 1977," *Space Sci. Rev.* **22**, 1978, pp. 659-666.
- W. R. Powell, "Simulation of the Community Annual Storage Energy System," *Efficient Comfort Conditioning: The Heating and Cooling of Buildings*, W. G. Berl and W. R. Powell (eds.), Westview Press, Boulder, 1979, pp. 25-51.
- A. J. Pue, "Implementation Trade-Offs for a Short-Headway Vehicle-Follower Automated Transit System," *IEEE Trans. Veh. Technol.* **VT28**, No. 1, 1979, pp. 46-54.
- A. J. Pue, "A State-Constrained Approach to Vehicle-Follower Control for Short Headway Automated Transit Systems," *J. Dyn. Syst. Meas. Control* **100**, Dec 1978, pp. 291-297.
- D. W. Rabenhorst, "Low Cost Flywheel Demonstration," *Proc. 1978 Mechanical and Magnetic Energy Storage Contractors' Review Meeting*, 1979, pp. 44-54.
- D. W. Rabenhorst, "Low Cost Flywheel Energy Storage System Demonstration," *Proc. 14th Intersociety Energy Conversion Engineering Conf.* **1**, 1979, pp. 374-378.
- J. D. Randall, "Numerical Solution to the Embedding Equations Applied to the Landau Melting Problem," *Int. J. Heat Mass Transfer* **21**, 1978, pp. 1447-1449.
- J. P. Reilly, "Electric Field Induction on Sailboats and Vertical Poles," *IEEE Trans. Power Apparatus Systems* **PAS-97**, No. 4, Jul-Aug 1978, pp. 1373-1383.
- J. P. Reilly, "Electric and Magnetic Field Coupling from High Voltage AC Power Transmission Lines—Classification of Short-Term Effects on People," *IEEE Trans. Power Apparatus Systems* **PAS-97**, No. 6, Nov-Dec 1978, pp. 2243-2252.
- J. P. Reilly, "Short-Term Effects on People," Chapter 4, *The Electrostatic and Electromagnetic Effects of AC Transmission Lines*, IEEE Course Text No. 79, EHO 145-3-PWR, 1979.
- E. C. Roelof, "Solar Energetic Particles: From the Corona to the Magnetotail," *Geophys. Monogr.* **21**, 1979, pp. 220-241.
- E. C. Roelof and R. E. Gold, "Prediction of Solar Energetic Particle Event Histories Using Real-Time Particle and Solar Wind Measurements," *AGARD PROC. No. 238* (Proc. Conf. on Operational Modelling of the Aerospace Propagation Environment), 1979, pp. 29-1 to 29-13.
- J. C. W. Rogers (APL) and A. E. Berger and M. Ciment (Naval Surface Weapons Center), "The Alternating Phase Truncation Method for Numerical Solution of a Stefan Problem," *J. Numer. Anal.* **16**, No. 4, 1979, pp. 563-587.
- N. Rubinstein and W. C. Caywood, "Flight Vibration Environments Defined from Mk 12 Booster Static Tests," *J. Spacecr. Rockets* **16**, No. 4, 1979, pp. 214-217.
- N. Rubinstein, V. G. Sizantov, and J. T. Stadter, "Bounds to Frequencies of Shafts in Torsional Vibration with

- Restraints and Attached Masses," *J. Sound Vib.* **61**, No. 1, 1978, pp. 31-44.
- N. A. Saffekos and T. A. Potemra (APL), P. M. Kintner, Jr. (Cornell Univ.), and J. L. Green (Univ. Iowa), "Field-Aligned Currents, Convection Electric Fields and ULF-ELF Waves in the Cusp," *J. Geophys. Res.* **84**, No. A4, 1979, pp. 1391-1401.
- J. A. Schetz and S. Favin, "Numerical Solution of a Body-Propeller Combination Flow Including Swirl and Comparisons with Data," *J. Hydronaut.* **13**, No. 2, 1979, pp. 46-51.
- D. M. Silver (APL) and S. Wilson (Science Research Council), "Universal Basis Sets for Electronic Structure Calculations," *J. Chem. Phys.* **69**, No. 8, 1978, pp. 3787-3789.
- D. M. Silver (APL), S. Wilson (Science Research Council), and C. F. Bunge (Univ. Nacional Autónoma México), "Comparison within the Algebraic Approximation of Configuration Interaction and Many-Body Perturbation Theory for the Be Ground State," *Phys. Rev. A* **19**, No. 4, 1979, pp. 1375-1382.
- D. M. Silver (APL), S. Wilson (Science Research Council), and W. C. Nieuwpoort (Univ. Groningen), "Universal Basis Sets and Transferability of Integrals," *Int. J. Quantum Chem.* **XIV**, 1978, pp. 635-639.
- J. T. Stadter and R. O. Weiss, "Analysis of Contact Through Finite Element Gaps," *Comput. Struct.* **10**, 1979, pp. 867-873.
- W. D. Stanbro and W. D. Smith, "Kinetics and Mechanism of the Decomposition of N-Chloralanine in Aqueous Solution," *Environ. Sci. Tech.* **13**, 1979, pp. 446-451.
- A. M. Stone, "Geothermal in Hungary," *Geothermal Energy Mag.* **6**, No. 11, 1978, pp. 27-28.
- C.-M. Tang, "Electromagnetic Fields Due to Dipole Antennas Embedded in Stratified Anisotropic Media," *IEEE Trans. Antennas Propag.* **AP-27**, No. 5, 1979, pp. 665-670.
- B. E. Tossman, D. L. Thayer, and W. A. Swartz, "An Underwater Towed Electromagnetic Source for Geophysical Exploration," *IEEE J. Oceanic Eng.* **OE-4**, No. 3, 1979, pp. 84-89.
- W. J. Toth, "Overview of Geothermal Energy Markets in the East," *Proc. Geothermal Resources Council Symp. on Geothermal Energy and Its Direct Uses in the Eastern United States*, Apr 1979.
- W. J. Toth and F. C. Paddison, "Geothermal Energy Markets on the Atlantic Coastal Plain," *Proc. Sixth Energy Technology Conf.*, Feb 1979. Also, *Proc. Geothermal Resources Council Symp. on Geothermal Energy and Its Direct Uses in the Eastern United States*, Apr 1979.
- H. K. Utterback, J. M. Whisnant, and R. E. Jenkins, "A System of Software for the TIP Spacecraft Computer," *J. Br. Interplanet. Soc.* **31**, 1978, pp. 455-461.
- V. J. Vigorita and P. K. Gupta (JHMI), C. B. Barger (APL), and J. K. Frost (JHMI), "Occurrence and Identification of Intracellular Calcium Crystals in Pulmonary Specimens," *Acta Cytologica* **23**, No. 1, 1979, pp. 49-52.
- P. J. Waltrup, F. S. Billig, and R. D. Stockbridge, "Procedure for Optimizing the Design of Scramjet Engines," *J. Spacecr. Rockets* **16**, No. 3, 1979, pp. 163-171.
- D. C. Wenstrand, "Measurements of Vertical Profiles of Oceanic Current and Richardson Number near St. Croix, U.S.V.I.," *J. Hydronaut.* **13**, No. 3, 1979, pp. 69-76.
- J. Wilhelm and E. Friis-Christensen (Danish Meteorological Inst.) and T. A. Potemra (APL), "The Relationship Between Ionospheric and Field-Aligned Currents in the Dayside Cusp," *J. Geophys. Res.* **83**, No. A12, 1978, pp. 5586-5594.
- S. Wilson (Science Research Council) and D. M. Silver (APL), "Diagrammatic Many-Body Perturbation Expansion for Atoms and Molecules: IV. Fourth-Order Linked Diagrams Involving Quadruply-Excited States," *Comput. Phys. Commun.* **17**, 1979, pp. 47-50.
- S. Wilson (Science Research Council) and D. M. Silver (APL), "Diagrammatic Perturbation Theory: Evaluation of Fourth-Order Energy Terms Involving Quadruply-Excited States for Closed-Shell Systems," *Mol. Phys.* **36**, No. 5, 1979, pp. 1539-1548.
- S. Wilson and D. M. Silver, "Fourth-Order Terms in the Diagrammatic Perturbation Expansion for the Electronic Energy of Atoms and Molecules," *Int. J. Quantum Chem.* **XV**, 1979, pp. 683-692.
- S. Wilson (Science Research Council) and D. M. Silver (APL), "Universal Basis Sets in Molecular Calculations," *Chem. Phys. Lett.* **63**, No. 2, 1979, pp. 367-369.
- S. M. Yionoulis, A. Eisner, V. L. Pisacane, H. D. Black, and L. L. Pryor, "Geos 3 Ocean Geoid Investigation," *J. Geophys. Res.* **84**, No. B8, 1979, pp. 3883-3888.
- M. L. Zeichner and P. J. Brusil (Mitre Corp.) and S. G. Tolchin (APL), "Distributed Processing Architecture for a Hospital Information System," *Proc. Third Annual Symp. on Computer Applications in Medical Care*, 1979, pp. 1-7.
- R. D. Zwickl, E. C. Roelof, R. E. Gold, and S. M. Krimigis (APL) and T. P. Armstrong (Univ. Kansas), "Z-Rich Solar Particle Event Characteristics 1972-1976," *Astrophys. J.* **225**, 1978, pp. 281-303.

PRESENTATIONS

- R. H. Andreo, J. A. Krill, and R. A. Farrell, "Variational Methods for Electromagnetic Wave Scattering from Aerosol Clusters," *CSL Scientific Conf. on Obscuration and Aerosol Research*, Aberdeen Proving Ground, Md., 17-21 Sep 1979.
- C. B. Barger and R. A. Farrell (APL), W. R. Green (JHMI), and R. L. McCally (APL), "Endothelial Alterations from Exposure to Infrared Radiation," 38th Clinical Meeting of Wilmer Ophthalmological Inst., Johns Hopkins Hospital, Baltimore, 25-27 Apr 1979.
- C. B. Barger and R. B. Givens, "Precursive Blistering in the Localized Corrosion of Aluminum," *Corrosion Research Conf.*, Atlanta, 12-14 Mar 1979.
- R. Bauer, "Improved Dead Reckoning Considering Wind and Current," *Institute of Navigation Meeting*, Springfield, Va., 6-8 Mar 1979.
- H. D. Black, "The Transit System, 1977 Performance Plans and Potential," *The Royal Society Discussion Meeting on Satellite Doppler Tracking and Geodetic Applications*, London, 10-11 Oct 1978.

- B. I. Blum (APL) and C. J. Johns, E. E. McColligan, C. R. Smith, and D. M. Steinwachs (JHMI), "A Low Cost Computerized Ambulatory Medical Information System," ACEMB Annual Conf., Atlanta, 21-25 Oct 1978.
- W. Ebert and M. Feen, "Ionosphere Refraction Correction," Institute of Navigation Meeting, Springfield, Va., 6-8 Mar 1979.
- L. W. Ehrlich, "Numerical Solution of the Flow of a Fluid of Second Grade," Fall SIAM National Meeting, Denver, 12-14 Nov 1979.
- L. W. Ehrlich, "On Some Iterative Methods for Solving Coupled Equations of Fluid Flow," 3rd IMACS International Symp., Lehigh Univ., 20-22 Jun 1979.
- B. M. Elder, S. F. Oden, and D. E. Buchholz, "A Data Formatter and Control Unit for the SEASAT-A Synthetic Aperture Radar Ground Support Network," International Telemetry Conf., Los Angeles, 14-16 Nov 1978.
- M. R. Feinstein, "Dynamics of Molten Salts," Gordon Conf. on Molten Salts and Metals, Wolfeboro, N.H., 20-24 Aug 1979.
- M. R. Feinstein, R. A. Farrell, and R. W. Hart, "Variational Calculations of Scattering from a Sphere," CSI Scientific Conf. on Obscuration and Aerosol Research, Aberdeen Proving Ground, Md., 17-21 Sep 1979.
- D. W. Fox, "Bounds for Frequencies of Elastic Structures at Johns Hopkins" and "Two-Sided Rayleigh-Ritz Bounds," EUROMECH Colloq. on Eigenfrequencies of Continuous Structures, Metrafured, Hungary, 21-23 Feb 1979.
- D. W. Fox, "A Method for Lower Bounds for Frequencies of Thin Skew Plates" and "An Initial Value Problem for Slow Flow in Stratified Fluids," 16th Midwestern Mechanics Conf., Kansas State Univ., 0-21 Sep 1979.
- G. Güter (JHMI) and L. J. Viernstein (APL), "Continuous Recording of ICP in the Normal Monkey," American Association of Neurological Surgeons Conf., Los Angeles, Apr 1979. Also presented at International Symp. on Intracranial Pressure, Williamsburg, Va., Jun 1979.
- G. Güter (JHMI) and L. J. Viernstein (APL), "New Developments in Continuous ICP Measurements," JHH Medical and Chirurgical Society Meeting, Baltimore, Feb 1979.
- H. S. Hopfield, "Improvements in the Tropospheric Refraction Correction for Range Measurement," The Royal Society Discussion Meeting on Satellite Doppler Tracking and Geodetic Applications, London, 10-11 Oct 1978.
- L. W. Hunter, "Analysis of Cable Tray Fires," Water Reactor Safety Research Information Meeting, Nuclear Regulatory Commission, Gaithersburg, Md., 6-9 Nov 1978.
- L. W. Hunter, "APL Models of Cable Fires," Joint Meeting, NBS/NRC, Gaithersburg, Md., 8 Nov 1979.
- L. W. Hunter, "Combustion of Poly(vinyl chloride) Studied by a Low Pressure Moving Wire Technique," Technical Meeting on Chemical and Physical Processes in Combustion, The Combustion Institute, Miami Beach, 29 Nov-1 Dec 1978.
- L. W. Hunter, "Models of Cable Tray Fires," Center for Fire Research, National Bureau of Standards, Gaithersburg, Md., 6 Jun 1978. Also presented at American Nuclear Society Meeting, Washington, 12-16 Nov 1978.
- L. W. Hunter, "Prediction of the Fire Resistance of Cable Penetration Seals," 7th Water Reactor Safety Research Information Meeting, Nuclear Regulatory Commission, Gaithersburg, Md., 5-9 Nov 1979.
- R. E. Jenkins (APL) and C. F. Leroy (Defense Mapping Agency), "'Broadcast' versus 'Precise' Ephemeris—Apples and Oranges," Proc. International Geodetic Symp. on Satellite Doppler Positioning, Jan 1979.
- A. N. Jette, "The Disturbance Due to a Line Source in a Semi-Infinite Elastic Medium. Three Dimensional Treatment," American Physical Society Meeting, New York, 1 Feb 1979.
- S. C. Jones, J. D. Colson, and P. J. Grunberger, "A Simulator for the SEASAT-A Synthetic Aperture Radar Ground Support Network," International Telemetry Conf., Los Angeles, 14-16 Nov 1978.
- S. M. Krimigis, "Energetic Particle Environment of Jupiter as Determined by Voyagers 1 and 2," Univ. Iowa Colloq., 15 Oct 1979.
- S. M. Krimigis, "Hot Plasma in the Jovian Magnetosphere," NASA/GSFC Space Physics Seminar, 18 Oct 1979.
- S. M. Krimigis, "Investigation of the Planet Jupiter and the Outer Planets by Voyagers 1 and 2," Greek National Academy of Sciences, Athens, 16 Nov 1979.
- S. M. Krimigis, "The Magnetosphere of Jupiter—A View from Voyager 1," APL Colloq., 18 May 1979.
- S. M. Krimigis, "Measurements of Hot Plasma in Jovian Magnetosphere by Voyagers 1 and 2," Univ. Calgary Seminar, 7 Dec 1979.
- G. E. Mitzel (APL) and S. J. Clancy and W. J. Rugh (The Johns Hopkins Univ.), "On Transfer Function Representations for Homogeneous Nonlinear Systems," IEEE Conf. on Decision and Control, San Diego, 10-12 Jan 1979.
- I. Monchick, "Vibrational Excitation of Oxygen and Enhanced Radiation of Δ_2 O₂ during Certain Aurorae," Max-Planck Inst. Physik und Astrophysik, Munich, 22 May 1979.
- L. Monchick (APL) and J. Schäfer (Max-Planck Inst. Physik und Astrophysik), "Ab Initio Calculations of the Transport Cross-Section of H₂," VIIIth International Symp. on Molecular Beams, Riva del Garda, Italy, 28 May 1979.
- J. C. Murphy, "Applications of Laser Interferometry to Photoacoustic Spectroscopy," Univ. Maryland Seminar, 19 Oct 1979.
- F. C. Paddison, C. S. Leffel, Jr., and W. J. Toth (APL) and R. S. P. Weissbrod (The Johns Hopkins Univ., Metro Center), "Direct Applications of Geothermal Energy in the Eastern United States and Estimates of Life Cycle Costs," AIIE Seminar, Washington, 31 Oct 1978.
- J. G. Parker, "Active Acoustic Detection of Leaks in Underground Pipelines," The Johns Hopkins Univ. Mechanics and Materials Seminar, 3 Oct 1979.
- V. L. Pisacane and S. C. Dillon, "Terrestrial Coordinates of the Pole from Multiple Satellite Data," 6th Annual Meeting, European Geophysical Society, Vienna, 11-14 Sep 1979.
- T. A. Potemra, "Characteristics of Auroral Currents as Determined by TRIAD," International Magnetospheric Study Workshop, Skokloster, Sweden, 3-7 Sep 1979.
- T. A. Potemra, "Hall Currents in the Aurora," Hall Symp., The Johns Hopkins Univ., 13 Nov 1979.

- E. Prozeller, "Spread-Spectrum from NOVA Satellites," Institute of Navigation Meeting, Springfield, Va., 6-8 Mar 1979.
- J. P. Reilly, "An Approach to the Realistic-Case Analysis of Electric Field Induction from AC Transmission Lines," Third International Symp. on High Voltage Engineering, Milan, Aug 1979.
- J. P. Reilly, "Electric Field Induction on Long Objects—A Methodology for Transmission Line Impact Studies," IEEE Winter Power Engineering Society Meeting, New York, Feb 1979.
- J. P. Reilly and M. Cwiklewski, "A Realistic Case Analysis of Electric Field Induction on Vehicles near AC Transmission Lines," IEEE Canadian Conf. on Communications and Power, Montreal, 18-20 Oct 1978.
- J. C. W. Rogers, "The Dam Problem" and "Free Boundary Problems as Conservation Laws," Univ. Florence, Italy, 2-3 Oct 1979.
- J. C. W. Rogers, "Downstream Boundary Conditions for Incompressible Flows," ICASE Colloq., Hampton, Va., 12 Dec 1979.
- J. C. W. Rogers, "Free Boundary Problems and Turbulence in Hydrodynamics," CNRS, Marseille, 25 Sep 1979, and Mathematics Colloq., Montpellier, 27 Sep 1979.
- J. C. W. Rogers, "Relation of the One-Phase Stefan Problem to the Seepage of Liquids and Electrochemical Machining" and "The Formulation of Free Boundary Problems as Conservation Laws," Intensive Seminar on Free Boundary Problems, Pavia, Italy, 19-20 Sep 1979.
- L. J. Rueger, "Navy Navigation Satellite System (NAV-SAT)," Baltimore Section, IEEE Aerospace and Electronics Systems Group, Baltimore, 27 Mar 1979.
- L. R. Scott, "Notation for Software Development," ACM Conf., Washington, 5 Dec 1978.
- D. M. Silver, "Application of Many-Body Perturbation Theory to the Calculation of Potential Energy Surfaces," 3rd International Congress of Quantum Chemistry, Kyoto, 2 Nov 1979.
- D. M. Silver, "Electron Correlation and Interaction Energies Between Closed-Shell Systems Using Many-Body Perturbation Theory," Symp. on Many-Body Theoretical Approaches to Electron Correlation in Molecules, Kobe, 28 Oct 1979.
- D. M. Silver, "Interaction Potentials for Chemical Reaction Systems," Howard Univ. Chemistry Seminar, 28 Sep 1979.
- D. M. Silver (APL), E. F. Jendrick and M. H. Alexander (Univ. Maryland), and B. E. Wilcomb and P. J. Dagdigan (The Johns Hopkins Univ.), "Rotationally Inelastic Scattering of LiH ($j=1$) by He," American Physical Society Meeting, Washington, 25 Apr 1979.
- D. M. Silver (APL) and S. Wilson (Daresbury Labs, Warrington, UK), "Universal Basis Sets in Molecular Calculations," American Chemical Society Meeting, Washington, 10 Sep 1979.
- W. J. Toth, "Geothermal Energy in Agri-Business," Maryland State Planning Office Workshop, Salisbury, 14 Dec 1978.
- J. M. Whsnant and R. E. Jenkins, "The TIP Navy Navigation Satellite and Its Onboard Computer System," IEEE Position Location and Navigation Symp., San Diego, 6-9 Nov 1978.
- The following papers were presented at the Spring Meeting of the American Geophysical Union, Washington, 28 May-1 Jun 1979:
- W. Baumjohann and H. Sulzbacher (Univ. Münster) and T. A. Potemra (APL), "Simultaneous Observations of a Westward Electrojet with TRIAD and the Scandinavian Magnetometer Array;"
- J. F. Carbary, "Periodicities in the Jovian Magnetosphere as Seen by the Voyager-1 Spacecraft;"
- R. E. Gold and E. C. Roelof, "Energetic Particle Recurrence and Escape During Solar Cycle 20;"
- R. A. Greenwald (Max-Planck Inst. für Aeronomie) and T. A. Potemra and N. A. Saffekos (APL), "Comparison of Ionospheric Electric Fields and Field-Aligned Currents Near the Harang Discontinuity;"
- G. Gustafsson, T. A. Potemra, and N. A. Saffekos, "Correction of Variations in the TRIAD Magnetic Field Data Due to Attitude Uncertainties;"
- E. Kirsch (Max-Planck Inst. für Aeronomie), and S. M. Krimigis, J. W. Kohl, and E. P. Keath (APL), "Search for Jupiter X Rays;"
- A. T. Y. Lui and C.-I. Meng, "Relevance of Southward Magnetic Fields in the Neutral Sheet to Anisotropic Distribution of Energetic Electrons and Substorm Activity;"
- C.-I. Meng, "Simultaneous Auroral and Electron Precipitation Observations Over the Dayside Oval;"
- D. G. Mitchell and E. C. Roelof, "Latitude Dependence of ~1 MeV Proton Flux Measured 1-5 AU;"
- T. A. Potemra, N. A. Saffekos, and G. Gustafsson, "Evaluation of Distant Magnetic Field Effects Associated with Field-Aligned Currents;"
- E. C. Roelof, "Interpretation of Energetic Particle Flux Anisotropies;"
- E. C. Roelof, "Superthermal Ions Near the Earth;"
- E. C. Roelof and R. E. Gold, "Enhancement of the Diffusive Walled Cavity Model for Interplanetary Propagation of Jovian Electrons;"
- N. A. Saffekos, T. A. Potemra, G. Gustafsson, and C.-I. Meng, "Simultaneous High- and Low-Altitude Cusp Boundary Observations;"
- L. J. Zanetti and T. A. Potemra (APL), J. P. Doering (The Johns Hopkins Univ.), R. L. Arnoldy (Univ. New Hampshire), and R. A. Hoffman (NASA/Goddard Space Flight Center), "Coincident Particle Observations from AE-C and ATS-6 During the Oct. 28, 1977 Geomagnetic Storm;"
- R. D. Zwickl, "Anisotropic Transport Properties of Low Energy Particles Observed During Energetic Particle Events;" and
- R. D. Zwickl and S. M. Krimigis (APL), L. J. Lanzerotti (Bell Telephone Labs.), and G. Gloeckler (Univ. Maryland), "Jovian (?) Proton and Electron Bursts Observed by Voyager 1."
- The following papers were presented at the American Physical Society Meeting, Chicago, 19-23 Mar 1979:
- M. E. Hawley, W. A. Bryden, A. N. Block, and D. O. Cowan (The Johns Hopkins Univ.), T. O. Poehler (APL), and J. P. Stokes (The Johns Hopkins Univ.), "Mott Transition and Magnetic Properties of HMTSF(TCNQ)_{1-x}(TCNQF₄)_x;"
- A. N. Jette and F. J. Adrian, "Structure of the V_1 -Center in LiF;"

- R. L. McCally and E. A. Michelson (APL) and E. S. Margolies (JHMI), "Photon Correlation Spectroscopy Investigations of Human Serum Low Density Lipoproteins;"
- R. S. Potember and T. O. Poehler (APL) and D. O. Cowan (The Johns Hopkins Univ.), "Switching and Memory in Organic Semiconductor Thin Film;"
- J. P. Stokes, A. N. Block, W. A. Bryden, D. O. Cowan, and M. E. Hawley (The Johns Hopkins Univ.) and T. O. Poehler (APL), "Mott Transition and Conductivity in the Organic Solid Solutions $\text{HMTSF}(\text{TCNQ})_x(\text{TCNQF}_4)_{1-x}$."

The following papers were presented to the Association for Research in Vision and Ophthalmology, Sarasota, 30 Apr-4 May 1979:

- R. H. Andreo and R. A. Farrell, "Calculated Corneal Small-Angle Light Scattering Patterns: Wavy Fibril Models;"
- C. B. Barger and R. A. Farrell (APL) and W. R. Green (JHMI), "Corneal Damage from Exposure to Infrared Radiation: Rabbit Endothelial Damage Thresholds;"
- R. A. Farrell, R. L. McCally, and C. B. Barger, "Corneal Damage from Exposure to Infrared Radiation: Calculated and Measured Endothelial Temperature Histories;"
- R. L. McCally and R. A. Farrell, "Structural Implications of Small Angle Light Scattering from Rabbit and Bovine Cornea."

The following papers were presented at the 16th International Cosmic Ray Conference, Kyoto, 6-18 Aug 1979:

- W. I. Axford (Max-Planck Inst. Aeronomie), S. M. Krimigis (APL), E. Kirsch (Max-Planck Inst. Aeronomie) and D. Hamilton and G. Gloeckler (Univ. Maryland), "Anisotropies of Low Energy Particles in Corotating Interaction Regions as Measured by Voyager 1 and 2;"
- R. E. Gold and E. C. Roelof, "Energetic Particle Recurrence and Escape During Solar Cycle 20;"
- R. Reinhard (ESTEC Corp., The Netherlands) and E. C. Roelof and R. E. Gold (APL), "Separation of Coronal from Interplanetary Propagation Effects in the Solar Particle Event of 10 April 1969;"
- R. D. Zwickl, E. C. Roelof, and R. E. Gold, "Transverse Interplanetary Propagation of <1 MeV Protons."

The following papers were presented at the American Geophysical Union Fall Meeting, San Francisco, 3-7 Dec 1979:

- T. P. Armstrong (Univ. Kansas) and S. M. Krimigis, J. F. Carbary, and R. D. Zwickl (APL), "Hot Plasma Bulk Motions in the Jovian Magnetosphere;"
- C. O. Bostrom, S. M. Krimigis, and J. F. Carbary (APL), L. J. Lanzerotti (Bell Labs.), T. P. Armstrong (Univ. Kansas), and G. Gloeckler (Univ. Maryland), "Observation of a Magnetospheric Wind in the Jovian Magnetosphere;"
- J. F. Carbary, "Periodicities in the Jovian Magnetosphere. Voyagers 1 and 2;"

- R. B. Decker and S. M. Krimigis (APL) and G. Gloeckler (Univ. Maryland), "Energy Spectra and Flux Anisotropies of CIR-Associated <25 keV Ions;"
- A. Eisner and H. D. Black, "Precision Orbit Determination with a Small Number of Ground Stations;"
- A. Eisner and S. M. Yionoulis, "Long Period Terms in the Upper Atmospheric Air Density;"
- G. Gloeckler (Univ. Maryland) and J. F. Carbary, S. M. Krimigis, and R. D. Zwickl (APL), "Hot Plasma in the Jovian Magnetosphere;"
- A. D. Goldfinger, "Refraction of Microwave Signals by Water Vapor;"
- D. C. Hamilton and G. Gloeckler (Univ. Maryland) and S. M. Krimigis (APL), "Charged Particle Composition in Jupiter's Magnetosphere;"
- E. P. Keath, S. M. Krimigis, and J. F. Carbary (APL), W. I. Axford (Max-Planck Inst. Aeronomie), and L. J. Lanzerotti (Bell Labs.), "Evidence for an Inner Jovian Plasmasphere Boundary;"
- S. M. Krimigis and R. D. Zwickl (APL), L. J. Lanzerotti (Bell Labs.), and T. P. Armstrong (Univ. Kansas), "Monoenergetic, Heavy Ion Plasma Beam Observed Near Jovian Magnetosphere Boundary by Voyager 2;"
- L. J. Lanzerotti (Bell Labs.), S. M. Krimigis and E. P. Keath (APL), and N. F. Ness, L. F. Burlaga, and K. W. Behannon (NASA/GSFC), "Energetics of the Jovian Plasma Sheet;"
- A. T. Y. Lui and C.-I. Meng (APL) and L. A. Frank and K. L. Ackerson (Univ. Iowa), "Substorm Behavior of the Magnetotail Plasma Sheet Near Its Midplane;"
- C.-I. Meng and J. F. Carbary (APL), S.-I. Akasofu (Univ. Alaska), J. P. Sullivan (M.I.T.), and R. P. Lepping (NASA/GSFC), "Association of the AE-Index with the Solar Wind Poynting Flux Incident on the Magnetosphere;"
- D. G. Mitchell and E. C. Roelof, " >50 keV Ion Events Upstream of the Earth's Bow Shock. 1. Dependence on Shock Parameters;"
- M. Paonessa, S. Brandon, J. Nonnast, and T. P. Armstrong (Univ. Kansas) and J. W. Kohl (APL), "Energy and Species Dependence of Charged Particle Absorption by Io and Europa;"
- V. L. Pisacane and S. M. Yionoulis, "Low-Low GRAVSAT Simulation Results;"
- E. C. Roelof and D. G. Mitchell (APL) and R. P. Lepping (NASA/GSFC), " >50 Ion Events Upstream of the Earth's Bow Shock. 2. Association with IMF Fluctuations;"
- N. A. Saffekos (APL), B. M. Shuman (AF Geophysics Lab.), and T. A. Potemra (APL), "Dual Satellite Observations of Geomagnetic Disturbances in Auroral Regions;"
- L. J. Zanetti and T. A. Potemra (APL) and J. P. Doering and J. S. Lee (The Johns Hopkins Univ.), "Characteristics of Low Energy Electron Precipitation;"
- R. D. Zwickl and S. M. Krimigis (APL), T. P. Armstrong (Univ. Kansas), and G. Gloeckler and D. C. Hamilton (Univ. Maryland), "Energetic Ion Events of Jovian Origin."

AUTHOR INDEX

AUTHOR INDEX

A

Adrian, F. J., 128, 131
Amey, W. S., 59
Anderson, R. J., 46

B

Bargeron, C. B., 96, 99
Barron, W. F., 83
Beal, R. C., 110
Berl, W. G., 144
Bird, J. F., 136
Blackburn, C. A., 101
Boyd, J. E., 19

C

Cronvich, L. L., 16

D

Davidoff, A. E., 90
Davis, E. A., 70
Deters, O. J., 96

E

Eckard, L. D., Jr., 37

F

Farrell, R. A., 134
Favin, S., 134
Fehlner, L. F., 19
Fischell, R. E., 101
Fountain, G. H., 43
Frost, J. K., 99
Funk, J. A., 74

G

Gates, M. H., 59
Gucer, G., 94
Gupta, P. K., 99

H

Halpin, B. M., 144
Heffernan, K. J., 43
Hester, R. B., 46
Hickerson, R. L., 113
Holland, R. L., 25
Hunter, L. W., 146

J

Jette, A. N., 125, 128

K

Kahn, S. A., 62
Keath, E. P., 34
Keirse, J. L., 74
Klein, D. B., 92
Konrad, T. G., 147
Krimigis, S. M., 34

L

Leffel, C. S., Jr., 32
Levy, L. J., 46
Liepman, H. P., 16

M

Mayr, M. J., 116
Meijer, P. H. E., 134
Meyer, J. H., 70
Monchick, L., 124, 131

O

Oden, S. F., 101

P

Paddison, F. C., 80, 83
Pandolfini, P. P., 74
Parker, J. G., 125
Peters, W. J., 111, 19
Plesser, K. T., 25
Pue, A. J., 142

R

Rankin, T. M., 116
Riedel, F. W., 108
Ronnenburg, C. H., 56
Rowland, J. R., 147

S

Schäfer, J., 124
Scheck, A. E., 25
Schneider, W., 92
Smola, J. F., 39
Sterne, D. F., 64
Sullivan, J. T., 134
Swartz, W. A., 43

T

Thompson, T., 46
Tisserand, L. E., 14
Toth, W. J., 76, 83
Trapp, R. L., 56

V

Viernstein, L. J., 94
Vigorita, V. J., 99
Vimolvanich, S., 134

W

Warnke, L. L., 49
Wozniak, J. J., 23

Y

Yu, K., 80, 83

Z

Zaremba, T., 43